



**QUEEN'S
UNIVERSITY
BELFAST**

DOCTOR OF PHILOSOPHY

Observations and modelling of intensity timeseries for biomedical and astrophysical applications

Dillon, Christopher

Award date:
2022

Awarding institution:
Queen's University Belfast

[Link to publication](#)

Terms of use

All those accessing thesis content in Queen's University Belfast Research Portal are subject to the following terms and conditions of use

- Copyright is subject to the Copyright, Designs and Patent Act 1988, or as modified by any successor legislation
- Copyright and moral rights for thesis content are retained by the author and/or other copyright owners
- A copy of a thesis may be downloaded for personal non-commercial research/study without the need for permission or charge
- Distribution or reproduction of thesis content in any format is not permitted without the permission of the copyright holder
- When citing this work, full bibliographic details should be supplied, including the author, title, awarding institution and date of thesis

Take down policy

A thesis can be removed from the Research Portal if there has been a breach of copyright, or a similarly robust reason. If you believe this document breaches copyright, or there is sufficient cause to take down, please contact us, citing details. Email: openaccess@qub.ac.uk

Supplementary materials

Where possible, we endeavour to provide supplementary materials to theses. This may include video, audio and other types of files. We endeavour to capture all content and upload as part of the Pure record for each thesis. Note, it may not be possible in all instances to convert analogue formats to usable digital formats for some supplementary materials. We exercise best efforts on our behalf and, in such instances, encourage the individual to consult the physical thesis for further information.

Observations and Modelling of Intensity Timeseries for Biomedical and Astrophysical Applications



Christopher John Dillon MSc

Faculty of Engineering and Physical Sciences
School of Maths and Physics
Queen's University Belfast

This dissertation is submitted for the degree of
Doctor of Philosophy

April 2022

*For all those who ask questions, and for all
those who answer them.*

DECLARATION

I hereby declare that except where specific reference is made to the work of others, the contents of this dissertation are original and have not been submitted in whole or in part for consideration for any other degree or qualification in this, or any other university. This dissertation is my own work and contains nothing which is the outcome of work done in collaboration with others, except as specified in the text and Acknowledgements. This dissertation contains fewer than 80,000 words.

Christopher John Dillon
April 2022

ABSTRACT

Statistical benchmarking was successfully applied to quantify and resolve below-noise-floor observations of intensity timeseries in both biomedical and astrophysical contexts. Noise models, and fully synthetic camera images were generated from Radox biochip tests, using statistical Z-score analysis and Monte-Carlo modelling techniques. These models were used to benchmark and develop a noise suppression code downstream. Additionally, image analysis software was created to automatically co-align and pre-process successive frames of observation. This resulted in greatly improved identification and extraction of below-noise-floor signatures, increasing the sensitivity and speed of important interventional biomedical testing, and directly leading to improvement in patient outcomes. These same techniques were then adapted for use for astrophysical analysis, in the investigation of stellar nanoflares. These small-scale flare events are below the noise floor for observation, but through combined statistical and Fourier analysis, alongside observation driven modelling, I extracted the underlying nanoflare characteristics in fully convective M dwarf stellar lightcurves. This analysis uncovered the hidden science in these stars, which are dominated by nanoflare energy hidden below seemingly quiescent and noisy lightcurves. There are two key parameters which govern the frequency and lifetime of flare signatures: α and τ . Flare events are believed to be governed by a power-law, equating the frequency of events to their rate of energy release. The index of this power-law is α , and is a key indication of the rate of energy release. Higher values of α correspond to more frequent flaring at lower energies. The other key nanoflare characteristic is the e -folding time or ' τ '. This is the time taken by a flare to lose approximately $1/e$ of its original energy through radiative cooling. In an initial study, I found the first observational evidence for stellar nanoflare activity in 3 fully convective M dwarf stars. These exhibited power-law indices in excess of $\alpha \geq 3$, a value much enhanced from power-law indices seen in other stars at higher energies. I then completed a follow up study, linking the enhanced rate of nanoflare activity to the convective nature of the stars finding that partially conductive MV stars exhibited little to no nanoflare activity signature. In contrast, fully convective MV stars exhibited α and τ values consistent with frequent nanoflare activity. This was likely due to altered plasma conditions, resulting in increased plasma resistivity and consequently enhanced Sweet-Parker reconnection at the nanoflare energy scale. This link to plasma resistivity suggests that the altered stellar

dynamo is not involved in nanoflare enhancement, lending support to emerging theories of solar-like dynamo activity in fully convective stars. This holds implications for the nature of the dynamo in our own Sun. The role of stellar nanoflares in answering these—and other—key questions have only just begun.

This synergistic statistical analysis has led to improved healthcare diagnostics and broadened our knowledge of poorly understood stellar nanoflares. Going forward, this style of cross-disciplinary research holds the potential to advance knowledge, while providing a key financial incentive to carry it out.

'Be curious, not judgemental.' Walt
Whitman

*'I cannae change the laws of
physics!'* Engineer Montgomery 'Scotty' Scott - Star Trek

TABLE OF CONTENTS

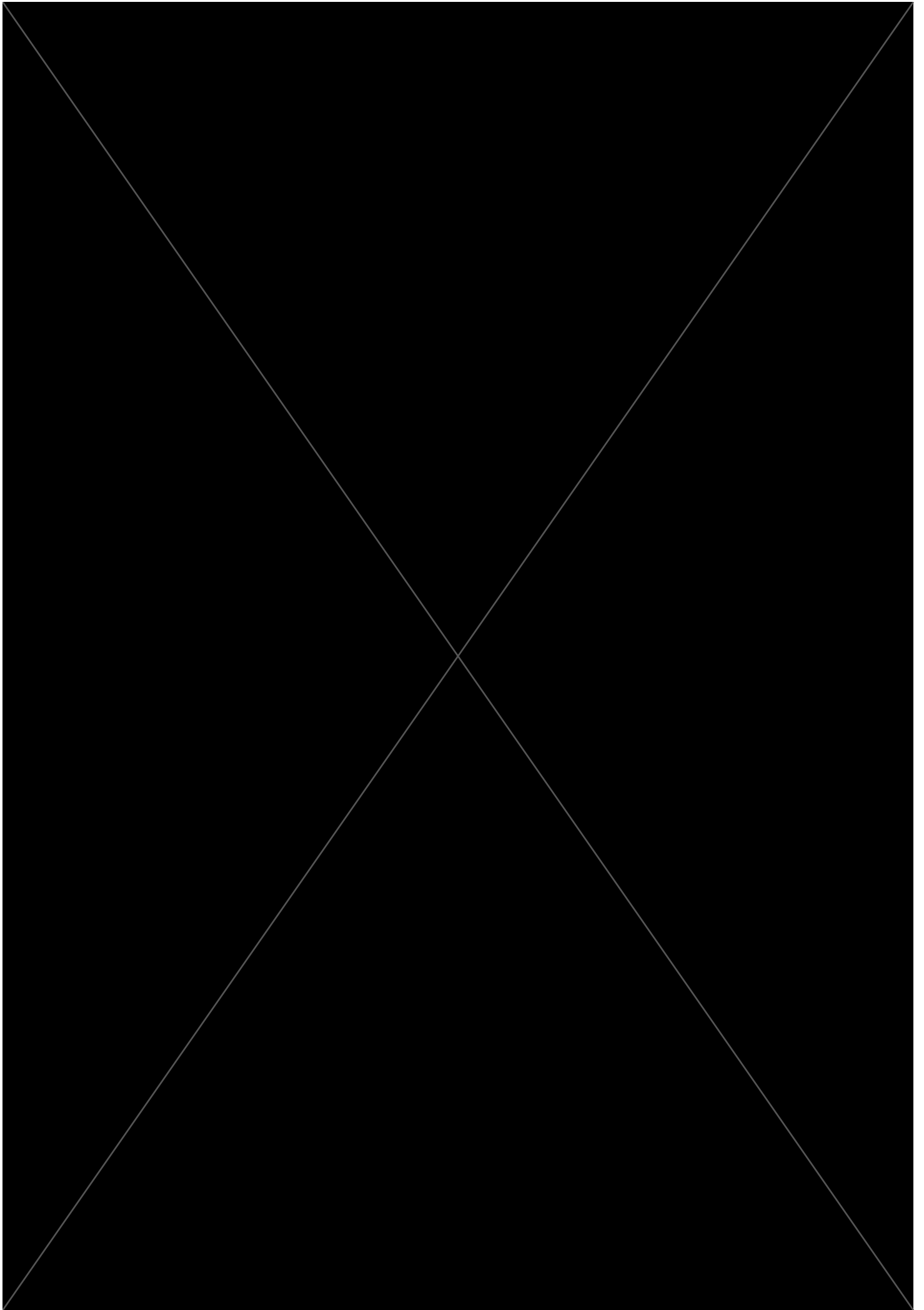
List of figures	ix
List of tables	xix
1 Introduction	1
1.1 How Do Astrophysics and Biomedical Applications Overlap?	3
1.2 What Are Nanoflares?	6
1.3 Thesis Overview	8
2 Theory	9
2.1 Signal and Noise in the Context of CCD Imaging	9
2.2 The Origin and Dynamics of Nanoflares	15
2.2.1 Magnetic Reconnection	15
2.2.2 Flares	19
2.2.3 Recent Advances in Stellar Nanoflares	26
2.3 Biomedical Imaging	30
3 Methods	40
3.1 Biomedical Modelling	41
3.1.1 Statistical Benchmarking of Noise and DTR Signatures	41
3.1.2 Monte-Carlo Simulation of Noise and Synthetic DTR Signals	44
3.1.3 Biochip ISolation Code Using Image Transforms : BISCUIT	45
3.2 Stellar Nanoflare Modelling	56
3.2.1 Choosing and Preparing the Timeseries	57
3.2.2 Statistical Analysis	60
3.2.3 Fourier Analysis	62
3.2.4 Observationally Driven Monte-Carlo Modelling of Nanoflare Time-series	64
3.2.5 Observational Considerations for Nanoflare Statistical and Fourier Analysis	68

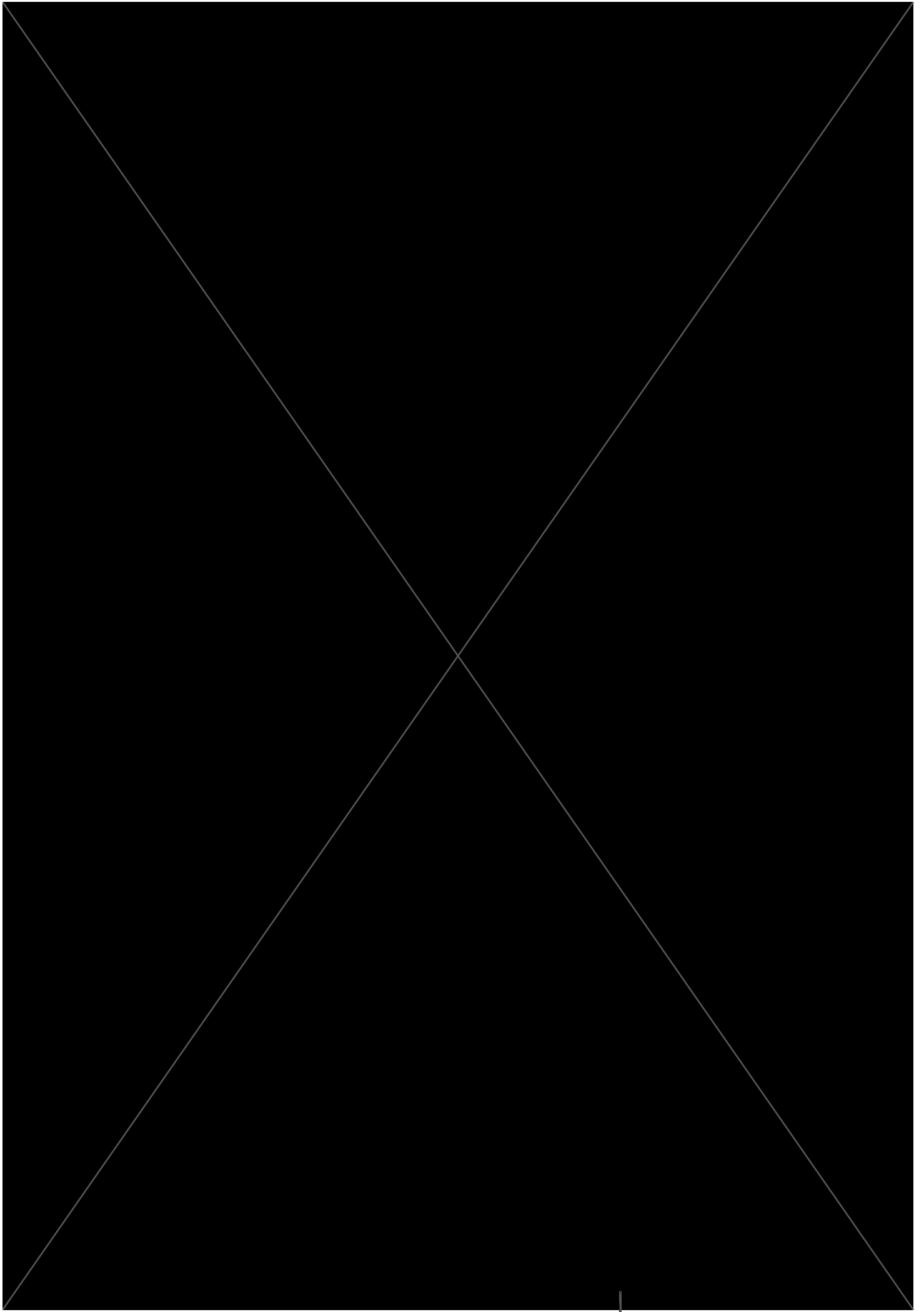
4	Biomedical Image Processing Outcomes	70
5	Statistical and Fourier Signatures of Stellar Nanoflare Activity	74
5.1	Introduction	74
5.2	Observations With NGTS	75
5.3	Analysis and Discussion	80
5.3.1	NGTS Datasets	83
5.3.2	Stellar Simulations	87
5.3.3	Comparing Simulation to Observation	89
5.3.4	Observed Stellar Nanoflare Activity Parameters	96
6	Stellar Nanoflares and the Link to Convective Atmospheres	99
6.1	Introduction	99
6.2	Background to Previous Statistical Stellar Nanoflare Analysis	100
6.3	Analysis and Discussion	104
7	Conclusions And Future Work	117
	References	121

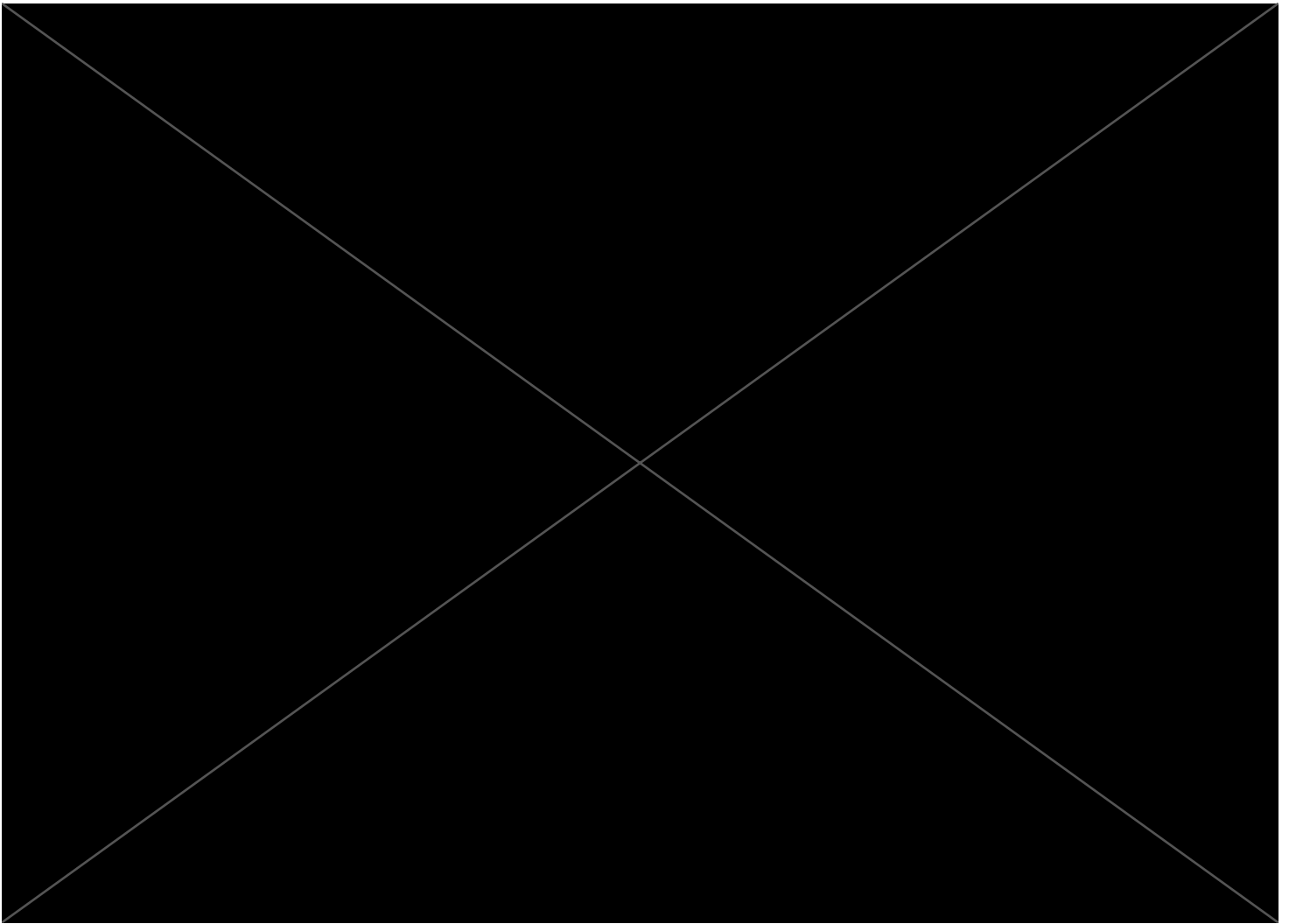
LIST OF FIGURES

- 2.1 A standard Gaussian distribution. The mean and median are centred at zero. The standard deviation is 1σ . The probability of a value drawn from the distribution at random falling within a given standard deviation is shown. $\sim 68\%$ of the values lie $\pm 1\sigma$, $\sim 95\%$ within $\pm 2\sigma$, and $\sim 99.7\%$ within $\pm 3\sigma$. Alongside the mean and median of zero, this Gaussian has a fisher skewness value of zero, a kurtosis of zero, and a FWHM to FW $\frac{1}{8}M$ Ratio of 1.73 14
- 2.2 An image of the Sun taken by the Solar Dynamics Observatory (SDO) satellite via the Atmospheric Imaging Assembly (AIA) instrument (Lemen et al., 2012), at 171Å. This wavelength is sensitive to the emission of Fe IX at around 600,000 K. This is ideal for imaging coronal loops, and other quiet coronal emission (Boerner et al., 2012). Many coronal loops are evident in the central portion of the image, wherein super-heated plasma is travelling through magnetic field lines in a distinct loop structure. Courtesy of NASA/SDO and the AIA, EVE, and HMI science teams (NASA, 2012). 17
- 2.3 A simplified model of flare energy release versus time, for impulsive flaring. The rapid conversion of magnetic energy to accelerated, hot, bright plasma manifests as an impulsive brightening. The superheated plasma then cools as energy is radiated away, following an approximately exponential decay timescale. This is the characteristic flare energy release. 23
- 2.4 A schematic of the sandwich assay. The DTR surface antibody binds with the corresponding analyte in the sample. This then binds to a labelled antibody which is added to the sample. This label is the chemiluminescent chemical. The analyte concentration is proportional to the intensity of light emitted. . . 32
- 2.5 A schematic of the competitive assay. The analyte and labelled antibodies compete to bind to the surface DTR, with the analyte binding preferentially. The unbound labelled antibody is then washed away. As such, the light intensity is inversely proportional to the analyte concentration. 33

-
- 2.6 A 3×3 biochip carrier. Each white well is an individual biochip, itself made up of distinct DTR. Image source [Randox \(2013\)](#). This carrier is approximately 50mm tall, by 40mm wide. The individual biochips are approximately 9mm tall by 9 mm wide. 34
- 2.7 A CCD exposure of a biochip, displayed on a linear scale. There are several problematic parts of the image. Two of the DTRs are not visible in this scale, and remain buried below the noise floor. Artefacts of reflection occur outside of the biochip itself, which could be mis-identified as a DTR signal. The high background noise is visible within the chip, as well as outside the biochip itself. The biochip only occupies approximately 25% of the entire image, leading to a lot of time wasted in processing, analysing, and storing the image. The colour bar displays the raw intensity values measured by the camera. 36
- 2.8 The same exposure as [Figure 2.7](#), but displayed on a logarithmic scale. This image shows the two DTR sources which were not visible in the linear scale. These are at approximately [220,180] and [150,180]. These DTR sources are barely above the background noise of the image, leading to difficulty in their identification and analysis. The units are camera intensities as before, but now on a log scale. 37
- 3.1 The Statistical Distribution of camera noise fluctuations. The fluctuations are plotted as a solid black line, and the Gaussian fit is overplotted as a dashed red line. The camera fluctuations match the Gaussian distribution. 43
- 3.2 A plot of the chi-square statistic, as a function of the number of camera frames encapsulated in the distribution. This statistic measures the agreement between the statistical distribution of camera fluctuations (i.e., [Figure 3.1](#)) and an idealised Gaussian distribution. This statistic minimises around 200 frames at ~ 0.03 43







5.1 Example NGTS J025840.5-120246 (A-type; above), NGTS J030000.7-105633 (K-type; middle) and NGTS J030047.1-113651 (M-type; below) lightcurves. These sample lightcurves have been cropped to a 36 000 s interval for clarity, but the analysis utilised the entire timeseries. The time interval between successive datapoints is ~ 12 s and the amplitudes have been mean-subtracted and normalised by their respective standard deviations. 79

- 5.2 Histograms of intensity fluctuations, each normalised by their respective standard deviations, σ_N , for the NGTS J025840.5-120246 (A-type; above), NGTS J030000.7-105633 (K-type; middle), and NGTS J030047.1-113651 (M-type; below) lightcurves. A standardised Gaussian profile is overplotted in each panel using a red dashed line for reference. The M-type distribution has a negative median offset with respect to the Gaussian, in addition to elevated occurrences at $\sim 2 \sigma_N$, which is consistent with the statistical signatures of nanoflare activity. On the other hand, the A-type and K-type intensity fluctuations provide no signatures of flare activity, with the resulting distribution remaining consistent with the presence of photon-based shot noise. Zoomed insets highlight the ranges spanning $-0.4 \leq \sigma_N \leq 0.0$ and $1.7 \leq \sigma_N \leq 2.2$, where M-type negative median offsets and occurrence excesses, respectively, are found. The blue and gold lines display the derived distributions, The M-type exhibited a small dip below the idealised Gaussian at around $-0.90 \sigma_N$, which is not seen in the A- and K-star. This may be connected to the negative median offset signal, which is causing a consequential dip elsewhere in the statistical distribution, but the exact nature of the signal is unknown. 81
- 5.3 The Fourier power spectral densities (PSDs) for example A- K- and M-type stellar sources NGTS J025840.5-120246 (upper panel) NGTS J030000.7-105633 (middle panel) and NGTS J030047.1-113651 (lower panel), respectively, displayed in normalised units of σ_N^2/mHz . The crosses in each panel depict the individual power values as a function of frequency, while the solid red line reveals a trendline calculated over ± 6 frequency elements ($\pm 0.427 \text{ mHz}$) using a Gaussian smoothing filter. It can be seen that the A- and K-type PSD are relatively flat, with no clear power enhancements, apart from slight enhancement in the K-type star, in the range of 1 – 10 mHz, indicative of the expected p-mode oscillations seen in Solar-like stars. Contrarily, the M-type PSD has a primary power peak at $\approx 0.8 \text{ mHz}$, followed by decreasing spectral power exhibiting a spectral slope of $\beta = -0.30 \pm 0.05$, followed by numerous power peaks in the range of 3 – 10 mHz, consistent with previous links to stellar *p*-mode spectra. 85

5.4 The generation of flare signals according to a power-law relationship, where the power-law exponent is $\alpha = 3.25$ and the decay timescale for each event is 245 ± 24.5 s. The superposition of all modelled flare signatures is displayed using the solid black line (upper panel). Red dots represent the shot noise distribution modelled using Poisson statistics. The time interval between successive datapoints is 12 s and the amplitude has been mean-subtracted and normalised by its standard deviation. The lower panel reveals the superposition of the synthetic flaring lightcurve with the Poisson noise model, highlighting the difficulty of extracting visual signatures of small-scale flaring events from both synthetic and observational timeseries. This final timeseries is comparable to the observed timeseries, as seen in Figure 5.1 88

5.5 The median offset (upper-left), ζ ($\text{FW}\frac{1}{8}\text{M}$ -to-FWHM ratio; upper-right), Fisher skewness (lower-left), and kurtosis (lower-right) characteristics extracted from the synthetic intensity fluctuation distributions as a function of the employed power-law index, α , and the decay timescale, τ . A negative median offset and positive Fisher skewness values support a wide range of flare conditions. The observational statistical characteristics (see Table 5.3 and Figure 5.2) compare to the modelled statistical distributions with overlapping parameters corresponding to $\alpha = 3.25 \pm 0.15$ and $\tau = 200 \pm 100$ s, in addition to $\alpha = 2.00 \pm 0.15$ and $\tau = 200 \pm 100$ s. 90

5.6 The Fourier power spectral densities, displayed in units of σ_N^2/mHz , corresponding to a power-law index $\alpha = 3.25$ and a flare decay timescale $\tau = 245 \pm 24.5$ s. The upper panel individually depicts PSD plots of the synthetic nanoflare and shot noise components as red crosses and blue squares, respectively. The solid black and gold lines represent trendlines for the nanoflare and shot noise profiles, respectively, computed over ± 6 frequency elements (± 0.427 mHz). The lower panel displays the PSD of the final synthetic timeseries, where the nanoflare signal is embedded within the synthetic noise floor. The synthetic PSDs corresponding to nanoflare activity are remarkably similar to those for the NGTS M-type stellar sources shown in the bottom panel of Figure 5.3. 91

- 5.7 The Fourier power spectral density (PSD) trendlines calculated over ± 6 frequency elements (± 0.427 mHz) for example A- K- and M-type stellar sources NGTS J025840.5-120246 (red line), NGTS J030000.7-105633 (orange line) and NGTS J030047.1-113651 (blue line), and a modelled timeseries corresponding to a power-law index $\alpha = 3.25$ and a flare decay timescale $\tau = 245 \pm 24.5$ s (black line), displayed in normalised units of σ_N^2/mHz . It can be seen that the A-type and K-type spectra are relatively flat across all frequencies with no evidence of distinct peak frequencies. The K-type does show some slight power enhancement between $\approx 1 - 10$ mHz, consistent with stellar p -mode oscillations, as have been previously observed in K-type Solar-like stars (e.g. Chaplin et al., 2009) . Contrarily, the M-type PSD has a primary power peak at ≈ 0.8 mHz, followed by decreasing spectral power exhibiting a spectral slope of $\beta = -0.30 \pm 0.05$, followed by numerous power peaks in the range of $3 - 10$ mHz, consistent with previous links to stellar p -mode spectra. The synthetic PSD is remarkably similar to the NGTS M-type stellar source, with peaks and spectral slopes in the same range and magnitude (see Figure 5.8 for the full range of peak frequencies and spectral slopes in modelled timeseries PSDs. 93
- 5.8 The primary peak frequencies (lower-left), spectral slopes (upper-left), dominant frequencies following detrending (upper-right), and the percentage of nanoflare power above the noise floor in the range of $1 - 5$ mHz (lower-right), displayed as a function of the power-law index, α , and the decay timescale, τ , used to generate the synthetic timeseries. The observational PSD characteristics (see Table 5.4 and Figure 5.3) compare to the modelled PSDs in the range of $\alpha = 3.3 \pm 0.2$ and $\tau = 200 \pm 100$ s. 94

- 6.1 Histograms of intensity fluctuations, each normalised by their respective standard deviations, σ_N , for the NGTS J052346.3-361114 (M0V-type; top panel) and NGTS J050423.8-373021 (M4V-type; lower panel) lightcurves. A standardised Gaussian profile is overplotted in each panel using a dashed red line for reference. The M4V-type distribution has a negative median offset with respect to the Gaussian, in addition to elevated occurrences at $\sim 2 \sigma_N$, which is consistent with the statistical signatures of nanoflare activity. On the other hand, the M0V-type intensity fluctuations provide effectively zero negative median offset, and no elevated occurrences at $\sim 2 \sigma_N$. This is inconsistent with clear statistical signatures of nanoflare activity, with the resulting distribution remaining more consistent with the presence of photon-based shot noise. Zoomed insets highlight the ranges spanning $-0.4 \leq \sigma_N \leq 0.0$ and $1.7 \leq \sigma_N \leq 2.2$, where negative median offsets and occurrence excesses, respectively, are clearly visible for the M4V stellar source. For improved clarity, the blue and gold lines display the corresponding distributions in each zoomed panel. 101
- 6.2 The bootstrap-averaged statistical properties of the intensity fluctuation histograms for each stellar classification. Beyond the convective boundary, at approximately M2.5V, sub-types begin to exhibit statistical signatures that are consistent with the presence of nanoflare activity, including larger median offsets (top panel), increasing levels of kurtosis (second panel from top), and higher Fisher skewness values (second panel from bottom). The ζ ($\text{FW}_{\frac{1}{8}}\text{M-to-FWHM}$ ratio) values do not vary significantly as a function of stellar classification. However, this is likely due to the interplay between the power-law index of the nanoflares and the duration of the e -folding timescales, which are able to counteract the statistical effects of one another. 105

- 6.3 The Fourier power spectral densities (PSDs) for example M0V (upper panel) and M4V (lower panel) stellar sources, displayed in normalised units of σ_N^2/mHz . The crosses in each panel depict the individual power values as a function of frequency, while the solid red line reveals a trendline calculated over ± 6 frequency elements (± 0.478 mHz). It can be seen that the PSD for the M0V star is relatively flat, with small-amplitude power enhancements in the range 3 – 10 mHz, which is consistent with typical p -mode oscillations. Conversely, the PSD for the M4V star exhibits a clear enhancement of spectral energy at lower frequencies, resulting in a spectral slope of $\beta = -0.57 \pm 0.05$ that begins at 0.32 ± 0.04 mHz, followed by numerous power peaks in the range of 1 – 10 mHz. This is consistent with the presence of both nanoflare activity and p -mode oscillations. 106
- 6.4 The bootstrap-averaged properties of the Fourier power spectral densities (PSDs) across each spectral type. The upper panel displays the peak frequency values (in mHz), which are found to reside within the range of approximately 1 – 4 mHz. This is consistent with both nanoflare activity and p -mode oscillations, and therefore cannot be used as an indicator of nanoflare activity by itself. The middle and lower panels display the turning point frequencies (in mHz) and subsequent spectral slopes, respectively, as a function of stellar classification. When compared to the Monte Carlo nanoflare simulation outputs depicted in Figure 6.5, the distinct jump in turning point frequency and spectral gradient at the convective boundary (M2.5V) provides clear evidence of prominent nanoflare activity in M2.5V – M4V stellar sources. 109
- 6.5 A reproduction of Figure 5.8 from Chapter 5 with the constituent PSDs re-calculated for 2095 datapoints to match the longest continuous timeseries used in the present study. The primary peak frequencies (lower-left), spectral slopes (upper-left), dominant frequencies following detrending (upper-right), and the percentage of nanoflare power above the noise floor in the range of 1 – 5 mHz (lower-right), is displayed as a function of the power-law index, α , and the decay timescale, τ , used to generate the synthetic timeseries. While a few individual values differ, the overall trends and the magnitude of the derived signals are consistent with the PSD properties generated from 2316 datapoints and reported by Dillon et al. (2020). 110

LIST OF TABLES

5.1	NGTS magnitudes of the stars used in the study.	77
5.2	The stellar parameters for the stars used in the analysis. The stellar masses, radi. and luminosity data is from the Tess Input Catalog release V8. (Stassun et al., 2018)	78
5.3	Characteristics of the intensity fluctuation histograms associated with the A-, K-, and M-type NGTS sources. Note that a standard Gaussian distribution will demonstrate $\zeta = 1.73$, hence deviations from this provide an indication of the intensity fluctuation occurrences taking place close to, and far away from the timeseries mean.	82
5.4	Characteristics of the PSDs associated with the M-type NGTS timeseries.	84
6.1	Averaged characteristics of the statistical properties by each spectral type.	102
6.2	The stellar parameters for the stars used in the analysis. The stellar masses, radi. and luminosity data is from the Tess Input Catalog release V8. (Stassun et al., 2018)	103
6.3	Nanoflare parameters per spectral type, derived from statistical and Fourier properties of Monte-Carlo modelled nanoflare timeseries respectively.	108
6.4	Average characteristics of the Fourier PSD properties by each spectral type.	111
6.5	Nanoflare parameters per spectral type, derived from combined statistical and Fourier properties of Monte-Carlo modelled nanoflare timeseries.	116

INTRODUCTION

Science is a hugely complex field, that can be massively over-simplified to ‘looking at stuff, carefully’.¹ Science requires observation, sifting meaningful signal from noise: of course, a key aspect of science is in that step, discerning and identifying the meaningful signal, but that still is beholden to signal gathering. The progress of science is accelerated when we increase our observational power. As such, the history of astronomy is in many ways co-incident with the history of technology. With advances in technology, astronomy leapt forward, and progress in astronomy itself led to the development of technology.

In pre-history, stars were recorded in cave drawings (Sweatman & Coombs, 2018). As civilisations emerged, knowledge of stoneworking allowed the creation of sites like Stonehenge and Machu Picchu, to track the passage of the Sun, and the dates of solstices and equinoxes (Aveni, 2003). This astronomical knowledge was used to create calendar systems, furthering the progress of society. There was immediate practical benefit, such as planning of agricultural seasons as well more philosophical implications related to the concept of time itself. Astronomers began to catalogue the sky, calculating approximate brightness of stars, and tracking their movements. Aiding this endeavour, mathematical advances such as trigonometry were made, alongside technology such as the astrolabe (Torode, 1992), leading to the rapid advancement of global navigation by sea. The major leap forward in astronomy came with the invention and subsequent development of the telescope at around 1600, by Hans Lipperhey and Galileo (King, 1956). Until this time, measurements were taken by the naked eye, limiting the minimum brightness of an object that could be observed. The apparent magnitude for naked-eye observations is around +6-6.5, limiting an observer to several thousand stars (Agrawal, 2018). These magnitude estimates were also very subjective.

¹ This simplification misses out on the nuance and importance of the Scientific method. Hypothesis, research, experiments, analysis and conclusions are all key steps, reduced here to the word ‘carefully’, but their importance cannot be overstated.

While the telescope didn't solve the subjectivity, it increased signal gathering capability by several orders of magnitude, increasing the number of visible objects to hundreds of thousands. This led to an explosion of new discoveries, such as Jupiter's moons, the rings of Saturn, and (unfortunately for Galileo) heretical evidence for Copernicus' heliocentric theory of planetary motion (Blackwell, 2006). Galileo's subsequent trials and arrests dampened his progress, but his work was instrumental to Issac Newton. During (an all-too-relateable) two-year period, Newton worked from home, as the Great Plague led to a lockdown and the closure of Cambridge University (Westfall, 1980). The incredible mathematical and scientific advances he made in this two year period led to the development of his most famous theories, and set unreasonable expectations for work-rate in a pandemic. His development of the Newtonian telescope—the first reflector telescope—set the standard for the next 200 years of astrophysics, until the invention of refracting telescopes in the 1800's. Reflecting telescopes remain popular today, and in some instances (such as the Hubble Space Telescope) are better suited than refracting telescopes. Newton's work on optics also led to the development of spectroscopy. Arguably one of the most important fields of astrophysics, this measurement of emission and absorption lines in the Sun, and stars led to the discovery of the elements contained within those objects, furthering our understanding of the structure and origins of stars.

The next great technological leap forward was the invention of photography. Until this point, measurements were relatively subjective. While the position of celestial objects could be made accurately, brightness measurements were subjective to human eyesight, which is poorly suited for such a task. Additionally, photography was a signal multiplier. By increasing the length of an exposure, more light could be gathered, allowing for fainter astronomical objects to be detected. This progress continued with the invention of the digital detector. Key to this was the parallel development of computing. Digital observations could be directly loaded onto computers for analysis. This led to the rapid development of new signal analysis techniques. Results could be easily extrapolated, and trends examined. Large-scale simulation of astrophysical data was also made possible via computers. In modern-day astrophysics, much 'technological' advancement is now synonymous with computer analysis and 'data science'. The universality of computing and digital imaging meant that modern astrophysical analysis techniques have direct applications outside of astronomy, and indeed vice-versa. New and improved techniques to analyse and benchmark large datasets are at the forefront of increasing our understanding allowing us to delve ever deeper into uncovering the unknown.

1.1 HOW DO ASTROPHYSICS AND BIOMEDICAL APPLICATIONS OVERLAP? 3

Every technological leap forward allows us to see more deeply, gathering more signal. This scientific advancement drives more innovation, and the cycle continues. This cycle of progress is often fortuitous, but it can also be deliberate. This thesis details the development of core techniques to characterise and model the complimentary issues of below-noise floor signatures in biomedical and stellar timeseries, alongside specialised analysis to deal with the specific demands arising within each. Utilising statistical and Fourier analysis, combined with Monte-Carlo modelling, signatures of previously unobserved stellar nanoflares were extracted, leading to observation of novel phenomena and better understanding of the energy budgets of fully convective M-type dwarf stars. These same analysis techniques were developed alongside biomedical image analysis considerations, due to the universality of techniques to improve low-signal observations and suppress noise when dealing with digital images. This led to the improvement of patient diagnostic outcomes for Radox Laboratories. The aim of this thesis is to further astrophysical and biomedical understanding of below-noise-floor signals, and act as an example of the benefits to all that come with interdisciplinary work.

The need for these medical diagnostics was brought to great attention during the span of my PhD, with the emergence of the COVID-19 pandemic. My contribution pales into insignificance compared to the front-line workers, doctors, nurses, vaccine scientists, and everyone else who helped in these dark days, but it brings me some comfort to know this analysis has already begun to improve the performance of Radox diagnostics of COVID-19, among other important medical applications.

1.1 HOW DO ASTROPHYSICS AND BIOMEDICAL APPLICATIONS OVERLAP?

My PhD was funded as part of a collaboration between Invest NI, Radox Laboratories, and Queen's University, working across multiple disciplines on a range of special projects to improve their diagnostic capabilities.² The Astrophysics Research Centre was tasked with creating and adapting techniques for improving the quantification and detection of below-noise-floor signatures, for both biomedical and astrophysical applications. The team was led by Professor D. Jess, and consisted of Dr S. Grant, Ms C. Gilchrist-Miller and myself. Radox are a biomedical company based in Northern Ireland who produce a wide-range of biomedical sensor tests using their 'biological microchip' technology. Section 2.3 explains

² These included working with the School of Engineering to create a fully automated sample loading robot, and with the School of Pharmacy to produce a minimally invasive blood sampling needle.

the operation of the biochips in much greater detail. In short, these ‘biochips’ identify the presence and concentration of ‘bio-markers’ (which can be anything from genetic markers related to health conditions, to the concentration of chemicals such as alcohol within a sample) using ‘lock and key’ chemistry. A key aim of Randox is to develop highly sensitive medical diagnostics tests, allowing for the early diagnosis of diseases such as heart disease. By packing multiple tests into one single biochip, the throughput of testing can be massively increased versus traditional tests. Biomedical samples in the biochip are treated with various chemicals, which bind with the bio-markers present. This will cause a varying degree of light to be emitted (or in the case of certain tests, no light to be emitted), which is detected by a charge-coupled device (CCD). To date this technique has been hugely successful, and Randox are one of the pre-eminent companies in biomedical sensing. However, as they develop more and more sensitive tests, often with more densely packed bio-chips, leading to more overlap between extremely faint and extremely bright signals, they have begun to hit signal-to-noise walls. These faint signals are often on or below the noise-floor, while the brightest signals in the image are orders of magnitude brighter. This led to the collaboration with the Astrophysics Research Centre. While biomedical imaging and astrophysics appear wholly disparate disciplines, they are both largely constrained by similar technological and physical issues. The issue of below noise-floor signatures mixed with challenging dynamic-range is prevalent in astrophysics, but particularly in the field of nanoflares. Neither field has the luxury of simply taking more exposures, or utilising more expensive and sensitive cameras. In the context of solar physics, the 2-D nature of the bio-chip images have direct comparison, to astronomical images with features of interest and other 2-dimensional information leading to increased complexity in the data analysis. Both use charge-coupled devices to image light sources which often have extreme dynamic range, with extremely bright and faint phenomena in the same field. These CCDs use semiconductors to convert photons into electrons through the photoelectric effect. This conversion, coupled with the photon nature of light, introduces noise sources which are consistent between astrophysics and biomedical imaging, due to the identical physical principles.³ When dealing with extremely faint signals, we must understand all the sources of noise within an image if we are to recover below noise-floor signals.

There is a rich history of techniques developed for astrophysical analysis being used in other fields, particularly medicine. Indeed, there are too many papers detailing the

³ Because, of course, you ‘cannae change the laws of physics!’

application of astrophysical techniques to medical imaging to recount. Most famously, Magnetic Resonance Imaging (MRI) scans utilise the radio interferometry techniques of ‘aperture synthesis’ which were initially developed by Martin Ryle at Cambridge (Ryle & Vonberg, 1946; Hewish, 1965; Lustig et al., 2008): Researchers are still finding new avenues to apply astrophysical signal-boosting techniques to medical imaging. Some recent examples from the NASA Astrophysical Data System (ADS)⁴ include Brewis & McLaughlin (2019)’s work developing 3-D models of hearts utilising astrophysical image-processing to greatly speed up and automate the process, ray-tracing simulations by Buitrago-Casas et al. (2020) modelling the optics in the Focusing Optics X-ray Solar Imager, which have direct applications in X-ray medical imaging, and the package *AstroPath*, detailed by Berry et al. (2021) & Green et al. (2021), which applies techniques initially developed for the analysis of large astrophysical spectral datasets (such as the Sloan Digital Sky Survey (SDSS) Gunn et al., 2006) to multi-wavelength immunofluorescent images allowing for more rapid and accurate tumour diagnosis.

The overall goal of the project with Radox was to use techniques developed within astrophysics to improve the dynamic range of their analysers and increase diagnostic sensitivity. Once this was achieved, an additional goal was to apply feature identification to the ensuing images, to better automate patient diagnosis. This combined package of dynamic range enhancement and feature identification would allow for earlier diagnosis, and therefore earlier intervention of life-saving treatment. My role was to carry out the initial statistical benchmarking of the underlying noise characteristics (i.e., the statistical distribution of intensity fluctuations in camera darks, and bias frames), and use those to generate observationally driven synthetic noise models. I then carried out a similar analysis for the bio-marker light signals, to allow for the generation of fully synthetic test images. The noise model, and the synthetic test images were then used by Dr S. Grant to design and verify the performance of a noise suppression code which was designed to identify and correct for hot pixels, then co-add successive exposures to minimise noise in the final image. This statistical modelling was also implemented as a camera diagnostic for maintenance. Approximately every six months, Radox cameras will re-run this statistical analysis, to determine if the camera noise statistics are diverging. As this first package was completed well in advance of expectation, I then created a fully automated feature recognition pipeline, termed BISCUIT,⁵ to identify key image features to carry out co-alignment, derotation and cropping of the camera images

⁴ <https://ui.adsabs.harvard.edu>

⁵ Biochip ISolution Code Using Image Transforms

producing a consistent product aligned with a reference schematic. This allowed for the removal of extraneous pixels, greatly speeding up downstream processing.⁶ This developed image and statistical skills which have direct application in solar analysis. These techniques are being added to Radox analysers, leading to the overall dynamic range improvement of these cameras, allowing for even more sensitive diagnostics, and directly improving real patient outcomes.

1.2 WHAT ARE NANOFLARES?

Nanoflares are flare events with energies in the range of 10^{22} – 10^{25} ergs (10^{16} – 10^{19} joules),⁷ below the noise-floor for individual observation in the Sun and in other stars. The concept of a nanoflare was explored by [Parker \(1988\)](#) in a seminal work. He theorised that incredibly frequent but individually low energy flare events would be undetectable as distinct flare events, while able to provide a significant component of the solar coronal energy budget. Due to being below the noise-floor for detection, nanoflares are analogous to Radox biomedical imaging. Both involve low-intensity signals beset by high levels of background noise and other bright sources within the data. In both instances, the noise is primarily due to CCD noise and photon statistics, and is consequently well-modelled with Poisson statistics. With a shared framework of observation and modelling of their respective intensity timeseries, it is possible to recover the seemingly unrecoverable. Below noise-floor nanoflare signatures are challenging, but they are now within our grasp.

While these below noise-floor nanoflares are considered ‘low-energy’ in solar and stellar contexts, they still release a substantial quantity of energy. A typical nanoflare with energies in the region of 10^{17} – 10^{18} Joules is comparable to the solar energy irradiating the Earth each second,⁸ the energy released by the Tsar Bomba (the largest man-made explosion in history),⁹ or to the entire yearly energy production of the United Kingdom ([CIA, 2008](#)).¹⁰ The highest end of nanoflare energies (10^{19} J) is approximately the yearly energy consumption for the entire world ([CIA, 2015](#)).¹¹ Nanoflares remain hidden below the noise-floor, but they

⁶ This also allowed me to achieve my lifelong goal of creating a slightly silly-sounding acronym, a rich tradition within astronomy ([Petitpas, 2019](#); [Cook, 2019](#)).

⁷ As Prof C. A. Watson once put it, ‘They’re like flares... but smaller...’

⁸ Total solar irradiance at the upper atmosphere is approximately 1365 Wm^{-2} ([Finsterle et al., 2021](#)). The cross-sectional area of the Earth is $\sim 1.3 \times 10^{14} \text{ m}^2$, giving an energy of $\sim 1.75 \times 10^{17} \text{ J}$.

⁹ A yield in the region of 50 megatons of TNT, $\sim 2 \times 10^{17} \text{ J}$ ([Khan, 2020](#)).

¹⁰ As measured in 2008. 0.3447 trillion kWh is $\sim 1.24 \times 10^{18} \text{ J}$.

¹¹ As measured in 2015. 21.78 trillion kWh is $\sim 1.8 \times 10^{19} \text{ J}$.

are incredibly energetic nonetheless. This is compounded by their relative frequency. The relationship between flare energy and flare occurrence rates is well-described by a power-law, denoting the frequency of events to the energy they produce. As the flare energy decreases, the occurrence rates increase (Aschwanden et al., 2000). Nanoflare occurrence rates could be as high as thousands per second over an entire stellar surface (Parker, 1988; Dillon et al., 2020), which would make them a considerable component of a stellar coronal energy budget. Indeed, nanoflares were initially theorised as a solution to a long standing energy problem in astrophysics: the coronal heating paradox. This paradox is that the outermost layer of the solar atmosphere is millions of degrees hotter than preceding layers, with no apparent mechanism to explain this heating (Grotian, 1939; Edlén, 1941; Alfvén, 1941; Edlén, 1943). Despite considerable research, the source of coronal heating remains unknown, but wave heating and nanoflaring are prominent candidates (Alfvén, 1947; Ulrich, 1970; Heyvaerts & Priest, 1983; Parker, 1988; Hudson, 1991; Aschwanden, 1999; Klimchuk, 2006; Aschwanden et al., 2007; Klimchuk, 2015). Flares occur primarily in the corona (Benz, 2016), so would be able to drive heating locally throughout. However, no flare observations to date can explain the radiative losses, due to the relative infrequency of larger flare events. Nanoflares were proposed as a series of small-scale impulsive events driving coronal heating, which as a consequence of their below noise-floor signal had been hitherto undiscovered, explaining why the source of coronal heating remained unobserved. This potential holds for stellar atmospheres as well as the Sun. While solar nanoflaring has been a considerable topic of interest over the last twenty years, stellar nanoflares remain almost entirely unexplored. As nanoflares are embedded within the noise floor of their measured intensity signals, it is difficult to identify individual nanoflare events. However, the frequency of nanoflares over an entire stellar surface means they can be recovered from timeseries data using statistical techniques that do not rely on the individual identification of above noise-floor intensity signals. Through the same statistical bench-marking and signal modelling steps used to characterise the Radox data, I was able to detect and characterise stellar nanoflares and their occurrence rates for the first time. Nanoflare signatures identified within light-curves that would have been previously identified as merely quiescent noise uncovered a novel link between nanoflaring and p -mode like periodic signatures, as well as a link between fully convective stars and enhanced rates of nanoflare activity, likely due to an increased plasma Lundquist number. This implies that the altered stellar dynamo believed to operate in fully convective stars is not involved in nanoflare enhancement, lending support to emerging theories of solar-like dynamo activity in fully convective stars. Section 2.2 details the underlying physics of flaring and nanoflares in much greater detail.

1.3 THESIS OVERVIEW

This chapter gave an introductory background to this uniquely dual-natured work. Chapter 2 detailed the underlying physics and data-science considerations driving this work. Chapter 3 is a general overview of the methods of observation and modelling of the biomedical and stellar nanoflare intensity timeseries. This embodied statistical analysis of both noise and signal sources, complemented by Monte-Carlo modelling of those sources. Additionally, an image recognition pipeline was developed for the biomedical image analysis, and Fourier analysis was developed to examine periodic signatures uncovered in the stellar nanoflare signals. The outcome of the Radox processing work is discussed in Chapter 4. Chapter 5 is formed from (Dillon et al., 2020, published in ApJ in Nov 2020), modified to fit within the frameworks of this thesis, and details the first application of these statistical, Fourier, and modelling techniques to identify and characterise stellar nanoflares, in order to investigate their role in periodic brightness signatures. Chapter 6 is formed from Dillon et al. (2022) (which is currently being prepared for submission), similarly modified to fit within the framework of this thesis. This work investigates the link between the enhanced stellar nanoflares rates first detailed in Chapter 5, examining the nanoflare activity across fully and partially convective stellar atmospheres to determine the role of the convective boundary in these enhanced flare rates. Chapter 7 contains the overall conclusions and results of this work to develop complimentary timeseries analysis tools. Please note that all software developed throughout this work was written in IDL.

THEORY

This chapter details the overlapping theory behind the image and signal processing for biomedical and astrophysical applications, alongside more detailed background theory on the biomedical and astrophysical phenomena itself.

2.1 SIGNAL AND NOISE IN THE CONTEXT OF CCD IMAGING

In any measurement, there are two components. The signal (i.e., the signatures we want to identify), and noise, an unwanted component inherent to all observation due to the underlying physics governing the measurement. This concept can be formalised to the equation

$$D = S + N, \tag{2.1.1}$$

where D is the final data product we detect, S the signal, and N the noise. Whenever the signal and noise are of a comparable magnitude (i.e., below-noise-floor signatures), the signal analysis will be limited by this noise.

Noise is inescapable. Even with a perfectly designed system, the inherent quantum-mechanical nature of reality will introduce some level of noise ([Brillouin, 1959](#); [Clerk et al., 2010](#)). To truly understand the signal, we must understand the noise inherent in the observation. Without accurately knowing N , it is impossible to solve for S . While this may appear hopeless, it is this same concept that allows for the detection of below-noise-floor signatures. While individual noise signals are inherently random, many sources of noise are well-described in the aggregate by known statistical distributions. With a sufficiently large sample, we can detect how our signal deviates from the predicted noise distribution.

The temptation to increase signal artificially with post-processing, instead of minimising noise must be avoided at all costs.¹ While this may seem appealing, any technique to ‘boost’ signal with post-processing is inherently photometrically inaccurate. The concept of ‘ethical imaging’ has emerged since the advent of digital processing (Anderson, 1994; Suvarna & Ansary, 2001; Cromey, 2010, 2013), particularly amongst the medical community, due to the human impact of mis-characterised data. The only ‘ethical’ way to improve the signal is either to increase the observational power, whether that be through longer exposures, or more sensitive observations (albeit, this carries with it an increase in the noise observed as well) or by accurately constraining the noise signal, so we can better distinguish our signal from the noise.

In the contexts of astrophysical and biomedical imaging, noise has two main sources. Firstly, there is noise from ambient conditions. This is noise due to the conditions between the camera and the subject. In astrophysical contexts, this could be due to any number of contaminants, notably atmospheric distortion giving rise to scintillation (Osborn et al., 2015), poor seeing conditions at the observatory, or any number of unwanted light sources.² This form of noise is not a major concern for the Radox imaging. Their diagnostic hardware is able to control most ambient conditions. Temperature is tightly controlled, and the imaging takes place within an effectively sealed unit, removing external light sources. The distance between the sample and the camera is on the order of centimetres, rather than the interstellar distances which cause distortions in astronomy (i.e., reddening and dimming due to distance and wavelength dependent extinction as the interstellar medium and the Earth’s atmosphere attenuate light (Cardelli et al., 1989), the distinct effects of scintillation due to the Earth’s atmosphere, alongside other effects such as Doppler broadening and gravitational lensing).

Secondly, there is the noise inherent to the observation system itself. This thesis is concerned with the signal processing of optical wavelength data. Charge-coupled devices (CCDs) remain the dominant technology for scientific optical photography (Howell et al., 2006). A CCD is a device to store, manipulate and readout electric charges through an array of small capacitors using the photoelectric effect. The photoelectric effect is the emission of an electron from a material due to an incident photon with an energy equal to or greater than the binding energy of the electron (Einstein, 1905; Arons & Peppard, 1965). Silicon, the

¹ It is of course advantageous to boost signal with improved observation power- for example by utilising a larger aperture telescope.

² These could be macroscopic flares within the timeseries, blended light from background stars, or more recently reflectance from a constellation of satellites launched by a power-mad billionaire without consideration for their impact on astronomy (Walker et al., 2020).

basis of CCDs, and virtually all electronic circuitry, is a semiconducting material. This means it acts as both an insulator and conductor. Silicon has an electronic structure consisting of a valence band with no free electrons, and a conduction band where electrons are free to move. The energy required to move an electron from the valence band to the conduction band is known as the band gap energy. Silicon has a band gap energy of ~ 1.1 electron volts (Hicks et al., 2003), meaning that incident light with an energy exceeding this will induce ‘photoemission’ of an electron. The effective photoelectric range of silicon is 1.1 to 10 eV³ (Howell et al., 2006), spanning infrared to soft X-ray photons, and centred around optical wavelengths.

By ‘doping’ this silicon with other materials, the electronic properties of the silicon can be changed. The silicon can be manipulated to have a diode structure, which restricts the flow of charge to one direction. This means the silicon can itself act as a capacitor, and store these photo-emitted electrons. Thus, the image sensor CCD was born. This device converts incident photons into electrons. These electrons are stored as charge in individual photosensitive capacitors known as ‘pixels’. The incidence of light is normally controlled with a shutter, which will ‘expose’ for a set time. At the end of each exposure, the stored charges will convert to voltages. These voltages are then moved through each pixel in rows or columns to be ‘read-out’. This is done by applying a bias voltage across the circuit. These voltages are amplified by a voltage amplifying circuit. This voltage is then converted into a digital ‘count’, equivalent to the intensity of the incident light using an analog-to-digital converter. While often called ‘photon-counters’, CCDs do not directly count photons, but rather infer their presence due to measured voltage. As such, every single step in this process is effectively another measurement, and is reliant on the underlying circuitry and inherent physics of the detector, thus introducing noise at every step.

There are 3 major noise sources present in CCD imaging. Read noise is an inherent feature of the electronics in the camera. As the charge is converted to a voltage and transferred across the CCD, it is subject to losses and noise. This is due to the inherent efficiency of the circuitry. The analog-to-digital conversion of the charge is also inherently noisy; voltages follow a continuous distribution, which are converted into discrete digital signals introducing a source of uncertainty. Read noise is described by Gaussian processes (Boyat & Joshi, 2015). This form of noise can be mitigated by re-binning the data. This means converting the original image of $X \times Y$ pixels into a new image $\frac{X}{B} \times \frac{Y}{B}$ pixels, where B is the binning

³ The equivalent of 125 - 1100 nm.

factor. A $B \times B$ array of pixels is co-added and forms a new larger re-binned pixel. Because this new pixel only needs to be ‘readout’ once, it will lead to a decrease in the sum of the read-noise by a factor of B^2 , while the sum of the signal will remain the same. This does however sacrifice resolution. The level of read-noise can be measured and mitigated with bias frames. These are frames generated with a zero-second exposure, revealing the inherent electronic noise (Gilliland, 1992). Read noise is seldom a limiting factor in imaging.

Dark noise is due to electrons being ‘detected’ by the CCD, which were not produced by incident photons. This is ‘dark’ noise, as these electrons are not generated by incident light. These are primarily generated by the thermal currents inherent in all matter above zero kelvin. The degree of these dark currents scale with temperature, but even at very low temperatures, this can cause the thermal excitation of valence electrons in the silicon semiconductor, freeing them so they are consequently ‘detected’ when the chip is readout. A thermally excited electron is indistinguishable to one produced by a photon.

While this noise can be minimised through cooling of the CCD, it is still vital to characterise this level of noise to aid low-signal processing. Dark frames are generated by exposing the camera in a dark environment for an exposure time matching the desired measurement time. This dark frame will consist of the read noise and the noise due to thermal currents. Dark noise electrons are detected as independent events, and consequently described with Poisson statistics (Aguerrebere et al., 2012).

Additionally, ‘hot’ pixels are another form of dark noise. Hot pixels are randomly distributed throughout a camera, and come and go over time. They manifest as pixels with a greatly increased intensity. These may be present for a single exposure, or remain for a time (Chapman et al., 2015). Hot pixels are primarily caused by radiation-induced ionisation, such as alpha emission within the chip itself, or due to cosmic ray incidence (Saad Saoud et al., 2016). They can also be caused by over-saturated pixels, or due to charge not ‘flushing’ out of the chip during the read process. Detecting and removing these transient noisy pixels can be challenging due to their random incidence. Permanently ‘hot’ pixels are also possible. Otherwise known as ‘dead’ pixels, these are due to defects within the CCD chip, and can be easily detected due to their invariance over time and consequently easily removed or mitigated in the final image. Dark currents, and thermal noise are inherently tied to the silicon quality. Over time, as the silicon degrades,⁴ the degree of dark current increases,

⁴ Cosmic ray strikes and other space radiation are a source of silicon damage, quickly ageing space-based cameras (Sirianni et al., 2005). This also affects ground level CCDs, but at a much reduced rate.

necessitating continual re-assessment of the cameras thermal noise (Sirianni et al., 2005; Marcelot et al., 2015).

Shot noise is due to the photon nature of light. Discrete photons will spread out temporally and spatially, and thus are detected stochastically at the detector. Shot noise follows Poisson statistics, as each detection is a discrete and distinct event. The shot noise scales with $\sqrt{\lambda}$ where λ is the mean photon count. Due to this scaling with $\sqrt{\lambda}$, for very bright sources shot noise is mostly insignificant, but it is dominant for faint signatures with a low λ (Gehrels, 1986; Zmuidzinas, 2015), i.e., signals on or below the noise-floor of observation. As such, it is a dominant source in stellar nanoflare signals, as well as for the faint biomedical signals.

Shot and dark noise are both Poisson processes. The Poisson distribution describes the expected distribution of independent and discrete events which have a known mean count rate of λ . The Poisson probability function is described by

$$p(x) = \frac{e^{-\lambda} \lambda^x}{x!}, \quad (2.1.2)$$

where λ is the mean number of Poisson events (i.e., the mean number of electrons detected as a consequence of the dark and shot noise per frame, and x is the number of occurrences). For events with a sufficiently large mean count rate (defined as $\lambda \geq 25$ by Port, 1994, p. 685), the Poisson events will tend towards the Gaussian distribution (this is a well known statistical phenomena, see e.g., Lupton, 1993, for a derivation of this). As such, when dealing with a large enough sample,⁵ the noise in a CCD can be treated as a Gaussian distribution, generated from a large-distribution of discrete Poisson noise events (e.g., see the Gaussian treatment applied by Terzo et al., 2011; Jess et al., 2014, 2019, to describe the distribution of large sample sizes of Poisson events).

The Gaussian (also known as the normal) distribution is described by the general formula

$$p(x) = \frac{1}{\sigma\sqrt{2\pi}} e^{-\frac{(x-\mu)^2}{2\sigma^2}}, \quad (2.1.3)$$

where μ is the mean (and by definition of the normal distribution, also the median) value of x . σ is the standard deviation of the distribution. The ‘standard distribution’ is a special case where $\mu = 0$ and $\sigma = 1$. Figure 2.1 shows a standard Gaussian distribution with μ centred at zero, and 1σ standard deviation. The mean and median of the distribution are equal.

⁵ A long timeseries (in excess of 10^4 frames) is essential to fully characterise the underlying distribution, as with a shorter timeseries it is not possible to confidently observe the full statistical distribution. The ‘error’ in the distribution scales with \sqrt{N} , where N is the number of frames. 10^4 frames gives an error of 1%

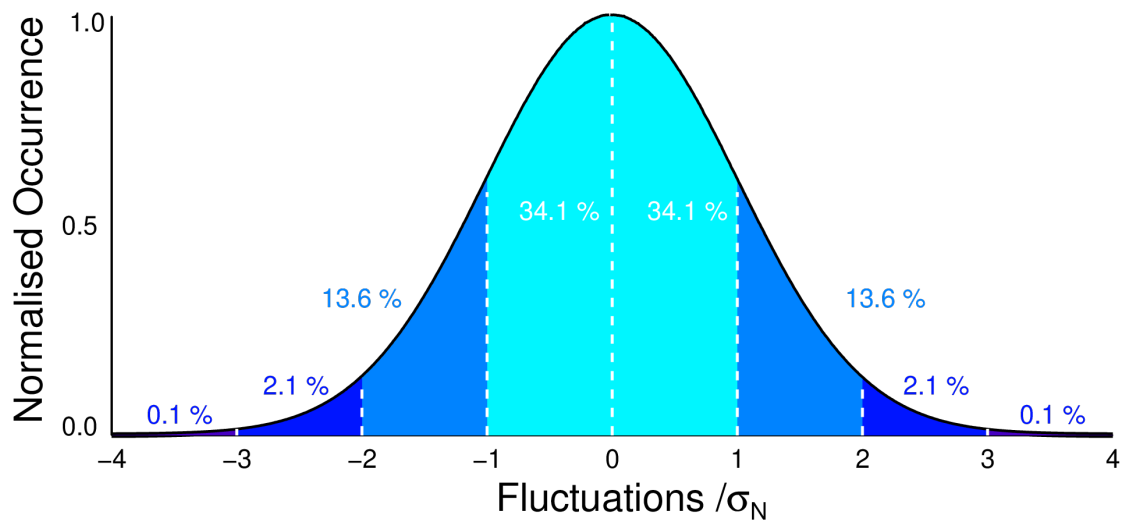


Fig. 2.1 A standard Gaussian distribution. The mean and median are centred at zero. The standard deviation is 1σ . The probability of a value drawn from the distribution at random falling within a given standard deviation is shown. $\sim 68\%$ of the values lie $\pm 1\sigma$, $\sim 95\%$ within $\pm 2\sigma$, and $\sim 99.7\%$ within $\pm 3\sigma$. Alongside the mean and median of zero, this Gaussian has a fisher skewness value of zero, a kurtosis of zero, and a FWHM to $FW \frac{1}{8}M$ Ratio of 1.73

The overall ‘shape’ of the distribution can be characterised with statistical measurements. The ‘kurtosis’ is a measure of the tailed-ness of the distribution. A highly kurtotic distribution would exhibit a narrow spread to the ‘tails’ of the distribution, and thus peak in the centre. The Fisher skewness is a measure of the right or left skew of the distribution. A distribution with a large positive skew would have more fluctuations on the right / positive side of the distribution, and vice-versa. A Gaussian would by definition have zero skewness or kurtosis. Finally, the width of the distribution can be calculated at different points of the distribution. By comparing the full width of the distribution at half the maximum (FWHM) to the same measurement at one eighth the maximum ($FW \frac{1}{8}M$), the width of the distribution can be reliably benchmarked. The expected value of these statistical benchmarks are clearly defined for the standardised Gaussian, which are described in 2.1.

Equation 2.1.3 describes the probability of a given value falling within a given standard deviation. These probabilities are shown in Figure 2.1 at the corresponding standard deviations. Alongside the ‘shape’ benchmarks, these probabilities allow us to determine deviations from the underlying noise distribution. Any signal deviating from this noise distribution can thus be detected due to its divergent statistical properties. Nanoflares, for example are

detected due to subtle asymmetries and deviations from the Gaussian distribution due to the nature of flare signals (this is explained in Section 2.2).

The probability confidence intervals also allow for the robust determination of hot pixels. Hot pixels will exhibit greatly enhanced intensities, and consequently large deviations away from the standard deviation. Due to the accurately constrained probabilities, we can determine the likelihood of these hot pixels belonging to the background noise. By combining these statistical analyses with observation-driven Monte-Carlo simulated timeseries, it is possible to accurately characterise and constrain the underlying signal of below noise-floor signatures.

2.2 THE ORIGIN AND DYNAMICS OF NANOFLARES

Nanoflares are a subset of the larger classification of flare events. As such, to fully explain their origins, a basic overview of magnetic reconnection and macroscopic flaring is needed.

2.2.1 *Magnetic Reconnection*

Magnetic reconnection is a process occurring throughout outer stellar atmospheres, often visible in the form of flares. The term ‘flare’ is used to describe a brightening event in a star, occurring over a timescale of minutes, with the flux increase occurring across the entire electromagnetic spectrum (Kretzschmar, 2011; Benz, 2016). The energy is provided via the reconnection of magnetic fields as these complex 3-D structures reconfigure to more energetically stable topologies (Shibata & Magara, 2011; Benz, 2016; Pedersen et al., 2017).

The generation and evolution of magnetic fields are a prerequisite for magnetic reconnection. Magnetohydrodynamics (MHD), initially theorised by Alfvén (1942), is the predominant framework to describe magnetic field behaviour in conductive ‘fluids’. MHD theory utilises a ‘fluid’ framework to describe the wave movement of the plasma and associated charges. This framework treats the plasma as an ideally conducting (zero resistivity) fluid, in which convective motion in the plasma allows the electric charges within the fluid to move around. In solar-like stars this induces an $\alpha - \omega$ dynamo (Parker, 1955; Babcock, 1961; Leighton, 1964), allowing for highly energetic magnetic fields to be generated. The ω component is the shearing of a pole-pole magnetic field due to differential rotation. The differential rotation is believed to occur at the tachocline, the interface between the convective

and radiative zones⁶ but recent research suggests this may occur elsewhere (these papers by [Wright & Drake, 2016](#); [Wright et al., 2018](#), are discussed below). This ω effect strengthens the field, as the shearing forces wrap the magnetic field around the star toroidally. The α effect is the lifting and twisting of these toroidal field lines. This is caused by convective motions of the plasma, and the stellar rotation. The rotation leads to direct twisting of the field. The convective motion causes twisting via turbulence, and also causes magnetic buoyancy which lifts the field through the plasma and away from the deep seated tachocline. This allows the magnetic fields to reach the surface of the star. These alpha-omega effects are believed to drive a dynamo which gives rise to global solar magnetic evolution, and consequently the flaring seen in solar-like stars.

Fully convective stars, such as mid M dwarf sub-types, are devoid of a radiative zone, and consequently lack the tachocline which is believed to amplify the solar-like dynamo. The dynamo in these stars is believed to operate via helical turbulence ([Browning, 2008](#); [Pipin & Seehafer, 2009](#)) whereby the turbulent motions of the plasma alone can create the complex magnetic field required to explain the magnetic activity observed (effectively operating via an α dynamo alone). While some studies predict that this helical dynamo would exhibit different magnetic properties to those induced by the existence of the tachocline ([Durney et al., 1993](#)), others suggest little difference from solar-like dynamo behaviour. [Wright & Drake \(2016\)](#) and [Wright et al. \(2018\)](#) investigated the relationship between stellar rotation and activity levels for fully-convective late M-type dwarf stars. They found that the rotation/activity relationship for fully convective stars was almost indistinguishable from partially convective stars, suggesting the solar-type dynamo is independent of the presence of a tachocline. As such, the differential rotation which causes the ω effect may be occurring elsewhere in the stars, allowing for an $\alpha - \omega$ dynamo in fully convective stars. The requirement of the α effect means that convection is a prerequisite for a star to host magnetic reconnection, and consequently flaring.⁷

Regardless of the precise dynamo behaviour, this results in highly energetic magnetic fields, arranged throughout the stellar atmosphere. These form a variety of structures, most prominently coronal loops (see [Figure 2.2](#) for an image of the Sun illustrating these loop structures). These magnetic field lines stretch from their footpoints in the photosphere, up

⁶ Tachocline from the Greek *tachos* meaning speed, and *klino* meaning to bend or slope ([Gough, 2007](#)), describing the change in rotation speed between the stationary radiative zone, and the rapidly rotating convective zone.

⁷ There is tentative evidence to suggest non-convective stars such as A-type stars flare ([Pedersen et al., 2017](#)), but that lies far beyond the scope of this thesis.

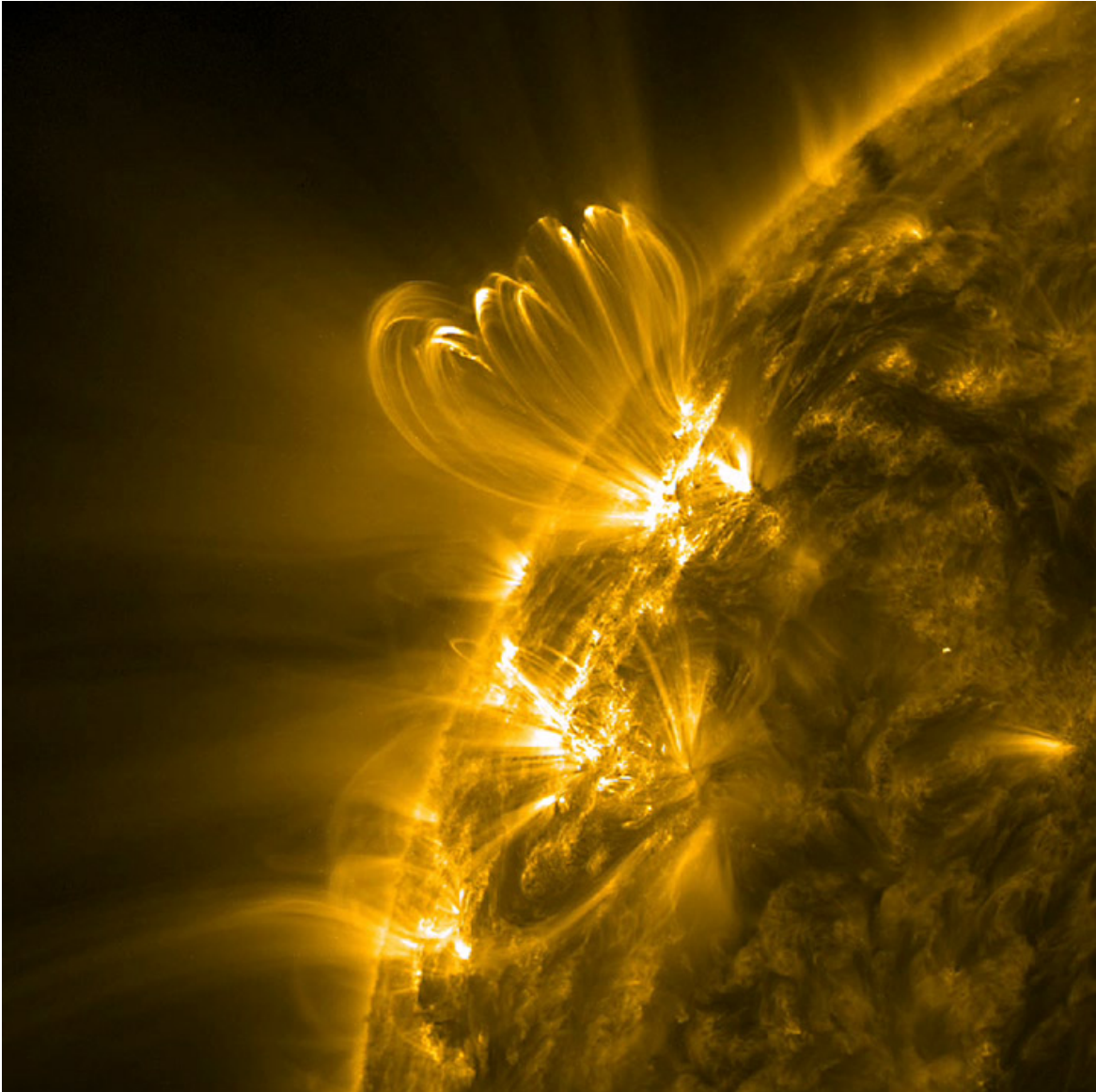


Fig. 2.2 An image of the Sun taken by the Solar Dynamics Observatory (SDO) satellite via the Atmospheric Imaging Assembly (AIA) instrument (Lemen et al., 2012), at 171\AA . This wavelength is sensitive to the emission of Fe IX at around 600,000 K. This is ideal for imaging coronal loops, and other quiet coronal emission (Boerner et al., 2012). Many coronal loops are evident in the central portion of the image, wherein super-heated plasma is travelling through magnetic field lines in a distinct loop structure. Courtesy of NASA/SDO and the AIA, EVE, and HMI science teams (NASA, 2012).

throughout the outer solar or stellar atmosphere, toward the corona (Reale, 2014). Plasma can flow along the field lines of these loops, or remain stationary within them. This hot plasma has a characteristic glow, which is dependent on the plasma temperature. This glow means the moving plasma directly illustrates the constantly evolving magnetic field structure

of the corona. However, [Alfvén \(1942\)](#) conceived of the MHD ‘ideal’ perfectly conducting plasma as having ‘locked-in’ field lines. As such, the field lines should be constant. In reality, the field lines evolve because the plasma is not ‘ideal’ and does exhibit resistivity. The introduction of resistivity into the plasma framework will allow for the plasma to diffuse and dissipate its energy via Ohmic heating. However, the timescales for the free diffusion of highly energetic magnetic fields are on the order of 10^{11} seconds ([Priest et al., 1991](#)), many orders of magnitude longer than the observed timescales of flaring, which are in the region of 10^3 seconds. The Sweet-Parker reconnection model ([Parker, 1957, 1963](#)) addressed this incongruity, and provided a theoretical framework wherein opposing magnetic field lines can undergo much more rapid diffusion. These oppositely directed field lines will attract, and move closer and closer together. They will be separated by extremely thin⁸ ‘current sheets’ extending the same length as the magnetic fields themselves. As these fields squeeze ever closer together, the plasma will flow through the current sheets. These sheets are very thin and the plasma is ‘forced’ through the sheets due to the attraction of the magnetic fields, so the diffusion of the magnetic energy can occur much quicker than the natural timescale would allow. The diffusion of the plasma within the current sheets induces Ohmic heating. The excess magnetic energy is released as kinetic and consequently thermal energy. The release of energy is a consequence of the reconfiguration of the magnetic fields, i.e., a change in their topologies allows the fields to relax into a more stable configuration. This is magnetic ‘reconnection’.

This Sweet-Parker model has a rate dependence on the plasma Lundquist number, S , scaling with $S^{-1/2}$ (i.e., increased reconnection rates for low Lundquist / poorly conducting plasma). The Lundquist number is defined as $S = \frac{Lv_a}{\eta}$. L is the plasma length scale, v_a is the Alfvén velocity⁹ and η is the plasma resistivity. The Lundquist number is a special case of the magnetic Reynolds number, where the MHD flow velocity is the Alfvén velocity. Highly-conductive plasma results in high Lundquist numbers, and vice-versa. This Lundquist number ratio is a measure of the relative timescales of the Alfvén wave to the plasma diffusion timescales. When the Lundquist number is small, plasma diffusion can occur relatively quickly, and the reconnection occurs more rapidly. As most solar plasma has a very large Lundquist number¹⁰ (i.e., highly conductive), Sweet-Parker reconnection was unable

⁸ These sheets have aspect ratios of 10^5 , meaning the sheet is 10^5 times wider than it is thick ([Biskamp, 1993](#)).

⁹ The phase velocity of the Alfvén wave, which propagate throughout MHD plasma.

¹⁰ Somewhere in the region $S \sim 10^{12} - 10^{14}$ for coronal plasma where the majority of flaring occurs ([Shibata & Magara, 2011](#); [Ng et al., 2012](#)).

to explain the fast reconnection rates observed for macroscopic solar flares (energies on the order of 10^{31} ergs), with the likely timescales on the order of 10^8 seconds. The Sweet-Parker model is also known as ‘slow reconnection’ for this reason.

This was later addressed by the Petschek model, first theorised by [Petschek \(1964\)](#). Here, ‘fast’ reconnection occurs in a much smaller current sheet. Standing MHD waves will form ‘shocks’ at each corner of the current sheet. This means the inflowing plasma will enter the current sheet, and then be forced out via the shock wave. The maximum reconnection rate is given by

$$M_{Ae} = \frac{\pi}{8 \ln R_{me}}, \quad (2.2.1)$$

where R_{me} is the magnetic Reynolds number, the general form of the Lundquist number. This logarithmic dependence on the plasma Lundquist number allows for much faster reconnection rates than the Sweet-Parker model.

While the exact mechanism responsible for magnetic reconnection remains elusive, some variation of the Petschek process appears likely for large-scale flares ([Loureiro & Uzdensky, 2016](#)). However, the Sweet-Parker model for magnetic reconnection is not irrelevant. A study by [Tsuneta & Katsukawa \(2004\)](#) suggested that Sweet-Parker reconnection would be the dominant reconnection process for very small-scale flare events¹¹ in poorly conductive plasma, i.e., plasma with a low Lundquist number. As such, we would expect enhanced rates of small-scale flaring in stars with especially resistive plasma, e.g., late-M-dwarf sub-types ([Mohanty et al., 2002](#)).

2.2.2 Flares

The most prominent signature of magnetic reconnection is flaring. Following the reconnection of magnetic field lines, the excess magnetic energy is delivered to local plasma, primarily in the form of kinetic energy, rapidly accelerating the plasma. The kinetic energy is converted into thermal energy, and this warm plasma will emit light. The intensity of light emitted decays over time, as the plasma cools. Additionally, the accelerated electrons will produce X-rays through bremsstrahlung processes. Energies associated with solar flares express a wide range of magnitudes and frequencies, from very large but infrequent X-class flares (with X-ray flux exceeding 10^{-4} W/m² at the Earth, or $\sim 10^{31}$ ergs per event; [Maehara et al.,](#)

¹¹ Flares in the pico/nanoflare range, with energies in the region of 10^{22} ergs.

2015), down to micro- and nano-flares. Micro- and nano-flares have energies on the order of 10^{-6} and 10^{-9} , respectively, of a typical X-class flare, but with occurrence rates that are orders of magnitude more frequent than the large-scale events.

Flares were first detected during the ‘Carrington Event’, by Carrington (1859) and Hodgson (1859). This was the detection of an extremely bright increase in flux on the solar surface, lasting only a few minutes. This flare remains one of the most powerful solar flares ever recorded, with estimates of its energy on the order of 10^{32-33} ergs (Tsurutani et al., 2003; Cliver & Dietrich, 2013). The flare was observed in whitelight. Flare emission occurs throughout the electromagnetic spectrum, but whitelight flares have historically been difficult to observe, as the enhancement in whitelight is small compared to the background luminosity of the Sun (Jess et al., 2008; Kretzschmar, 2011). This whitelight flare was observable due to its immense energy, allowing it to become visible despite the considerable background noise. Later flare analysis was made possible with advancements in the technology necessary to observe in hydrogen-alpha, extreme ultraviolet, X-ray, and radio emission, where the flare signal is easier to detect against the background.

The ‘Carrington’ flare also caused a coronal mass ejection (CME). This is the eruption of highly magnetised coronal plasma from the outer layer of the solar atmosphere, due to a weakening in the magnetic field containing the plasma (Aschwanden, 2004). CMEs are a common side effect of powerful flares, but are also associated with sunspots and other solar phenomena. It should be noted that solar flares do not directly cause CMEs, but they are connected because the magnetic reconnection which drives the particle acceleration leading to flaring is also the source of CMEs (Vršnak et al., 2005).

The electromagnetic radiation associated with flares interact with Earth, but it is CMEs which lead to an explosive emission of plasma and accelerated particles directly interacting with Earth.¹² As a result CMEs are a major driver of ‘space-weather’ affecting the Earth (Gosling, 1993). For example, the Carrington CME hit the Earth’s magnetosphere around 18 hours after the flare. This induced the largest geomagnetic storm on record, disrupting the Earth’s magnetic field, and causing telegraph machines to actually spark and start fires, due to the massive magnetic fields inducing electrical currents in wiring. Telegraph operation was also impaired for several hours, due to the noise induced in the magnetosphere (Muller, 2014). The widespread disruptive effect this event had on a world only beginning to rely on electronic communication highlights how vulnerable humanity is to another massive solar

¹² The Solar wind is also a source of accelerated particles at the Earth, but this is a steady stream compared to the more dramatic outburst of a CME (Parker, 1965)

flare. Even with preparation time, another massive flare would cause widespread communications blackout, electrical grid malfunctions and other issues. Other, lesser manifestations of space weather generated by solar activity include the aurora, and disruption of satellite communications. It also has implications for human space travel. Predicting the next ‘Carrington Event’ is one of the most important reasons to study solar and stellar flares.

Flare events are sometimes preceded by a ‘gradual phase’ in extreme ultraviolet (EUV) and soft X-ray (SXR) wavelengths, where the coronal plasma slowly warms up (Benz, 2016). Then there is an ‘impulsive phase’, where the majority of the stored magnetic energy is released, emitting over much of the electromagnetic spectrum. This is emitted in two forms : thermal, and nonthermal. As the fields reconnect in more stable configurations, the sudden change in magnetic energy accelerates local plasma and electrons in the corona. Some of these rapidly accelerated electrons travel along coronal loops to the footpoints in the more dense chromosphere, wherein they produce hard X-rays through ‘thick-target’ bremsstrahlung interactions with plasma ions (Güdel et al., 1996). Some electrons remain trapped in the loop and produce gyrosynchrotron radiation, in the form of microwave emission (Gary et al., 2018). These microwave and HXR emissions are known as ‘nonthermal emission’ (Minoshima et al., 2008). After an initial impulsive rise, nonthermal emission decreases rapidly. Alongside this, the accelerated electrons will more gradually heat the chromospheric plasma to the order of 1 to 30MK (Benz, 2016). This accelerated heating will cause plasma to expand and ‘evaporate’ into the corona. This hot bright coronal plasma will lose energy due to radiative losses, i.e, ‘thermal emission’. This thermal emission occurs across the electromagnetic spectrum, at SXR energies and below. The energy emitted in this process will have a relatively impulsive ‘rise phase’ as the plasma heats up, followed by a sustained decay phase. The relationship between the impulsive HXR, and the more gradual rise in SXR is known as the Neupert effect (Neupert, 1968).¹³ The hot plasma cools on a timescale which can be modelled as approximately exponential (Terzo et al., 2011; Jess et al., 2014, 2019; Dillon et al., 2020), and is often expressed in terms of the ‘ e -folding time’, the time taken for the flare to lose $1/e$ of its original energy. This e -folding time is also denoted as ‘ τ ’. This decay phase is much longer than the initial heating phase. The overall timing of flare phases vary dependent on the energy emitted. For a very large flare event the timescale might be on the order of seconds for the gradual phase, minutes for the impulsive, and hours in the decay phase (Benz & Krucker, 2002).

¹³ The rise phase of the SXR matches the time integral of the HXR, as the electrons associated with the HXR emission cause the plasma heating required for SXR emission.

White-Light flares (WLFs), are the emission of flaring signatures in the optical continuum. They are believed to be produced in all flare events (Neidig, 1989; Woods et al., 2006; Jess et al., 2008; Kretzschmar, 2011; Schmitt et al., 2016). WLFs are produced as a result of heating induced by non thermal electrons interacting with the dense chromosphere (the heating induces blackbody emission in the optical; Neidig, 1989; Machado et al., 1989; Neidig & Kane, 1993; Benz & Güdel, 2010), alongside heating induced by ‘back-warming’ radiation produced in the corona and upper chromosphere (Jess et al., 2008). The chromospheric emission caused by the electron heating is known as ‘core’ emission, while the coronal induced component is described as ‘halo’ emission (with the halo caused by ‘back-warming’ due to EUV radiation produced in the corona and upper atmosphere resulting in heating and subsequent black-body emission in the lower atmosphere; Machado et al., 1989; Isobe et al., 2007; Kawate et al., 2016). The WLF will peak impulsively; this is typically cotemporal with the HXR component (Hudson et al., 1992), but this relationship has been disputed in more recent work (Song et al., 2020, suggests whitelight flares could be a result of magnetic reconnection occurring in the lower atmosphere, heating the chromosphere through localised electron production) and they lose energy as the plasma cools, with the energy radiating away on an approximately exponential timescale. This ‘core-halo’ structure leads to WLFs exhibiting two approximately exponential cooling rates; chromospheric decay timescales in the core emission (on the order of 50s; Jess et al., 2014), and coronal timescales in the halo region (on the order of 500 s; Kawate et al., 2016). This longer coronal decay dominates the WLF signature in a large statistical study, due to the large time series integration and consequently the increased number statistics associated with the longer decay tail. Additionally, recent work has suggested this coronal emission can be stronger than the chromospheric signal (Kawate et al., 2016), further increasing the perceived coronal contribution.

Figure 2.3 shows a simple model of flare energy release over time. In this simplified model, the flare energy is released impulsively at the 20 second mark. This flare intensity then drops off, via an approximately exponential cooling phase. This simple flare model is the basis for the Monte-Carlo nanoflare simulation I used extensively throughout my research.

Macroscopic flares in the Sun have energies around 10^{29} to 10^{31} ergs (Benz, 2016), and are the large dramatic events the word ‘flare’ brings to mind. However, they are relatively infrequent. These flares might occur anywhere from once a week to several times a day depending on the current solar cycle. This means that macroscopic flaring is not a constant source of energy in the Sun. The relationship between flare energy and the frequency of occurrence is commonly described by a powerlaw (Aschwanden et al., 2000), which applies at both low and high flare energies (Aschwanden, 2019). The power-law exponent governs the

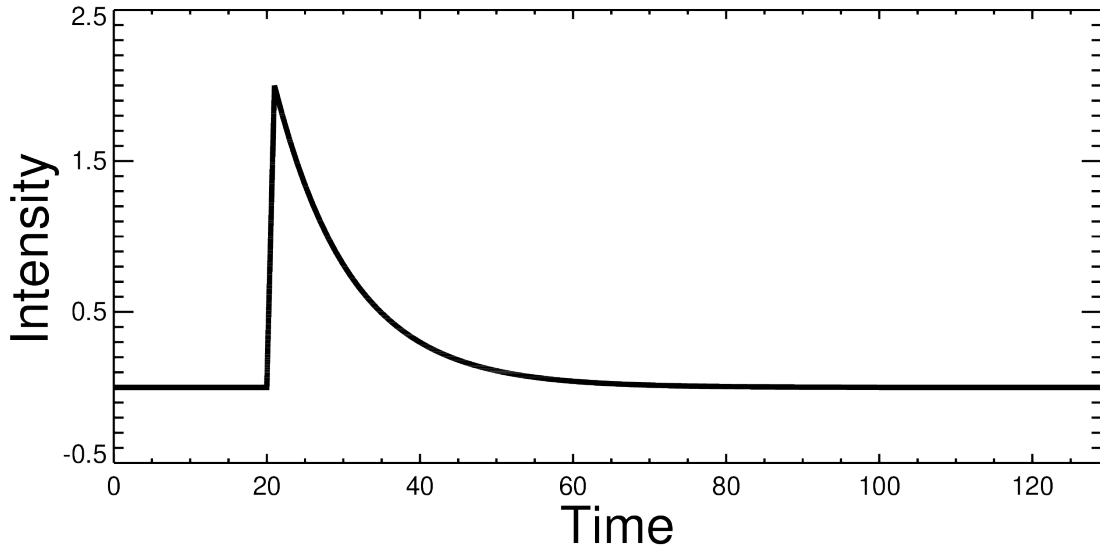


Fig. 2.3 A simplified model of flare energy release versus time, for impulsive flaring. The rapid conversion of magnetic energy to accelerated, hot, bright plasma manifests as an impulsive brightening. The superheated plasma then cools as energy is radiated away, following an approximately exponential decay timescale. This is the characteristic flare energy release.

frequency, dN/dE , of flaring events with an associated energy, E , through the relationship,

$$\frac{dN}{dE} \sim E^{-\alpha}, \quad (2.2.2)$$

where α represents the power-law index. For $\alpha > 2$, low-energy flares would dominate energetically, and allow for coronal heating by low-energy flare events. This critical value of $\alpha > 2$ is a consequence of the power-law distribution. If we integrate equation 2.2.2 (assuming $E_{min} \ll E_{max}$ and that $\alpha > 2$) to obtain the total energy contained under the powerlaw distribution, it is of the form,

$$E_{tot} = \int_{E_{min}}^{E_{max}} \frac{dN}{dE} E dE \approx \frac{1}{\alpha - 2} E_{min}^{-(\alpha-2)}. \quad (2.2.3)$$

As E_{min} tends towards zero (a natural consequence of a power-law distribution of energies), this total energy will tend towards infinity if $\alpha > 2$. In reality low-energy flaring cannot supply infinite energy, but it would form the dominant component of the overall energy budget when $\alpha > 2$.

Low-energy solar and stellar flares have long been a topic of wide interest, due to this potential to heat the corona. The power-law relation dictates that low-energy flares will

be many, many times more frequent than larger events, allowing for low-energy events to contribute significantly to the stellar coronal energy budget. Milli- and micro- flares have energies 10^{-3} and 10^{-6} that of larger flares, but with much increased frequency.

The next energy regime down is nanoflare activity. The idea of small and impulsive events which would be capable of heating the corona were first proposed by Gold (1965)¹⁴ and then much expanded upon and dubbed ‘nanoflares’ by Parker (1988). Nanoflares are, as the name would suggest, nano-scale flares, with energies spanning between 10^{22} to 10^{25} ergs: 10^{-9} times less energetic than typical macroscopic flaring. While milli- and micro-flares have been relatively well observed, nanoflares lie below the noise floor of current observation, leaving them individually undetectable in the Sun. Despite their individually low energies, nanoflares are correspondingly much more frequent than larger flares, as the power-law relationship between flare energy and flare occurrence would naturally suggest. An entire stellar surface is capable of supporting hundreds or even thousands of nanoflares per second, depending on the power-law index (Benz, 2016). As such, nanoflares hold the potential to form a large proportion of a stellar coronal energy budget, despite remaining individually undetectable. It was due to this property of ‘hidden energy’ that led Parker (1988) to propose that low-energy (but highly frequent) nano-flares could supply sufficient thermal energy to the outer solar atmosphere to maintain its so far inexplicable elevated temperatures. This ‘coronal heating problem’ is a major outstanding problem in solar physics. The solar corona has temperatures in excess of 1MK well beyond the temperature of the preceding photosphere and chromosphere layers,¹⁵ but with no apparent energy source providing the necessary flux of 10^7 ergs cm^{-2} s^{-1} (Withbroe, 1988; Aschwanden et al., 2007) to maintain that temperature. As discussed above, low-energy nanoflares with a powerlaw index of $\alpha > 2$ would provide sufficient energy to warm the corona (Parker, 1988; Narain & Pandey, 2006) due to their dominant contribution to the coronal energy budget.

As nanoflares cannot be directly observed, researchers have had to turn their attention to other approaches, such as spectroscopic techniques to compare the scaling between kinetic temperatures and emission measures of coronal plasma (e.g., Klimchuk & Cargill, 2001; Sarkar & Walsh, 2008; Sarkar & Walsh, 2009; Bradshaw et al., 2012), comparisons drawn between EUV and X-ray emission (e.g., Sakamoto et al., 2008; Vekstein, 2009), or the examination of the time delays between different temperature-sensitive EUV imaging

¹⁴ Regrettably I was unable to source a copy of this discussion, but it is cited by Cargill et al. (2015) as the first discussion of small-scale coronal current sheets.

¹⁵ Which are on the order of $10^3 - 10^4$ K.

channels (e.g., Viall & Klimchuk, 2011, 2012, 2013, 2015, 2016, 2017). In addition, Terzo et al. (2011) and Jess et al. (2014) employed statistical techniques to provide evidence of solar nanoflares.

Recent development in these statistical approaches was carried out in my Masters project.¹⁶ These findings were then adapted and published as Jess et al. (2019).¹⁷ In this work, the presence of nanoflares in a seemingly quiescent solar dataset was inferred by comparing intensity fluctuations extracted from high-time-resolution imaging with those from Monte Carlo synthetic lightcurves designed to replicate the presence of small-scale nanoflare events. Monte-Carlo modelling to generate synthetic light curves had previously been applied to replicate stellar microflare events by Kashyap et al. (2002). Jess et al. (2019) further suggested that similar nanoflare statistical techniques could also be directly applied to high time resolution observations of stellar sources, through the comparisons of intensity fluctuations with nanoflare-specific simulations. The primary advantage of this statistical analysis combined with Monte-Carlo modelling is the wider applicability of these techniques. While specific emission bands and spectral features can be examined to infer the presence of nanoflaring, only this statistical approach directly searches for the intensity signatures associated with nanoflares. As such, it is applicable across a wide band of wavelengths, and well suited to carry out stellar nanoflare analysis. The statistical analysis, and subsequent Monte-Carlo modelling code was written in IDL.

Nanoflares exist on or below the noise-floor of observation. As such, they are detected due to their distinction from that noise. In a large sample, the underlying noise of a seemingly quiescent lightcurve will tend toward a Gaussian distribution (as discussed in Section 2.1). Nanoflares exhibit two statistical signatures which distinguish them from that Gaussian distribution. These can be identified through statistically benchmarking the fluctuations around the mean of the lightcurve.¹⁸ Viewing these statistical fluctuations via a histogram of their occurrence provides a robust method for their characterisation.

The first characteristic statistical signature is a negative median offset, whereby the median value of the distribution is $< 0 \sigma_N$,¹⁹ i.e., offset from the mean of the distribution that

¹⁶ My Masters thesis was entitled ‘Solar Nanoflares : How Big? How Many? How Powerful?’ (2017). Available upon request.

¹⁷ I was the second author on this publication, having contributed the analysis and simulation code during my Masters project.

¹⁸ This statistical analysis methodology is fully explained in Chapter 3

¹⁹ σ_N is a measure of deviations away from the mean-normalised standard deviation of the distribution; $0 \sigma_N$ is the centre of a standard Gaussian. See 2.1 for a graphical representation.

is equal to $0 \sigma_N$. This is a characteristic signal associated with an exponentially decaying lightcurve, i.e., the decay phase following an impulsive deposition of energy occurs over a longer timescale than the impulsive timescale, hence providing more negative fluctuations that are beneath the elevated signal mean caused by the impulsive event itself. The second nanoflare signature is an excess of fluctuations at $\sim 2 \sigma_N$, which is caused by the impulsive nature of the nanoflare energy release. The excess of impulsive signatures give rise to an asymmetric distribution with an excess of fluctuations visible at $\sim 2 \sigma_N$ in the corresponding histogram, which can be further benchmarked using Fisher skewness coefficients.

Therefore, a seemingly quiescent lightcurve exhibiting both of these statistical signals is a strong candidate to contain embedded nanoflare signatures. If no nanoflare signal was present, the embedded noise fluctuations would follow a standard Gaussian distribution as a result of Poisson statistics tending to a Gaussian in the limit of large-number statistics (Terzo et al., 2011). In the case of very weak nanoflare activity, only a negative median offset would be present, since the weak impulsive signatures are too faint to provide a fluctuation excess at $\sim 2 \sigma_N$ in the corresponding distribution.

In addition to these primary indicators, nanoflare activity will impact the benchmarks of the shapes and widths of the intensity fluctuation distributions. Namely, the kurtosis and ζ values, where ζ is the ratio of the full-width at eighth-maximum to that of the full-width at half-maximum (i.e., FW $\frac{1}{8}$ M-to-FWHM ratio) of the resulting distribution. Note that a Gaussian distribution will have $\zeta = 1.73$, hence deviations from this provide an indication of the intensity fluctuation occurrences taking place close to, and far away from the timeseries mean. Measurement of these statistical signatures allow for further parameterisation of the underlying nanoflare signatures. This statistical technique has been useful in furthering the understanding of solar nanoflares particularly due to its wide applicability across wavelengths, but much debate remains as to their exact nature and energy release rates.

2.2.3 *Recent Advances in Stellar Nanoflares*

Stellar flares with energies similar to and exceeding those of our own Sun have been observed in many observations of stellar sources (e.g., Lacy et al., 1976; Audard et al., 2000; Maehara et al., 2012; Shibayama et al., 2013; Jackman et al., 2018), predominantly occurring in stars with the convective atmospheres required to generate the magnetic fields necessary for reconnection to take place (Pedersen et al., 2017). While much of our understanding of stellar flares builds upon solar flare studies, stellar flare analysis is invaluable for better understanding the Sun. The number of flaring stars, and their varying conditions, provide

stellar laboratories to investigate the full spectrum of flaring in stars. Low energy stellar flares have been investigated by a number of authors (e.g., [Hudson, 1991](#); [Robinson et al., 1995, 1999](#); [Kashyap et al., 2002](#); [Güdel et al., 2003](#); [Güdel, 2004](#); [Welsh et al., 2006](#); [Reale, 2016](#), to name but a few).

Much like their solar counterparts, there has been no clear consensus on the flaring rates of small-scale stellar flares, with the proposed power-law indices in the aforementioned studies spanning the range $1.5 \leq \alpha \leq 2.7$. A review by [Güdel \(2004\)](#) suggested that power-law indices with $\alpha > 2$ may be present in M-dwarfs. [Butler et al. \(1986\)](#) reported the presence of small-scale microflares in observations of dMe flare stars previously considered quiescent. Other authors (e.g., [Brasseur et al., 2019](#)) have investigated near-ultraviolet (NUV) flare events, with powerlaws of $\alpha = 1.72 \pm 0.05$ uncovered. These authors concluded that NUV flare mechanics are governed by the same physical processes as captured in solar events. Optical microflare signatures on M-dwarfs have also exhibited short time-scale variability, as discussed by [Schmitt et al. \(2016\)](#), who found flare rise timescales on the order of seconds, with flare signatures of comparable brightness to the M-dwarf quiescent B-band luminosity. These studies highlight the growing interest in small-scale stellar flare events, and demonstrate the synergy between stellar and solar observational and modelling efforts.

However, few studies have investigated the role of nanoflares in other stellar sources. This unexplored potential motivated my interest in studying stellar nanoflare activity. At the outset of my PhD, the only substantial publication discussing stellar nanoflaring was [Falla & Potter \(1999\)](#). The authors examined the production of nanoflare energies in the X-ray emission of RS CVn systems, and concluded that while nanoflares may be produced in these stars, current observational limits would prohibit the direct detection of nanoflare events in the X-ray band. True to the predictions of [Falla & Potter \(1999\)](#), currently the lowest energy stellar flares that have been directly observed are on the order of 10^{28} ergs ([Güdel et al., 2002](#); [Benz & Güdel, 2010](#)), which are orders of magnitude above the traditional range of individual nanoflare energies. It is generally predicted that the flare occurrence rate will be higher on magnetically active stars, such as dMe flare stars ([Walkowicz et al., 2011](#)). As such, nanoflares may be even more frequent on these stellar sources when compared to the Sun, thus producing power-law indices substantially larger than estimates for the solar case. These stars are ideal candidates for the identification of highly frequent but individually low-signal nanoflares.

Stellar nanoflares are well below the noise floor for individual observation, but over an entire stellar surface, the interplay of hundreds or even thousands of nanoflares per second over a sufficiently long enough timeseries can produce an detectable signal – provided that

you know how to find it. By using statistical and simulation modelling, the characteristic statistical signatures of flaring can be extracted from seemingly flare-free timeseries. These statistical and simulation techniques are complimentary to the statistical quantification and Monte-Carlo simulation applied to the Radox biochip images. Stellar nanoflares were thus an avenue rich for exploration, with the potential to examine nanoflare activity across a range of stellar types. This ‘stellar laboratory’ of unexplored small-scale flaring would hold implications for behaviour in the Sun as well, helping to further explore solar nanoflare activity.

Initially, I investigated a nanoflare link to ‘periodic’ brightening events seen in MV stars, by searching for stellar nanoflare statistical signatures and any associated periodic signature. On the contrary to the flare frequencies predicted by the dN/dE power-law relationship, several studies have documented evidence for ‘periodic’ brightness variability through the examination of stellar intensity fluctuations, with periods ranging between 1 – 1000 s (Andrews, 1989; Rodríguez et al., 2016; McLaughlin et al., 2018). These periodic brightenings are of uncertain origin, but were believed to be linked to ubiquitous p -mode oscillations or other magnetohydrodynamic (MHD) wave behaviour (e.g., Aschwanden et al., 1999; Nakariakov & Verwichte, 2005; Nakariakov et al., 2010; McLaughlin et al., 2018) generated in the convective layers of stars. The link to p -mode oscillations is due to a comparable period range (1 – 1000 s), in addition to them being observed during periods of quiescence (i.e., no associated macroscopic flaring signatures). In a number of publications, Andrews (1989, 1990a,b) examined dMe flare stars across a range of conditions, from immediately after large-scale flare events, to during relatively long periods of quiescence, and found that the dMe flare stars exhibited small periodic brightenings, on a scale of seconds to minutes. The author interpreted these periodic signals as a likely consequence of MHD wave behaviour, as the periodic signals were observed during times of quiescence, with no impulsive activity witnessed in the timeseries. A follow up study by Andrews & Doyle (1993) investigated whether flaring events can reproduce signals with 1 – 1000 s periodicities, and while they suggested that individual small-scale flares may contribute to such signatures, they were unable to provide sufficient evidence to directly link flaring events to the periodic signals.

However, flare-related variability giving rise to periodic phenomena has been documented across a range of solar observing sequences. McLaughlin et al. (2018) discuss self-oscillatory

flaring²⁰ (perhaps due to magnetic dripping,²¹ as discussed by Nakariakov et al., 2010), which can produce a periodic signal, despite non-periodic driving. Additionally, Arzner & Güdel (2004) discussed flare clustering, and the relationship between the mean flaring interval and expected count rates. This led me to speculate that small-scale flaring may have a quasi-periodic nature, due in part to the power-law governing its occurrence rates. With this in mind, the superposition of hundreds or thousands of (quasi-) periodic nanoflare signatures each second may give rise to a periodic brightness signal, without any ‘flare-like’ impulsive signatures seen in the corresponding stellar lightcurve. By combining the statistical parameterisation techniques developed for solar nanoflare detection with a novel Fourier spectral analysis, I linked stellar nanoflare signals to periodic brightenings found in stellar M dwarf lightcurves. This was published in Dillon et al. (2020), which is included in this work as Chapter 5.

The resulting nanoflare power-law indices found in that work were greatly enhanced from the values seen in other stars and the Sun, with $\alpha > 3$. This is well in excess of the $\alpha = 2$ required for coronal heating, so these nanoflares are responsible for a significant portion of the energy budget in these stars, an exciting result in its own right. This is in addition to nanoflare activity producing periodic signatures which had previously been attributed solely to wave behaviour.

One theory for the power-law enhancement was that the fully convective nature of the stars studied led to enhanced stellar nanoflare activity. As discussed in Section 2.2.1, fully convective stars lack the radiative zone powering the tachocline dynamo seen in solar-like stars. I speculated that the nanoflare enhancement in the fully convective stars may have been due to this change in dynamo leading to enhanced small-scale reconnection. However, the results of Wright & Drake (2016) and Wright et al. (2018) would appear to discredit that, finding that solar-like stars appear to operate a dynamo independent of the tachocline, and hence consistent with that present in fully convective stellar stars. An alternative explanation may lie with the type of magnetic reconnection powering these nanoflares. Sweet-Parker reconnection is more favourable for nano/pico scale flare energies, provided the stellar Lundquist number is small (i.e., highly resistive plasma).

To investigate this, I carried out a followup study (see Chapter 6) examining nanoflare parameters across partially to fully convective M dwarf stars. I found that full convection was

²⁰ Periodic flaring driven by a non-periodic energy input.

²¹ A buildup of magnetic flare energy analogous to a water droplet, which builds until it overcomes resistance and ‘drips’. This ‘drip’ can be periodic, even when driven by continuous input of energy.

linked to increased nanoflare activity, and that for the latest M4V type stars, the power-law and e -folding time increased the most. I speculated this was an indication that the enhanced Sweet-Parker reconnection explanation is more likely, due to the increased resistivity in later M-type stars (Mohanty et al., 2002).

At the beginning of my PhD, there were no observed signatures of stellar nanoflare activity. Now, there are measured nanoflare power-law indices and e -folding times for 18 fully convective MV stars, with a host of new science to explore. Continued research in this area is needed to answer key questions. Do the enhanced reconnection rates and e -folding times continue to increase with later MV sub-types? What are the long-term variability trends in these stellar nanoflare signatures? Can we recover stellar nanoflares in other spectral-types? What will this teach us about nanoflare activity in the Sun? Answering these questions with continued application of statistical, Fourier and simulation methods will help to uncover the true nature of nanoflare activity on distant stars, answer questions relating to these key phenomena in stars, and explore the implications for our own Sun.

2.3 BIOMEDICAL IMAGING

While the biomedical applications of this work do not strictly fit within the traditional framework of a thesis submitted for the title of ‘Doctor of Philosophy’ in Mathematics and Physics, they are perhaps the most important outcome of this work for the general public. While I hope that my contributions to the field of stellar flare analysis will have some impact in the astrophysics community, those same signal and noise modelling techniques have already begun to have a meaningful impact improving medical diagnostic sensitivity on hundreds of thousands of analysers installed across the world. My PhD would not have been possible without the funding awarded to carry out this dual-natured research, and I feel it is important to preserve the findings and advocate for similar research to continue in this vein in the future.

Radox utilise a ‘biological microchip’, or ‘biochip’ to carry out their medical diagnostics. FitzGerald et al. (2005) describes the operation of the Radox biochip in detail. These biochips are a chemiluminescent ‘immunoassay’. Immunoassays are used extensively throughout diagnostic medicine and in industrial biomedical applications; the most visible example might be home pregnancy tests.²² Immunoassays are a method for detecting the

²² Or an example which rose to unprecedented global prominence during the final span of my PhD: a COVID-19 lateral flow test.

presence of certain chemical or biological compounds by utilising a ‘lock and key’ mechanism. This is the binding of an anti-body²³ analogous to a ‘lock’, and a corresponding ‘key’ in the form of an ‘anti-gen’(or analyte ; Darwish, 2006).²⁴ This is achieved through combining a sample with enzymes and reagents containing the corresponding anti-body for each desired test. This anti-body and anti-gen mechanism is (as ‘immuno’ suggests) the same principle by which the immune system works. By implementing a ‘label’ mechanism we can determine the quantity of the analyte present in the sample. The ‘label’ can take many forms, such as a colour change—or the process used by Randox—chemiluminescence.²⁵ Chemiluminescence is the emission of light due to a chemical reaction, resulting in the emission of a de-excited photon (Byrne et al., 2013). By measuring the intensity of this light with a CCD, the concentration of analyte can be determined.²⁶ This means the photometric accuracy of the subsequent analysis is incredibly important. As a diagnostic medical test, extremely stringent standards must be met. These biochips are subject to rigorous manufacturing and sample preparation steps to ensure consistency from chip to chip. Before the sample and chemiluminescent reagents are added, samples can undergo multiple runs of cleaning and preparation. A huge variety of different biological samples can be tested, with a correspondingly large range of reagents and enzymes used to carry out different tests. The chip contains a number of Discrete Test Regions (DTRs). Each DTR is essentially a self contained immunoassay, a small point in the biochip where reactions occur and subsequently where light will be emitted. Distinct tests can be placed at each DTR spot, allowing for multiple tests to be carried out per biochip imaged. The exact grid and layout varies from product to product, but a typical chip contains a grid of 5×5 DTRs, each separated by around a millimetre. In every biochip, a set number of calibration DTR are added. This is achieved by the addition of a known amount of reagent, to produce a signal of known brightness. The calibration DTRs are placed in the same position in every chip, and (theoretically) are consistent in brightness from chip to chip. This allows for calibration of the brightness levels of the other DTRs.

These bio-chips consist of two main types: competitive and sandwich assays. These operate on opposite principles (Cox, 2012). Sandwich assays bind an antibody at the DTR surface to the analyte. Then, this analyte will bind to a labelled / luminescent antibody,

²³ The reagent or enzyme used to test for the anti-gen.

²⁴ The substance being tested for.

²⁵ This is a simplified and condensed description of the immunoassay process. Many variations of the process exist, with a wide diversity in the exact mechanism.

²⁶ Depending on the exact test, the analyte concentration may be inversely proportional to the light intensity.

effectively forming a ‘sandwich’ of the three structures, as seen in Figure 2.4. Competitive assays are the inverse of this. The more analyte present, the less light produced. In this scheme, luminescent antibodies are added to the sample, alongside the sample analyte. These will ‘compete’ to bind to the DTR surface antibody, with only one structure binding to the DTR.²⁷ The analyte more favourably binds to this spot. The unbound luminescent antibodies will be washed away before being imaged. The more analyte present in the sample the less of the luminescent antibodies and consequently, the less light produced. This is shown in Figure 2.5.

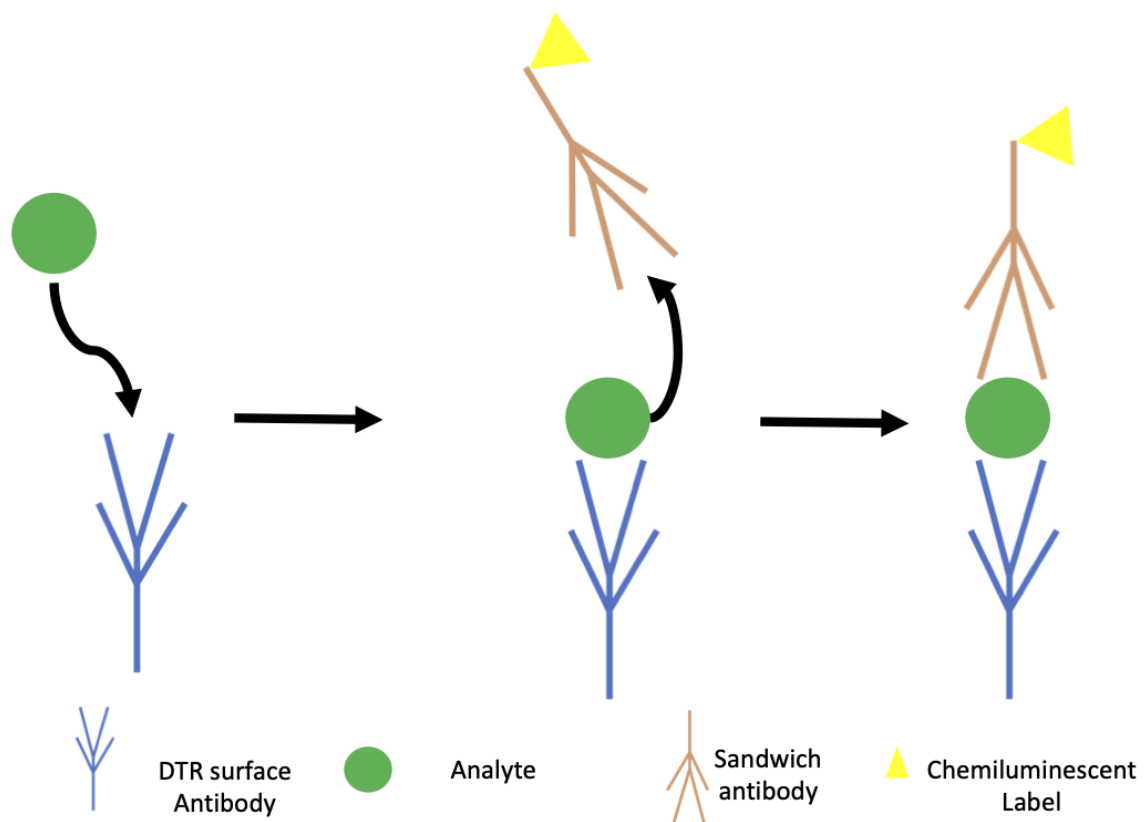


Fig. 2.4 A schematic of the sandwich assay. The DTR surface antibody binds with the corresponding analyte in the sample. This then binds to a labelled antibody which is added to the sample. This label is the chemiluminescent chemical. The analyte concentration is proportional to the intensity of light emitted.

In many tests, both assay types are present. Very faint and relatively bright signals separated by a few pixels all need to be imaged in detail. This causes an issue with the

²⁷ This competitive binding resembles an open sandwich, if you prefer your biomedical diagnostic analogies to be consistently sandwich-themed.

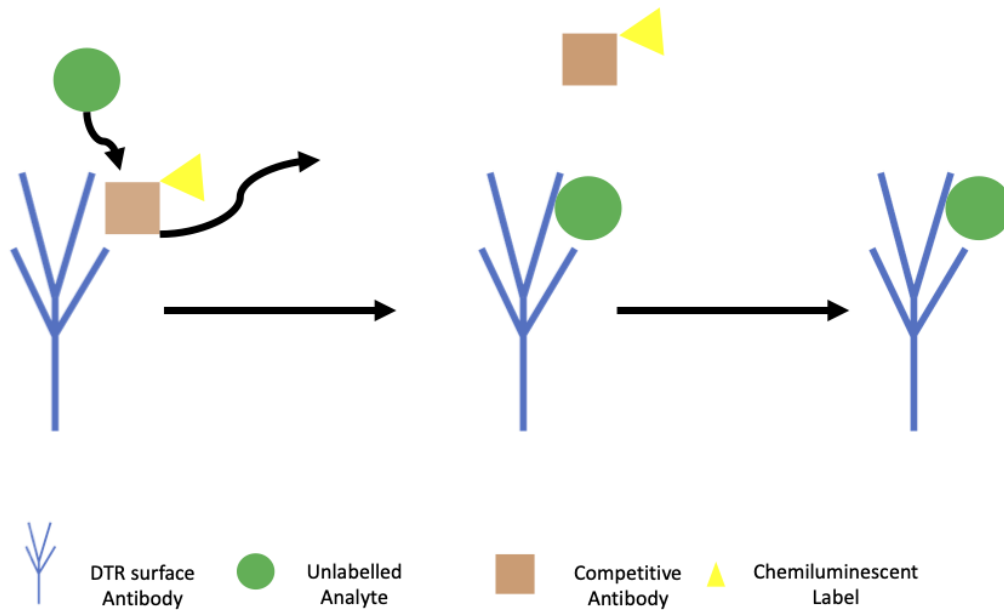


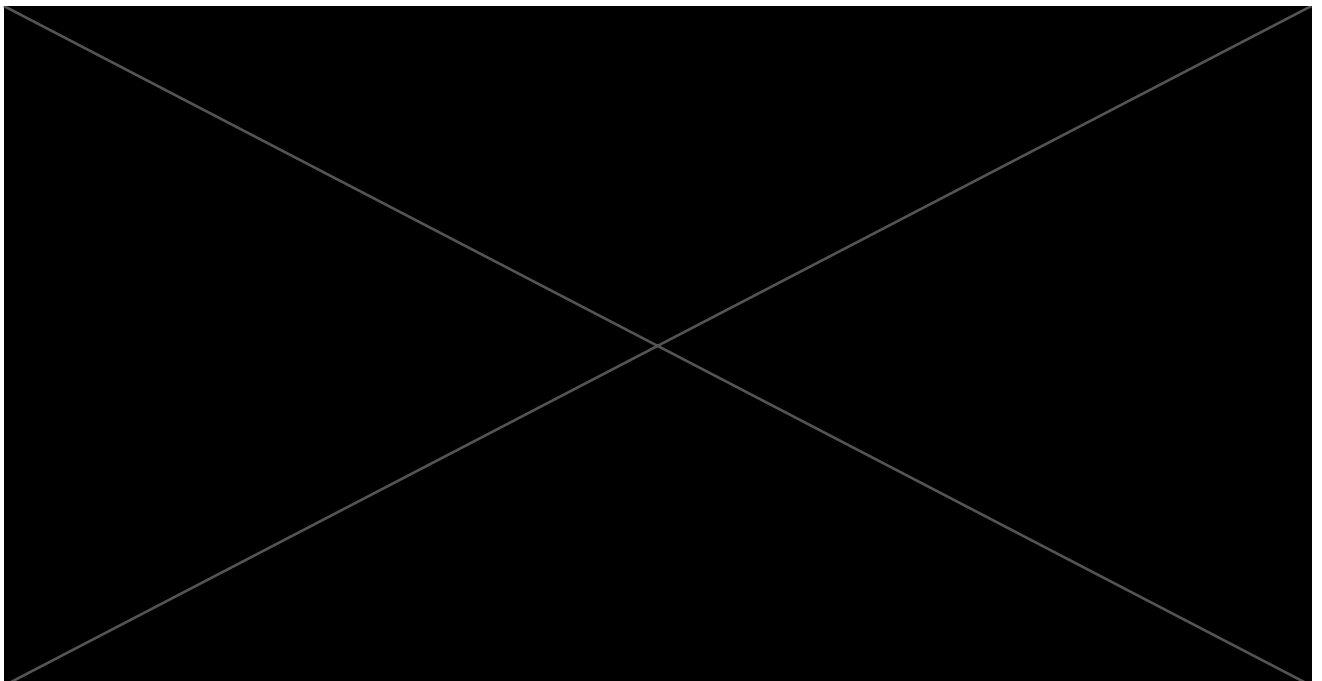
Fig. 2.5 A schematic of the competitive assay. The analyte and labelled antibodies compete to bind to the surface DTR, with the analyte binding preferentially. The unbound labelled antibody is then washed away. As such, the light intensity is inversely proportional to the analyte concentration.

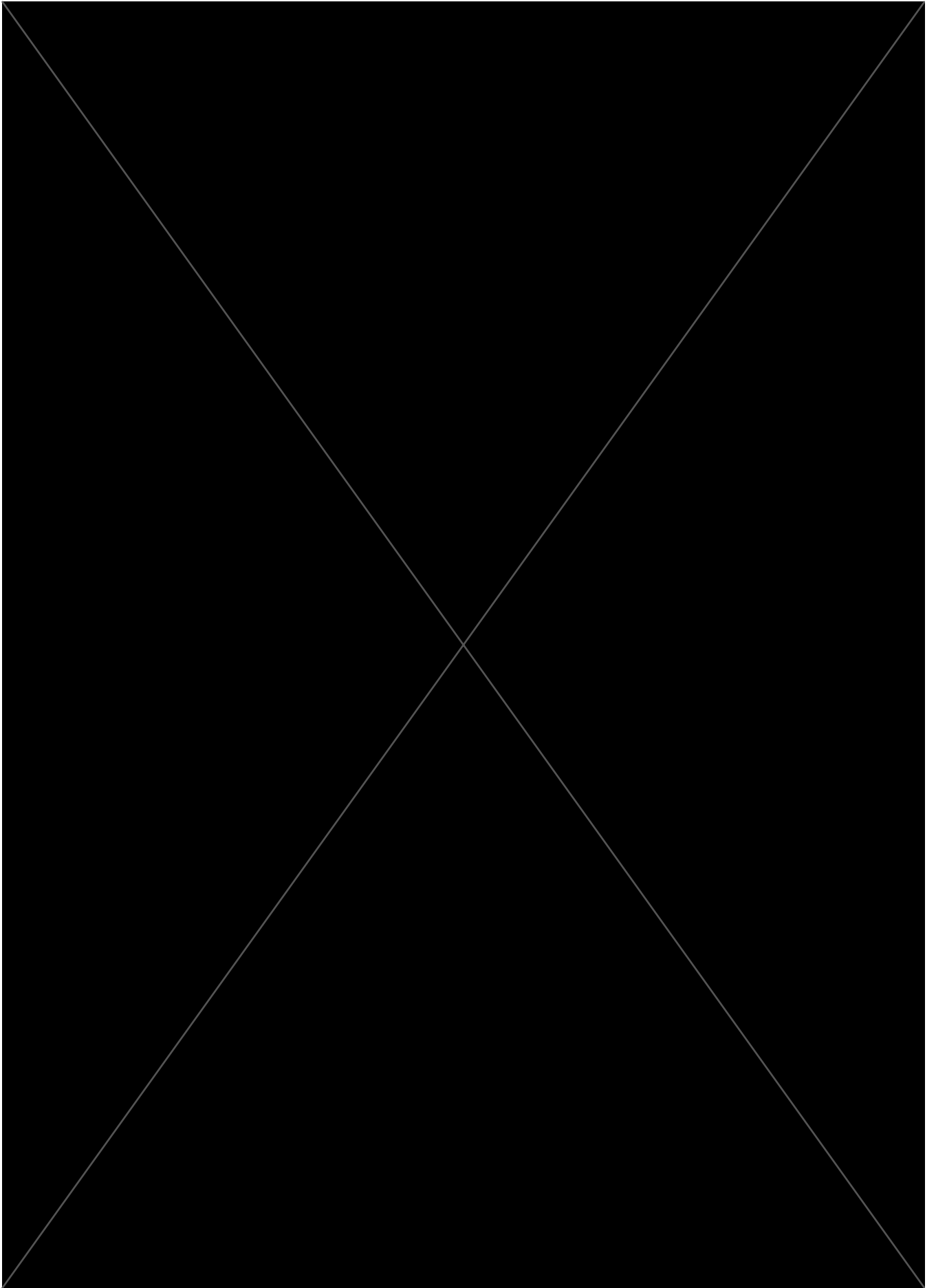
dynamic range. This problem was analogous to issues in solar and stellar astrophysics, when searching for very dim signals (e.g., nanoflares) next to the bright background of the Sun or star. The first step to combating these signal to noise and dynamic range issues is understanding the noise sources in the image. By understanding the noise characteristics, we can better distinguish the DTR signals from background noise. Further compounding these issues are the speed of imaging required. While some platforms are relatively unconstrained by observation time, the fastest analysers have through-puts on the order of 60 seconds. This means the imaging and image processing need to complete within this span. Finally, it is important to note the scale of the Radox analyser install base. Thousands of distinct analysers are in use all over the world, each with their own particular noise performance and characteristics. An approach with the widest possible generality was needed for the noise characterisation, and subsequent mitigation techniques.

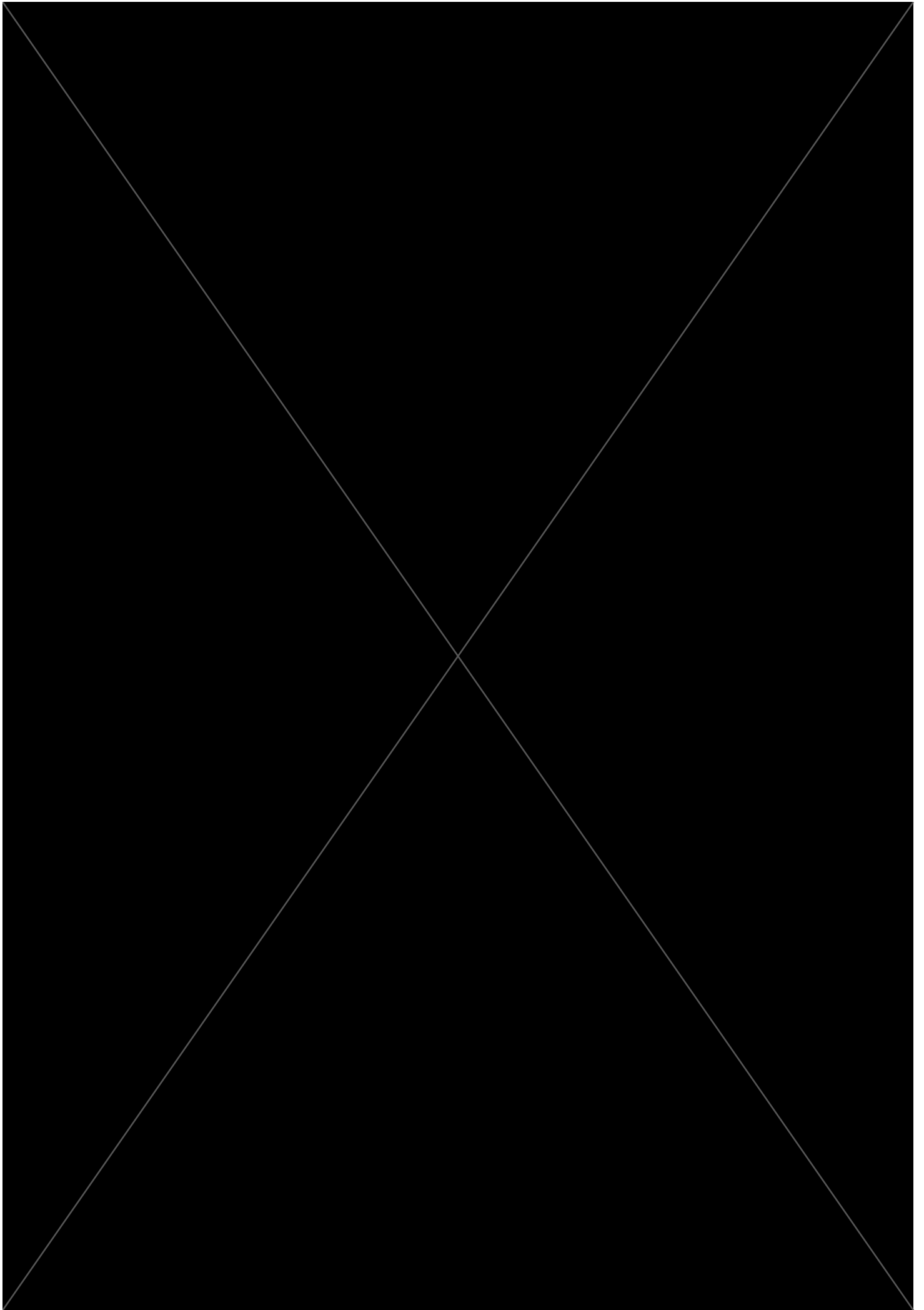
Figure 2.6 shows a biochip carrier with a 3×3 configuration. This image was sourced from Radox (2013). These carriers can hold a large number of biochips so they can be more easily loaded for testing. Single and double biochip carriers are also common. Each white well on the carrier is an individual biochip, containing tens of DTR spots. These DTRs will

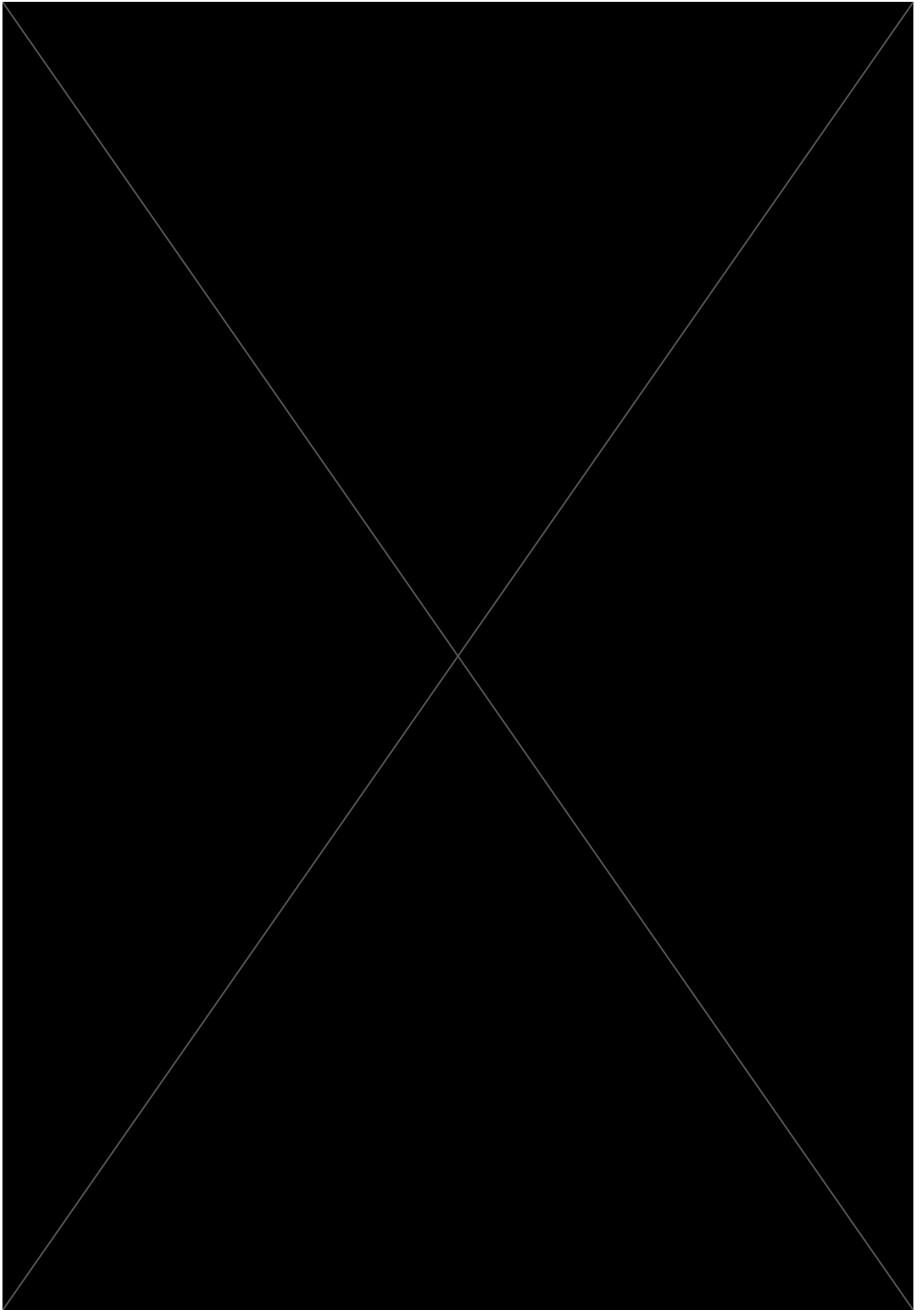


Fig. 2.6 A 3×3 biochip carrier. Each white well is an individual biochip, itself made up of distinct DTR. Image source [Radox \(2013\)](#). This carrier is approximately 50mm tall, by 40mm wide. The individual biochips are approximately 9mm tall by 9 mm wide.





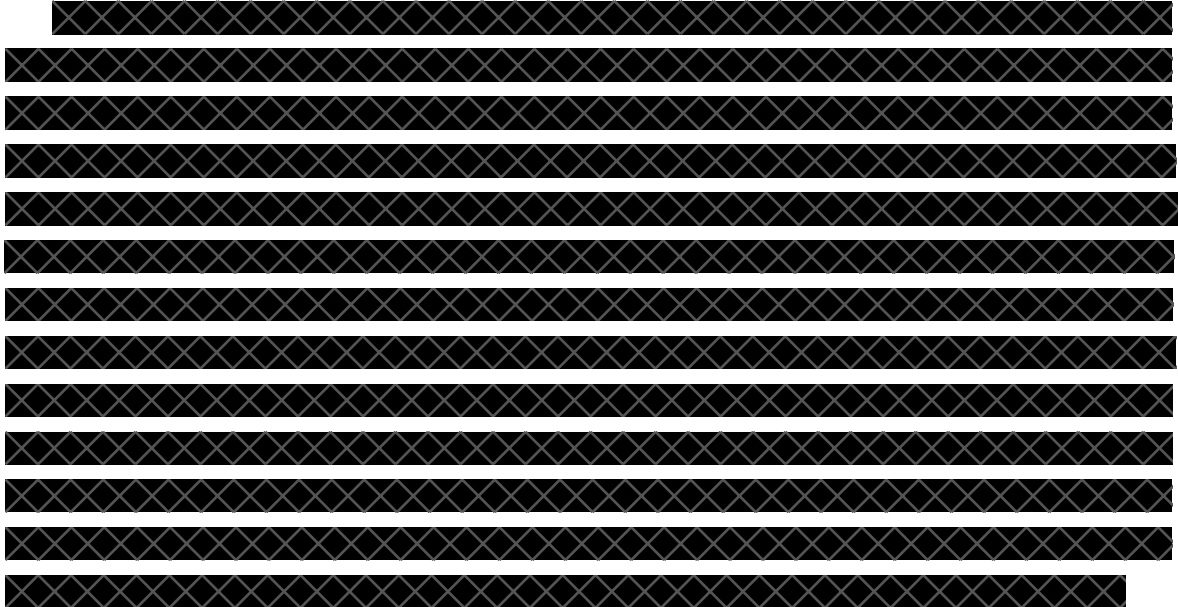




ing. Computers cannot ‘see’ in the human sense,²⁹ when provided with an image they do not understand it as a whole connected series of shapes, but as a mathematical grid of distinct pixel intensity values. However, through the application of mathematical rules, features can be reliably identified. Computer vision relies on simplifying an image, and focusing on strong and defined features like edges. This allows for the reliable identification of shapes within images. This process of reducing complex ‘raw’ images to simplified symbolic representations is the key underpinning of computer vision (Leavers, 1992; Shapiro & Stockman, 2001). This is achieved through ‘image transforms’, effectively matrix operators which when applied to an image produced the desired geometric isolation. This machine vision problem has direct analogy to solar image processing. Identifying transient solar features is a focus of 2-D solar image analysis. Traditional analysis has relied on ‘simple’ techniques (e.g., papers utilising edge detection, Hough transforms, and other image transforms designed to identify relatively simple geometric shapes, e.g., Zharkova et al., 2005; Walker, 2012; Tavabi, 2012; Schad, 2017), while more recent advancements have introduced ‘machine-learning’ for more complicated feature recognition (these approaches train neural networks to make decisions on new data, based on the statistical inferences it produces from classified training data e.g., Colak & Qahwaji, 2008; Armstrong & Fletcher, 2019). The approximate distinction between ‘machine vision’ and ‘machine-learning’ is their evolution over time. Simple machine vision uses image transforms to apply the same processing to every image. These image transforms are the application of a consistent rule. Machine-learning is trained to identify more complicated features. It can apply different analysis to different features, making ‘decisions’ on its own. This can be incredibly powerful, and has the power to find new features it wasn’t trained on. However, there is the major disadvantage of being ‘unknowable’. The decision tree used by the machine learning algorithm is not designed, but learned. While recent advancement in machine vision has focused on ‘machine-learning’, I decided to avoid this approach for several key reasons. BISCUIT required the identification of bright circular features, which are characteristically arranged. While the programming to achieve this remained challenging, it was at the start a clearly defined problem, with a known solution. This software was ultimately destined for medical diagnostics. Software used for medical diagnostics needs to conform to a wide array of rules and regulations. Chief among these are justifications and explanations for every step in the code. While machine-learning is becoming accepted in medical diagnostics, this carries with it a complicated certification process. I also wanted

²⁹ This statement is valid at the time of writing, but due to rapid advancements in artificial intelligence will likely change sooner than one might think.

to keep the processing time to a minimum, which would not be guaranteed with a complex machine-learning solution.



METHODS

Due to the dual-nature of this research, this chapter details the development of signal- and noise-modelling techniques for both biomedical and astrophysical applications. Both of these applications involved below-noise-floor observations, which required benchmarking of the underlying noise distribution. Statistical analysis was used to benchmark and characterise the signals within both of these datasets. Likewise, a similar technique to generate Monte-Carlo simulations of both synthetic noise and modelled signals was used in both areas. These statistical techniques were inspired by statistical analysis of solar nanoflares first developed by [Terzo et al. \(2011\)](#) and [Jess et al. \(2014\)](#). These techniques were further developed and combined with accompanying Monte-Carlo modelling during my Masters project. This work led to the publication of [Jess et al. \(2019\)](#), which was based on the results of nanoflare Monte-Carlo simulation code developed during my Masters project.

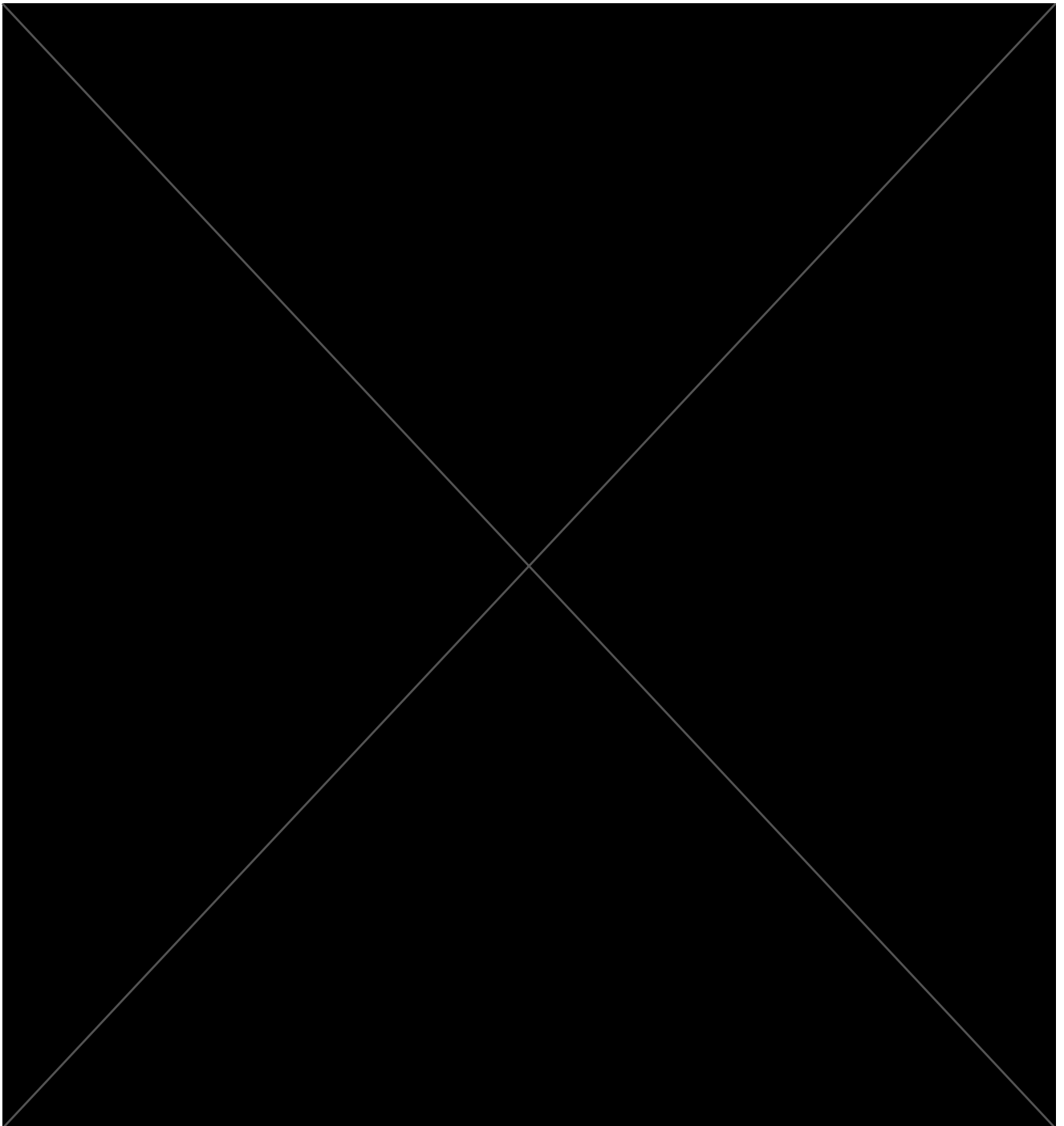
These statistical tests were primarily derived from the concept of ‘Z-score’ testing. The Z-score of a given point x , within a timeseries, is described by the equation,

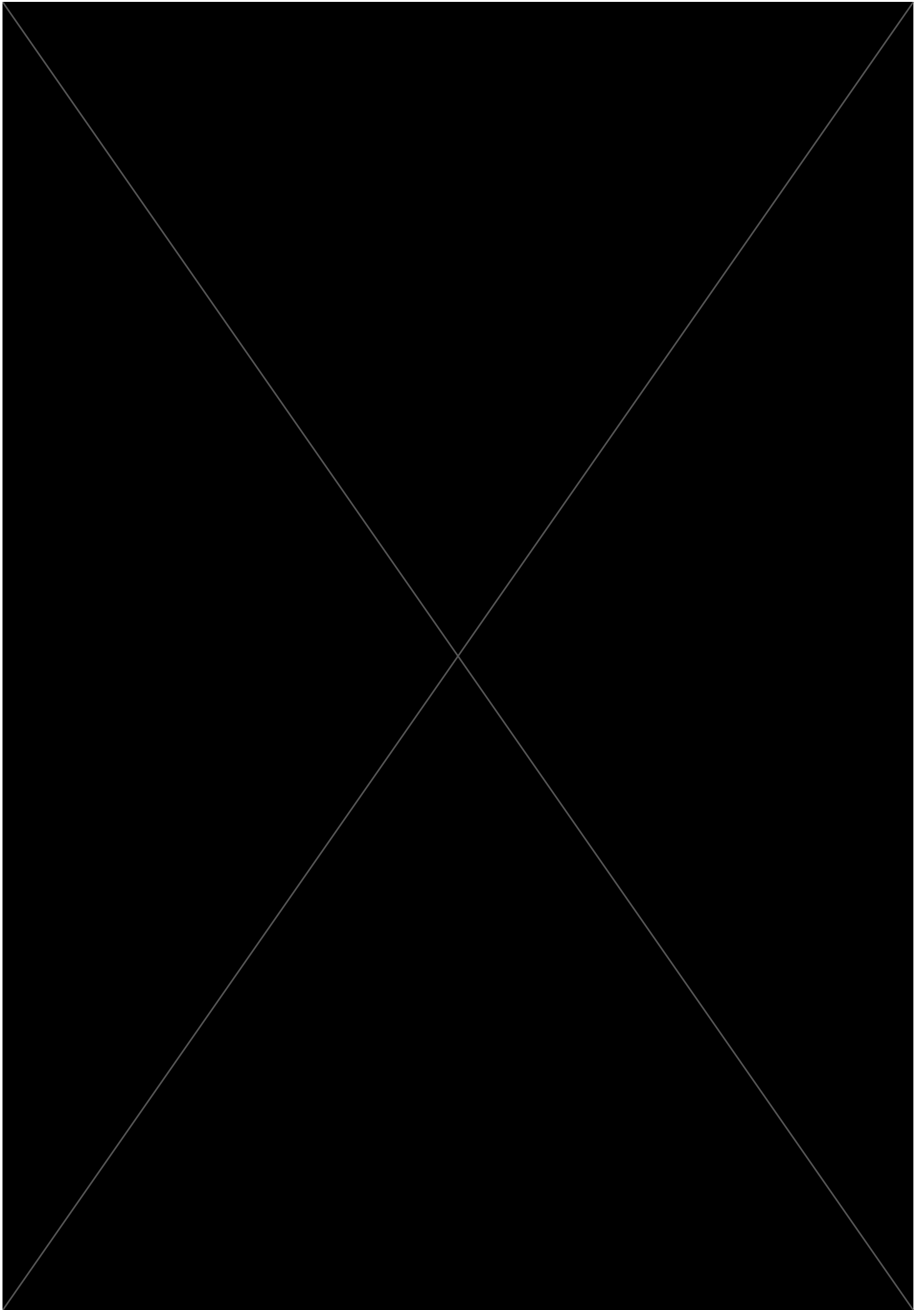
$$Z = \frac{x - \mu}{\sigma}, \quad (3.0.1)$$

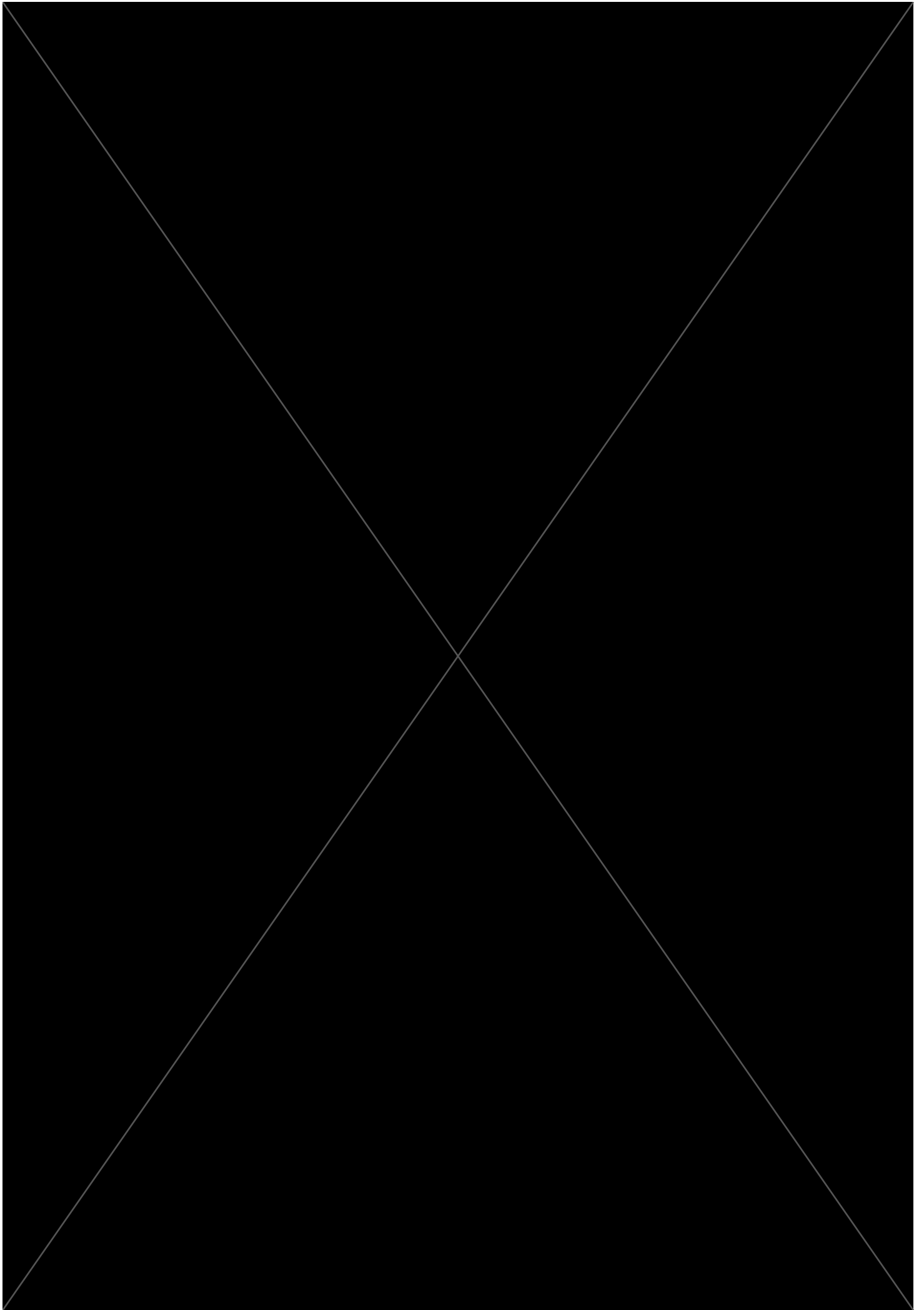
where μ is the mean, and σ the standard deviation of the timeseries.

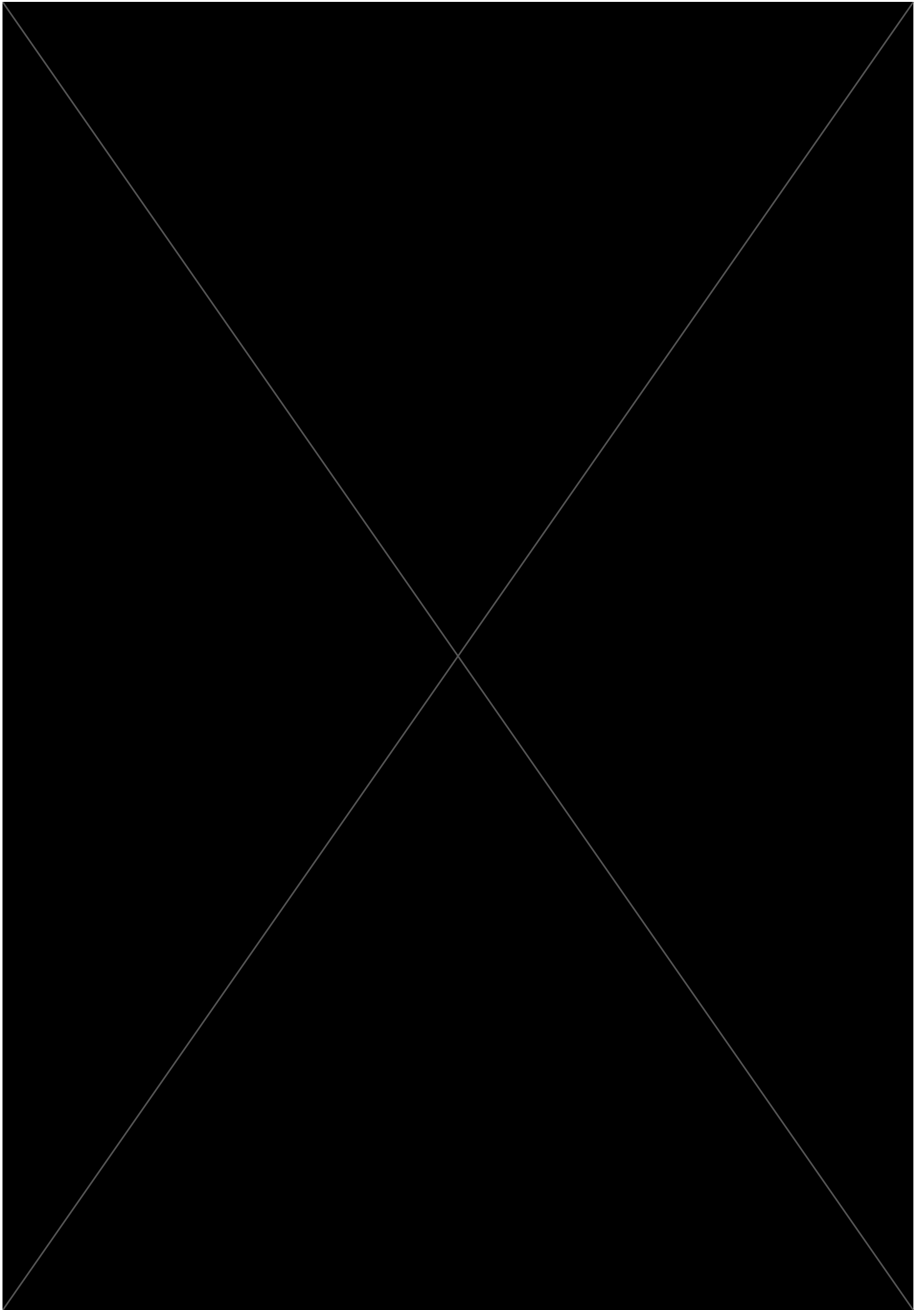
Z-scores are a statistical technique primarily utilised in the fields of physical and social sciences ([Sprinthall, 2012](#)). The first step is to subtract the mean of the timeseries. This mean-normalised timeseries is then divided by its standard deviation. This produces a normalised timeseries of standard deviation fluctuations around a common mean which can be easily cross-compared with other data products, as they exist within a shared standard deviation space. This is of particular importance when comparing the statistical distribution of observed data to that generated in a Monte-Carlo simulation, or to data from different sources (i.e., across the many Radox analyser cameras). The Z-score reveals the fluctuations of data around a mean. A Z-score of 1 is one standard deviation above the mean, and -1

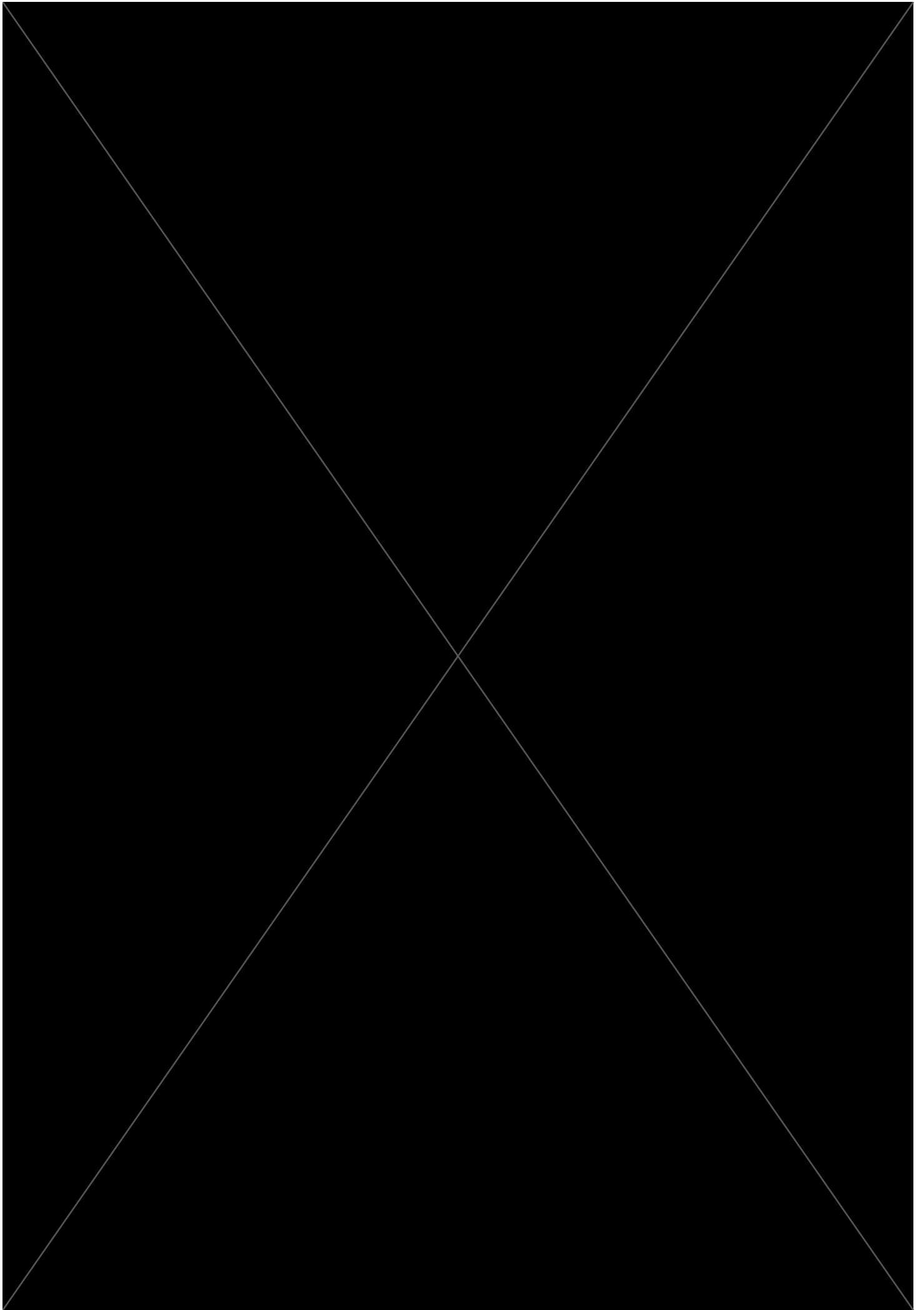
would be one standard deviation below the mean. This allows for analysis of the shape of the statistical distribution. As was discussed in Chapter 2.1, the primary noise sources in signal-limited data will follow Poisson statistics, that tend towards a Gaussian distribution in a large sample. The shape of a Gaussian is well-defined and centered about its mean, so any deviations away from this can reveal the presence of below noise-floor signatures, or unaccounted-for noise sources in the data.

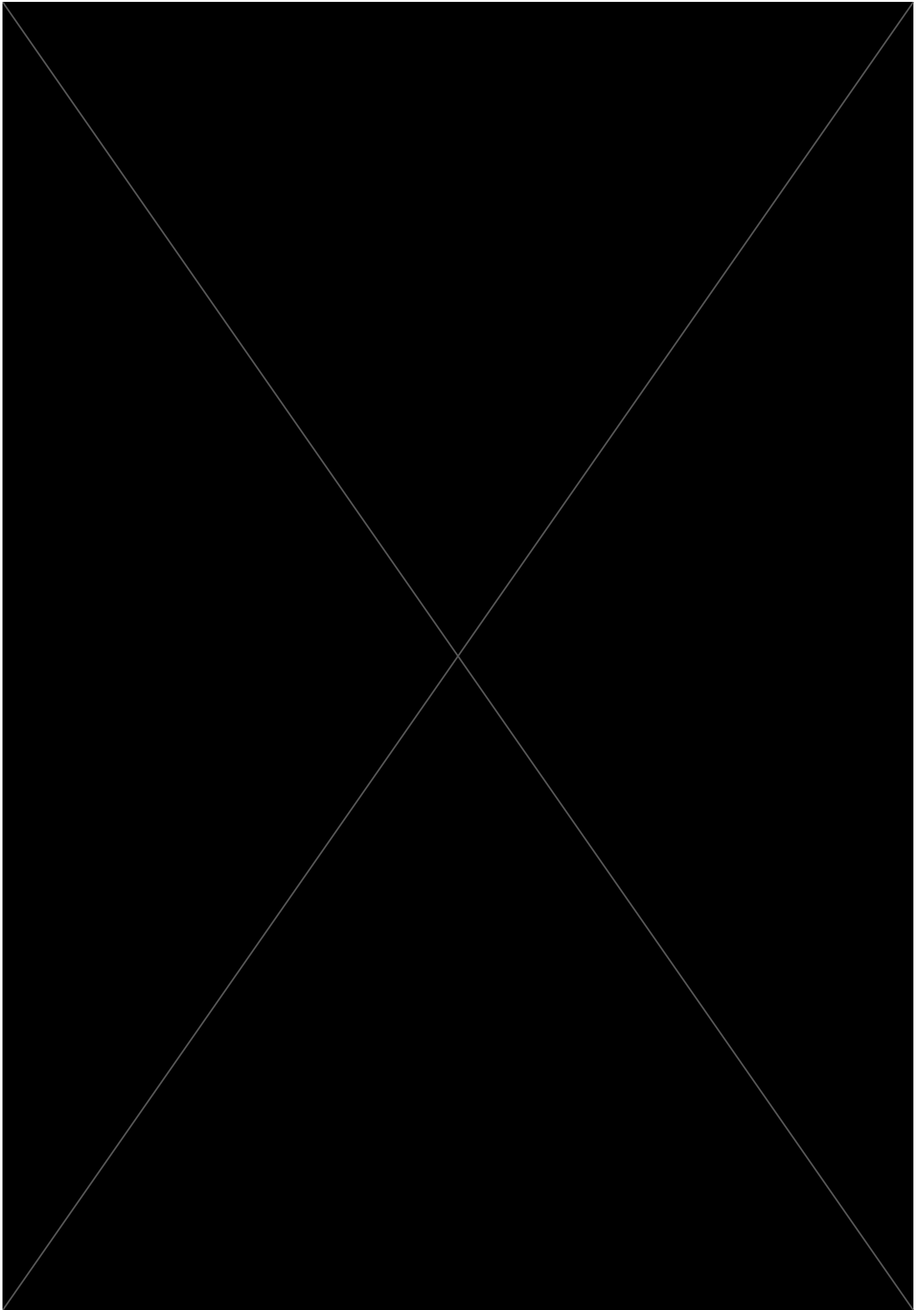


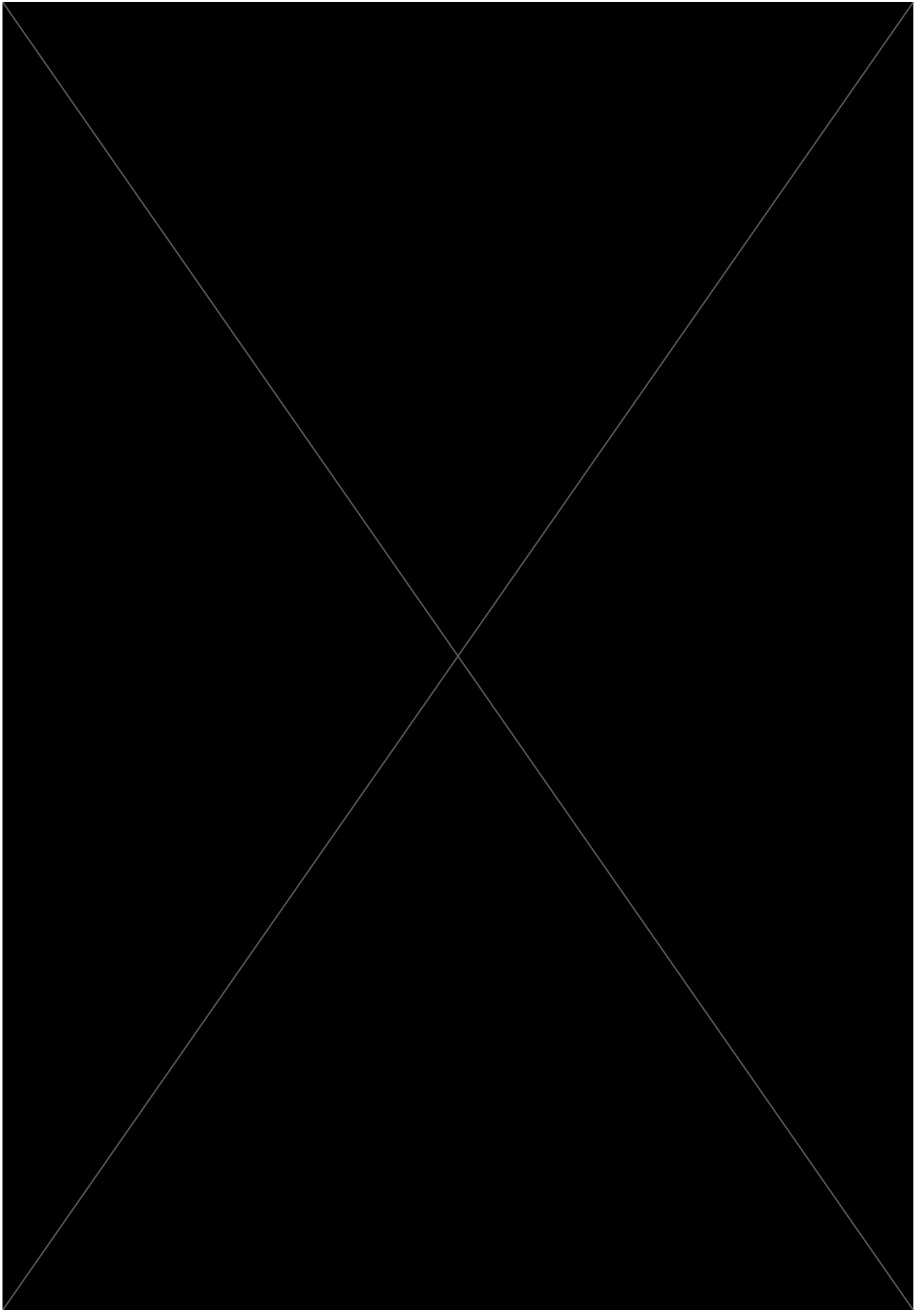


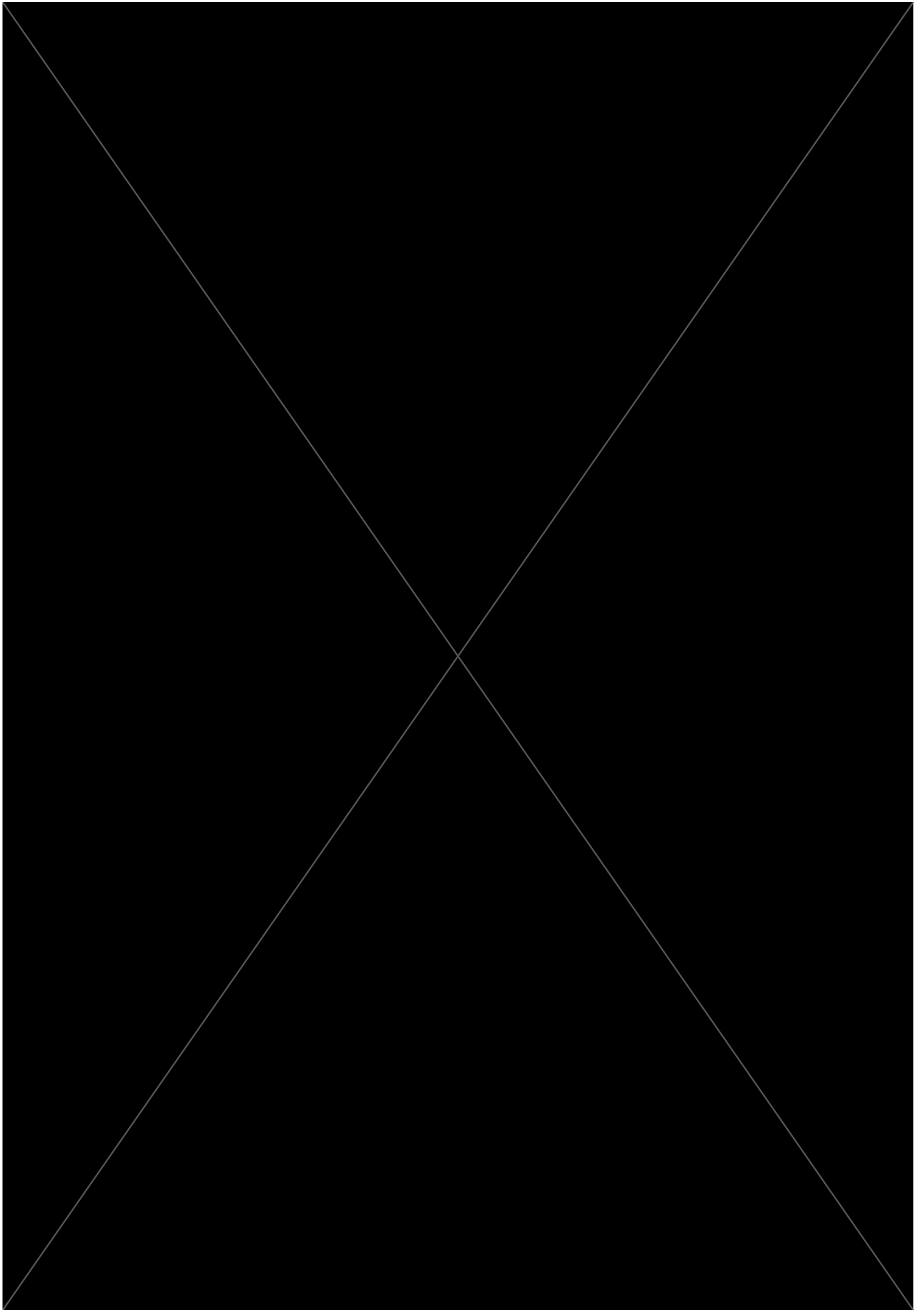


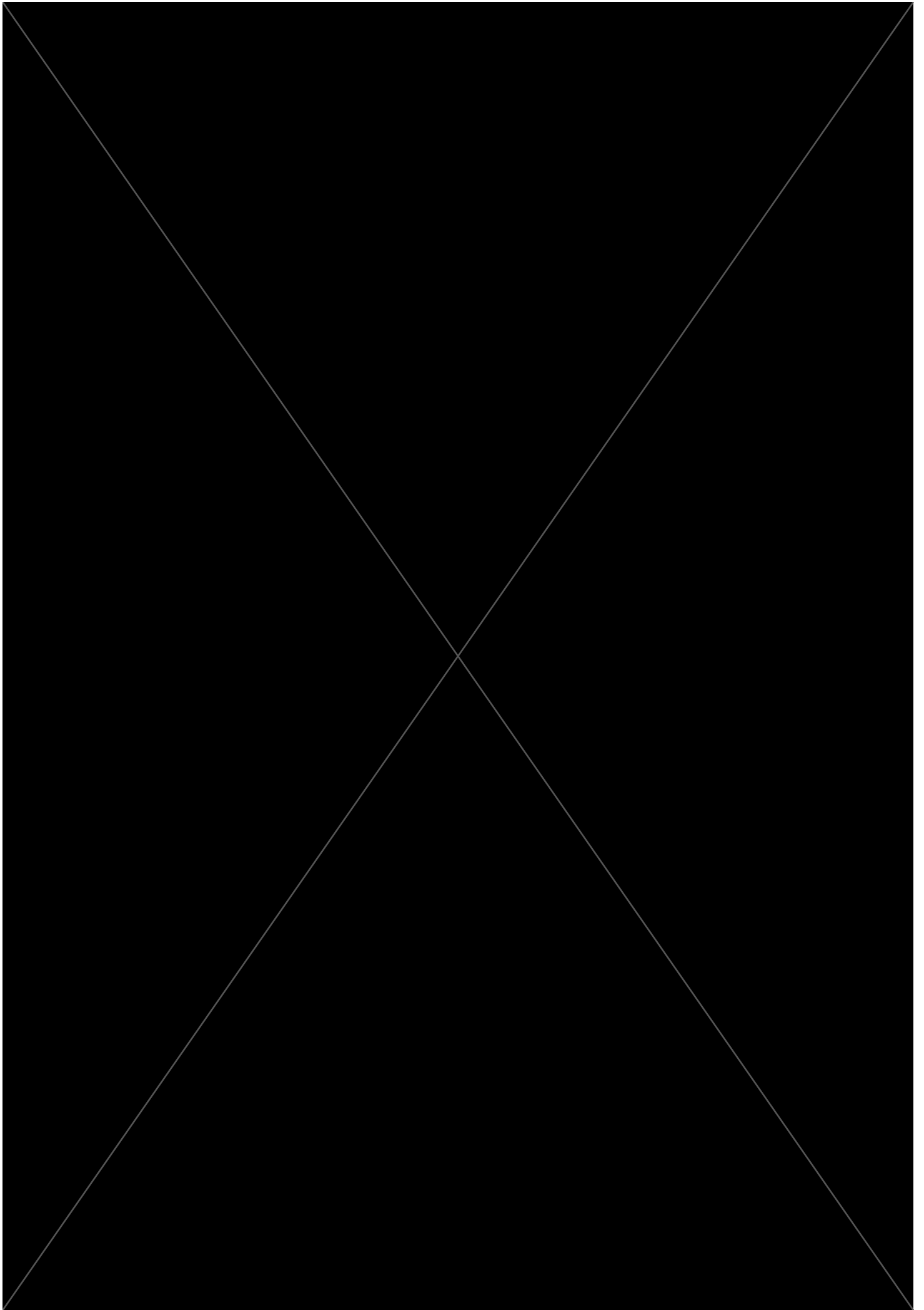


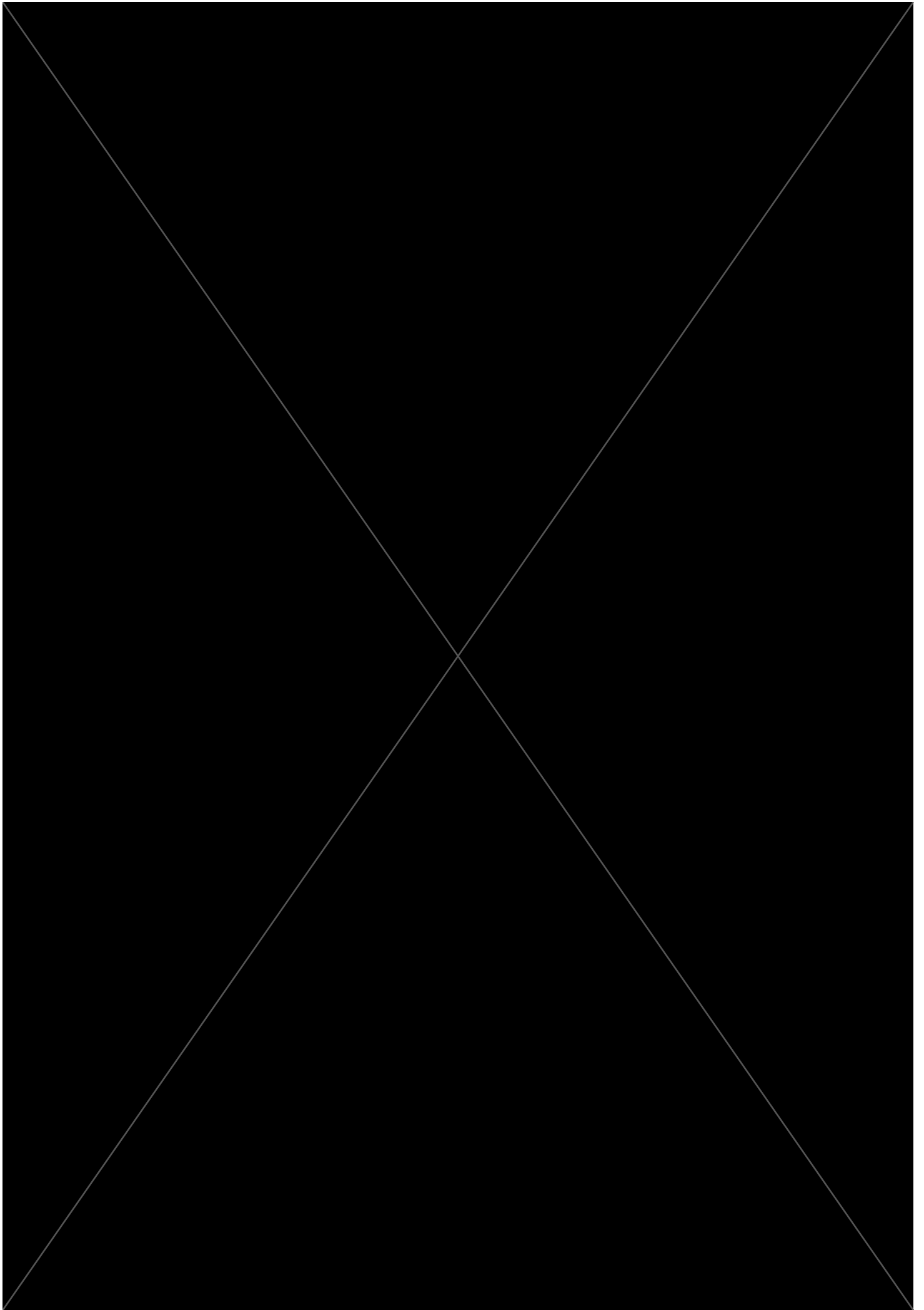


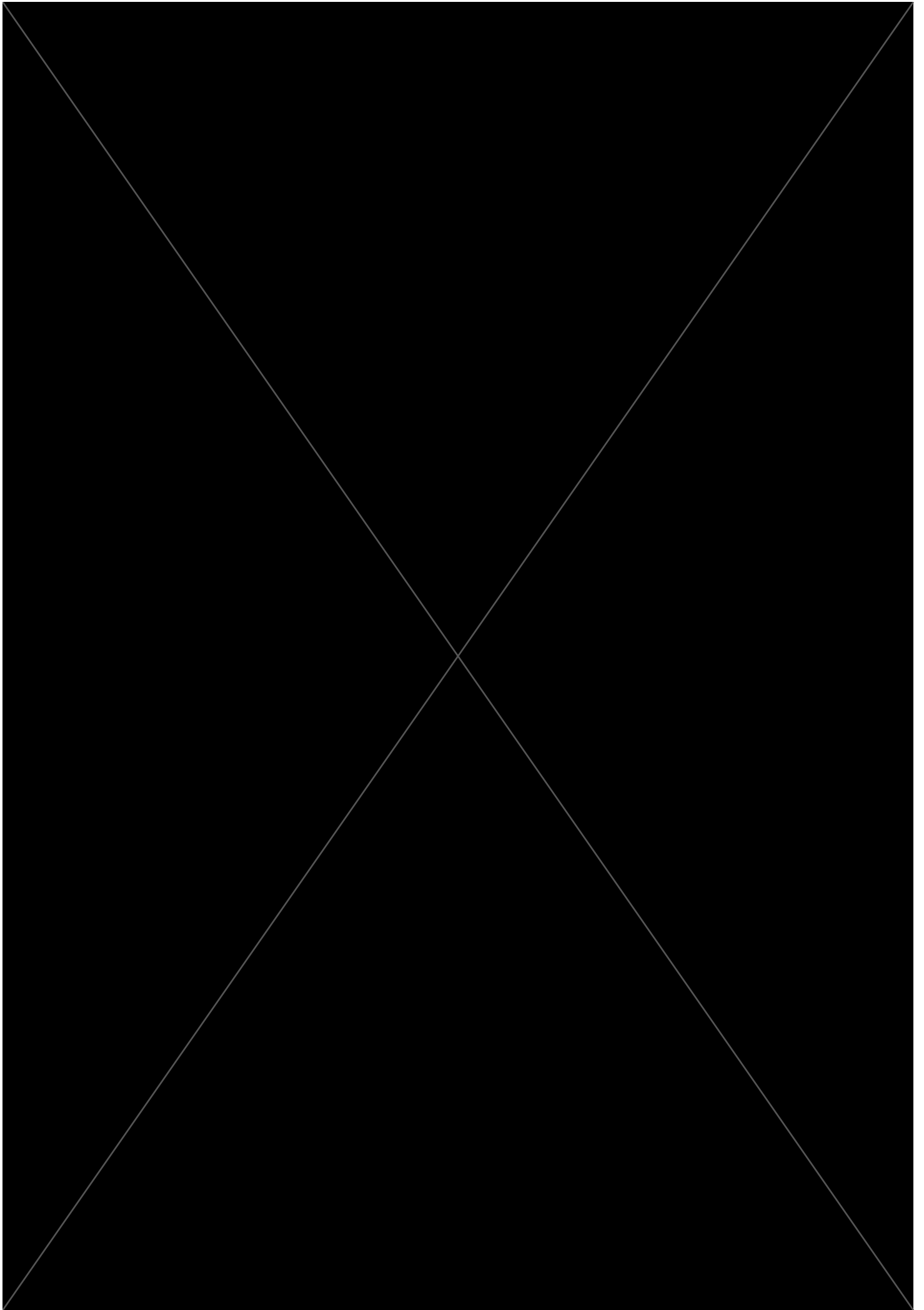


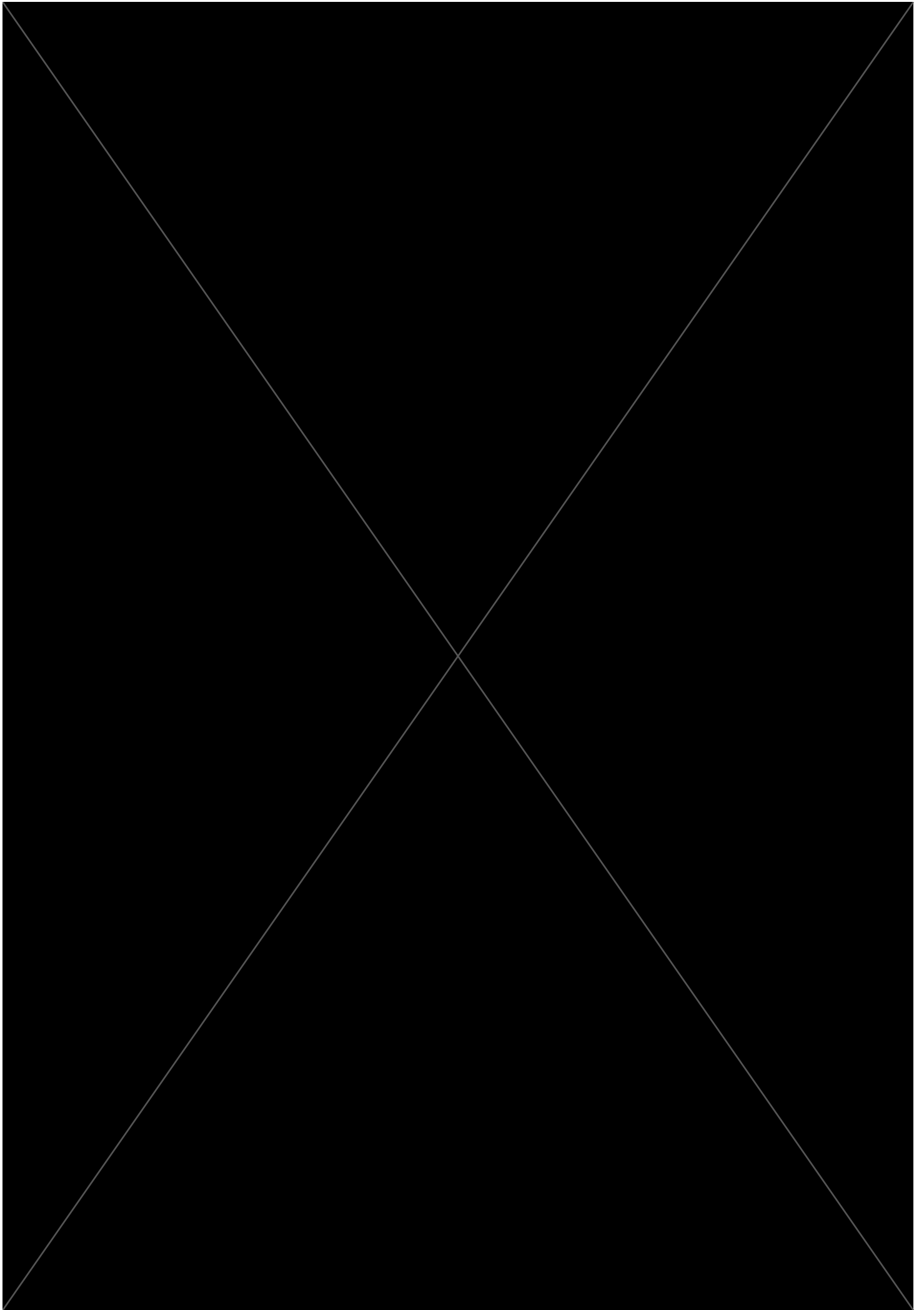


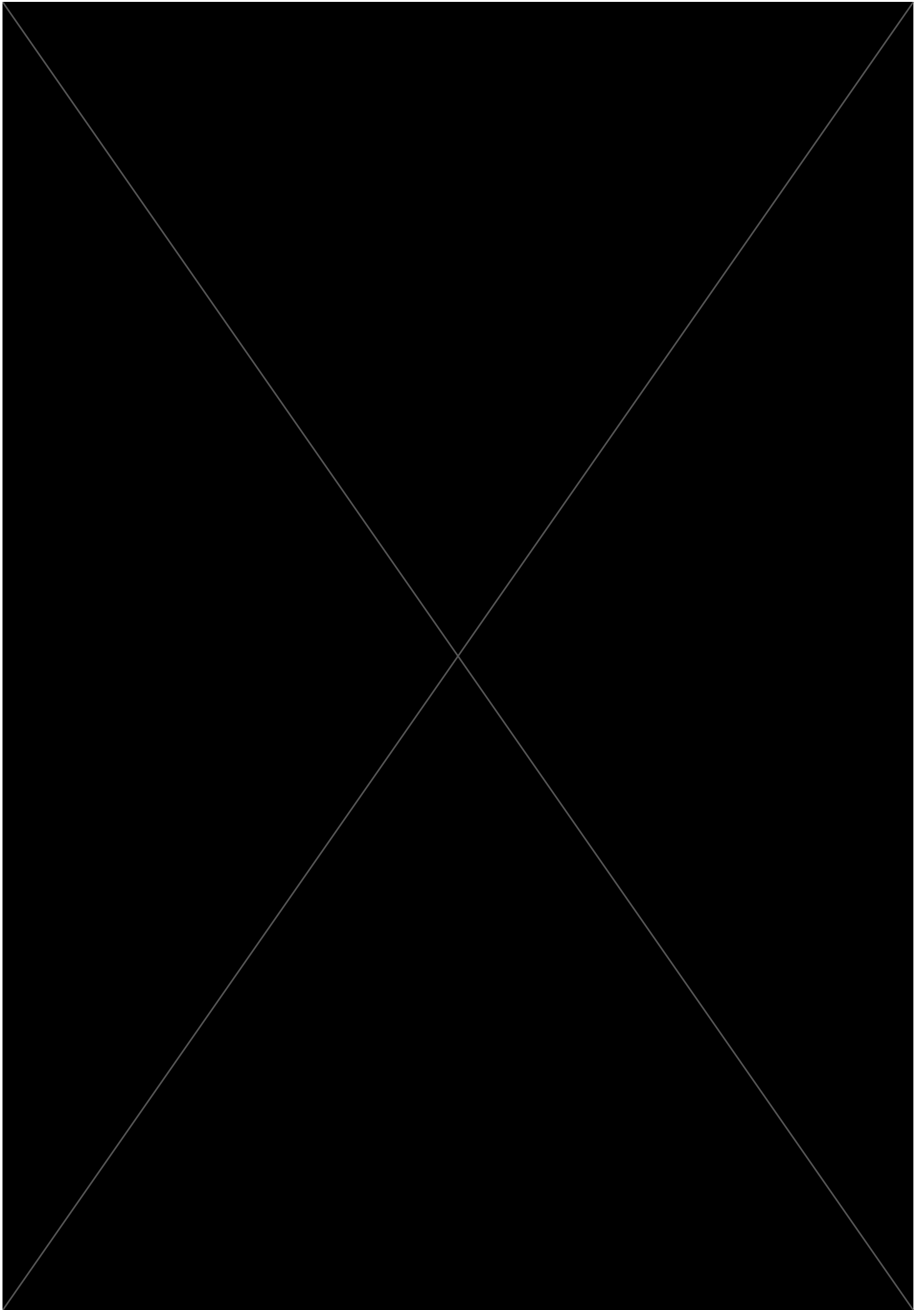


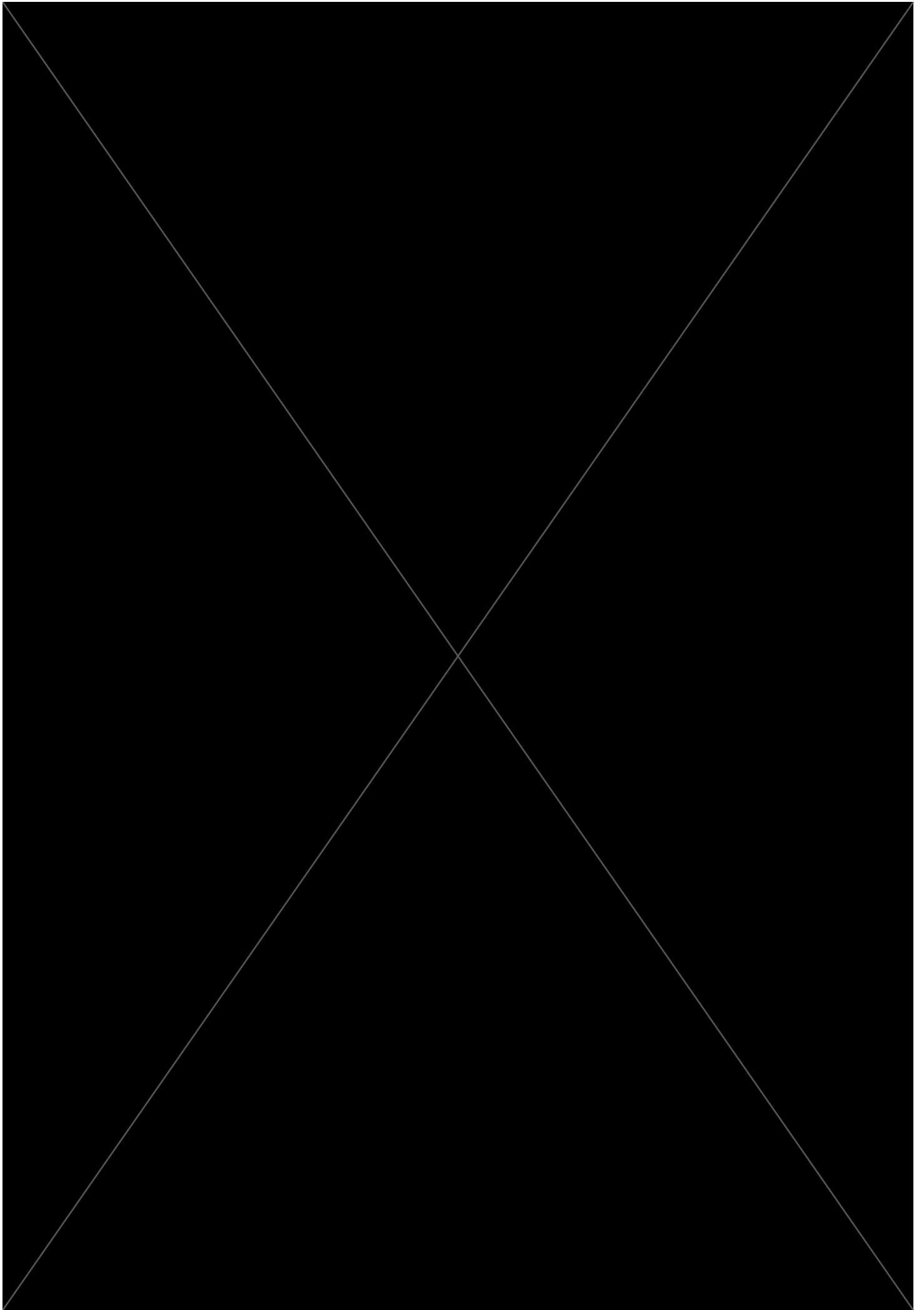


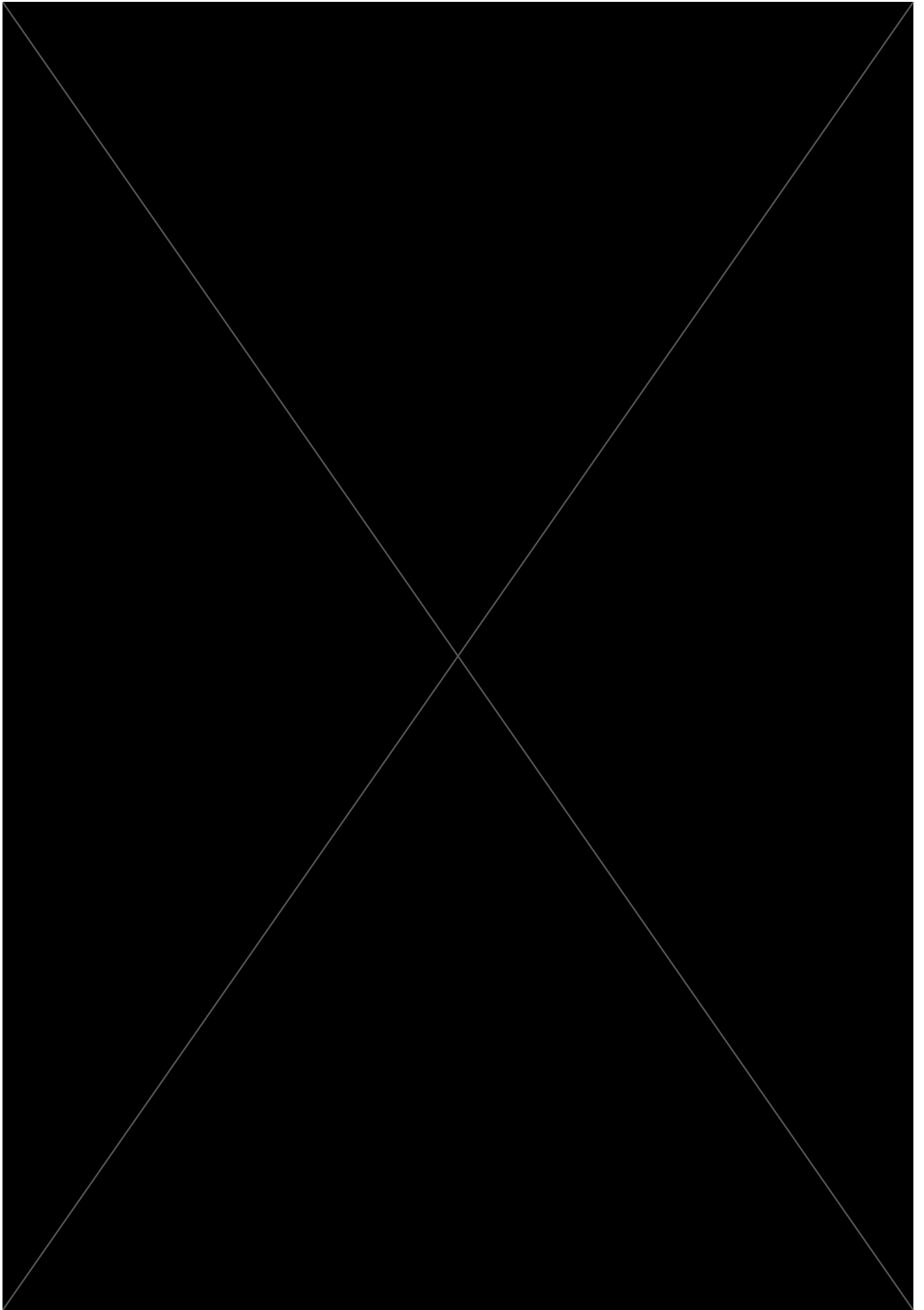












3.2 STELLAR NANOFLARE MODELLING

This section details the adaptation of the same core techniques of Z-score statistical analysis and Monte-Carlo simulations for the analysis of below-noise-floor nanoflare signatures, which were detailed in the Section 3.1. Additionally, the development of Fourier-based analysis is discussed. These techniques are described in a general way, detailing the steps to carry out this analysis with any suitable observational timeseries. Chapters 5, and 6 build upon this methods chapter, detailing the precise considerations and steps which were carried out to detect and diagnose stellar nanoflaring in real timeseries.

The data in Chapters 5, and 6 was gathered using the Next Generation Transit Survey (NGTS; Wheatley et al., 2018). This platform was chosen due to its relatively high cadence (~ 12 s) and the large number of frames available ($\sim 10^5$) for thousands of stars. As a guide for future investigations, Section 3.2.5 describes the ideal observational properties for analysis of faint nanoflare signals. The impulsive rise and subsequent decay phase for solar nanoflares are on the order of tens to hundreds of seconds (Jess et al., 2019). Stellar flare decay rates on UV Ceti-type stars are around one order of magnitude shorter than for the Sun, leading to even faster signal evolution, on the order of tens of seconds (Gershberg, 1975). As a result, high-frequency resolution and a short temporal cadence are required to fully capture these dynamic signals.

When adapting these techniques from the realm of biomedical analysis, consideration is needed for the astrophysical source of these timeseries. In contrast to the better controlled conditions of the Radox data, here it is necessary to account for atmospheric distortions and contaminating light sources (including macroscopic flaring). This is in addition to the noise sources inherent to the CCD imaging as discussed in Chapter 2.1. The nanoflare analysis requires the detection of subtle asymmetries in the statistical distribution of intensities, necessitating ‘quiescent’ lightcurves. While the CCD noise sources will tend towards a quiescent Gaussian distribution, contaminants such as macroscopic flares would introduce their own asymmetries to the statistical distribution. The dimensions of these stellar lightcurves are also very different. The two-dimensional Radox image cubes were only a few hundred frames long, but their two-dimensional nature meant they contained millions of total pixels. To achieve the large pixel numbers required for the statistical analysis, the one-dimensional stellar timeseries must be considerably longer, preferably on the order of 10^5 frames or above.

3.2.1 *Choosing and Preparing the Timeseries*

When searching for nanoflaring signatures, the spectral class of the star is very important. Obviously only stars which exhibit flaring can host nanoflares. However, there are considerations beyond this. Brighter stars have increased quiescent flux and therefore a more pronounced noise floor that must be combated when searching for nanoflare signals on top of this brighter background. Even at solar-like luminosities, the detection of microflare energies becomes difficult, let alone nanoflares on stellar sources that cannot be spatially resolved. As such, searching for stellar nanoflares on G-type stars requires a dedicated observation campaign to overcome the contrast issues.

This thesis focuses on stellar nanoflaring occurring on M-type stars. Due to their lower quiescent background flux, M-dwarf flares have a higher contrast than is typically seen on G and K stars (Günther et al., 2020). This increased contrast is essential to capture nanoflare signals below the noise floor. Additionally, M-star flares have a strong contribution in white-light (Walkowicz et al., 2011), ideal when utilising datasets from optical surveys, i.e., the NGTS. These benefits outweigh an increased photometric noise level, which is itself minimised by leveraging the large number statistics of statistical nanoflare analysis. Finally, as these are flare-active stars, flare occurrence rates will be higher than in ‘solar-like’ stars. This means M-dwarf stars are likely to provide the best conditions for the manifestation of detectable nanoflare signals.⁵ However, exploring stellar nanoflaring on G-type stars remains an area of interest, and could be addressed with a dedicated observational campaign to overcome the nanoflare contrast issues.

It is also vitally important to examine a companion non-flare-active star. This serves as a control test to ensure these data analysis techniques are not incorrectly mistaking residual systematic signals as evidence for stellar nanoflares. Since A-type stars are absent of a convective zone, their resulting lack of flare-like behaviour provides an ideal set of complementary data products. Some recent studies (Balona, 2012; Fossati et al., 2018; Balona, 2021) do suggest A-stars are capable of flaring, but this has also been disputed (Pedersen et al., 2017). If the observed signals are indeed A-star flares, then only extremely energetic flares have been observed; Balona (2021) discuss A-star flares with energies in the range $10^{35} - 10^{36}$ ergs, 10 orders of magnitude above traditional nanoflare activity. If only highly energetic events can rise above the high background luminosity on A-stars, this

⁵ These stars were also chosen due to the periodic brightenings seen in similar M-dwarf stars which, as theorised in Chapter 2.2, may be due to nanoflaring.

would explain the rarity of A-star flare observations. As such, low-energy nanoflaring would be entirely lost within the lightcurves of these stars due to the minimal contrast invoked, meaning A-type stars would appear quiescent at small-scale flare energies, regardless of their true flaring behaviour, and would not exhibit a signal consistent with nanoflares. It is important to note that A-type stars have a very different spectral energy distribution (or SED) to M-dwarf stars, so are not a conventional choice for relative photometric comparison. To ensure robust null testing, it is also necessary to utilise low-activity K stars which have a more comparable SED to M-type stars (i.e., choosing similar spectral types as is standard for photometric comparison, e.g., [Amado et al., 2000](#)). Low-activity K-type stars are preferable over low-activity M-dwarf stars due to their higher luminosity, leading to decreased low-energy flare contrast when compared to the M-types. While the low-activity K-type stars could theoretically have some weak nanoflaring signature present, it would be minimised compared to the M-types, so this still serves as a valid null test. The processing steps and number of datapoints of these null stars should be identical to the flare-active stars, to ensure consistent number statistics. For the same reasons, these null stars should be chosen from the same camera and observation campaign, where applicable.

Another important consideration is matching the noise statistics of the sources in a study. Sources with similar apparent magnitudes should be chosen, to ensure ‘like-for-like’ noise statistics. Very faint magnitudes will be extremely photon limited. When using ground-based observation higher magnitude stars will start to be dominated by scintillation noise ([Osborn et al., 2015](#)). Scintillation is due to the turbulence induced by Earth’s atmosphere leading to intensity fluctuations. This ‘speckling’ of the incoming light scales inversely the wavelength of the light, with increased scintillation at shorter wavelengths. Scintillation becomes the dominant noise source for brighter sources ([Wheatley et al., 2018](#); [Föhring et al., 2019](#)), and introduces an offset in the otherwise Gaussian distribution of the background noise. While this frequency-dependent noise would be distinct from the nanoflare statistical signature, it is still an undesirable source of noise, increasing the difficulty of identifying the already faint nanoflare signatures. To utilise observations with a large degree of scintillation noise, it would be necessary to add modelled scintillation noise to the Monte-Carlo modelling. However, this scintillation noise is best avoided altogether, either by utilising space-based observations or by choosing lower-magnitude stars.

The rotation period of the stars might also need to be considered. As M-dwarf stars evolve and age, their stellar-wind driven mass loss will tend to cause them to ‘spin down’, increasing their rotation period ([Weber & Davis, 1967](#); [Johnstone et al., 2021](#)). However, some late M-type stars are fast rotators, with periods on the order of a day or less. Stellar

rotation is an indicator of stellar activity, as magnetic activity increases with the increase in stellar dynamo spin rate (a relationship which has also been identified in fully convective stars, despite their seemingly distinct dynamo mechanism, e.g., [Wright & Drake, 2016](#); [Wright et al., 2018](#)). The rapidly rotating M-dwarf stars will exhibit enhanced flare activity compared with slower-rotating stars at the same effective temperature. When selecting mid to late M-stars for a large-scale study, care should be taken to ensure they are consistent in rotation speed. If selecting for the slow rotation group, any periods of rotation less than ≈ 25 days might be a cause for concern. These rapidly rotating stars will have increased flare activity which is not representative of their spectral class at large. Identification of the stellar rotation period can be quite difficult, as the majority will be slow-rotating stars with long periods (> 40 days; [Newton et al., 2018](#)) which are missed in relatively short observation campaigns, whereas the shorter period stars begin to overlap with common aliasing signals due to day/night cycles and the lunar cycle.⁶ By utilising a Lomb-Scargle periodogram (a common tool to identify stellar rotation periods, with methodologies described in stellar studies such as [Oelkers et al., 2017](#); [Jackman et al., 2021](#)), an estimation of this rotation period is possible. This Lomb-Scargle periodogram is similar to a power-spectral density plot (see Section 3.2.3 for much more detail on these), and utilises a Fourier transform to calculate the relative power of periodic signatures in a timeseries.⁷ A normalised power of 1.0 would indicate a fully periodic signal, whereas 0.0 would be a signal with no periodic nature. In practice, any signal greater than 0.1 is a possible periodic signature. To identify these rotation periods, the methods of [Oelkers et al. \(2017\)](#) and [Jackman et al. \(2021\)](#) serve as a guide. The period search can be split into multi-day and sub-day bins. A ‘frequency grid’ of evenly spaced candidate periods can be generated, with the corresponding frequency resolution tuned to probe candidate stellar periods. Common observation aliases such as the day/night cycle, and the lunar cycle should be ignored, along with the harmonics of those periods.⁸

Once a candidate M-dwarf is selected, and companion A- and K-star timeseries are chosen (taking into account the above considerations, while also trying to match consistent

⁶ These aliases are a natural consequence of the observation sampling. Ground-based observation can only operate at night, and their scheduling is also affected by the lunar cycle. These sampling limits introduce aliases, ambiguous periodic signatures related to this sampling.

⁷ The LS periodogram and the considerations needed when utilising it for astrophysics are described in detail by [VanderPlas \(2018\)](#).

⁸ Space-based telescopes will avoid day/night cycles, but other aliases will be present related to the sampling rates.

processing, and magnitudes, and—where possible—the same camera and /or processing run), the first step is filtering each timeseries to remove large-scale fluctuations. These will be primarily due to macroscopic flaring in the M-dwarf, but the same processing steps are applied to the A and K star for consistency. This can be done by removing fluctuations in excess of $3\sigma_N$ above the lightcurve mean for a sustained number of frames, where σ_N is the standard deviation of the quiescent timeseries. This is consistent with the various macroscopic flare-removal techniques used throughout stellar analysis.⁹ It is also important to remove any observations with a large uncertainty. These are primarily associated with poor seeing conditions, leading to variability with the flux detection. These steps provide a lightcurve that is comprised solely of shot and readout noise (Terrell, 1977; Delouille et al., 2008), alongside the background small-scale (nanoflare) stellar activity. Then, the lightcurve should be normalised on a night-by-night basis. This is achieved by subtracting a linear line of best fit to remove any intensity trends over the night of observing. Finally, detrending by a low-order polynomial ensures the robust removal of any remaining trends in the data which would affect the nanoflare detection. The Z-score normalisation (see Equation 3.0.1) is then applied. This produces a timeseries of fluctuations normalised about a common mean. These fluctuations in σ_N can be easily compared to other similarly normalised timeseries from other sources, whether they be simulation or observation.

3.2.2 Statistical Analysis

Once filtered and normalised, the statistical distribution of the timeseries can be investigated. By benchmarking the shape and characteristics of these fluctuation distributions with the Z-score, they can be compared to the Gaussian distribution expected from the underlying noise. This is done via the same histogram process used to visualise the Radox camera fluctuations shown in Figure 3.1, wherein the statistical fluctuations are plotted against a normalised occurrence rate. Chapter 2.2 details these statistical signatures associated with nanoflaring, namely the median offset, Fisher skewness, kurtosis and the ratio of the full-width at eighth-maximum of the distribution to that of its full-width at half-maximum (i.e., $\text{FW}_{\frac{1}{8}}\text{M-to-FWHM}$ ratio).¹⁰ When nanoflaring signatures are present, these are apparent as deviations away from the expected Gaussian distribution. The negative median offset will manifest as the median value of the distribution being offset ‘below’ the mean. The

⁹ The exact ‘sigma clip’ varies, but is in the range of $\sim 2 - 3\sigma_N$ (Nevalainen et al., 2005).

¹⁰ Defined as ‘ ζ ’ for simplicity.

Fisher skewness refers to the ‘skew’ or bias towards positive or negative in the ‘tails’ of the distribution. A positively-skewed distribution will have a longer ‘tail’ spreading into the positive fluctuations, and vice-versa. Skewness may also be caused by an asymmetric bump within the distribution, leading to an asymmetric excess of fluctuations. Kurtosis is a measure of how centralised the distribution is. Positive kurtosis values describe a distribution spread out towards the tails, whereas negative values will be closely peaked in the centre. Finally, the ζ ratio defines the width of the distribution. By definition, a Gaussian will exhibit zero median offset, a skewness of zero, a kurtosis of zero,¹¹ and a ζ of 1.73.¹²

These statistical parameters are easily calculated from the statistical distribution. The median offset is simply the difference between the median value in the distribution and the mean. The Fisher skewness and the kurtosis are both estimated using the moment function. The calculation of the moment of a probability distribution allows for the estimation of key parameters describing the centre, shape, and overall scale of a distribution (Brookes & Dick, 1969; Spanos, 1999).¹³ Each order of the moment contains different information about the distribution:

- The first moment is the mean, the central value of the distribution;
- The second moment is the variance, detailing the spread of the distribution;
- The third moment is the skewness, a value describing the dominant ‘tail’ of the distribution;
- The fourth moment is the kurtosis, a value describing how centred the distribution is.

While orders beyond this exist, they are essentially variations of the third and fourth moment. Moments are a standard statistical tool to describe probability distributions, with implementations in all major scientific analysis software. Finally, the ζ ratio can be calculated by dividing the width of the distribution at one-eighth its maximum by that at half maximum. Once these four key statistical parameters are calculated, then they can be used to compare the relative nanoflare-related signatures across studies.

¹¹ Strictly speaking the kurtosis value of a normal distribution is 3, but in practice the ‘excess kurtosis’ is most commonly reported, i.e., the difference in the kurtosis from 3 (Balanda & MacGillivray, 1988).

¹² In a Gaussian distribution, the $\text{FW}\frac{1}{8}\text{M}$ occurs at $2\sqrt{2\sigma^2\ln 8}$, and FWHM at $2\sqrt{2\sigma^2\ln 2}$, giving a ratio of $\sqrt{\frac{\ln 8}{\ln 2}}$, or ~ 1.73 .

¹³ While not strictly an academic source, a blog post written by Gundersen (2020) explains the concept of moments in a concise and clear manner which I found more instructive than those found within the literature.

To help facilitate this comparison, the errors in these parameters are also readily calculated. The standard error of the median for a normal distribution is given by $\sigma_{median} = 1.253 \frac{\sigma}{\sqrt{n}}$, where n is the number of points in the sample and σ is the standard deviation (Eugene, 1935). This ratio of $\frac{\sigma}{\sqrt{n}}$ is the standard error, and scales with sample size (Altman & Bland, 2005). The errors of the skewness and kurtosis are also related to the sample size of the statistical distribution. For large sample sizes,¹⁴ the Fisher error is $\sqrt{\frac{6}{n}}$, and the kurtosis error is $\sqrt{\frac{24}{n}}$ (as stated by, e.g., Barndorff-Nielsen & van Lieshout, 1998; Tabachnick & Fidell, 2006).¹⁵ The error in determining ζ is calculated by propagating the errors in FWHM and $FW\frac{1}{8}M$ (i.e., ζ is these values divided by one another, so the error propagates via the standard error formula ; $\frac{\delta\zeta}{\zeta} = \sqrt{\left(\frac{\delta FWHM}{FWHM}\right)^2 + \left(\frac{\delta FW\frac{1}{8}M}{FW\frac{1}{8}M}\right)^2}$). The errors in FWHM and $FW\frac{1}{8}M$ are given by the standard error, i.e., $\frac{\sigma}{\sqrt{n}}$

3.2.3 Fourier Analysis

Fourier analysis is complimentary to the statistical analysis. As was discussed in Chapter 2.2, nanoflares can give rise to periodic signatures, despite non-periodic driving. These periodic signatures are benchmarked through use of power spectral density (PSD) plots. These are a variation of a fast Fourier transform, where the relative power contributed per unit frequency is calculated. As these show relative power, they are easily cross-compared between different data products, similar to the mean-and-standard-deviation-normalised lightcurves.

These PSD plots are described in detail by Welch (1961) and Vaughan (2012), and are a standard tool for analysing spectral power contribution throughout the physical sciences. However, these PSD plots can only utilise continuously observed data: the analysis is limited by day/night gaps,¹⁶ dips due to poor seeing conditions, and other disruptions in the observation. Any gaps or discontinuities cause the Fourier transform to attempt to fit a sinusoidal across these discontinuities, hence extracting unreliable periodicities. This can greatly limit the subsequent resolution of the PSD analysis. Once the longest continuous timeseries has been identified, a fast Fourier transform can be applied. A Fourier transform

¹⁴ i.e., when the data approaches a normal distribution.

¹⁵ These errors are often stated as fact, but their origin rarely cited. These errors are calculated from the variance of the skewness and kurtosis as given by Fisher (1930), where in the limit of a large N the higher order terms approach zero.

¹⁶ If utilising ground-based observation.

will return complex numbers, consisting of real and imaginary components. In order to calculate the ‘power’ contained, it is necessary to apply the formula,

$$\text{Power} = 2 \times (\text{Real}^2 + \text{Imaginary}^2) . \quad (3.2.1)$$

The maximum frequency F_N which can be measured is known as the Nyquist frequency. This is given by the equation $F_N = \frac{1}{2T}$, where T is the cadence of the observation. The frequency resolution, Δf will be $\frac{F_N}{N}$, where N is the total number of datapoints in the timeseries. Consequently, this analysis benefits from large datasets with frequent sampling, in order to derive the highest resolution and widest frequency span. To calculate the density of this power spectra, it is necessary to divide the spectral power by the frequency resolution of the FFT. This produces a power spectral density plot in units of power per unit frequency. The PSD normalisation allows the comparison of relative power within the power spectrum of data from disparate sources, i.e., comparing multiple timeseries of different lengths, or comparing simulated to observational data. This is similar to the how Z-Score normalisation allows for comparison of relative statistical distributions across different timeseries. Beyond the identification of periodic signatures associated with nanoflares, a distinct benefit of this PSD analysis is that it allows for further parameterisation of the nanoflare signature. The distribution of statistical signatures across simulated nanoflare conditions was found to be symmetric, giving rise to self-similar nanoflare parameters (this is discussed in Chapters 5, and 6). These self-similar parameters were two sets of distinct nanoflare properties corresponding to a given set of statistical parameters. This Fourier analysis also serves as an important way to distinguish the underlying nanoflare conditions, while also allowing for the determination of any periodic component to the stellar nanoflare signals.

In addition to the periodic signals, nanoflares also give rise to a distinct power spectral gradient in these PSD plots (see Figure 3.13). This decrease in spectral power at higher frequencies resembles the turbulent cascade commonly associated with MHD wave phenomena,¹⁷ but can be produced solely through nanoflare activity.¹⁸ The spectral gradient and the ‘turning point’ where this gradient occurs are key parameters in measuring underlying nanoflare activity. To characterise the spectral gradient and associated features, a trendline should be established over several frequency elements, highlighting the overall evolution of

¹⁷ See [Podesta \(2011\)](#) and [Huang et al. \(2017\)](#) which detail turbulent power cascades due to plasma wave behaviour with gradients in the range $-2 \leq \beta \leq -1$.

¹⁸ These PSD gradients are seen in Monte-Carlo nanoflare simulations, directly linking nanoflares to these signatures; see Section 3.2.4 for more on this.

the PSD. In this work, PSD smoothing trendlines were calculated using a Gaussian smoothing function. Due to the Fourier transform of a Gaussian profile being yet another Gaussian (Abramowitz & Stegun, 1972), the application of a Gaussian smoothing function acts to reduce the PSD's high-frequency components believed to be associated with noise, and hence the applied Gaussian smoothing is therefore a low-pass filter. The width of the Gaussian kernel was 12 frequency elements (i.e., ± 6 frequency elements), and the standard deviation was 2 (therefore calculating the Gaussian smoothing over 3 standard deviations in each dimension). This ensures that measured trends and peak frequencies are robustly established over multiple frequency elements, and are not the result of individual noisy points or spikes. The turning point in these plots will be the point where initial power peaks are followed by a downward spectral slope in the trendline. The spectral gradient can be calculated by determining the gradient of the trendline, following the turning point until the end of the downward slope. The dominant periodic signature following detrending by the spectral gradient allows for an estimation of the strongest periodic signature, allowing for convenient parameterisation of the nanoflare periodicities. The minimum error in the turning point and the peak frequency are given by $\pm \frac{f_N}{N}$, i.e., the frequency resolution, Δf but these errors may be larger if the precise frequency is not apparent. The error in the spectral gradient may be estimated by fitting spectral slopes between the turning point and subsequent end of the spectral gradient, within the uncertainties induced by the frequency resolution.

3.2.4 *Observationally Driven Monte-Carlo Modelling of Nanoflare Timeseries*

While these statistical and Fourier analysis techniques can determine the presence of signals compatible with nanoflaring, they do not directly reveal the underlying nanoflare conditions. This can be resolved with simulated timeseries, containing both observationally-driven modelled noise and simulated nanoflare signals. These nanoflare simulation techniques are adapted from Jess et al. (2019), based on work carried out in my Masters project for the initial simulation of two-dimensional solar images. Adapting this work for stellar simulations meant altering the simulations to be one-dimensional. By generating a fully synthetic timeseries, layered with noise and nanoflare signal embedded within that noise, it is possible to investigate a full range of possible nanoflare conditions. By then applying the same statistical and Fourier analysis to these simulated timeseries, the parameters corresponding to a given α and e -folding timescale (or τ) can be determined. As with the Radox noise models, these simulated timeseries incorporated noise characteristics of the underlying observational timeseries, and were matched to the specific dimensions and cadence of the observational data.

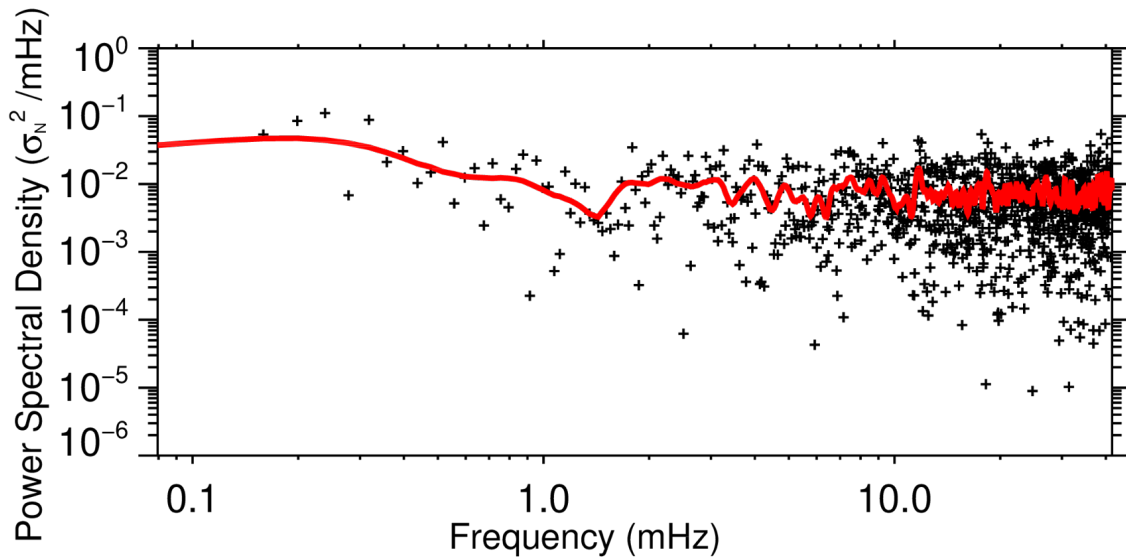


Fig. 3.13 An example PSD plot for a star exhibiting nanoflare signatures, displayed in normalised units of σ_N^2/mHz . The black crosses depict the individual power values as a function of frequency. The red line is a trendline calculated over ± 6 frequency elements. The PSD exhibits a clear enhancement of spectral energy at lower frequencies, resulting in a spectral slope. The gradient of this slope along with the turning point where the gradient begins and the peak frequency, can all be measured to determine the underlying nanoflare conditions

The noise characteristics are derived from the underlying quiescent distribution of the non flare-active stars, which are taken as representative of the noise statistics of the observation system. This underlying Poisson noise is generated in the same way as Section 3.1, using a Poisson noise generation function. If the average count rate of the observations is known, this can be used directly as the Poisson count rate in the simulation. If these count rates are not directly available, it is possible to estimate the Poisson amplitude from the square root of the background intensity of the timeseries. This corresponds with the approximate Poisson amplitude. It may then be necessary to tune the modelled noise amplitude. This is checked by comparing the spread in the Z-score fluctuations, ensuring the the observational and modelled timeseries match.

The nanoflare simulation requires several key input parameters. The simple flare model seen in Figure 2.3 in Chapter 2.2 forms the basis of these simulations. The flare begins with an impulsive energy deposition followed by approximately exponential decay. The α and τ values will dictate the frequency of energy release and the time taken for the flare to decay, respectively. The modelled flare-decay rate, τ should be varied by $\pm 10\%$, as these decay rates are a function of the underlying plasma conditions and hence are not consistent over time: a variation of $\pm 10\%$ allows for a more realistic representation of the

approximately exponential decay timescales (Christe et al., 2008). The energy range of the simulated nanoflares should span $10^{22} - 10^{25}$ ergs, placing them within the energy regime synonymous with solar nanoflares.¹⁹ As we are studying the effect of small-scale impulsive events, this upper cutoff ensures no larger energy events are simulated. The lower cutoff will minimise processing time, by not simulating statistically insignificant events below 10^{22} ergs. Combining this energy span, and the power-law index, flare energies can be generated randomly according to the power-law distribution, i.e., these events are randomly chosen from the power-law distribution spanning these energies at the given power-law index. These events are then ‘decayed’ via an exponential decay with a characteristic timescale within $\pm 10\%$ of the input τ value.

The power-law distribution (Equation 2.2.2) only gives information about the relative frequency and energy release of flare events: it does not provide the number of occurrences of these events. As such, the number of flare events needs to be normalised, ensuring a given power-law index leads to the correct flare energy release rate. This normalisation is achieved through comparison with the work of Aschwanden et al. (2000) and Parnell & Jupp (2000). Figure 10 of Aschwanden et al. (2000) and Figure 1 of Parnell & Jupp (2000) show flare frequency distributions giving the expected flare frequency (in units of $\text{erg}^{-1}\text{cm}^{-2}\text{s}^{-1}$) as a function of flare energy in ergs. Parnell & Jupp (2000) find that for an energy of 10^{25} ergs, the expected flare frequency is $\sim 2000 \times 10^{-50} \text{ erg}^{-1}\text{cm}^{-2}\text{s}^{-1}$. It is important to note that this value is for observed nanoflare events within the Sun, for the specific power-law index operating therein. However, at this upper range of nanoflare energies, the flare frequency is naturally lower due to the power-law relationship. As such, this normalisation is appropriate to set a lower limit to the number of flare events in the stellar simulations. This normalisation requires the underlying stellar surface area to be known. One-dimensional lightcurves contain no resolvable spatial information of the stellar sources, so the area of the simulation should be set to the entire Earth-facing area of the star (i.e., the star is a point-source, so the entire surface fluctuations will be embedded within the timeseries). While larger flares require specific high energy magnetic conditions (e.g., large-scale spots that may only cover a small proportion of the stellar surface and are generally aligned with the stellar equator), it is expected that nanoflares can effectively occur anywhere across the stellar atmosphere,

¹⁹ dMe flare stars are not ‘solar-like’; arguably, the energy span of M-type stellar nanoflares may be orders of magnitude larger than for the solar case, due to the increased flare energies associated with M-type stars. However, various authors (Falla & Potter, 1999; Robinson et al., 1999; Güdel et al., 2002) have applied the solar energy span derived by Aschwanden et al. (2000) directly to stellar investigations, leading me to follow this convention for consistency

requiring only small-scale magnetic activity to trigger them hence, the entire surface area is a source of nanoflare activity. This area, along with an exposure time and cadence matched to observations, is used to re-compute the number of flaring events expected (following Equation 2.2.2 and the work by Aschwanden et al., 2000; Parnell & Jupp, 2000) for a given power-law index α and across a specific time interval.

The conversion of flare energies to peak detector counts, DN , is performed via a direct one-to-one scaling relationship. According to Yang et al. (2017), the flare energy is linear with area, which is linear with flux, assuming a constant black-body emission temperature. As flares emit primarily in optical and UV wavelengths (Neidig, 1989; Woods et al., 2006; Schmitt et al., 2016), whitelight observations are likely to capture the resulting nanoflare emission (Kretzschmar, 2011), particularly for M-dwarf flares which emit strongly in white light (Walkowicz et al., 2011), resulting in a $DN \propto E$ relationship. This is similar to the pulse-heating model for EUV nanoflare activity proposed by Jess et al. (2019), whereby $DN \propto E^{4/3}$. For the energy range relevant to nanoflares (i.e., spanning only 3 orders-of-magnitude; $10^{22} - 10^{25}$ ergs), the differences between the linear scaling and pulse-heated models is relatively small. However, if accurate modelling and replication of full-scale flaring events (i.e., $10^{22} - 10^{31}$ ergs) was required, then more precise whitelight emission models would need to be developed (Procházka et al., 2018). The flare energies are converted to counts through the use of a ‘ 1σ ’ flare energy. This is an estimate of the flare energy corresponding to a 1σ fluctuation, and is dependent on the observation platform. This should be set to the approximate energy level of the noise floor, i.e., the energy of an event within the noise floor. A value in the range $10^{24} - 10^{25}$ ergs would set the noise floor at the upper span of nanoflaring energies, an appropriate estimate for most observation systems, as these nanoflares remain on or below the noise-floor. The value of 5×10^{24} ergs was used as the 1σ value in this work. This matches the value used in Jess et al. (2019). This energy ensures that the span of these nanoflare fluctuations remain within the noise envelope, with a maximum fluctuation of 2σ at the upper energy of 10^{25} ergs. This ensures that the modelled timeseries remain seemingly ‘quiescent’, matching their companion observational timeseries.

By combining the Poisson noise and nanoflare generation, fully synthetic timeseries matched to the characteristics of any observational dataset may be generated. The grid of input α and τ values can be modified to cover the desired span of modelled nanoflare characteristics. The same statistical and Fourier analysis applied to the observational timeseries can be applied to the simulated data. The ensuing arrays of statistical and Fourier properties are viewed through two-dimensional maps of the underlying statistical or Fourier characteristic corresponding to a given α and τ value, e.g., as seen in Figure 3.14, which shows the

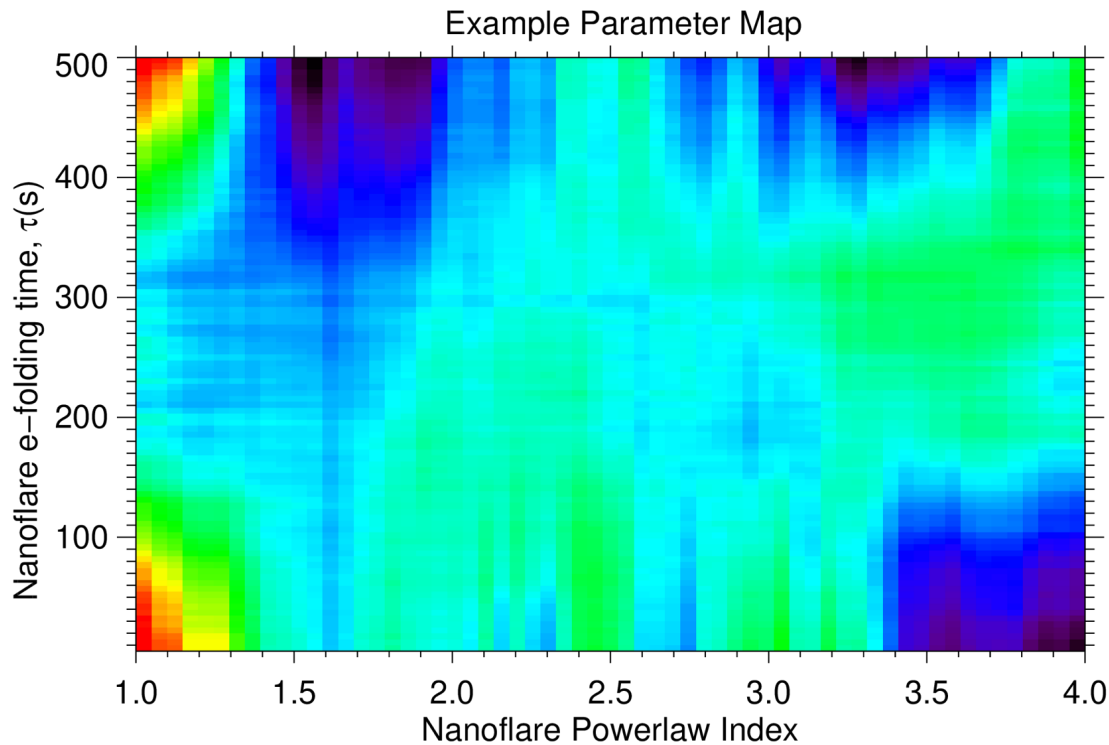


Fig. 3.14 An example two-dimensional ‘map’ illustrating how to visualise the Monte-Carlo simulation results for a dense grid of input nanoflare α and τ values. It should be noted that the data contained is randomised example data i.e., this is purely for visualisation and does not contain any usable data products. This style of map can be used to identify the possible range of nanoflare parameters corresponding to observational results.

two-dimensional mapping of an extracted parameter at each combination of α and τ .²⁰ This can be used to extract and characterise the underlying nanoflare conditions in a given observational timeseries.

3.2.5 Observational Considerations for Nanoflare Statistical and Fourier Analysis

The detectability of nanoflare signals via statistical and periodic analyses are dependent on the underlying observational parameters, including,

- Timeseries length. The statistical analysis is dependent on the number of frames, N . The error in statistical analyses scales with \sqrt{N} , while the signal scales with N . Periodic

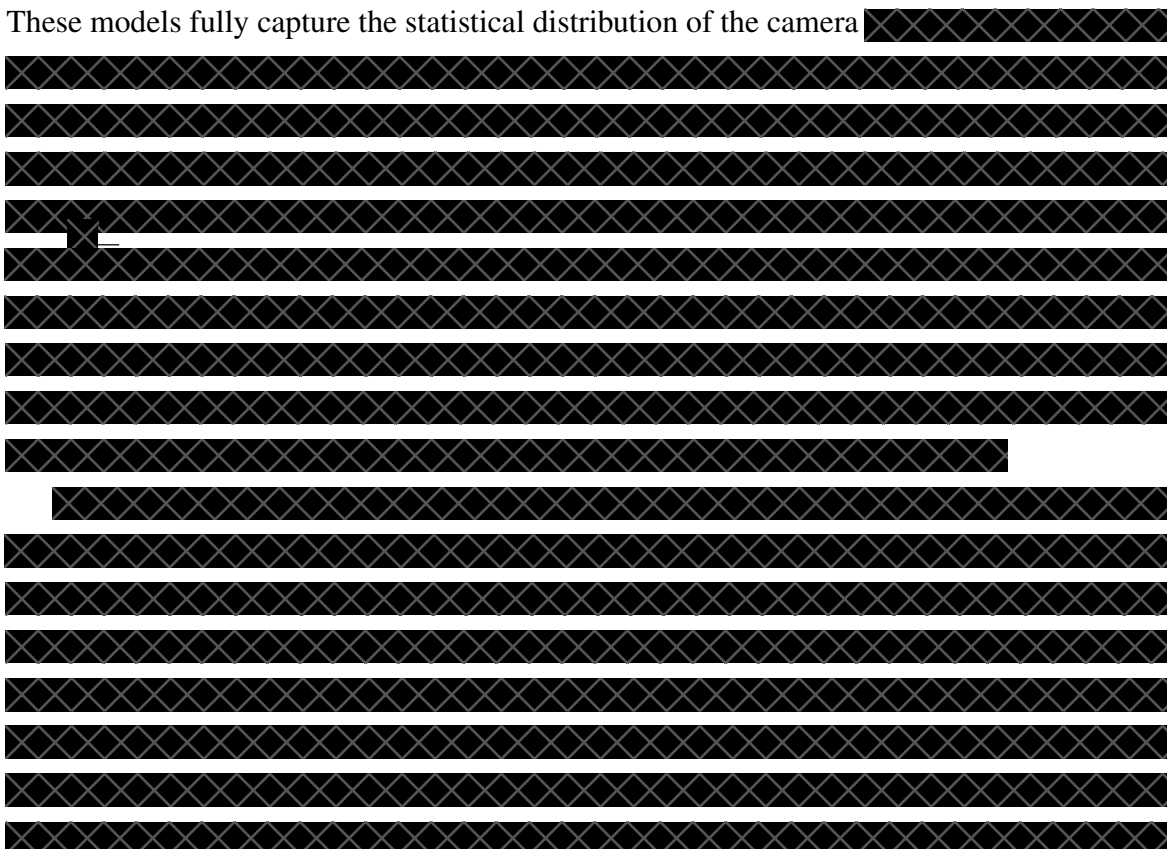
²⁰ This example plot shows randomised example data ; see Figures 5.5 and 5.8 in Chapter 5 to see these Monte-Carlo maps with real simulation data.

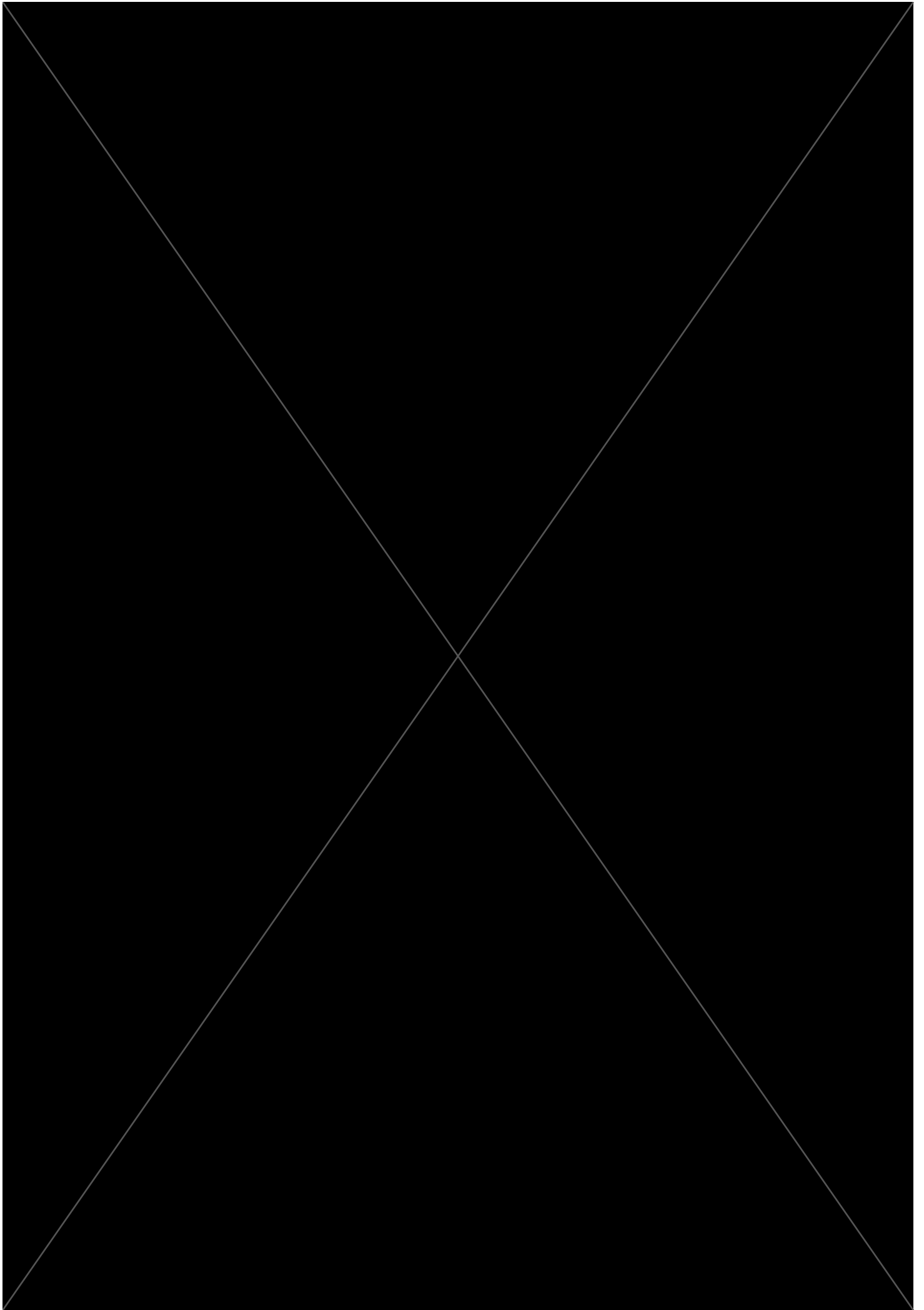
analysis is also dependent on the timeseries length, and crucially dependent on the length of successive uninterrupted frames. Increasing the duration of the observations will provide increased frequency resolution. The periodic signal also benefits from increased number statistics, as the number of nanoflares captured increases with longer observing sequences, hence providing more accurate quantification of any associated periodicities. When using modelled lightcurves (which are not subject to day/night cycles), increasing the number of successive frames had the effect of increasing the ratio of nanoflare power above the noise floor in the range 1 – 5 mHz . As a result, the nanoflare periodic signatures became more prominent over the noise. Space-based (e.g., TESS) observation would allow for a longer continuous timeseries, hence uncovering more of the underlying spectral slopes, particularly for the highest power-law values.

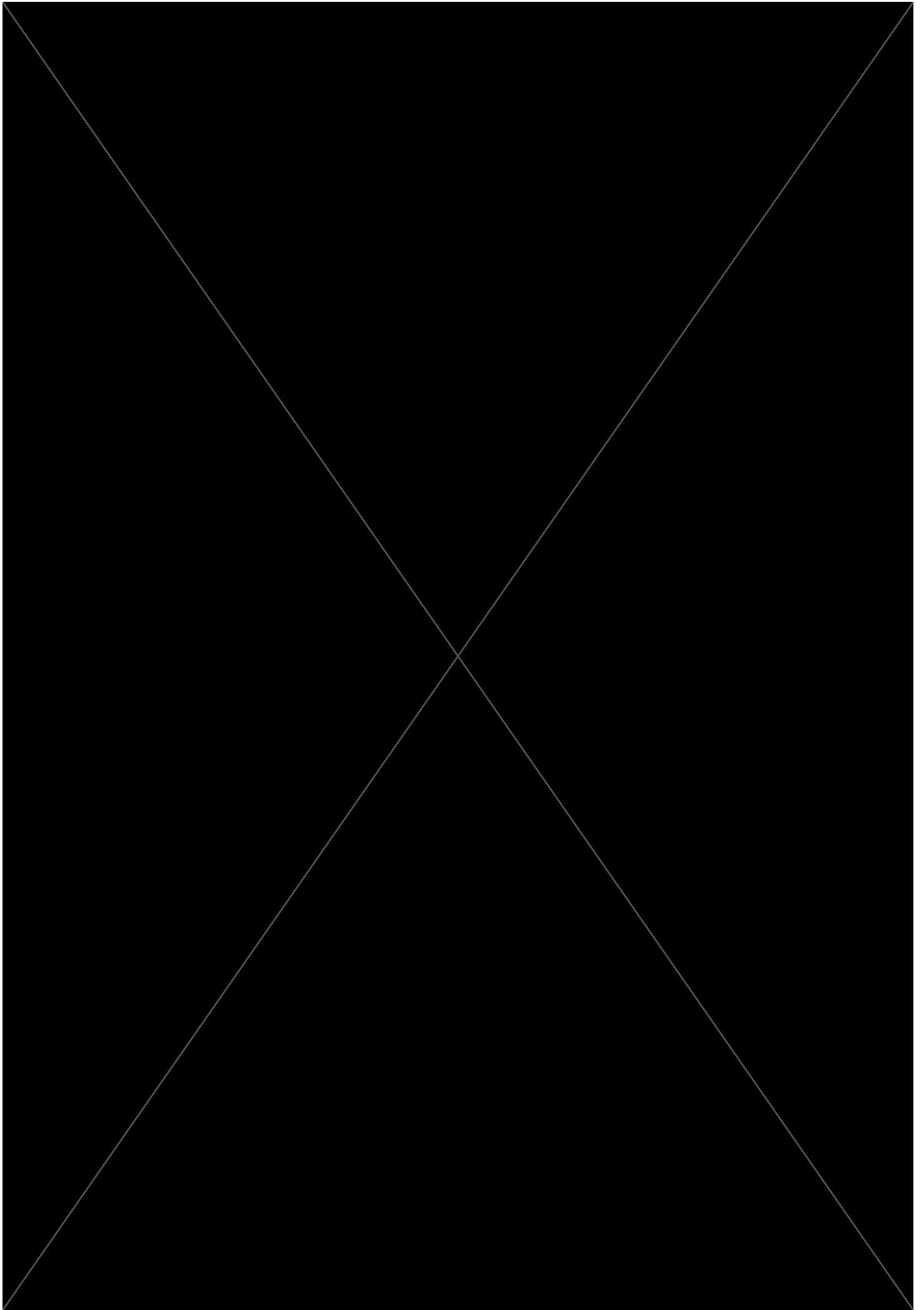
- **Cadence.** Shorter cadences allow for increased Nyquist frequencies to better resolve rapid and short-lived periodic signatures. Sub-second cadences (e.g., HiPERCAM, with exposures on the order of milliseconds; [Dhillon et al., 2016](#)) could allow for a very large frequency range and excellent number statistics to be achieved in a very short observation window.
- **Apparent magnitude.** As the observed magnitude increases, the scintillation noise begins to increase also (this is not an issue with space-based observations). This affects the frequency distribution of the noise, since the scintillation introduces a frequency-dependent noise component that needs to be considered. Searching for nanoflares embedded within this more complex noise distribution would require the seeding of a scintillation model into the numerical simulations. A future study could explore low-magnitude stars, to determine whether the increased scintillation is balanced by the increased nanoflare signal, or future space observations could mitigate this entirely. However, the star itself should still be of low intrinsic stellar brightness; see below.
- **Intrinsic stellar brightness.** Brighter stars have increased quiescent flux and therefore a more pronounced noise floor that must be combated when searching for nanoflare signals on top of this brighter background.

BIOMEDICAL IMAGE PROCESSING OUTCOMES

The overall Randox project has been very successful. The work packages that I was involved with are now able to dramatically increase dynamic range, suppress camera noise, identify key image features to co-align and crop the image, and finally apply intensive processing to fully isolate each DTR from any remaining noise and blemishes. The result is isolation of the diagnostic DTR signatures, with consistent co-alignment from image to image. These developments have begun to be implemented into analyser technology, in cameras all across the globe. The statistical analysis techniques I developed and detailed in Chapter 3.1 were instrumental to characterise the camera noise performance, and create fully synthetic models. These models fully capture the statistical distribution of the camera







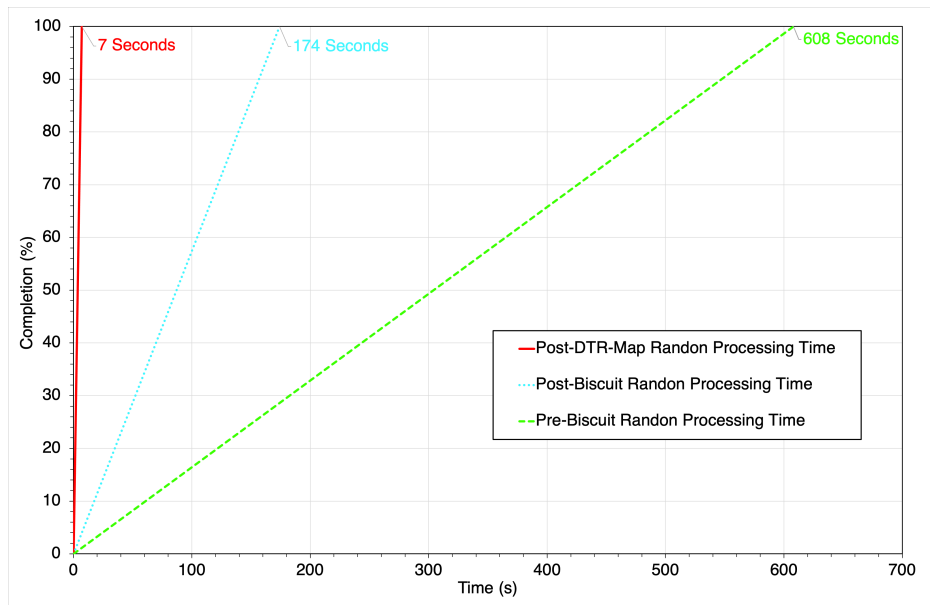


Fig. 4.3 This chart illustrates the processing time improvement to RANDOM when utilising the output of BISCUIT. A time reduction of 71% is achieved through use of the BISCUIT cropping. Combining the BISCUIT cropping with a map of expected DTR positions, the processing time was reduced further, to 98.8% the original processing time. This radical reduction in processing time means the RANDOM processing is achievable within a realistic timescale.

the processing times downstream, and ensuring a consistent DTR positioning within the camera frame.

STATISTICAL AND FOURIER SIGNATURES OF STELLAR NANOFLARE ACTIVITY

The content of this chapter is adapted from work previously published as [Dillon et al. \(2020\)](#) by APJ. It has been modified to fit within the confines and structure of this thesis, with the majority of the introduction and methods moved to the appropriate chapters. Some sections have been expanded, and the material contained within the appendices has been worked into the main body of the text.

5.1 INTRODUCTION

As established in Chapter 1.2, magnetic reconnection in the form of flares can occur across a wide range of energies. Flares with energies approximately 10^{-9} that of ‘traditional’ flare events are known as ‘nanoflares’. By virtue of their low energies ($10^{22} - 10^{25}$ ergs) these events lie below the noise-floor for individual observation, but with the techniques described in Chapter 3.2 it becomes possible to recover nanoflare signatures from seemingly quiescent lightcurves. These nanoflare signatures were believed to be a possible source of the quasi-periodic brightness signatures which had been observed in the timeseries of several dMe flare stars (i.e. [Andrews, 1989, 1990a,b](#)) with periodic signatures on the order 1-1000s. While co-incident with typical p -mode periods, quasi-periodic continuous nanoflare activity across an entire stellar surface could also cause this periodicity. To investigate the role of nanoflares in these periodic signatures, a series of stellar timeseries were investigated using the statistical and Fourier analysis described in Chapter 3.2.

5.2 OBSERVATIONS WITH NGTS

As discussed in Chapter 3.2, a high cadence and a large number of datapoints are needed to detect and analyse these faint nanoflare signatures in observational timeseries, through the use of large number statistics. Jackman et al. (2018, 2019a,b,c, 2020) employed the high cadence of the Next Generation Transit Survey (NGTS; Wheatley et al., 2018) to apply techniques developed for solar flare analysis to stellar flare oscillations, inspiring the use of the NGTS in this chapter to extend statistical solar nanoflare techniques to stellar lightcurves. The NGTS is an automated ground-based array of 12 telescopes located at the ESO Paranal Observatory in Chile, that scan the sky in the optical domain, primarily searching for transiting exoplanet signals: however, it has also become a platform for stellar flare analyses. The NGTS has a cadence of ≈ 12 s, providing a Nyquist frequency of ≈ 41.6 mHz, with the observations spanning up to hundreds of thousands of frames for a single star.

Each camera has a 20cm lens with a f 2.8 aperture. Each camera has a field of view of 2.8 deg^2 , giving a total field of view of 96 deg^2 . The NGTS has a bandpass of 520-890 nm, which was designed to maximise detection of K and M dwarf stars. The camera typically runs in survey mode scanning through a list of star fields, but can also operate follow-up for interesting candidates. Each camera will typically observe two fields in a given night, and the same telescope will return to a field each night for as long as the field is visible. Fields are typically observed across 4-8 months, resulting in 400-500 hours of data. At a cadence of ≈ 12 s, this leads to over 10^5 frames of data.

Several lightcurves of M-dwarf stars were extracted from NGTS data to search for signatures of nanoflare activity. As discussed in Chapter 3.2, M-dwarf flares have a higher contrast against their quiescent background flux, vital to detect these below noise-floor nanoflare signatures. The strong white-light signal in these M-star flares (Walkowicz et al., 2011) is also ideal given the optical wavelengths utilised by the NGTS. Taking this into consideration, the M-dwarf stars NGTS J030047.1-113651¹, NGTS J030415.6-103712, and NGTS J031800.1-212036 were chosen as each of these had more than 10^5 datapoints available for study, hence maximising the available number statistics for analyses.

As this scientific analysis revolved around flare-active M-type stars, it was deemed important to also examine non-flare active stars, which (as discussed in Chapter 3.2) can

¹ These are NGTS object identifiers of the form NGTS JXXXXXXX.X+XXXXXXX, and generated from the RA and Dec of the object. While primarily internal identifiers, these have been used in previous publications, e.g. Jackman et al. (2018)

act as a control test, ensuring that the analysis is not mistaking underlying or systematic signatures inherent to the NGTS as nanoflares. The A-type stars NGTS J025840.5-120246, NGTS J030958.4-103419, and NGTS J030129.4-110318 were chosen for this purpose. As discussed in Section 3.2.1, these A-type stars are not a match in their spectral energy distribution to M-type stars. This necessitated the additional use of low-activity K-type stars for comparison. These have a comparable SED, but should have minimal detectable nanoflare signal due to their enhanced quiescent background compared to the M-dwarf stars. The K2V-type stars NGTS J030000.7-105633, NGTS J030848.9-112217, and NGTS J030538.9-114145 were chosen for this purpose, as they were low-activity and had no macroscopic flare events in their observed timeseries. All of the A-type stars, the K-type stars, and two of the three M-type stars were obtained from the same observational field (NG0304-1115) and camera (809), hence ensuring consistency across the processed A-, K-, and M-type data sequences. NGTS J031800.1-212036 was from a different field (NG0313-2230), but had noise statistics, magnitude, and stellar parameters consistent with the other M-stars used in the present study.

The magnitudes of the stars employed were comparable (see Table 5.1), with the majority around magnitude 13. This was important to ensure the noise statistics were consistent across the stars. At this magnitude, the dominant noise source is photon noise (see Figures 3 & 14 of Wheatley et al., 2018), with scintillation noise only becoming dominant at the highest frequencies in the data, which are beyond the typical p -mode periodicities which were under investigation (Osborn et al., 2015). The A-star NGTS J030129.4-110318 was the brightest, with an NGTS magnitude of 11.69. At this magnitude, scintillation became a dominant source of noise. This allowed me to investigate the effect of increased scintillation noise on the analysis techniques. Stellar parameters from the TESS Input Catalog Version 8 (TIC V8) (Stassun et al., 2018), along with the initial spectral classification provided via Spectral Energy Distribution (SED) fitting performed by the NGTS pipeline (see Section 5.1.1 in Wheatley et al., 2018) were used to assign the spectral types. This, and other observational parameters are shown in Table 5.2. The full observing run took place over an approximately four month timespan, from November 2015 to March 2016.

NGTS Identifier	Spectral type	NGTS Magnitude
NGTS J030047.1-113651	M2.5V	13.23
NGTS J030415.6-103712	M3V	13.85
NGTS J031800.1-212036	M2.5V	13.03
NGTS J025840.5-120246	A5V	13.22
NGTS J030958.4-103419	A5V	12.55
NGTS J030129.4-110318	A7V	11.69
NGTS J030000.7-105633	K2V	13.58
NGTS J030848.9-112217	K2V	13.59
NGTS J030538.9-114145	K2V	13.57

Table 5.1 NGTS magnitudes of the stars used in the study.

Sp Type	NGTS ID	GAIA ID	TIC ID	RA	Dec	Mass (M_{\odot})	Radius (R_{\odot})	Luminosity (L_{\odot})	Distance (pc)	Approximate Flare Rate per Hour	$\log\left(\frac{L_{\text{flare}}}{L_{\text{bol}}}\right)$
M2.5V	NGTS J030047.1-113651	5160579407177989760	141307298	45.196372	-11.614197	0.40	0.41	0.021	67.5	0.012	-3.09
M3V	NGTS J030415.6-103712	5160771340676667776	23138344	46.065155	-10.620268	0.55	0.55	0.036	125.6	0.027	
M2.5V	NGTS J031800.1-212036	5099679725858611840	92249704	49.500502	-21.343482	0.40	0.41	0.021	59.6	0.003	
A5V	NGTS J025840.5-120246	5160183681775577472	98757710	44.66885	-12.046304	2.28	3.03	54.916	3464.1	0	
A5V	NGTS J030958.4-103419	5165979280580778624	23221987	47.493582	-10.572118	1.27	1.16	2.0	690.6	0	
A7V	NGTS J030129.4-110318	5160773569763964416	141309114	45.372827	-10.572118	1.81	1.65	8.6	737.7	0	
K2V	NGTS J030000.7-105633	5160700765773865600	141287385	45.003119	-10.942633	0.77	0.85	0.342	375.1	0	
K2V	NGTS J030848.9-112217	5165722991292368384	23192572	47.203979	-11.371446	0.78	1.16	0.647	532.2	0	
K2V	NGTS J030538.9-114145	5159884962505997184	23169095	46.412072	-11.696004	0.78	0.78	0.356	381.1	0	

Table 5.2 The stellar parameters for the stars used in the analysis. The stellar masses, radii, and luminosity data is from the TESS Input Catalog release V8. (Stassun et al., 2018)

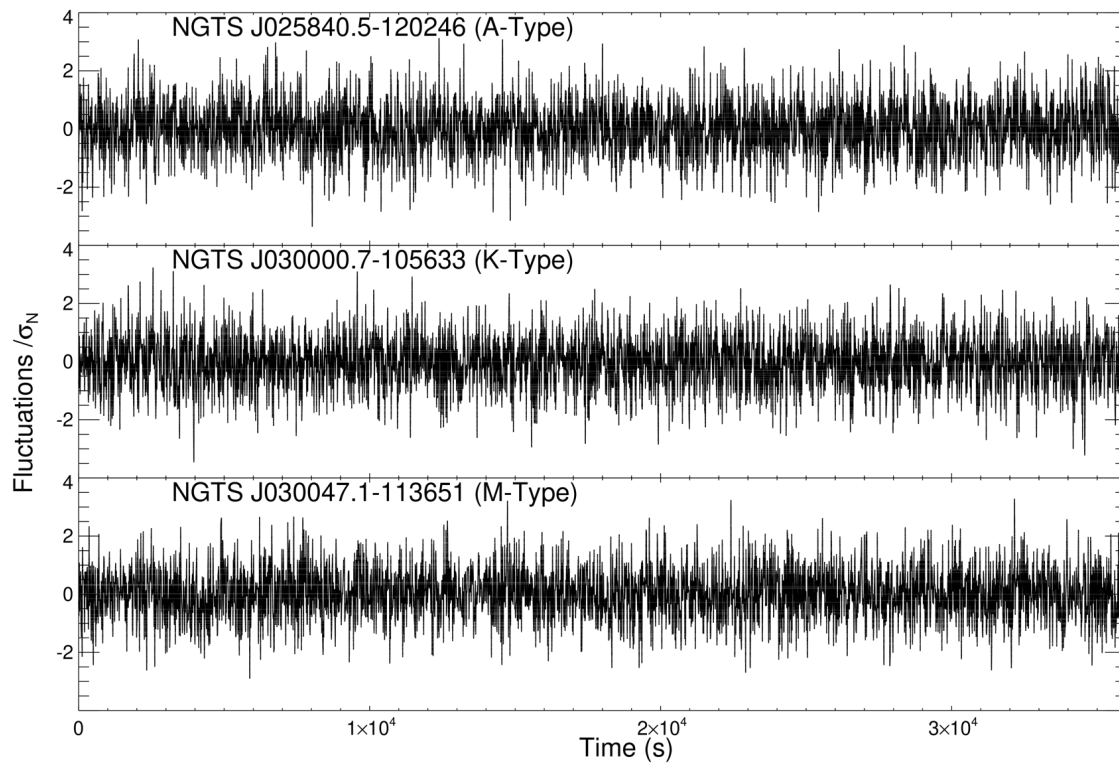


Fig. 5.1 Example NGTS J025840.5-120246 (A-type; above), NGTS J030000.7-105633 (K-type; middle) and NGTS J030047.1-113651 (M-type; below) lightcurves. These sample lightcurves have been cropped to a 36 000 s interval for clarity, but the analysis utilised the entire timeseries. The time interval between successive datapoints is ~ 12 s and the amplitudes have been mean-subtracted and normalised by their respective standard deviations.

These timeseries were prepared for analysis following the steps detailed in Section 3.2.1. The lightcurves were corrected for background and flat-fielded according to the NGTS data reduction pipeline described in [Wheatley et al. \(2018\)](#). This pipeline provides a relative error in the flux at each point in the timeseries. These error bars are affected by cloudy weather and high airmass. Any fluctuations in this error exceeding 1σ above the mean value were removed, resulting in $\sim 10\%$ of each timeseries being omitted. This removed any data that had statistically significant increases in its associated flux uncertainties, therefore preventing any large flux errors (largely due to poor seeing conditions) from contaminating the final timeseries. Next, the lightcurves extracted for each observing sequence were examined for the presence of macroscopic flare signatures, something which occurred in $\sim 0.2\%$ of the remaining M-type timeseries (i.e., following the removal of datapoints exceeding 1σ in their relative flux errors). To isolate the macroscopic brightenings, each lightcurve was searched for emission signatures exceeding 3σ above the mean value, which lasted continually for a minimum of 1 minute (5 datapoints). Based on a normal distribution, the probability of this

occurring by chance is $\lesssim 2 \times 10^{-13}$, and hence allowed for the robust detection of intensity fluctuations resulting from macroscopic flaring activity. Once the larger scale flare signatures had been identified, they were cut from the timeseries using an interval of ± 5 minutes (25 datapoints) from the first and last detection above the 3σ threshold. For consistency, the same processing steps were applied to the A-type and K-type stellar lightcurves, but no macroscopic brightenings were found for these sources. The number of macroscopic flares removed were used to calculate approximate flare rates for the M stars. These are listed in Table 5.2. The flare rates were of a comparable magnitude for the three M stars, with rates of 0.012, 0.027 and 0.003 flares removed per hour for NGTS J030047.1-113651, NGTS J030415.6-103712, and NGTS J031800.1-212036 respectively. The only M-star with an X-ray luminosity measurement was NGTS J030047.1-113651, which had a X-ray flux measurement available from the 4XMM XMM-Newton Serendipitous Source Catalogue (Webb et al., 2020). This corresponded to an X-ray luminosity of 6.47×10^{28} ergs s⁻¹. The ratio of X-ray luminosity to the bolometric luminosity is an indication of the activity rate of the star. This star exhibited $\log\left(\frac{L_x}{L_{Bol}}\right) = -3.09 \pm 0.21$, which compares to the literature values for a young and active M-type star, with saturated X-ray emission of $\log\left(\frac{L_x}{L_{Bol}}\right) \sim -3$ (Kastner et al., 2003; López-Santiago et al., 2010). Given the similar flare rates, I extrapolated that all three stars were macro-flare active, with comparable activity levels.

Upon completion of the lightcurve filtering, the lowest number of datapoints remaining was 97 060. To ensure consistency across all subsequent analyses, each of the other eight M-K- and A-type timeseries were cropped to the same 97 060 datapoints.

Once the macroscopic flare signatures had been extracted from the timeseries, each of the remaining lightcurves were normalised according to the methods described in Chapter 3.2. Night-by-night normalisation was achieved by subtracting a linear line of best fit that was derived from the corresponding timeseries. Next, the lightcurves were divided by their respective standard deviations, σ_N , providing a timeseries of fluctuations around a common mean that can be readily cross-compared with other star types and data products. To ensure that the output data products did not contain any long-term and/or instrumental trends that were not accounted for using the initial preparatory routines, they were subsequently detrended using low-order polynomial fits.

5.3 ANALYSIS AND DISCUSSION

As documented by Terzo et al. (2011) and Jess et al. (2014, 2019), as well as in Sections 2.2 and 3.2 timeseries commonly referred to as ‘quiescent’ may in fact contain a wealth of small-

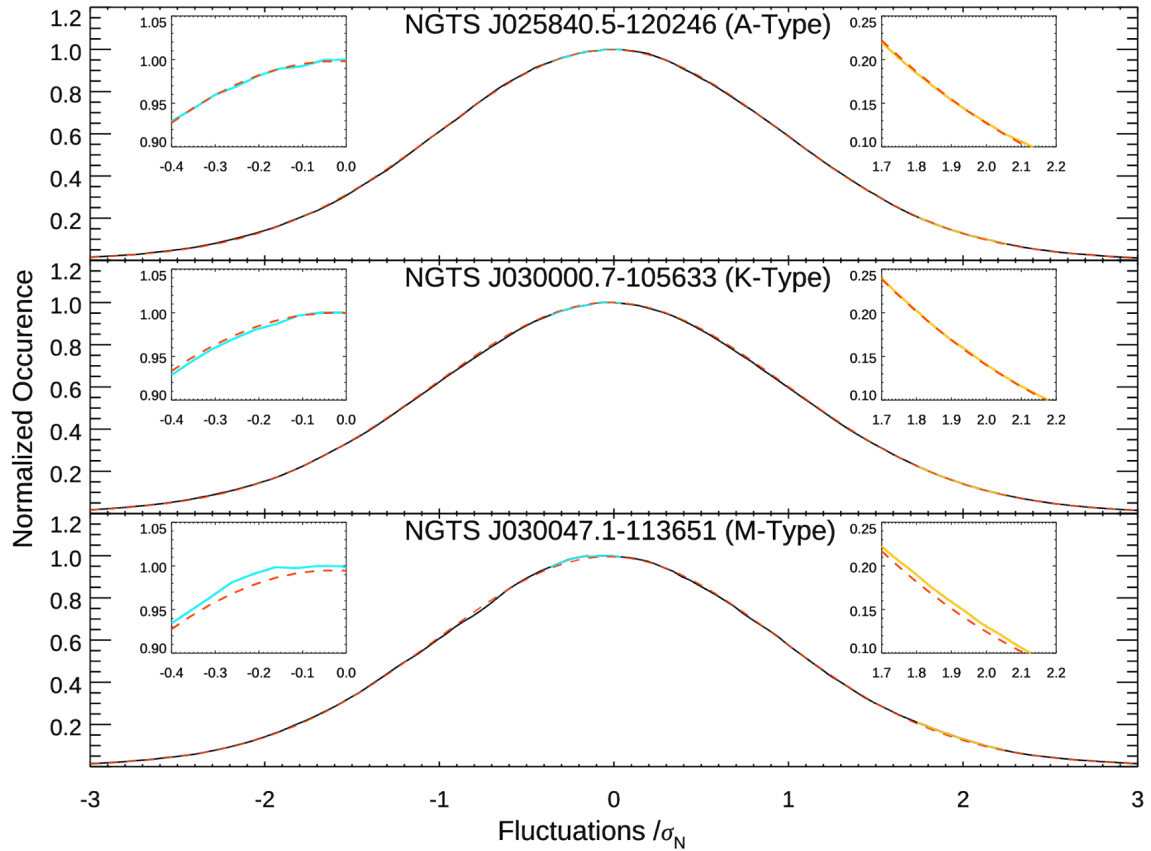


Fig. 5.2 Histograms of intensity fluctuations, each normalised by their respective standard deviations, σ_N , for the NGTS J025840.5-120246 (A-type; above), NGTS J030000.7-105633 (K-type; middle), and NGTS J030047.1-113651 (M-type; below) lightcurves. A standardised Gaussian profile is overplotted in each panel using a red dashed line for reference. The M-type distribution has a negative median offset with respect to the Gaussian, in addition to elevated occurrences at $\sim 2 \sigma_N$, which is consistent with the statistical signatures of nanoflare activity. On the other hand, the A-type and K-type intensity fluctuations provide no signatures of flare activity, with the resulting distribution remaining consistent with the presence of photon-based shot noise. Zoomed insets highlight the ranges spanning $-0.4 \leq \sigma_N \leq 0.0$ and $1.7 \leq \sigma_N \leq 2.2$, where M-type negative median offsets and occurrence excesses, respectively, are found. The blue and gold lines display the derived distributions, The M-type exhibited a small dip below the idealised Gaussian at around $-0.90 \sigma_N$, which is not seen in the A- and K-star. This may be connected to the negative median offset signal, which is causing a consequential dip elsewhere in the statistical distribution, but the exact nature of the signal is unknown.

scale nanoflare signatures that are embedded within the inherent noise of the photometric signals. It was possible to uncover these signatures through statistical analyses of the intensity fluctuations.

The dominant source of noise in seemingly ‘quiescent’ NGTS lightcurves will be shot noise, which follows a Poisson distribution (Wheatley et al., 2018). As discussed in Sec-

NGTS Identifier	GAIA Source ID	Spectral Type	Datapoints	Median Offset (σ_N)	Fisher Skewness	ζ Ratio	Kurtosis
NGTS J030047.1-113651	5160579407177989760	M2.5V	97060	-0.050 ± 0.004	0.031 ± 0.008	1.745 ± 0.015	0.102 ± 0.016
NGTS J030415.6-103712	5160771340676667776	M3V	97060	-0.050 ± 0.004	0.009 ± 0.008	1.783 ± 0.015	0.130 ± 0.016
NGTS J031800.1-212036	5099679725858611840	M2.5V	97060	-0.049 ± 0.004	0.041 ± 0.008	1.761 ± 0.015	0.169 ± 0.016
NGTS J025840.5-120246	5160183681775577472	A5V	97060	0.000 ± 0.004	-0.032 ± 0.008	1.766 ± 0.015	0.133 ± 0.016
NGTS J030958.4-103419	5165979280580778624	A5V	97060	0.000 ± 0.004	-0.004 ± 0.008	1.761 ± 0.015	0.183 ± 0.016
NGTS J030129.4-110318	5160773569763964416	A7V	97060	0.000 ± 0.004	0.003 ± 0.008	1.814 ± 0.015	0.688 ± 0.016
NGTS J030000.7-105633	5160700765773865600	K2V	97060	0.000 ± 0.004	-0.010 ± 0.008	1.745 ± 0.015	0.144 ± 0.016
NGTS J030848.9-112217	5165722991292368384	K2V	97060	0.000 ± 0.004	-0.008 ± 0.008	1.723 ± 0.015	0.119 ± 0.016
NGTS J030538.9-114145	5159884962505997184	K2V	97060	0.000 ± 0.004	-0.013 ± 0.008	1.723 ± 0.015	0.118 ± 0.016

Table 5.3 Characteristics of the intensity fluctuation histograms associated with the A-, K-, and M-type NGTS sources. Note that a standard Gaussian distribution will demonstrate $\zeta = 1.73$, hence deviations from this provide an indication of the intensity fluctuation occurrences taking place close to, and far away from the timeseries mean.

tion 2.1, this was also the dominant noise source for the Radox images. The fluctuations will be random, and in the limit of large number statistics, will demonstrate equal numbers of positive and negative fluctuations about the timeseries mean (Frank, 2009). Therefore, plotting a histogram of the inherent shot noise fluctuations for a truly quiescent timeseries would produce a symmetric distribution, with the mean and median centred at zero. Any subtle offsets and/or asymmetries from this idealised case may be interpreted as signatures of impulsive events, with subsequent exponential decays, embedded within the noise floor of the lightcurve (Terzo et al., 2011).

As discussed in Section 2.2, and in Jess et al. (2019), nanoflares give rise to two distinct signals in the resulting intensity fluctuation histograms. The first is a negative median offset, where the median value of the histogram is $< 0 \sigma_N$. This is a characteristic signal associated with an exponentially decaying signature: the decay phase following an impulsive deposition of energy occurs over a longer timescale, hence providing more fluctuations that are beneath the elevated signal mean caused by the impulsive event. The second signature is an excess of fluctuations at $\sim 2 \sigma_N$, caused by the impulsive nature of the nanoflare intensity rises, and gives rise to an asymmetric distribution that can be benchmarked using Fisher skewness coefficients. As the evolution of a nanoflare produces an almost discontinuous increase in the lightcurve intensity, a distinct positive peak manifests in the resulting histogram of intensity fluctuations. Therefore, a seemingly quiescent lightcurve exhibiting both of these signals is a strong candidate to contain embedded nanoflare signatures. Additionally, I benchmarked the shape and widths of the distributions through calculation of the histogram kurtosis values, and the ratio of its full-width at eighth-maximum to that of its full-width at half-maximum (i.e., $\text{FW}_{\frac{1}{8}\text{M-to-FWHM}}$ ratio), which I defined as ‘ ζ ’ for simplicity. Note that a standard Gaussian distribution will have $\zeta = 1.73$, hence deviations from this provide an indication of

the intensity fluctuation occurrences taking place close to, and far away, from the timeseries mean.

5.3.1 NGTS Datasets

Figure 5.1 displays sample lightcurves, cropped to a 36 000 s interval, where the intensity fluctuations are normalised about their respective means and standard deviations. Figure 5.2 displays the intensity fluctuation histograms for the example A- K- and M-type stellar sources NGTS J025840.5-120246, NGTS J030000.7-105633, and NGTS J030047.1-113651, respectively. As expected, the non-flare active A-type star and low-activity K-star show little variation from the standardised Gaussian distribution (dashed red lines in Figure 5.2), with median offsets of $0.000 \pm 0.004 \sigma_N$ and no visible excess at $\sim +2 \sigma_N$. This suggests that the A-type and K-type stars have no embedded nanoflare characteristics, and therefore reiterates their importance as a control test for subsequent M-type star analysis. On the other hand, the M-type star displays both of the characteristic nanoflare signatures, with a negative median offset equal to $-0.050 \pm 0.004 \sigma_N$, and a visible occurrence excess at $\sim +2 \sigma_N$, culminating in an associated positive Fisher skewness value of 0.031 ± 0.008 that is above the expectations of a pure Gaussian distribution.

The other candidate stars exhibited consistent signals, with the M-type stars showing histogram signatures consistent with nanoflare activity, while the A- and K-type stars showed no indication of impulsive behaviour beneath the noise floor. A-type star NGTS J030129.4-110318 exhibited a small positive skew of 0.003 ± 0.008 , but the associated uncertainty makes this less definitive when compared to the positive skewness values exceeding 0.040 for some M-type sources. Furthermore, NGTS J030129.4-110318 also demonstrated zero median offset, remaining inconsistent with a distribution comprised of impulsive events followed by gradually decaying tails. This star had a much larger deviation from Gaussian statistics, evidenced by a kurtosis value of 0.688 ± 0.016 , and ζ ratio of 1.814 ± 0.015 . This deviation from Gaussian statistics is due to the increased brightness of this star (see Table 5.1) compared to the other candidates, resulting in scintillation becoming a more significant noise source (Osborn et al., 2015; Wheatley et al., 2018; O’Brien et al., 2021). It is important to note that while the scintillation noise produces statistics offset from a Gaussian, it is still distinct from the characteristic signatures of nanoflare activity. This highlights the robustness of the statistical nanoflare analysis. The characteristics derived for all nine stellar sources are documented in Table 5.3. The M-type stars exhibited a small dip below the Gaussian around $-0.90 \sigma_N$, which was not seen in the A- or K-stars. This may be connected to the negative

NGTS Identifier	Spectral Type	Datapoints	Gradient	Turning Point (mHz)	Peak Frequency (mHz)
NGTS J030047.1-113651	M2.5V	2316	-0.30 ± 0.05	0.81 ± 0.04	2.90 ± 0.04
NGTS J030415.6-103712	M3V	2316	-0.28 ± 0.05	0.90 ± 0.04	2.58 ± 0.04
NGTS J031800.1-212036	M2.5V	2316	-0.26 ± 0.05	0.64 ± 0.04	3.09 ± 0.04

Table 5.4 Characteristics of the PSDs associated with the M-type NGTS timeseries.

median offset signal, which is causing a dip elsewhere in the statistical distribution, but the exact nature of the signal is unknown. Future investigation could uncover the source of this dip, and potentially use it as a further diagnostic.

Employing the high time resolution and long duration imaging sequences of the NGTS data products enabled the first tentative evidence of nanoflares occurring on stellar sources (see, e.g., Fig. 5.2 and Table 5.3). However, while these statistical signatures derived for the NGTS M-type lightcurves resembled those expected for nanoflare activity, they did not provide any indication of the specific underlying plasma conditions at work.

As previously demonstrated by Andrews (1989), Rodríguez et al. (2016), and McLaughlin et al. (2018), small-scale brightenings – here hypothesised to be the result of nanoflare activity – often give rise to periodic signatures in the corresponding lightcurves. This has also been observed in the case of small-scale solar activity (Terzo et al., 2011). These small-scale brightenings are also discussed in Section 2.2. Following the steps described in Section 3.2.3, timeseries were extracted for each star that contained the maximal number of successive frames, where no breaks resulting from problematic flux calibrations, macroscopic flare events, or day/night cycles were present, i.e., the longest consecutive number of frames consistent across the 9 stars. The lowest number of viable consecutive frames was 2316 from M-type star NGTS J031800.1-212036. As such, each of the remaining five lightcurves were cropped to an identical 2316 datapoints ($\approx 27\,800$ s duration) so that the final A-, K-, and M-type timeseries had identical lengths, helping to ensure consistency between both the Nyquist frequency and frequency resolution in the subsequent analyses.

Each of the extracted NGTS lightcurves were passed through a Fast Fourier Transform (FFT) to determine whether power existed at frequencies synonymous with a typical p -mode spectrum (often in the range of 1 – 1000 s; Kjeldsen et al., 1995; Guenther et al., 2008; Handler, 2013; Di Mauro, 2016). The input data resulted in a Nyquist frequency of ≈ 41.6 mHz, complemented by a frequency resolution $\Delta f = 0.0356$ mHz, in the corresponding FFTs. However, it must be pointed out that a strictly periodic wave signal would not manifest as median offsets and/or asymmetries in the fluctuation histograms documented in Figure 5.2, since the evolution of a purely sinusoidal wave signal is symmetric about its given

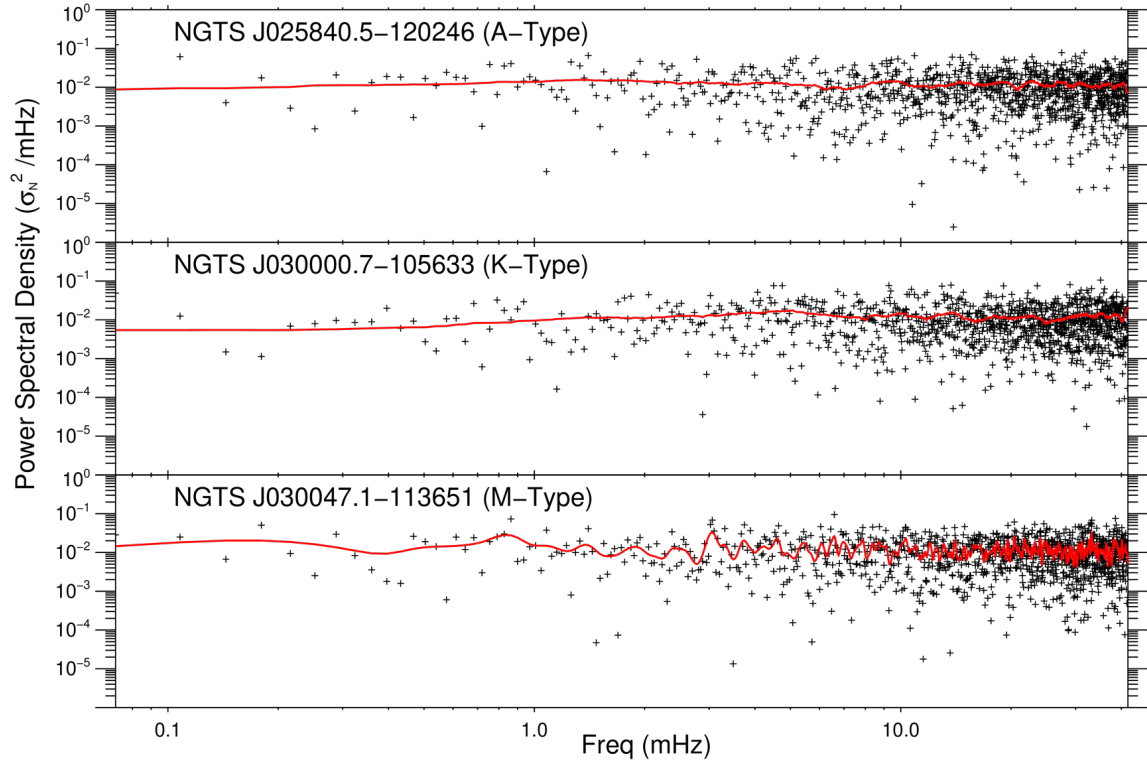


Fig. 5.3 The Fourier power spectral densities (PSDs) for example A- K- and M-type stellar sources NGTS J025840.5-120246 (upper panel) NGTS J030000.7-105633 (middle panel) and NGTS J030047.1-113651 (lower panel), respectively, displayed in normalised units of σ_N^2/mHz . The crosses in each panel depict the individual power values as a function of frequency, while the solid red line reveals a trendline calculated over ± 6 frequency elements (± 0.427 mHz) using a Gaussian smoothing filter. It can be seen that the A- and K-type PSD are relatively flat, with no clear power enhancements, apart from slight enhancement in the K-type star, in the range of 1 – 10 mHz, indicative of the expected p -mode oscillations seen in Solar-like stars. Contrarily, the M-type PSD has a primary power peak at ≈ 0.8 mHz, followed by decreasing spectral power exhibiting a spectral slope of $\beta = -0.30 \pm 0.05$, followed by numerous power peaks in the range of 3 – 10 mHz, consistent with previous links to stellar p -mode spectra.

mean. The resulting Fourier power spectra were transformed into power spectral densities (PSDs) following the methods defined by Welch (1961) and Vaughan (2012), as described in Section 3.2.3

Following the generation of PSDs from the nine NGTS lightcurves, it was found that the A-, K-, and M-type sources exhibited consistent and distinct features in their corresponding PSDs, with examples depicted in Figure 5.3. The upper, middle, and lower panels of Figure 5.3 display the PSDs for the A-, K-, and M-type stars NGTS J025840.5-120246, NGTS J030000.7-105633, and NGTS J030047.1-113651, respectively. In each panel, the crosses represent the individual frequency-dependent power, while the solid red line depicts a trendline created using a ± 6 frequency element (± 0.427 mHz) smoothing (as discussed in Section 3.2.3 this Gaussian smoothing had a standard deviation of 2 elements, therefore applying smoothing over 3 standard deviations). It can be seen from the solid red lines in Figure 5.3 that the A-type and K-type spectra are relatively flat across all frequencies with no evidence of distinct peak frequencies. The K-type does show some slight power enhancement between $\approx 1 - 10$ mHz, consistent with stellar p -mode oscillations, as had been previously observed in K-type Solar-like stars (e.g. Chaplin et al., 2009). The M-type PSD exhibits more pronounced fluctuations across the frequency domain. In the lower panel of Figure 5.3, the solid red line highlights the presence of a primary power peak at ≈ 0.8 mHz, followed by a gradual decline in power as the frequency increases. This reduction in power, as a function of frequency, can be represented by a spectral slope, β , following the form f^β . In the lower panel of Figure 5.3, the spectral slope was calculated to be $\beta = -0.30 \pm 0.05$. For each M-type star the position of the primary peak, and its associated spectral slope, were calculated. The primary peaks (or ‘turning points’) were found in the range of $0.6 - 0.9$ mHz, with the corresponding spectral slopes calculated to span $-0.30 \leq \beta \leq -0.26$. Once the spectral slopes had been calculated, they were subsequently subtracted from each PSD to better highlight power fluctuations above the background level (similar to the processing undertaken by Prasad et al., 2017). Following the detrending of the PSDs, the frequency demonstrating maximal power above the background was subsequently extracted, and found to reside in the range of $2.58 - 3.09$ mHz for the M-type stellar sources, which is consistent with previous interpretations related to the presence of p -mode oscillations (Andrews, 1989, 1990a,b). The specific characteristics derived from the M-type PSDs are displayed in Table 5.4.

With the lightcurve intensity fluctuations statistically benchmarked, and the corresponding power spectra uncovered, the next step was to generate Monte Carlo nanoflare simulations that were tailored for stellar sources. As discussed in Section 3.2.4, this enabled direct com-

parisons to be made between the observed and simulated timeseries (for both the statistical fluctuations and the power spectra features), to help quantify the specific plasma parameters at work in each of the stellar sources. The modelled timeseries were cropped to the same length as the NGTS timeseries, i.e., 97 060 data points (at a cadence of ~ 12 s) for the statistical analysis, and 2316 data points for the PSDs, to ensure consistency in their number statistics.

5.3.2 *Stellar Simulations*

The Monte Carlo simulation techniques described in Section 3.2.4 were used to synthesise the intensity timeseries expected for a broad range of initial plasma conditions. One-dimensional lightcurves contain no resolvable spatial information of the stellar sources, meaning the modelled area represented the entire Earth-facing surface area of the star. This meant setting the pixel area to around 10^{21} cm², or approximately 10% of the surface area of the Sun, which corresponds to the surface area of a typical M-dwarf stellar source (Reid & Hawley, 2005). This area, along with an exposure time (10 s) and final cadence (12 s) matched to the NGTS observations, was used to re-compute the number of flaring events expected (following Equation 2.2.2 and the work by Aschwanden et al., 2000; Parnell & Jupp, 2000), for a given power-law index, α , and across a specific time interval. The quiescent flux of the A-, K-, and M-stars was used to generate the underlying Poisson noise in the flare models and the nanoflare energies were then calibrated to this noise level, following the steps described in Section 3.2.4.

Due to the large spatial integration ($\approx 10^{21}$ cm²), the simulations were computationally intensive. As a result of integrating over the entire stellar disk, the generation and superposition of hundreds of thousands of independent nanoflare events became a time consuming endeavour, requiring approximately 300 s on a 2.90 GHz Intel Xeon processor to generate a synthetic NGTS timeseries incorporating 97 060 individual frames (~ 13.5 continuous days of data at a cadence of 12 s). Future investigation with timeseries longer than $\sim 10^5$ frames would require increased computational processing.

An example depicting the generation of a synthetic NGTS lightcurve is shown in Figure 5.4. Here, the lightcurve is cropped to a 36 000 s interval to more clearly reveal its constituent components. The upper panel of Figure 5.4 displays (black line) modelled flaring events using a power-law index $\alpha = 3.25$ and a decay timescale (i.e., reflecting the e -folding time of the flare decays) of $\tau = 245 \pm 24.5$ s. Note that the decay timescale varies by $\pm 10\%$ (i.e., $\tau = 245 \pm 24.5$ s) to allow for subtle variations in the mechanisms responsible for cooling in the immediate aftermath of the flaring events (Antiochos & Sturrock, 1978). This

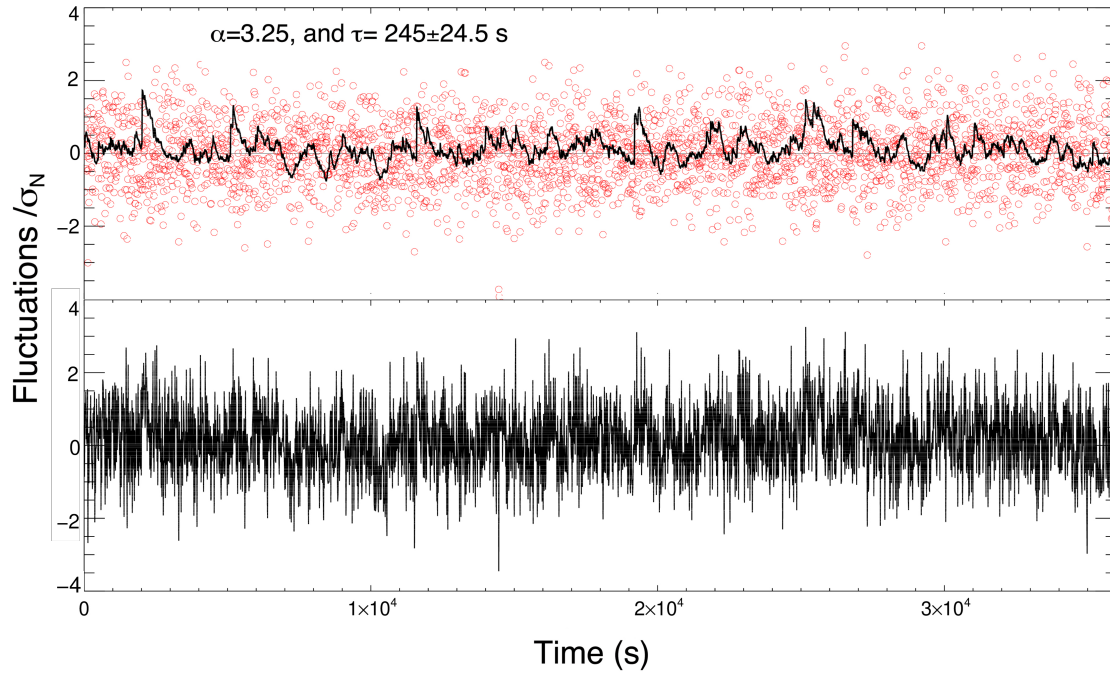


Fig. 5.4 The generation of flare signals according to a power-law relationship, where the power-law exponent is $\alpha = 3.25$ and the decay timescale for each event is 245 ± 24.5 s. The superposition of all modelled flare signatures is displayed using the solid black line (upper panel). Red dots represent the shot noise distribution modelled using Poisson statistics. The time interval between successive datapoints is 12 s and the amplitude has been mean-subtracted and normalised by its standard deviation. The lower panel reveals the superposition of the synthetic flaring lightcurve with the Poisson noise model, highlighting the difficulty of extracting visual signatures of small-scale flaring events from both synthetic and observational timeseries. This final timeseries is comparable to the observed timeseries, as seen in Figure 5.1

nanoflare timeseries is the superposition of individually generated flare events. The red dots represent the background shot noise, which follows a Poisson distribution. According to the limits of large number statistics, this Poisson profile will transform into a Gaussian distribution, with $\approx 68.3\%$, $\approx 95.5\%$, and $\approx 99.7\%$ of the noise fluctuations contained within the intervals of $\pm 1\sigma_N$, $\pm 2\sigma_N$, and $\pm 3\sigma_N$, respectively. It is visible from the upper panel of Figure 5.4 that even larger flaring events, e.g. occurring at ~ 200 s and ~ 500 s, are contained within the noise envelope. Once the shot noise contributions have been added to the synthetic flaring signals, the resulting timeseries (lower panel of Fig. 5.4) mimics very closely typical stellar lightcurves (i.e. the NGTS lightcurves in Fig. 5.1), with the original nanoflare signal now indiscernible from the embedded noise.

Figure 5.4 documents the steps taken to generate a synthetic lightcurve for a specific power-law index ($\alpha = 3.25$) and e -folding timescale ($\tau = 245 \pm 24.5$ s). However, in order to more accurately constrain the observational findings using these synthesised models required repeating the processing steps documented in Figure 5.4 using a dense grid of nanoflare input parameters. Specifically, power-law indices spanning $1 \leq \alpha \leq 4$ (in intervals of 0.05) and e -folding timescales ranging across $5 \leq \tau \leq 500$ s (in steps of 5 s, consistent with previous estimations for solar nanoflares; Terzo et al., 2011; Jess et al., 2014) were employed. This produced a dense grid of 6100 final synthetic NGTS lightcurves, each with 97 060 datapoints to remain consistent with the observational NGTS timeseries, ensuring identical number statistics and allowing direct comparisons to be made between the observations and simulations.

5.3.3 Comparing Simulation to Observation

Each synthetically generated lightcurve was treated in an identical manner to that of the NGTS observations, whereby each of the 6100 simulated timeseries were detrended and normalised by their respective standard deviations, before generating their intensity fluctuation distributions and subjecting them to FFT analyses. It must be noted that there were no instances in any of the 6100 simulated timeseries where a sequence of 5 successive time steps exceeded $+3\sigma_N$ above the mean, hence highlighting the consistency between the simulated lightcurves and the final timeseries extracted from the NGTS observations.

First, to compare the observational intensity fluctuation distributions depicted in Figure 5.2 to those extracted from the dense grid of simulation input parameters, I generated a number of statistical maps (Fig. 5.5) where the parameter values extracted from the intensity fluctuation histograms were displayed as a function of the power-law index, α , and the corresponding decay timescale, τ . These statistical benchmarks are the same as those calculated for the NGTS stars in Table 5.3, only now graphically displayed in a two-dimensional format to aid visual clarity, i.e., following the example given in Figure 3.14.

The measured output parameters depicted in Figure 5.5 allowed cross-correlation between the observational signatures to those synthetically generated via the Monte Carlo modelling work, hence allowing estimation of the specific plasma conditions (i.e. the α and τ values) responsible for the observational signatures. Importantly, the synthetic stellar lightcurves are consistent with those expected from solar modelling efforts (Terzo et al., 2011; Jess et al., 2014, 2019), where a negative median offset is coupled with an increase in the Fisher skewness value. From Figure 5.5 it can be seen that the majority of nanoflare conditions

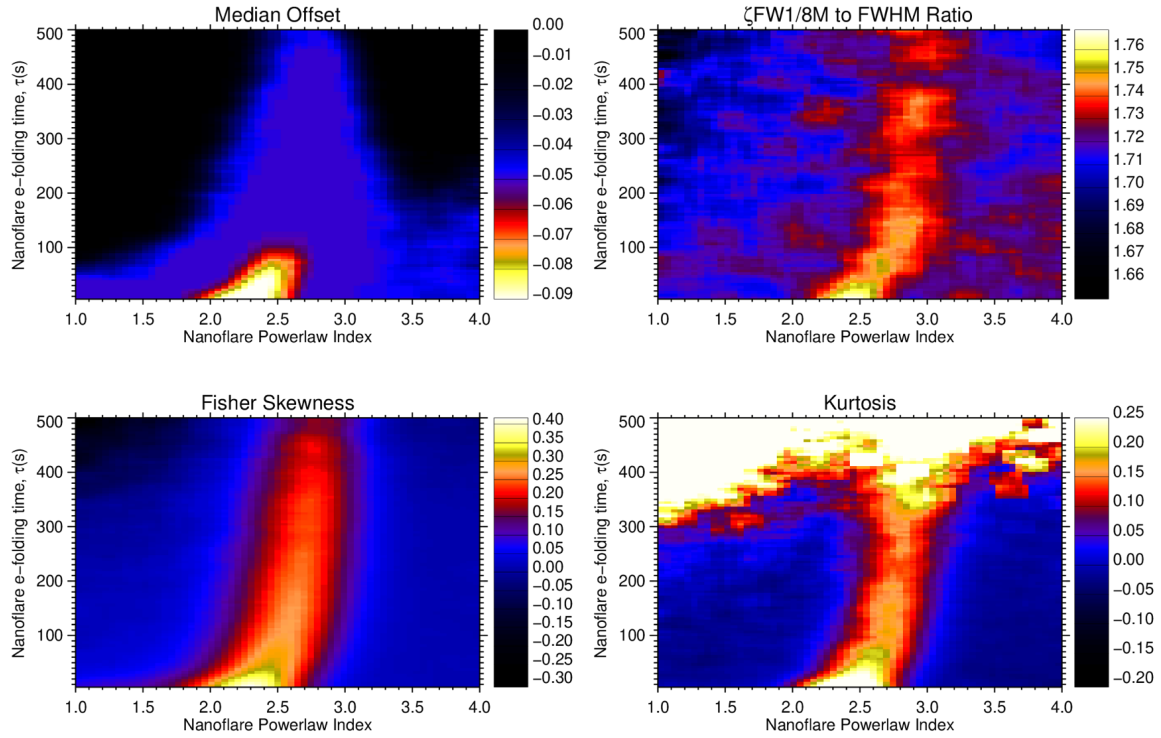


Fig. 5.5 The median offset (upper-left), ζ ($\text{FW}\frac{1}{8}\text{M}$ -to-FWHM ratio; upper-right), Fisher skewness (lower-left), and kurtosis (lower-right) characteristics extracted from the synthetic intensity fluctuation distributions as a function of the employed power-law index, α , and the decay timescale, τ . A negative median offset and positive Fisher skewness values support a wide range of flare conditions. The observational statistical characteristics (see Table 5.3 and Figure 5.2) compare to the modelled statistical distributions with overlapping parameters corresponding to $\alpha = 3.25 \pm 0.15$ and $\tau = 200 \pm 100$ s, in addition to $\alpha = 2.00 \pm 0.15$ and $\tau = 200 \pm 100$ s.

produced a negative median offset and positive Fisher skewness in the resulting statistical intensity fluctuation distribution, despite the presence of seemingly quiescent lightcurves (see, e.g., the lower panel of Fig. 5.4). Similar dips below the idealised Gaussian at approximately $-0.90\sigma_N$ (as were seen in the M-type stars) were exhibited in the simulations, suggesting these are linked to the embedded nanoflare signals.

When comparing the intensity fluctuation statistical outputs for the M-type stars to those derived from the Monte Carlo simulations, there was overlap in the median offset, Fisher skewness, kurtosis, and ζ ratio corresponding to two distinct plasma conditions governed by the flare power-law index, α , and the associated decay timescale, τ . The first set of self-similar parameters corresponded to $\alpha = 3.25 \pm 0.15$ and $\tau = 200 \pm 100$ s, while the second set of parameters consisted of $\alpha = 2.00 \pm 0.15$ and $\tau = 200 \pm 100$ s. These values highlight the fact that the observational M-type NGTS lightcurves show remarkable agreement with

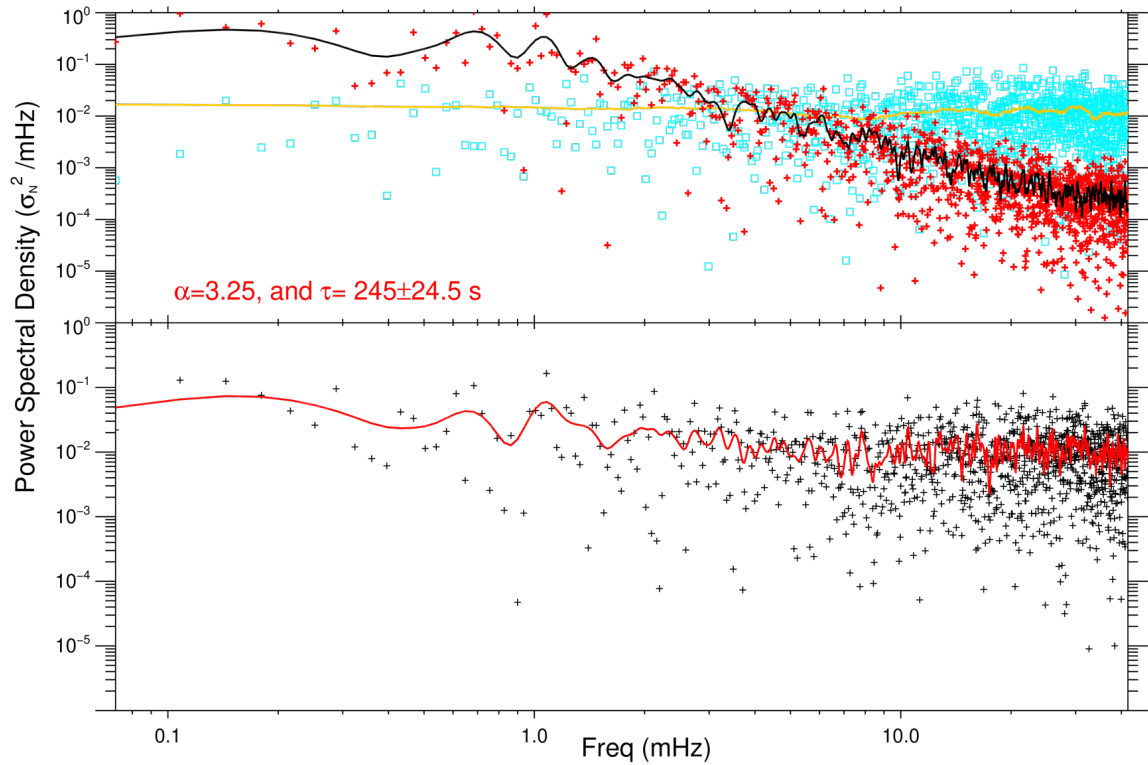


Fig. 5.6 The Fourier power spectral densities, displayed in units of σ_N^2 /mHz, corresponding to a power-law index $\alpha = 3.25$ and a flare decay timescale $\tau = 245 \pm 24.5$ s. The upper panel individually depicts PSD plots of the synthetic nanoflare and shot noise components as red crosses and blue squares, respectively. The solid black and gold lines represent trendlines for the nanoflare and shot noise profiles, respectively, computed over ± 6 frequency elements (± 0.427 mHz). The lower panel displays the PSD of the final synthetic timeseries, where the nanoflare signal is embedded within the synthetic noise floor. The synthetic PSDs corresponding to nanoflare activity are remarkably similar to those for the NGTS M-type stellar sources shown in the bottom panel of Figure 5.3.

the statistical signals derived from Monte Carlo synthetic lightcurves consisting of nothing but nanoflare signals embedded in characteristic shot noise. Contrarily, the A-type and K-type stellar parameters did not map consistently onto the statistical parameters depicted in Figure 5.5, strengthening the interpretation that the A-type and K-type sources do not exhibit nanoflare signatures.

In order to further examine the link between nanoflare activity and periodic variability in the synthetic lightcurves, I generated PSDs for each of the 6100 simulated timeseries, which could then be compared directly with the PSD features found in the NGTS observations. To remain consistent with the observational PSDs depicted in Figure 5.3, the synthetic timeseries was cropped to 2316 datapoints ensuring the frequency resolution was maintained at $\Delta f = 0.0356$ mHz. As the comparison between the observed and modelled intensity fluctuation distributions revealed a self-similar set of statistical parameters corresponding to a power-law index $\alpha = 3.25 \pm 0.15$ and a decay timescale $\tau = 200 \pm 100$ s, I provide example PSDs for $\alpha = 3.25$ and $\tau = 245 \pm 24.5$ s in Figure 5.6. Such Fourier analysis offers an additional parameterization of the nanoflare signal, resolving any ambiguities arising through examination of the statistical signatures alone.

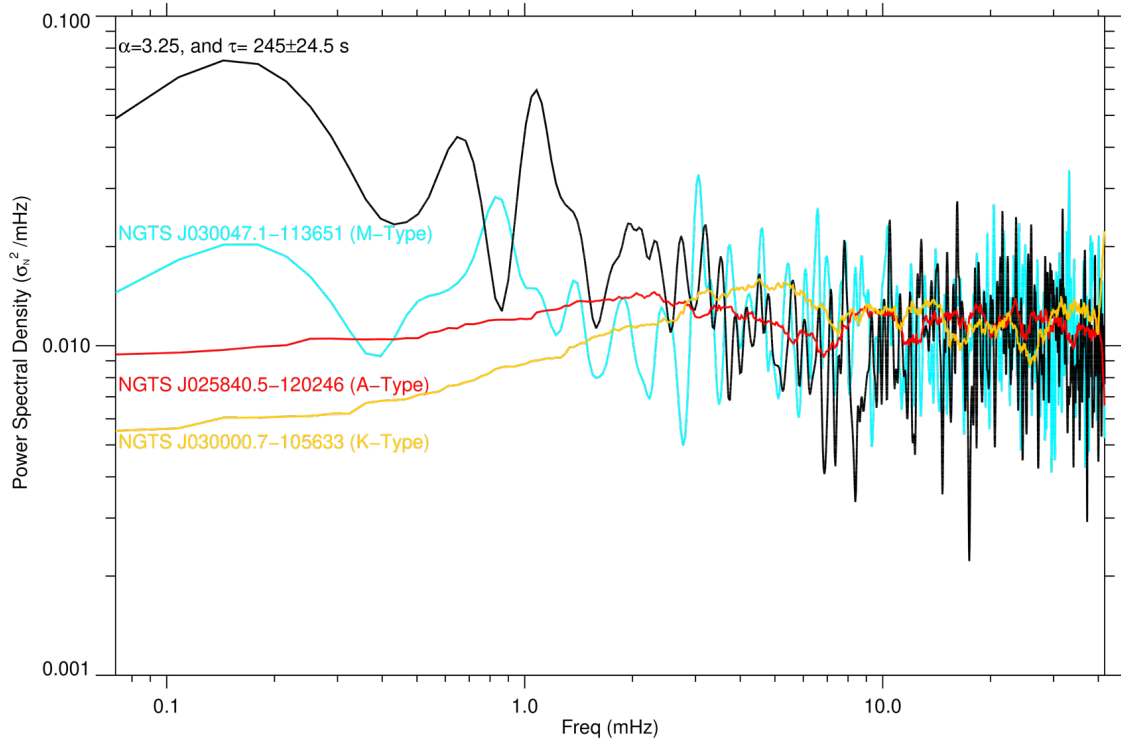


Fig. 5.7 The Fourier power spectral density (PSD) trendlines calculated over ± 6 frequency elements (± 0.427 mHz) for example A- K- and M-type stellar sources NGTS J025840.5-120246 (red line), NGTS J030000.7-105633 (orange line) and NGTS J030047.1-113651 (blue line), and a modelled timeseries corresponding to a power-law index $\alpha = 3.25$ and a flare decay timescale $\tau = 245 \pm 24.5$ s (black line), displayed in normalised units of σ_N^2/mHz . It can be seen that the A-type and K-type spectra are relatively flat across all frequencies with no evidence of distinct peak frequencies. The K-type does show some slight power enhancement between $\approx 1 - 10$ mHz, consistent with stellar p -mode oscillations, as have been previously observed in K-type Solar-like stars (e.g. Chaplin et al., 2009). Contrarily, the M-type PSD has a primary power peak at ≈ 0.8 mHz, followed by decreasing spectral power exhibiting a spectral slope of $\beta = -0.30 \pm 0.05$, followed by numerous power peaks in the range of 3 – 10 mHz, consistent with previous links to stellar p -mode spectra. The synthetic PSD is remarkably similar to the NGTS M-type stellar source, with peaks and spectral slopes in the same range and magnitude (see Figure 5.8 for the full range of peak frequencies and spectral slopes in modelled timeseries PSDs).

The upper panel of Figure 5.6 shows the corresponding PSDs for both the raw nanoflare (red crosses) and Poisson-based shot noise (blue squares) signals. The solid black and gold lines in the upper panel of Figure 5.6 depict the trendlines for the nanoflare and shot noise signals, respectively, established over ± 6 frequency elements (± 0.427 mHz). It can be seen that at lower frequencies ($\lesssim 5$ mHz) the nanoflare signal dominates over the corresponding noise profile, while at higher frequencies the noise becomes dominant and begins to mask the frequency-dependent signals of nanoflare activity. The lower panel of Figure 5.6 displays

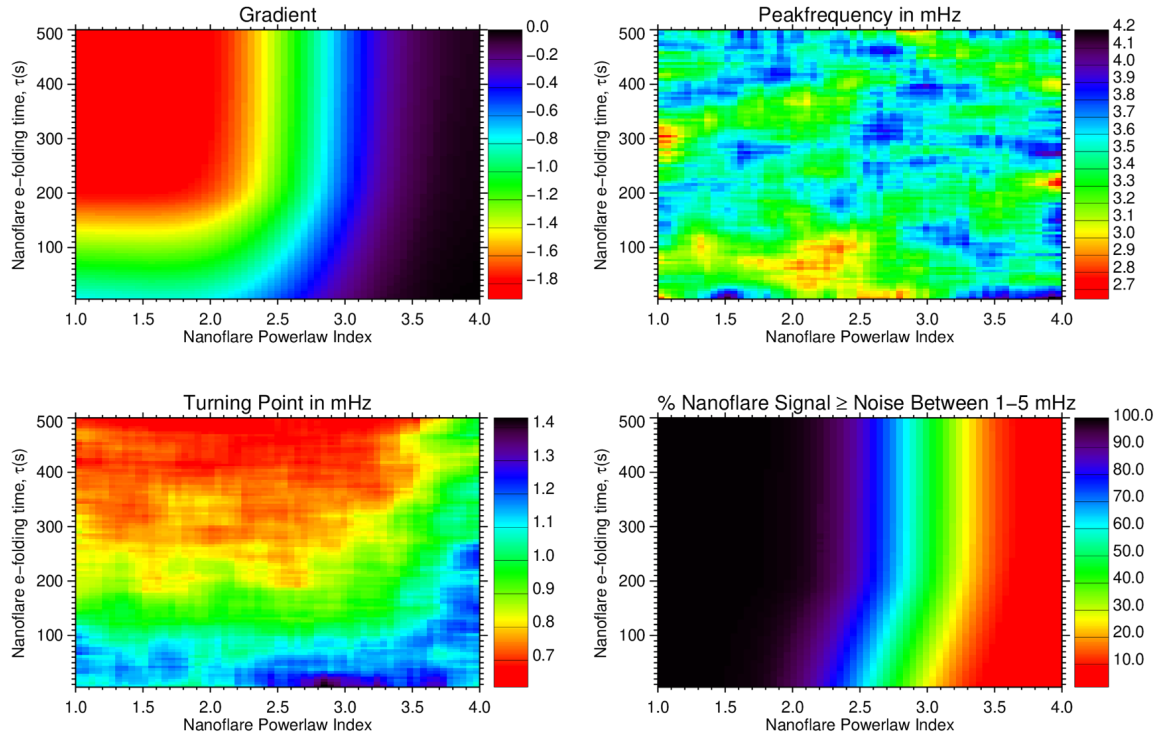


Fig. 5.8 The primary peak frequencies (lower-left), spectral slopes (upper-left), dominant frequencies following detrending (upper-right), and the percentage of nanoflare power above the noise floor in the range of 1 – 5 mHz (lower-right), displayed as a function of the power-law index, α , and the decay timescale, τ , used to generate the synthetic timeseries. The observational PSD characteristics (see Table 5.4 and Figure 5.3) compare to the modelled PSDs in the range of $\alpha = 3.3 \pm 0.2$ and $\tau = 200 \pm 100$ s.

the PSDs extracted from the final simulated lightcurve, where the nanoflare signal has been embedded within the synthetic noise profile. To remain consistent with the lower panel of Figure 5.3, the black crosses represent the individual frequency-dependent power measurements, while the solid red line depicts a trendline established over ± 6 frequency elements (± 0.427 mHz). The similarities between the lower panels of Figures 5.3 and 5.6 are remarkable, exhibiting similar primary power peaks at ~ 1 mHz, followed by a decrease in spectral power with increasing frequency, before finally demonstrating a number of power peaks within the range commonly associated with p -modes. It must be remembered that the A-type and K-type stellar sources provided flat and relatively featureless spectra, with no spectral slopes visible in their corresponding PSDs. Hence, the A- and K-type PSDs (see, e.g., the upper and middle panel of Figure 5.3) show no agreement with the synthetic PSD depicted in Figure 5.6, which serves as a further indicator that there was no nanoflare activity present in the A- and K-type stellar samples. This can be seen via Figure 5.7 which shows

the trendlines (calculated over ± 6 frequency elements or ± 0.427 mHz) of Fourier power spectral densities (PSDs) for the example A-, K-, and M-type stars, as well as for a modelled timeseries with a power-law index $\alpha = 3.25$ and a flare decay timescale $\tau = 245 \pm 24.5$ s. This plot highlights the agreement in the observational M-type and modelled timeseries PSDs, with comparable spectral slopes of approximately $\beta = -0.30 \pm 0.05$, and peaks around ≈ 0.8 mHz. This was in contrast with the A- and K-type PSD, which were relatively flat and featureless by comparison.

In a consistent manner with how the M-type stellar PSDs were processed, each of the 6100 synthetic lightcurves were examined and their corresponding primary frequencies, spectral slopes, and dominant frequencies (following detrending by the computed spectral gradients) were calculated. In order to more readily display these sets of measured parameters, these are displayed in Figure 5.8 in a two-dimensional format as a function of the power-law index, α , and the corresponding decay timescale, τ . This is similar to the intensity fluctuation statistical measurements depicted in Figure 5.5, but Figure 5.8 now displays the corresponding parameters extracted from the analysis of the synthetic PSDs.

Figure 5.8 documents interesting behaviour of the key Fourier-based parameters as a function of the power-law index, α , and the corresponding decay timescale, τ . As the power-law index increases, the spectral slopes (upper-left panel of Fig. 5.8) associated with the PSDs begin to flatten. This is likely a consequence of increased energy being spread across the entire frequency spectrum as a result of the larger power-law indices (Jess et al., 2020). Previous work on turbulent cascades have revealed spectral slopes within the range of $-2 \leq \beta \leq -1$ in both solar and stellar plasma (Podesta, 2011; Huang et al., 2017), believed to be a feature of wave behaviour. The spectral slopes found in the simulation outputs vary largely within this range ($-1.85 \leq \beta \leq 0.00$), but are a result of pure nanoflare signals, with no presence of strictly wave-based signatures. An explanation could be that nanoflares are individually low-energy events, but they occur very frequently all over the surface of a star. They may come together with an additive effect to form (quasi-)periodic signals, as opposed to the breaking effect of a wave cascade. This cascade-like signal has been documented previously by Hudson (1991), wherein solar nanoflare simulations produced a similar power spectrum cascade, but here I present the first evidence in stellar-specific simulations. This cascade signal is also similar to the ‘inverse magnetic cascade’ process discussed in Christensson et al. (2001), who found a reverse turbulence effect in 3-D MHD simulations, lending support to an inverse cascade signal generated by magnetic behaviour.

Furthermore, the primary frequency (lower-left panel of Figure 5.8) is sensitive to the nanoflare decay timescale, rising from ~ 0.7 mHz at the longest e -folding times (≈ 500 s) to

~ 1.4 mHz at the most rapid decay timescales (≈ 10 s). Interestingly, once the PSDs have been detrended by their corresponding spectral slopes, the dominant frequencies (upper-right panel of Figure 5.8) present are within the range of 2.7 – 4.2 mHz. This frequency range is often synonymous with the presence of p -mode waves (Andrews, 1989, 1990a,b), even though these simulations contain no strict wave activity.

An interesting metric to benchmark how significant the power peaks are within the range of 1 – 5 mHz involves the calculation of the percentage of the nanoflare spectral power equal to, or greater, than the corresponding power found in the synthetic noise PSD (lower-right panel of Figure 5.8). The spectral power arising from strictly nanoflare signatures is 10 – 100% greater than the corresponding (flat) noise power arising from a Poisson-based shot noise distribution. This can be seen in the upper panel of Figure 5.6, whereby the power arising from nanoflare signals is above that corresponding to the noise floor.

Comparing the simulated PSD features to the M-type stars (see Table 5.3), there were overlaps with the two-dimensional maps shown in Figure 5.8 for a power-law index $\alpha = 3.3 \pm 0.2$ and a nanoflare decay timescale $\tau = 200 \pm 100$ s. These values were consistent with the first set ($\alpha = 3.25 \pm 0.15$ and $\tau = 200 \pm 100$ s) of plasma conditions extracted from the intensity fluctuation statistical distributions. Importantly, I did not find self-similar PSD results substantiating the second set ($\alpha = 2.00 \pm 0.15$ and $\tau = 200 \pm 100$ s) of plasma conditions extracted from the intensity fluctuation statistical distributions. This demonstrates the usefulness of employing both statistical and Fourier-based benchmarking of the observational and synthetic timeseries, since it has alleviated a potentially ambiguous result found using just a single analysis method.

5.3.4 Observed Stellar Nanoflare Activity Parameters

Combining both the statistical and PSD benchmarks, I found evidence for stellar nanoflare activity across the sampled M-type stars for a power-law index $\alpha = 3.25 \pm 0.20$ and a decay timescale $\tau = 200 \pm 100$ s. Considering the observation is integrated over an entire stellar disk, one would expect some variation in the local plasma conditions, hence the relatively large uncertainties placed on the decay timescales. While the e -folding timescale is comparable to those put forward in solar studies, the power-law index is much higher than the range ($1.82 \leq \alpha \leq 1.90$) observed in solar plasma by Jess et al. (2019). It also exceeds the full range ($1.35 \leq \alpha \leq 2.90$) reported across the literature for all solar events (Berghmans et al., 1998; Krucker & Benz, 1998; Aschwanden, 1999; Parnell & Jupp, 2000; Benz & Krucker, 2002; Winebarger et al., 2002; Aschwanden & Freeland, 2012; Aschwanden

et al., 2014, 2015). This also exceeds the typical range of stellar flare power-law indices $1.5 \leq \alpha \leq 2.7$ reported by, e.g., Hudson (1991); Robinson et al. (1995, 1999); Kashyap et al. (2002); Güdel et al. (2003); Güdel (2004); Welsh et al. (2006); Reale (2016).

M-type stars are nearly or fully convective, with more powerful magnetic activity than the Sun, leading to increased flare activity. However, this alone cannot explain a higher power-law index, as a general boost to activity levels would enhance all frequencies and energies, thus preserving the same power-law index. Instead, it is possible that small-scale nanoflare energies in the range $10^{22} - 10^{25}$ ergs are boosted disproportionately in these flare active stars. While low energy flares are likely to be governed by the same underlying physical processes (Lu & Hamilton, 1991), and the power-law relationship is scale-free (applying to both small and large flares; Aschwanden, 2019), Robinson et al. (1995) and Vlahos et al. (1995) suggested that a discontinuity in the power-law indices of high and low-energy flare events would be an inherent feature of the self-organised criticality model of flaring (wherein small magnetic reconnections occur very frequently, each with the potential to set off another reconnection nearby, causing an avalanche effect, and following a power-law distribution of energies). They suggest that while high energy flaring would exist at power-law indices of $\alpha = 1.8$, the power-law index of low energy (i.e. micro and nanoflares) would range around $3 \leq \alpha \leq 4$. This is in agreement with the stellar nanoflare activity power-law index of $\alpha = 3.25 \pm 0.20$. Another explanation for this enhanced rate of small-scale flare activity in M-dwarf stars could lie in the reconnection process itself. As was discussed in Chapter 2.2, Sweet-Parker reconnection may be the cause. Tsuneta & Katsukawa (2004) suggested that low energy (pico-/nano-)flares may occur more favourably via Sweet-Parker reconnection (instead of Petschek processes). If such flare stars have lower Lundquist numbers (i.e., higher plasma resistivity) with respect to the Sun, then this may help explain the enhanced nanoflare rates found in this study. The mostly convective atmosphere of these flare stars may be able to modify the underlying Lundquist number, allowing for enhanced low-energy nanoflare rates via Sweet-Parker reconnection, but not modifying the rates of the higher energy events that will proceed (as normal) via Petschek reconnection processes.

This enhanced nanoflare activity may also be linked to the dynamo in these stars. The M-stars in this study sit on the boundary of fully convective atmospheres. While the spectral sub-type where full convection begins is still under debate, estimates are in the range M3 and above (Wright & Drake, 2016) to more recent studies suggesting M2.1 to M2.3 (Mullan & Houdebine, 2020). Fully convective stars lack the tachocline between convective and radiative zones which powers the solar dynamo. A dynamo powered by helical turbulence is believed to operate in these fully convective stars (Durney et al., 1993; Browning, 2008;

Pipin & Seehafer, 2009). This may operate in tandem with the enhanced Sweet-Parker reconnection, through altering the Lundquist number. Investigating the power-law indices of nanoflare activity signatures for stars either side of this convective boundary (i.e., M0 to M4) was the focus of the next Chapter, to determine what role the convective boundary plays, and to determine the source of this enhanced activity.

STELLAR NANOFLARES AND THE LINK TO CONVECTIVE ATMOSPHERES

The content of this chapter is adapted from work which is being prepared for submission. It has been modified to fit within the confines and structure of this thesis, with the majority of the introduction and methods moved to the appropriate chapters. Some sections have been expanded.

6.1 INTRODUCTION

Small-scale magnetic reconnection in the form of nanoflares was observed in seemingly quiescent, fully convective M-dwarf stars in Chapter 5. Displaying a histogram of nanoflares as a function of their energy revealed power-law slopes that greatly exceeded the previous power-law indices seen for both solar nanoflares and solar/stellar flares at higher energies. The reason for the enhanced nanoflare power-law indices for M dwarfs was not known, but it was theorised that the fully convective nature of these stars may be responsible.

As discussed in Chapter 2.2, while solar-like stars have a combination of convective and radiative zones bridging their core and visible surface, some stars operate in a fully convective manner. The change from a partially to fully convective atmosphere has been related to the convective boundary or ‘tachocline divide’ (Browning, 2008). Wright & Drake (2016) estimate that this divide occurs in M-dwarf stars around M3V and beyond, with recent studies suggesting a more precise transition at approximately M2.1–2.3V (Mullan & Houdebine, 2020).

Convection is a primary driver of magnetic reconnection in stars (Pedersen et al., 2017). As magnetic reconnection is the driving force behind flares, changes to the convective nature of a star have important implications for the resulting flare dynamics. Fully convective stars lack a tachocline, where the radiative interior of the star meets the convective exterior (Spiegel & Zahn, 1992). The tachocline is believed to be responsible for the magnetic dynamo, hence

driving magnetic reconnection processes in solar-like stars (Parfrey & Menou, 2007). In stars with a fully convective atmosphere, the dynamo is theorised to be driven by helical turbulence (Durney et al., 1993; Browning, 2008; Pipin & Seehafer, 2009), but this theory is still under debate. Indeed, Wright & Drake (2016) and Wright et al. (2018) investigated the relationship between stellar rotation and activity levels for fully-convective late M-type dwarf stars. They found that the rotation/activity relationship for fully convective stars was almost indistinguishable from partially convective stars, suggesting that the activity levels of fully convective stars may somehow be driven by a solar-like dynamo.

Returning to the results of Durney et al. (1993), Browning (2008) and Pipin & Seehafer (2009), it is possible to hypothesise that the enhancement of nanoflaring rates is linked to the change in the convective nature of these stars, and hence to the consequent changes induced in the helical dynamo processes. As discussed in Chapter 5, one alternative explanation for the enhanced small-scale reconnection may be a result of fully convective stars having plasma with a higher resistivity value (Mohanty et al., 2002), which lowers the associated plasma Lundquist numbers. Small-scale flaring has been shown to occur more favourably via Sweet-Parker reconnection (Tsuneta & Katsukawa, 2004), and the rate of Sweet-Parker reconnection is inversely connected to the plasma Lundquist number, leading to enhanced nanoflaring in stars with low plasma Lundquist numbers. If nanoflare rates are enhanced in fully convective stars, then investigating whether this is due to the change in dynamo, or down to the plasma resistivity, would answer important questions regarding the dynamo physics in operation in these stars.

6.2 BACKGROUND TO PREVIOUS STATISTICAL STELLAR NANOFLARE ANALYSIS

To examine the role of convection in the nanoflare activity, I examined a range of M dwarf sub-types. As in Chapter 5, this study utilised observations from the Next Generation Transit Survey (NGTS; Wheatley et al., 2018), due to its high cadence and large datasets which make it well suited for this statistical study. After selecting similar magnitudes,¹ avoiding blended sources, and ensuring TIC matching, five stars for each spectral sub-type were found, consisting of the types M0V, M1V, M2V, M2.5V, M3V, and M4V. The stellar properties (NGTS identifier, RA/Dec, magnitude, etc.) of these candidates are provided in Table 6.2.

¹ These magnitudes were around 13, as in Chapter 5.

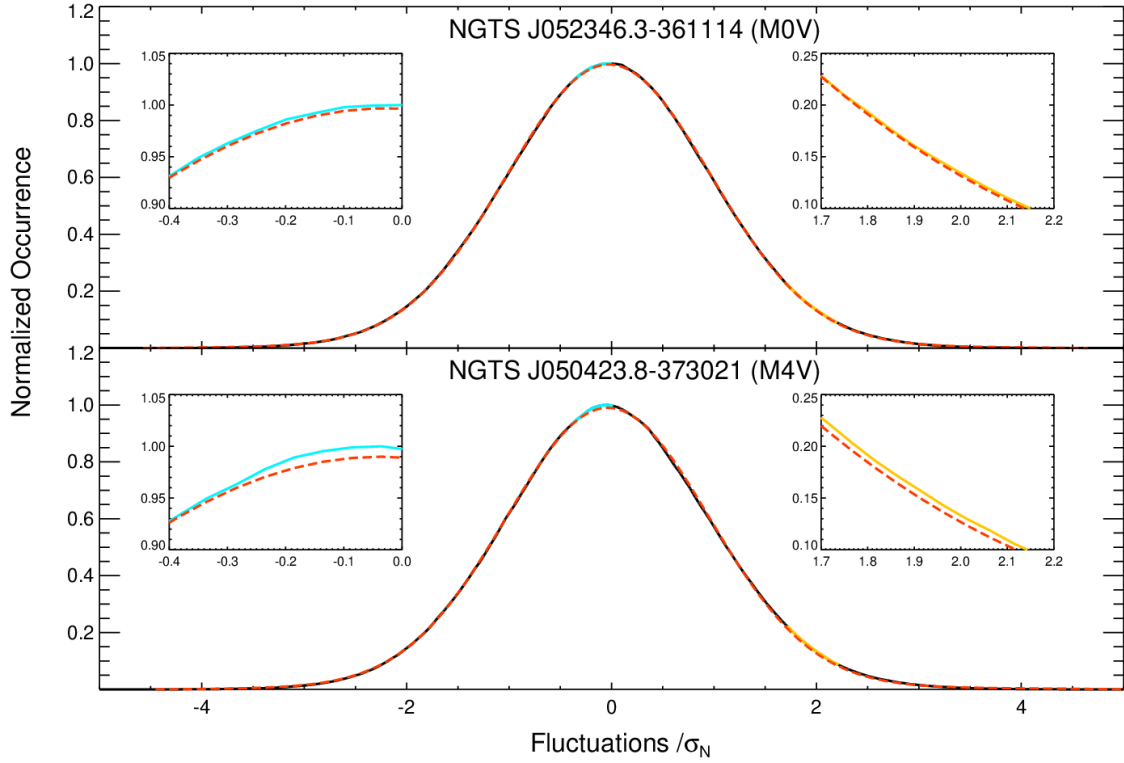


Fig. 6.1 Histograms of intensity fluctuations, each normalised by their respective standard deviations, σ_N , for the NGTS J052346.3-361114 (M0V-type; top panel) and NGTS J050423.8-373021 (M4V-type; lower panel) lightcurves. A standardised Gaussian profile is overplotted in each panel using a dashed red line for reference. The M4V-type distribution has a negative median offset with respect to the Gaussian, in addition to elevated occurrences at $\sim 2 \sigma_N$, which is consistent with the statistical signatures of nanoflare activity. On the other hand, the M0V-type intensity fluctuations provide effectively zero negative median offset, and no elevated occurrences at $\sim 2 \sigma_N$. This is inconsistent with clear statistical signatures of nanoflare activity, with the resulting distribution remaining more consistent with the presence of photon-based shot noise. Zoomed insets highlight the ranges spanning $-0.4 \leq \sigma_N \leq 0.0$ and $1.7 \leq \sigma_N \leq 2.2$, where negative median offsets and occurrence excesses, respectively, are clearly visible for the M4V stellar source. For improved clarity, the blue and gold lines display the corresponding distributions in each zoomed panel.

Only one suitable M5V star with TIC-derived stellar parameters could be identified, and no sub-types later than this were found. The intrinsic brightness of M-dwarfs decreases with increasing sub-type (Yang et al., 2017), leading to difficulty in identifying suitable candidate stars with the desired brightness properties. Future investigations of post-M4V stars may be fruitful, but identifying a suitable number of candidates may prove difficult with existing instrumentation. Hence, the study was limited to the range of M0V – M4V, where there were multiple candidates available for comparison. This range also overlapped well with the

Spectral Type	Median offset (σ_N)	Fisher Skewness	ζ ratio	Kurtosis
M0V	-0.040 ± 0.001	0.004 ± 0.002	1.740 ± 0.005	0.128 ± 0.010
M1V	-0.040 ± 0.001	0.008 ± 0.004	1.746 ± 0.008	0.180 ± 0.013
M2V	-0.030 ± 0.001	0.003 ± 0.011	1.766 ± 0.010	0.196 ± 0.037
M2.5V	-0.050 ± 0.000	0.019 ± 0.003	1.739 ± 0.004	0.227 ± 0.072
M3V	-0.050 ± 0.000	0.025 ± 0.004	1.750 ± 0.006	0.180 ± 0.017
M4V	-0.050 ± 0.000	0.051 ± 0.014	1.754 ± 0.010	0.267 ± 0.029

Table 6.1 Averaged characteristics of the statistical properties by each spectral type.

predicted convective boundary (M2.1–2.3V; Mullan & Houdebine, 2020), making it suitable for the study of the role convection plays in the resulting nanoflare activity.

To ensure these MV stars had similar activity levels, the stellar rotation was estimated. As discussed in Section 3.2.1, the stellar rotation period can be estimated with Lomb-Scargle periodograms. The majority of the stars did not exhibit candidate rotation periods less than 30 days, indicating that they belong to the same population of slow-rotating stars, and hence had similar activity properties. Only the M2V star NGTS J045136.3-321720 deviated from this, with a possible rotation period of ~ 21 days. While the associated macroscopic flare activity was elevated with respect to the other partially convective stars (see Table 6.2), this star still exhibited lower activity than any fully-convective star. Additionally, it exhibited no associated nanoflare activity. As such, this possibly increased rotation rate was deemed acceptable.

The lightcurves were processed identically to those in Chapter 5, i.e., following the methodology described in Section 3.2. This was the removal of macroscopic flares, nights with high uncertainties, the night-by-night detrending, and the Z -score normalisation.

Sp Type	NGTS ID	GAIA ID	TIC ID	RA	Dec	Mass (M_{\odot})	Radius (R_{\odot})	Luminosity (L_{\odot})	Distance (pc)	Approximate Flare Rate per Hour	Magnitude
M0V	NGTS J23315.1-385757	6538313140873424640	224245757	353.312913	-38.965817	0.487596	0.489513	0.04772778	100.33	0.0123635	13.10
M0V	NGTS J045221.8-312424	4874911889552910000	1310695	73.090834	-31.406834	0.597557	0.611732	0.07879962	137.421	0.0154544	13.26
M0V	NGTS J052346.3-361114	4822374303400198144	167745038	80.942877	-36.187338	0.566358	0.574022	0.07396496	123.332	0.00618174	13.04
M0V	NGTS J061346.1-362248	2885025813007881728	267248553	93.442125	-36.380098	0.585147	0.596407	0.07490093	137.363	0.0123635	13.24
M0V	NGTS J061054.6-370701	2884885281677800448	300200809	92.72739	-37.116954	0.575812	0.585163	0.06398756	112.406	0.0401813	12.99
M1V	NGTS J233248.3-382456	6538532356004046592	224244565	353.201262	-38.415564	0.542372	0.546805	0.05344092	90.7535	0.0123635	12.97
M1V	NGTS J051250.6-361938	4821058497219315328	14173066	78.210928	-36.327354	0.596268	0.61012	0.06084004	201.14	0.0123635	14.16
M1V	NGTS J052652.1-373123	4821222942926810752	192785958	81.717213	-37.523125	0.567364	0.575197	0.05580399	83.9291	0.00309087	13.57
M1V	NGTS J233034.7-373312	2310510165491596672	183536494	357.644544	-37.553375	0.506923	0.509045	0.04646323	83.9291	0.00927262	12.84
M1V	NGTS J111257.7-331216	5403344977522967424	23438898	168.240279	-33.20455	0.460039	0.462724	0.03412572	73.1095	0.0185452	12.92
M2V	NGTS J045136.3-321720	4874656837214833664	1309522	72.901424	-32.288803	0.56	0.806538	0.1124733	247.955	0.0278178	14.32
M2V	NGTS J050254.6-352000	482506629419253632	1526841	75.72729	-35.333409	0.469279	0.471581	0.03436859	69.7222	0.0185452	12.72
M2V	NGTS J051926.5-253444	2957763042671388416	30960826	79.860208	-25.578811	0.460925	0.463568	0.03302738	90.6288	0.00927262	13.49
M2V	NGTS J053614.4-353309	4821870486556489216	24612475	84.059908	-35.552443	0.501857	0.503859	0.03897486	90.6101	0.0154544	13.2
M2V	NGTS J062005.7-372555	5575203489668007936	393481864	95.023721	-37.431899	0.400268	0.407808	0.02305492	87.7167	0	13.83
M2.5V	NGTS J045008.8-362401	4818804257863710336	77369893	72.536742	-36.400372	0.545633	0.550421	0.05525498	118.868	0.0494539	13.07
M2.5V	NGTS J050359.5-305327	4876285488813663232	1439071	74.755373	-30.999599	0.456069	0.458954	0.02748212	54.6863	0.00618174	12.8
M2.5V	NGTS J045901.2-305958	4875598534564509312	1535810	75.997888	-30.890807	0.380031	0.389898	0.01965184	68.7496	0.0710901	13.65
M2.5V	NGTS J050810.8-371850	4823535318959536256	14084620	77.044884	-37.313753	0.514811	0.517217	0.03755042	59.1582	0.0309087	12.29
M2.5V	NGTS J061516.4-360818	2885223381503521536	267327257	93.818249	-36.138454	0.496041	0.497965	0.03437556	118.666	0.0278178	13.99
M3V	NGTS J035219.1-311459	4886786408973741568	166804322	58.079759	-31.249846	0.548884	0.549588	0.03602405	123.566	0.0216561	13.63
M3V	NGTS J050230.0-355301	4824660428592359552	13982951	75.624229	-35.883643	0.308218	0.327511	0.01185441	41.1162	0.00927262	13.1
M3V	NGTS J051925.5-235535	2958246827787260032	30961390	79.856241	-23.926311	0.564934	0.572365	0.04099549	131.705	0.0865444	13.94
M3V	NGTS J052116.1-322429	4826608831916384640	78053729	80.317094	-32.357958	0.401901	0.409266	0.01826787	39.3307	0.0494539	12.52
M3V	NGTS J000722.8-293528	2320750123439437184	12418184	1.845141	-29.5912	0.22872	0.257223	0.007069197	40.1093	0.0216561	13.44
M4V	NGTS J035624.7-311140	4886831592030178944	166869904	59.102836	-31.194413	0.402508	0.409808	0.01474621	37.7653	0.10509	12.7
M4V	NGTS J044312.0-322643	4874430475258301184	170882537	70.800028	-32.445142	0.512283	0.514585	0.02822354	21.8796	0.0834535	12.6
M4V	NGTS J045519.0-321222	4873878176823736192	1357792	73.829291	-32.206129	0.170431	0.201449	0.003005163	21.8796	0.0865444	13.72
M4V	NGTS J050423.8-373021	482347646072785728	14001734	76.099199	-37.505698	0.434448	0.438763	0.02066878	0	0.148362	12.42
M4V	NGTS J2341092-363819	2311548448064869120	224276435	355.288136	-36.638609	0.253768	0.279818	0.005977345	38.7917	0.0649083	13.79

Table 6.2 The stellar parameters for the stars used in the analysis. The stellar masses, radii, and luminosity data is from the TESS Input Catalog release V8. (Stassun et al., 2018)

The number of macroscopic flares removed were used to calculate approximate flare rates for the M stars, which are displayed in Table 6.2. To ensure consistency, these filtering steps employed were identical to those used in Chapter 5, with the filtered lightcurves subsequently cropped to 97 060 datapoints each to match the number statistics to Chapter 5. This allowed the nanoflare simulations to be re-used due to identical number statistics, filtering techniques, desired α (power-law index) and τ (e -folding time) ranges, in addition to sharing the specific NGTS-modelled noise characteristics.

6.3 ANALYSIS AND DISCUSSION

To investigate possible changes in nanoflare properties with spectral type, the same statistical and Fourier properties as before were examined. As outlined in Chapter 2.2, nanoflares give rise to two distinct statistical signatures, which can be used to diagnose stellar nanoflare activity. Two example histograms of intensity fluctuations are shown in Figure 6.1 for stars NGTS J052346.3-361114 (M0V spectral type; top panel) and NGTS J050423.8-373021 (M4V spectral type; lower panel). From Figure 6.1 it is clear that the opposite ends of the included spectral types, which lie on either side of the predicted convective boundary, demonstrated distinctly different statistical signatures. The M0V star exhibited very weak and inconclusive nanoflare signatures, with little negative median offset and no elevated intensity fluctuations at $\sim 2 \sigma_N$. Conversely, the M4V star showed a clear excess of $\sim 2 \sigma_N$ intensity fluctuations in addition to a prominent negative median offset. The signatures of the M4V star shown in Figure 6.1 are consistent with the positive stellar nanoflare identifications from Chapter 5. The distinct increase of visible nanoflare signatures within the expected regime of full convection was a promising sign that the enhanced nanoflare rates were related to the underlying convective nature of the star.

These examples illustrated in Figure 6.1 clearly identify the vastly different nanoflare signatures present at either end of the investigated range of spectral sub-types. Interestingly, the small dip in the Gaussian at $-0.90 \sigma_N$, as seen in Chapter 5, was not seen in these histograms. The explanation for this dip remains unclear. To better examine the change in nanoflare activity across the given spectral range (M0V – M4V), the derived properties were averaged according to their specific spectral type following the bootstrap method documented by Efron et al. (1979). As these features are dependent on the underlying stellar plasma conditions, straightforward averaging over multiple stars is challenging due to uncertain behaviour of the standard errors of the given parameters. Hence, bootstrapping techniques are used extensively throughout the physical sciences to better calculate confidence intervals

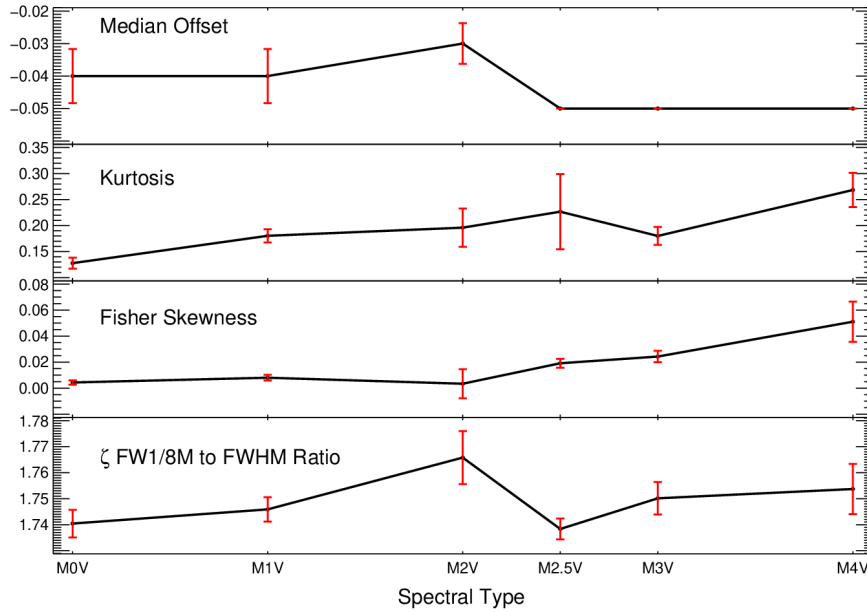


Fig. 6.2 The bootstrap-averaged statistical properties of the intensity fluctuation histograms for each stellar classification. Beyond the convective boundary, at approximately M2.5V, sub-types begin to exhibit statistical signatures that are consistent with the presence of nanoflare activity, including larger median offsets (top panel), increasing levels of kurtosis (second panel from top), and higher Fisher skewness values (second panel from bottom). The ζ (FW $_{\frac{1}{8}}M$ -to-FWHM ratio) values do not vary significantly as a function of stellar classification. However, this is likely due to the interplay between the power-law index of the nanoflares and the duration of the e -folding timescales, which are able to counteract the statistical effects of one another.

for data following non-standard or unknown distributions (Simpson & Mayer-Hasselwander, 1986; Desmars et al., 2009; Yao et al., 2017).

Figure 6.2 shows the change in the median offset, kurtosis, Fisher skewness, and ζ values, as a function of spectral sub-type. The results are also tabulated in Table 6.1. As can be seen in Figure 6.2, there was a distinct change in the nanoflare statistical signatures as a function of spectral sub-type, suggesting that the convective boundary may play an important role in the generation of efficient nanoflare conditions. M2.5V (and beyond) stars exhibited distinct nanoflare statistical signatures that were consistent with those seen in the previous chapter. Specifically, the average median offset for the pre-M2.5V stars exhibited a large spread around a weakly offset value (upper panel of Figure 6.2), while the post-M2.5V stars demonstrated a larger consistent offset magnitude (with less uncertainty) of approximately $-0.05\sigma_N$.

The Fisher skewness value was effectively zero for pre-M2.5V stars (second panel from bottom in Figure 6.2), suggesting no, or very weak, nanoflare activity. From M2.5V onward,

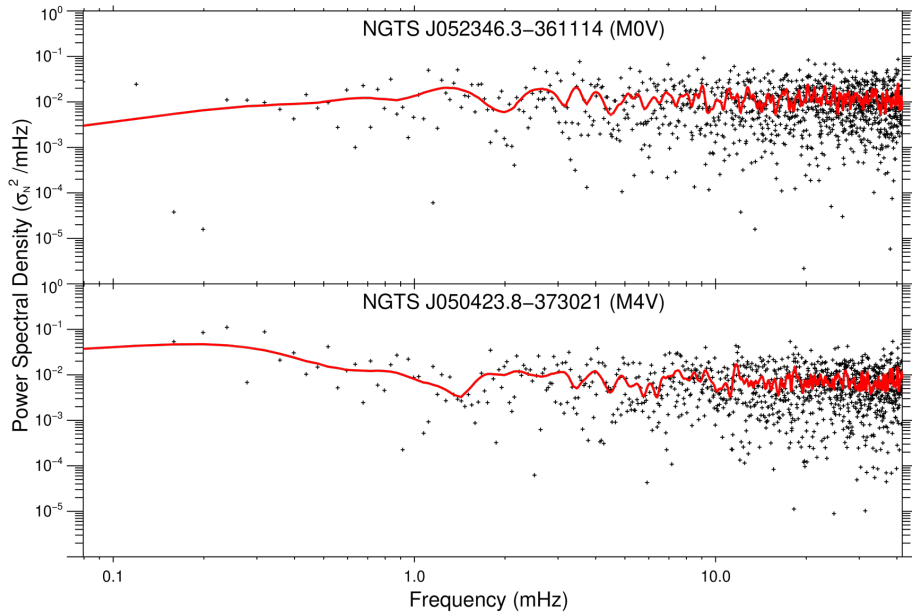


Fig. 6.3 The Fourier power spectral densities (PSDs) for example M0V (upper panel) and M4V (lower panel) stellar sources, displayed in normalised units of σ_N^2/mHz . The crosses in each panel depict the individual power values as a function of frequency, while the solid red line reveals a trendline calculated over ± 6 frequency elements (± 0.478 mHz). It can be seen that the PSD for the M0V star is relatively flat, with small-amplitude power enhancements in the range 3 – 10 mHz, which is consistent with typical p -mode oscillations. Conversely, the PSD for the M4V star exhibits a clear enhancement of spectral energy at lower frequencies, resulting in a spectral slope of $\beta = -0.57 \pm 0.05$ that begins at 0.32 ± 0.04 mHz, followed by numerous power peaks in the range of 1 – 10 mHz. This is consistent with the presence of both nanoflare activity and p -mode oscillations.

there was a clear increasing trend in the Fisher skewness value of the fluctuation distribution, with the M4V sub-type displaying a Fisher skewness equal to 0.051 ± 0.014 , providing strong evidence for the presence of nanoflares.

The values of kurtosis (second panel from top in Figure 6.2) showed a clear trend, whereby changes in spectral type from M0V to M4V produce increased levels of statistical kurtosis in the corresponding fluctuation distributions. It appears that the degree of statistical kurtosis is influenced directly by the spectral sub-type, with more fully-convective M4V stars demonstrating heightened levels of kurtosis compared with their M0V counterparts. It must be noted that the M3V sub-type does show a dip in its associated kurtosis value, which cannot presently be explained.

There was no clear trend visible in the corresponding ζ values (lower panel of Figure 6.2) as a function of spectral sub-type. It must be remembered that the ζ value is a measure of the deviation away from a standard Gaussian distribution, which has a value of $\zeta = 1.73$. As discussed in Jess et al. (2019), increased nanoflare decay timescales (i.e., larger τ values)

result in broader tails of the intensity fluctuation distributions, hence giving rise to $\zeta > 1.73$. Conversely, large power-law indices help reduce the widths of the tails in the intensity fluctuation distributions due to the superposition of positive intensity fluctuations (e.g., new nanoflares) superimposed on top of decaying (i.e., negative) intensity fluctuations, resulting in $\zeta < 1.73$. As such, the interplay between the power-law index and the nanoflare e -folding time produces the specific value of ζ measured. The relatively consistent values of ζ found across the spectral range M0V – M4V may therefore result from an increased nanoflare rate expected for M4V stars being negated by an increase in the associated decay timescales of the resulting nanoflares, i.e., a larger α term coupled with longer τ values.

Comparing the intensity fluctuation statistical measurements (see, e.g., Table 6.1 and Figure 6.2) to those produced by the Monte Carlo nanoflare simulations documented in Chapter 5, it was possible to estimate both the power-law index, α , and the nanoflare decay timescale, τ , by establishing which combination of flare characteristics best matches the observational signatures. For pre-M2.5V stars, it was not possible to establish values for the power-law index and e -folding time that were self-consistent with the Monte Carlo models. For example, it was possible to find self-similarity between the observational and model power-law indices, but this resulted in decay timescales that were incompatible and inconsistent. As a result, I was unable to define nanoflare characteristics for pre-M2.5V stars, suggesting that nanoflare activity was very weak (or not present) on these specific stellar sub-types.

The statistical parameters for the M2.5V, M3V and M4V stars, which were believed to be beyond the convective boundary and therefore could be described as fully convective, exhibited values consistent with the power-law indices of $\alpha = 2.25 \pm 0.25$ or $\alpha = 3.00 \pm 0.25$, $\alpha = 2.25 \pm 0.20$ or $\alpha = 3.00 \pm 0.20$, and $\alpha = 2.30 \pm 0.20$ or $\alpha = 3.10 \pm 0.20$, alongside the e -folding timescales of $\tau = 200 \pm 100$ s, $\tau = 200 \pm 100$ s, and $\tau = 450 \pm 50$ s, respectively (see Table 6.3_a). As discussed in Chapters 3.2.4 and 5, the approximate symmetry of the statistical distributions about their peak values leads to ambiguity in the derived power-law indices (see, e.g., the bands of similar values shown in each panel in Figure 6.5). As a result, it is possible to map each sub-type onto two distinct solutions for the power-law index. Irrespective of this ambiguity, both sets of possible nanoflare conditions found were highly active (i.e., $\alpha > 2$), in stark contrast to the effectively zero statistical nanoflare signals observed in the pre-M2.5V spectral sub-types. The larger uncertainty in the M2.5V power-law indices were due to the larger uncertainty associated with the kurtosis value for these spectral sub-types. M2.5V stars are at the boundary of predicted full convection, so a larger

(a) Nanoflare parameters per spectral type, derived from statistical properties of Monte-Carlo modelled nanoflare timeseries. The approximately symmetrical distribution of statistical properties leads to an ambiguity in the derived power-law indices, hence α_1 and α_2 .

Spectral Type	α_1	α_2	$\tau(s)$
M2.5V	2.25 ± 0.25	3.00 ± 0.25	200 ± 100
M3V	2.25 ± 0.20	3.00 ± 0.20	200 ± 100
M4V	2.30 ± 0.20	3.10 ± 0.20	450 ± 50

(b) Nanoflare parameters per spectral type, derived from Fourier properties of Monte-Carlo modelled nanoflare timeseries. There is no ambiguity in the derived power-law indices.

Spectral Type	α	$\tau(s)$
M2.5V	3.00 ± 0.15	200 ± 100
M3V	3.00 ± 0.15	250 ± 100
M4V	3.10 ± 0.15	450 ± 50

Table 6.3 Nanoflare parameters per spectral type, derived from statistical and Fourier properties of Monte-Carlo modelled nanoflare timeseries respectively.

spread in their nanoflare properties was expected if full convection is the cause of the spectral ‘break’ in associated power-law indices.

Interestingly, the M4V stars displayed evidence for longer e -folding timescales and larger power-law indices when compared to their M2.5V and M3V counterparts. As discussed above, this is likely an explanation for the relatively constant ζ values throughout the spectral sub-type range, whereby the statistical effects of higher power-law indices are negated by the slower decay timescales associated with those stars (Jess et al., 2019). The specific value for the e -folding timescale of the M2.5V and M3V stars of $\tau = 200 \pm 100$ s is consistent with the M2.5 and M3V results in Chapter 5. Overall, the changes in the statistical parameters indicate that post-convective boundary M-dwarf stars (i.e., M2.5V and beyond) exhibit greatly enhanced stellar nanoflare activity when compared to the pre-convective boundary M-dwarfs that show little-to-no evidence for nanoflare activity.

As highlighted in Chapter 5, the examination of Fourier signatures, which are derived directly from the stellar lightcurves, can help disambiguate any derived nanoflare characteristics and further substantiate the evidence for specific activity levels. Following the same procedure as before, PSDs were derived from the stellar timeseries. The longest contin-

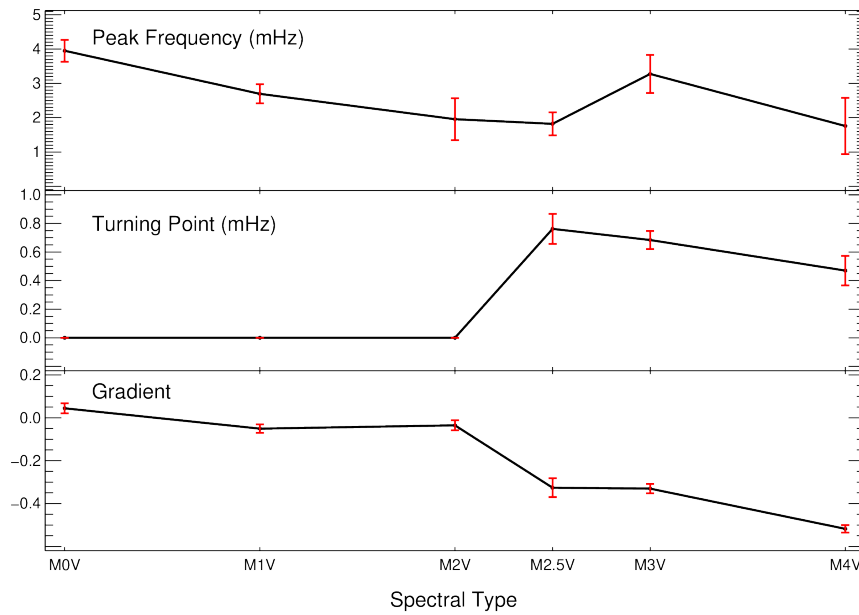


Fig. 6.4 The bootstrap-averaged properties of the Fourier power spectral densities (PSDs) across each spectral type. The upper panel displays the peak frequency values (in mHz), which are found to reside within the range of approximately 1 – 4 mHz. This is consistent with both nanoflare activity and p -mode oscillations, and therefore cannot be used as an indicator of nanoflare activity by itself. The middle and lower panels display the turning point frequencies (in mHz) and subsequent spectral slopes, respectively, as a function of stellar classification. When compared to the Monte Carlo nanoflare simulation outputs depicted in Figure 6.5, the distinct jump in turning point frequency and spectral gradient at the convective boundary (M2.5V) provides clear evidence of prominent nanoflare activity in M2.5V – M4V stellar sources.

uous timeseries (i.e., the longest uninterrupted series of frames) common to all stars was 2095 datapoints, slightly shorter than the 2316 consecutive frames employed in Chapter 5. This resulted in the frequency resolution being slightly reduced from $\Delta f = 0.0356$ mHz to $\Delta f = 0.0398$ mHz. In order to readily compare the observational PSDs to those calculated from the Monte Carlo nanoflare models, the Fourier signatures needed to be re-calculated adhering to the new frequency resolution. Hence, utilising the new frequency resolution, I re-computed the PSDs and corresponding ‘heat map’ of the simulated Fourier properties (c.f., Figure 5.8 of Chapter 5) as a function of both the nanoflare power-law and e -folding time. The recalculated heat map is displayed in Figure 6.5. Due to the change in frequency resolution being a relatively small value (0.0042 mHz), no noticeable deviations from Figure 6.5 and the original distribution Figure 5.8 can be seen, with the trends identical in both studies. This is likely a result of the Fourier nanoflare trends being relatively broad in frequency with peak values sufficiently away from the lowest and highest (i.e., Nyquist) frequencies of

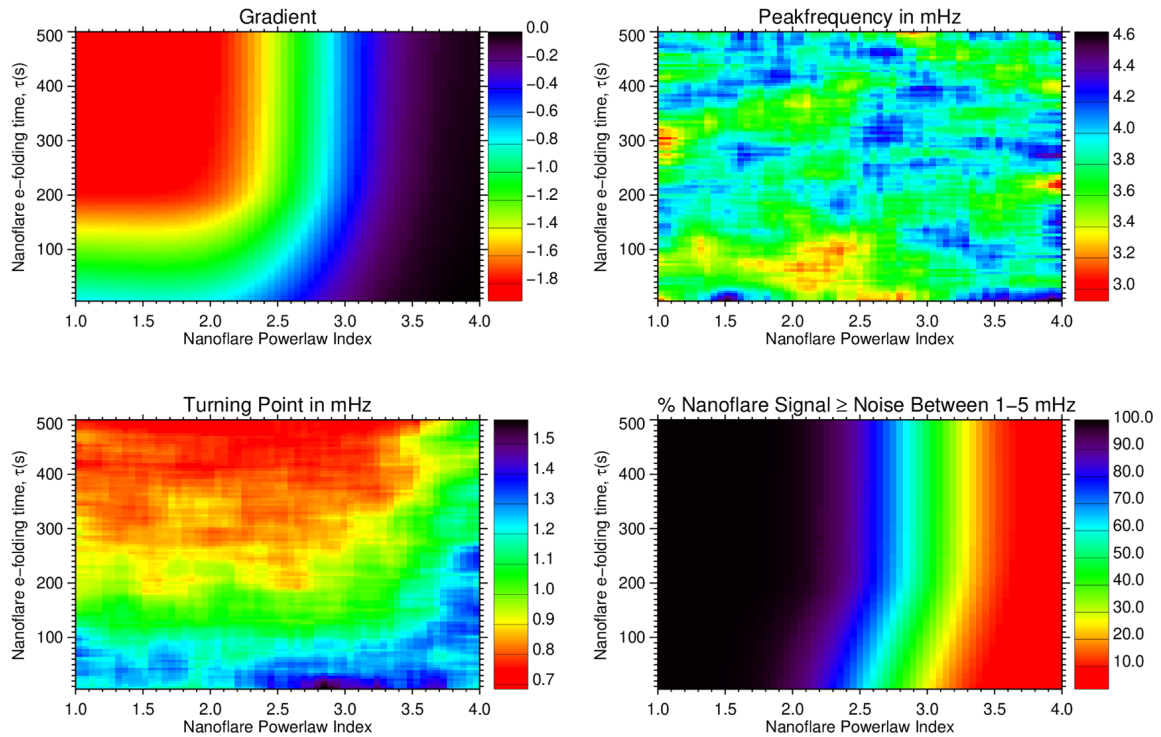


Fig. 6.5 A reproduction of Figure 5.8 from Chapter 5 with the constituent PSDs re-calculated for 2095 datapoints to match the longest continuous timeseries used in the present study. The primary peak frequencies (lower-left), spectral slopes (upper-left), dominant frequencies following detrending (upper-right), and the percentage of nanoflare power above the noise floor in the range of 1 – 5 mHz (lower-right), is displayed as a function of the power-law index, α , and the decay timescale, τ , used to generate the synthetic timeseries. While a few individual values differ, the overall trends and the magnitude of the derived signals are consistent with the PSD properties generated from 2316 datapoints and reported by Dillon et al. (2020).

the timeseries, hence are not significantly affected by very small changes in the underlying frequency resolution.

As with the statistical signatures shown in Figure 6.2, there are dramatic differences in the Fourier properties between M0V and M4V stars. As seen in Figure 6.3, the M0V displayed an effectively flat power spectrum suggesting that no nanoflare signal was present. This was contrasted by the M4V star, which demonstrated a spectral slope of $\beta = -0.57 \pm 0.05$ between the frequencies $\sim 0.3 - 6.0$ mHz. In Figure 6.3, the black crosses represented the individual frequency-dependent power measurements, while the solid red line depicts a

Spectral Type	Gradient	Turning Point (mHz)	Peak frequency (mHz)
M0V	$+0.044 \pm 0.023$	0.000 ± 0.000	3.952 ± 0.320
M1V	-0.051 ± 0.019	0.000 ± 0.000	2.695 ± 0.278
M2V	-0.035 ± 0.022	0.000 ± 0.000	1.956 ± 0.611
M2.5V	-0.326 ± 0.044	0.762 ± 0.105	1.821 ± 0.338
M3V	-0.330 ± 0.022	0.684 ± 0.063	3.276 ± 0.557
M4V	-0.518 ± 0.018	0.467 ± 0.103	1.757 ± 0.822

Table 6.4 Average characteristics of the Fourier PSD properties by each spectral type.

trendline established over ± 6 frequency elements (± 0.478 mHz).² In the lower panel of Figure 6.3, the PSD slope was consistent with enhanced rates of stellar nanoflare activity, which began at the ‘turning point’ of 0.32 ± 0.04 mHz. As discussed in Chapter 5, the turning point was defined as the initial peak before the gradual reduction in Fourier power with increasing frequency. It must be noted that both PSD plots shown in Figure 6.3 (i.e., for M0V and M4V spectral types) exhibited numerous power peaks in the range of 1 – 10 mHz, consistent with both the stellar nanoflare signatures seen in Chapter 5 and the presence of *p*-mode oscillations generated in the convective layers of M-dwarf stellar sources (M-dwarf stars are believed to exhibit solar-like oscillations, hence *p*-modes synonymous with the typical solar frequency range; Rodríguez-López et al., 2014; Rodríguez et al., 2016). As the entire range of spectral types included in this study (M0V – M4V) were expected to exhibit *p*-mode oscillations, the peak frequencies within this interval were not conclusive evidence alone of nanoflare activity.

The averaged Fourier properties (following bootstrap procedures) per spectral type are shown in Figure 6.4, and tabulated in Table 6.4. As with the averaged statistical signatures shown in Figure 6.2, there was a marked change in Fourier features consistent with nanoflare activity for spectral classifications M2.5V and beyond. Evidence for this is shown in the averaged PSD spectral gradient (lower panel of Figure 6.4), where pre-M2.5V stars have relatively flat spectral slopes ($\beta \sim 0$), yet stellar sources beyond the convective boundary at M2.5V demonstrate increased magnitude spectral slopes in the range of $-0.6 \leq \beta \leq -0.3$. Note that the peak frequency values (upper panel of Figure 6.4) were relatively consistent across all M-dwarf stellar sources, approximately in the range of 2 – 4 mHz. As discussed

² This trendline was calculated by applying Gaussian smoothing, as discussed in Section 3.2.3

above, this alone does not constitute evidence of nanoflare activity since all of these sources were expected to demonstrate p -mode oscillations spanning that particular frequency interval (Guenther et al., 2008; Rodríguez-López et al., 2014).

The corresponding ‘turning point’, where the spectral slopes were observed to begin, was, of course, equal to zero for the pre-M2.5V stars since they do not exhibit any associated spectral slopes (middle panel of Figure 6.4). However, for spectral classifications beyond M2.5V, where the stars were believed to be fully convective, a relatively constant value (when errors are included) in the range of $0.3 \leq f \leq 0.9$ mHz was found, which is consistent with the results in Chapter 5. In those nanoflare simulations, an increased flare decay rate (i.e., a longer τ value) gave rise to a decreased frequency of the Fourier turning point. Examination of the middle panel of Figure 6.4 shows that while the turning point frequencies were distinctly different from the pre-M2.5V stars, there did appear to be tentative evidence that the average turning point frequency decreases across the M2.5V, M3V, and M4V spectral types. This is further evidenced in Table 6.4, where the turning points of the M2.5V, M3V, and M4V stars were computed as 0.762 ± 0.105 mHz, 0.684 ± 0.063 mHz, and 0.467 ± 0.103 mHz, respectively. The evidence suggests that the e -folding timescales associated with the M4V stars are longer than their M2.5V counterparts, consistent with the intensity fluctuation statistical signatures discussed above.

Comparing the derived Fourier properties to the heat maps shown in Figure 6.5, it was possible to estimate the power-law indices and decay timescales for each of the M2.5V, M3V, and M4V stellar types that show clear evidence for nanoflare activity (see Table 6.3_b). These gave power-law indices of $\alpha = 3.00 \pm 0.15$, $\alpha = 3.00 \pm 0.15$, and $\alpha = 3.10 \pm 0.15$, alongside nanoflare e -folding timescales of $\tau = 200 \pm 100$ s, $\tau = 250 \pm 100$ s, and $\tau = 450 \pm 50$ s, for the M2.5V, M3V, and M4V spectral types, respectively. Importantly, these values were consistent with the statistical analysis, with the Fourier techniques providing additional benchmarks to validate the nanoflare properties extracted from the observational timeseries and resolve the ambiguity in power-law index arising from the statistical analysis. In contrast to the statistical mapping, the derived Fourier parameters of the M3V stars were consistent with a marginal e -folding time enhancement compared to the M2.5V classifications. This was likely related to the same physical processes that caused enhanced e -folding timescales in the M4V star. However, this was difficult to ascertain due to the relatively large errors in determining the plasma decay rate over the entire stellar surface.

Combining the Fourier and statistical analyses (see Table 6.5), I found that the fully convective M2.5V and M3V sub-types exhibited nanoflare power-law indices of $\alpha = 3.00 \pm 0.20$ and $\alpha = 3.00 \pm 0.18$, respectively. The M2.5V sub-types were consistent with a decay

timescale of $\tau = 200 \pm 100$ s, whereas the M3V stars displayed tentative evidence for a slightly enhanced e -folding timescale of $\tau = 225 \pm 100$ s. These e -folding timescales and power-law indices were values consistent with the similar M-dwarf spectral types discussed in Chapter 5. The M4V stars exhibited elevated power-law indices of $\alpha = 3.10 \pm 0.18$, with an increased decay timescale of $\tau = 450 \pm 50$ s, which may be related to Sweet-Parker reconnection processes. As was proposed by Tsuneta & Katsukawa (2004), small-scale pico/nano-scale flares occur more favourably via Sweet-Parker than Petschek reconnection (see Section 2.2.1). This would explain a discontinuity in the power-law relationship between nanoflares and their larger scale counterparts, which would remain driven by Petschek-like reconnection (Loureiro & Uzdensky, 2016). The Sweet-Parker reconnection process is inversely proportional to the square root of the plasma Lundquist number, which is itself inversely proportional to the plasma resistivity. As such, Sweet-Parker reconnection is more favourable in poorly conducting plasmas. The increased decay timescale of $\tau = 450 \pm 50$ s, found for the M4V sub-type alongside the associated increased power-law index of $\alpha = 3.10 \pm 0.18$, may be related to increased plasma resistivity, which matches expectations for mid-to-late M-dwarfs (mid M-dwarf sub-types should have decreased optical depths and increased plasma resistivities, a trend which continues to late M9 sub-types Mohanty et al., 2002).

It should be noted that there does not yet exist a statistically significant trend in these increased values of α and τ for the M4V stars. Despite the large difference in the τ values, their relatively high uncertainties mean this increased τ is within 3σ of the values for the M3 and M2.5V star. The α values were also contained within their errors, remaining within 1σ of one another. To determine if a statistically significant trend in these values exists, two things are needed. Firstly, multi-colour observations; the measurement of τ is highly dependent on the underlying plasma conditions, particularly temperature. A multi-band study looking at distinct spectral bands across the visible spectrum would allow for the measurement of individual signatures of different atmospheric heights and temperatures, and hence plasma conditions. This could allow for more precise determination of the underlying τ values related to these different plasma conditions. Secondly, sourcing M5V and later type stars; even with the current uncertainties, if this trend continues then it could be statistically significant to 3σ or beyond with sufficient later star types. These initial results highlight the need for further analysis and observation to determine if this behaviour is significant.

In contrast to the fully convective sub-types, pre-convective boundary M0V – M2V stars exhibited weak (if any) nanoflare signals, suggesting that fully convective stellar atmospheres lead to a large enhancement of nanoflare activity. These enhanced small-scale flare rates

in fully convective stars hold profound implications for the energy budgets of those stellar sources. The energy output of rapid and continuous nanoflares may be a major component of the overall stellar coronal energy budget: yet they are hidden within the noise envelope of the observations, and can only be extracted through use of large-scale statistical and Fourier analyses.

Due to the comparable magnitudes of these stars, there is a general downward trend in the intrinsic brightness with later star types. This does mean the effective noise floor lowers as we move to these later stars, which could be a factor in the measured nanoflare signals differing across stellar types. However, several of the fully convective stars have luminosities which are comparable to partially convective stars, and hence similar noise floors (see Table 6.2). Despite this no partially convective star exhibits a signal which is compatible with nanoflare activity, while all the fully convective stars exhibit nanoflare activity. This suggests that there is more at work than simply the change in noise floor causing the enhanced nanoflare activity observed in these fully convective stars. Future studies could source fainter partially convective stars as a further confirmation that no retrievable nanoflare signatures are present in these stars.

While the observed trend of fully convective stars exhibiting enhanced nanoflare activity is clear, the exact mechanism leading to this is still a matter of debate. While the Sweet-Parker hypothesis is plausible, there is also a potential issue. If enhanced nanoflare activity occurs in the corona, it would lead to enhanced heating of that plasma. Consequently, this would lower the resistivity and hence lower the rate of Sweet-Parker reconnection. This ‘feedback loop’ behaviour may reach some natural and stable equilibrium, but it may be necessary to incorporate additional theory to ensure the stability of this mechanism. Referring to the original nanoflare mechanism theorised by Parker (1988) may provide this. In that paper, Parker suggested random convective motion in the photosphere causes ‘shuffling’ and subsequent deformation and braiding of the photospheric footpoints of the coronal magnetic fields and consequently the generation of free energy. The coupling of the magnetic field lines between the photosphere and corona provides the framework to allow this free energy to flow into the corona. This energy is then dissipated in coronal current sheets, leading to small-scale reconnection. As such, enhanced heating leading to decreased resistivity would improve the magnetic coupling between these footpoints and the corona, consequently enhancing the flow of free energy available for nanoflare activity. One can imagine a combination of these scenarios, wherein the sympathetic transfer of hot plasma and free energy through these coupled fields regulates the resistivity and drives a stable rate of Sweet-Parker reconnection. To uncover the source of this enhanced activity in fully convective stars (and determine if a

statistically significant trend exists in further enhancement for M4V and later types), it's vital to obtain two sets of observations; multi-band photometry, and observations of later MV star types. The multi-colour observation of these stars will allow us to make a limited analysis of the change in nanoflaring properties across different wavelengths and consequently the contribution at different atmospheric heights. Comparing relative photospheric and coronal signatures could diagnose the underlying mechanism powering this enhanced nanoflare activity. This will also allow for more precise determination of the underlying τ across these different plasma conditions and temperatures, increasing the statistical significance of further trends in τ within the fully convective star sample. Secondly, sourcing M5V and beyond stars would allow the continuation of the trend in flare decay rate (if any) to be investigated. If later MV stars continue to exhibit enhanced activity it would support the Sweet-Parker reconnection theory, as it would suggest the enhanced resistivity is key. Ultimately, observations of older MV stars, and across multiple photometry bands will need to be coupled with detailed physical modelling to try and uncover what changes in these stars are driving their nanoflare behaviour. These multi-band observations would need to address several key challenges of this analysis, to ensure suitable number statistics and Fourier resolution are obtained. Simultaneous observations³ across multiple colour-bands in the optical ($\approx 400\text{-}900\text{ nm}$) would be required. Filters such as g' , r' , i' , z' would allow for investigation across the optical and also into the infrared in multiple bins. A cadence and exposure in the $\approx 10\text{s}$ range would be preferential, to ensure the short-lived flare decay signatures are captured. A consequence of these separate colour bands would be decreased flux in each filter, so a larger aperture telescope would be required to ensure that the signal to noise ratio can be maintained at the same cadences and exposure settings used in this whitelight observation. Telescopes such as the Rapid Eye Mount telescope (REM Antonelli et al., 2003) would be a good choice due to its larger aperture than the NGTS, comparable cadence, and g' , r' , i' , z' filters on the ROS2 instrument. It also allows for observation in the deeper infrared, with the REMIR instrument which may prove interesting if any appreciable nanoflare signatures can be observed deeper in the IR. There may be existing datasets of quiescent timeseries on MV stars, but these would require combing through telescope archives. Quiescent timeseries have not been a major focus of study, so no literature details suitable timeseries. However, there are likely

³ While the statistical nature of the analysis is agnostic to the exact occurrence time of the nanoflares, the Fourier analysis would require simultaneous observation to allow for the PSD plots at each colour to be compared directly. Building the large number statistics will also be much easier if the observations are simultaneous.

Spectral Type	α	$\tau(s)$
M2.5V	3.00 ± 0.20	200 ± 100
M3V	3.00 ± 0.18	225 ± 100
M4V	3.10 ± 0.18	450 ± 50

Table 6.5 Nanoflare parameters per spectral type, derived from combined statistical and Fourier properties of Monte-Carlo modelled nanoflare timeseries.

suitable datasets which have been captured by multi-band optical surveys with a reasonable cadence, and a long timeseries of observations. ULTRACAM (Dhillon et al., 2007), the REM ROS2, and other multi-colour instruments may hold promise in this area, which could prove fruitful if suitably investigated. To directly ensure the acquisition of suitable observational data, I have secured observing time on the REM for the summer of 2022, to investigate one the M4V stars from this chapter, NGTS J035624.7-311140 (please see Chapter 7 for more on this, and other ideas for future observations).

Regardless of the specific physical mechanism causing this enhancement across the convective boundary, it is there. The observational evidence points to observed nanoflare activity only in the fully convective M2.5V and older stars. This novel result is independent of the modelled nanoflare lightcurves, which serve only to diagnose the parameters of the nanoflare signatures within observed lightcurves. Finding the source of this convective divide should be a key focus of future study.

CONCLUSIONS AND FUTURE WORK

In this work, I have demonstrated the joint application of statistical modelling techniques to quantify below-noise signatures for biomedical and astrophysical applications. This has led to vastly improved biomedical signal identification and has unearthed the first observational evidence for stellar nanoflares.

Initial statistical analysis and Monte-Carlo modelling was developed for use in both astrophysical and biomedical contexts. Initially, it was applied to quantify the underlying noise present in biomedical camera data. This was used to generate fully synthetic noise models, and later entirely synthetic test images for the bench-marking of noise suppression software. This was developed alongside bespoke feature-recognition and image reduction code, which led to a 98.8% reduction in the final biochip processing time. This work resulted in faster and more detailed extraction and identification of below-noise floor biomedical signatures. These techniques are being implemented in diagnostic analysers, leading to earlier intervention in healthcare, and improving patient outcome. This synthesis of astrophysical processing with biomedical requirements highlights the applicability of techniques developed for astrophysical analysis in other fields.

Indeed, these same statistical analysis techniques were used for novel analysis of the properties of below-noise-floor stellar nanoflares. Chapter 5 details the combination of statistical and Fourier-based analysis techniques alongside Monte-Carlo simulation to search for novel evidence of nanoflare activity in M-type stars observed by NGTS. The intensity fluctuation distributions of the M-type stars produced the first observational signatures of stellar nanoflares. Combining Fourier analysis with Monte-Carlo modelling, it was found that impulsive nanoflare signatures and Poisson-based shot noise demonstrated spectral power peaks across the frequency range $\approx 1 - 10$ mHz, suggesting that previously detected p -mode signatures may actually arise from nanoflare activity in the host star. Finally, the combination of the Fourier and statistical analyses found evidence for stellar nanoflare activity across the three sampled M-type stars for a power-law index $\alpha = 3.25 \pm 0.20$ and a decay timescale

$\tau = 200 \pm 100$ s. These power-law indices were greatly enhanced from those seen in solar nanoflares, or in stars at different flare energies. This enhancement was believed to be linked to the fully convective nature of these MV stars. It goes without saying that enhanced small-scale reconnection in fully convective stars may mean that nanoflare activity could be a significant component of their overall energy budget.

A follow-up study investigated the role of convection in this enhanced nanoflare activity. Chapter 6 provided evidence for stellar nanoflares on a further 15 post-convective-boundary (M2.5V, M3V, and M4V classification) stars, with nanoflare power-law indices and e -folding times consistent with the enhanced rates of nanoflare activity put forward by Dillon et al. (2020) / Chapter 5. A marked increase in nanoflare activity was found in M2.5V and beyond sub-types, suggesting that the change from partial to fully convective atmospheres may be responsible. The post-convective boundary stars exhibit nanoflare rates that are enhanced from those seen at larger energies in other stars and the Sun, with power-law indices found to be in the region of $\alpha = 3.00 \pm 0.20$ for M2.5V and M3V sub-types, with slightly larger values of $\alpha = 3.10 \pm 0.18$ for M4V sub-types. The decay timescales for M2.5V and M3V stars were found to be on the order of $\tau = 200 \pm 100$ s, while evidence was presented for increased plasma e -folding times of $\tau = 450 \pm 50$ s in the M4V stars. Conversely, pre-convective boundary M-dwarf stars (M0V, M1V, and M2V classification) exhibited little-to-no statistical or Fourier-based nanoflare signals, suggesting that full convection is a requirement for enhanced nanoflare activity. Answering definitively whether this is due to an altered dynamo, due to other plasma changes such as modification of the corresponding Lundquist number, or other unexplored possibilities would answer key questions about both the role of the stellar dynamo in these stars and the importance of the tachocline in our own Sun. One avenue of exploration will be to examine M5V (and later) stellar types to investigate if there is a continuing trend in the flare decay rate and associated power-law index, which could be linked to increasing plasma resistivity and thus increased Sweet-Parker reconnection rates. It is likely such observations would need to be coupled to detailed theoretical and modelling efforts using well-developed numerical simulations (e.g., Takahashi et al., 2011; Tenerani et al., 2015; Shi et al., 2018; Papini et al., 2019).

Another key focus of the future will be to investigate potential nanoflare signals across a number of different colour photometry bands. The nanoflare activity parameters observed in the Sun by Jess et al. (2019) varied with wavelength; one would expect a similar result for stellar nanoflares. Such multi-wavelength observations could allow for a limited analysis of how the nanoflare signals differ throughout the stellar atmosphere. To this end, observing time has been secured on the Rapid Eye Mount (REM) telescope (Antonelli et al., 2003)

for the summer of 2022. This telescope allows for simultaneous observation across 4 filters (g' , r' , i' , z') alongside the IR. These observations will have matched cadence to the current NGTS observations, and revisit the nanoflare active M4V star NGTS J035624.7-311140 which was investigated in Chapter 6. It is hoped these observations will answer some of the outstanding questions surrounding the origin of the enhanced nanoflare signatures.

Other areas to explore include higher cadence observations from instruments such as HiPERCAM (Dhillon et al., 2016) which would allow for the more rapid accumulation of suitable number statistics, alongside multi-band observation. Investigating young Sun-like stars with HiPERCAM is also an area of interest, as the high cadence and multi-colour observation can overcome the difficulties of increased flare contrast on these young and active stars. Due to their highly active X-ray emission and coronal temperatures (Johnstone & Güdel, 2015), a very high degree of nanoflare activity would be expected, possibly leading to stellar coronal heating via nanoflare activity. ‘Sun-as-a-star’ nanoflare observations would also be of great interest. By integrating over the entire stellar surface, it might be possible to leverage the statistical analysis to overcome the difficulty in identifying solar nanoflare activity. The HARPS North facility may be suitable for this, and it has previously been used for point-source solar integration (Dumusque et al., 2015).

To further improve the Fourier-based PSD analyses, a more continuous observational platform would further increase the frequency resolution possible, such as the Transiting Exoplanet Survey Satellite (TESS; Ricker et al., 2014), which can operate in both 240 s and 20 s cadences. The obvious advantages of space-based observations lie in minimising any high frequency (scintillation) noise present in the stellar lightcurves, while also allowing for a much higher frequency resolution in the subsequent PSD analyses. Longer-duration observations have been proposed to study stellar oscillations in greater detail (Ball et al., 2018), and this capability would extend the same advantages to nanoflare PSD analyses. Long-term variability is also an area of interest. While these small-scale flare events are expected to follow the same multi-year activity cycles seen in their stars, any subtle differences therein may uncover more about these emerging flare events.

These astrophysical results have added exciting new avenues to explore the role and importance of low-energy but highly frequent flaring on fully convective stars. Stellar nanoflares represent an unexplored trove of information which had previously remained hidden below the noise floor but is now able to be investigated. Stellar nanoflares have been identified in 18 fully-convective M-type stars, with their novel properties opening up opportunities for future investigation. These properties included a nanoflare induced quasi-periodic brightening which had previously been ascribed solely to wave behaviour,

greatly enhanced nanoflare activity in MV stars compared to nanoflare activity in the sun, and furthermore this nanoflare activity was only observed in fully convective MV stars. The potential to expand this M-type analysis to investigation of nanoflares in other stellar types is great. Doing so will answer important questions about the nature of flaring, in other stars and in the Sun. While I wish these mysteries were solved within the span of my PhD, I am excited for the future of this field. Small scale stellar reconnection holds a wealth of new science to explore, of which this work has only begun to scratch the surface.

I hope that this work will encourage other cross-discipline and industrially linked work. Ultimately, the same physics and statistical laws govern seemingly disparate fields. The cross-discipline application of a shared framework allowed me to make connections and develop skills which would not have been possible otherwise. This process has worked both ways, with the biomedical analysis sparking new ideas for astronomical progress. This style of cross-discipline work of course has economic benefits, but also I believe philosophical ones. Astronomy has always been about looking outward. We have everything to gain by looking outward, embracing new approaches, and remaining curious.

REFERENCES

- Abramowitz, M., & Stegun, I. A. 1972, Handbook of Mathematical Functions. <https://ui.adsabs.harvard.edu/abs/1972hmfw.book.....A>
- Agrawal, D. C. 2018, Physics Education, 53, 055005, doi: [10.1088/1361-6552/aacae5](https://doi.org/10.1088/1361-6552/aacae5)
- Aguerrebere, C., Delon, J., Gousseau, Y., & Musé, P. 2012, Study of the digital camera acquisition process and statistical modeling of the sensor raw data, Tech. rep. <https://hal.archives-ouvertes.fr/hal-00733538>
- Alfvén, H. 1941, Arkiv för Matematik, Astronomi och Fysik, 27A
- Alfvén, H. 1942, Nature, 150, 405, doi: [10.1038/150405d0](https://doi.org/10.1038/150405d0)
- Alfvén, H. 1947, MNRAS, 107, 211, doi: [10.1093/mnras/107.2.211](https://doi.org/10.1093/mnras/107.2.211)
- Altman, D. G., & Bland, J. M. 2005, BMJ (Clinical research ed.), 331, 903, doi: [10.1136/bmj.331.7521.903](https://doi.org/10.1136/bmj.331.7521.903)
- Amado, P. J., Doyle, J. G., Byrne, P. B., et al. 2000, A&A, 359, 159. <https://ui.adsabs.harvard.edu/abs/2000A&A...359..159A>
- Anderson, C. 1994, Science, 263, 317, doi: [10.1126/science.8278802](https://doi.org/10.1126/science.8278802)
- Andrews, A. D. 1989, A&A, 210, 303. <https://ui.adsabs.harvard.edu/abs/1989A&A...210..303A>
- . 1990a, A&A, 229, 504. <https://ui.adsabs.harvard.edu/abs/1990A&A...229..504A>
- . 1990b, A&A, 239, 235. <https://ui.adsabs.harvard.edu/abs/1990A&A...239..235A>
- Andrews, A. D., & Doyle, J. G. 1993, Irish Astronomical Journal, 21, 83. <https://ui.adsabs.harvard.edu/abs/1993IrAJ...21...83A>
- Antiochos, S. K., & Sturrock, P. A. 1978, ApJ, 220, 1137, doi: [10.1086/155999](https://doi.org/10.1086/155999)
- Antonelli, L. A., Zerbi, F. M., Chincarini, G., et al. 2003, MmSAI, 74, 304, doi: [10.1117/12.459511](https://doi.org/10.1117/12.459511)
- Armstrong, J. A., & Fletcher, L. 2019, Solar Physics, 294, 80, doi: [10.1007/s11207-019-1473-z](https://doi.org/10.1007/s11207-019-1473-z)
- Arons, A. B., & Peppard, M. B. 1965, American Journal of Physics, 33, 367, doi: [10.1119/1.1971542](https://doi.org/10.1119/1.1971542)
- Arzner, K., & Güdel, M. 2004, The Astrophysical Journal, 602, 363, doi: [10.1086/381026](https://doi.org/10.1086/381026)
- Aschwanden, M. J. 1999, SoPh, 190, 233, doi: [10.1023/A:1005288725034](https://doi.org/10.1023/A:1005288725034)

- . 2004, *Physics of the Solar Corona. An Introduction*. <https://ui.adsabs.harvard.edu/abs/2004psci.book.....A>
- . 2019, *ApJ*, 880, 105, doi: [10.3847/1538-4357/ab29f4](https://doi.org/10.3847/1538-4357/ab29f4)
- Aschwanden, M. J., Boerner, P., Ryan, D., et al. 2015, *ApJ*, 802, 53, doi: [10.1088/0004-637X/802/1/53](https://doi.org/10.1088/0004-637X/802/1/53)
- Aschwanden, M. J., Fletcher, L., Schrijver, C. J., & Alexander, D. 1999, *ApJ*, 520, 880, doi: [10.1086/307502](https://doi.org/10.1086/307502)
- Aschwanden, M. J., & Freeland, S. L. 2012, *ApJ*, 754, 112, doi: [10.1088/0004-637X/754/2/112](https://doi.org/10.1088/0004-637X/754/2/112)
- Aschwanden, M. J., Tarbell, T. D., Nightingale, R. W., et al. 2000, *ApJ*, 535, 1047, doi: [10.1086/308867](https://doi.org/10.1086/308867)
- Aschwanden, M. J., Winebarger, A., Tsiklauri, D., & Peter, H. 2007, *ApJ*, 659, 1673, doi: [10.1086/513070](https://doi.org/10.1086/513070)
- Aschwanden, M. J., Xu, Y., & Jing, J. 2014, *ApJ*, 797, 50, doi: [10.1088/0004-637X/797/1/50](https://doi.org/10.1088/0004-637X/797/1/50)
- Audard, M., Güdel, M., Drake, J. J., & Kashyap, V. L. 2000, *ApJ*, 541, 396, doi: [10.1086/309426](https://doi.org/10.1086/309426)
- Aveni, A. F. 2003, *Journal of Archaeological Research*, 11, 149, doi: [10.1023/A:1022971730558](https://doi.org/10.1023/A:1022971730558)
- Babcock, H. W. 1961, *ApJ*, 133, 572, doi: [10.1086/147060](https://doi.org/10.1086/147060)
- Balanda, K. P., & MacGillivray, H. L. 1988, *The American Statistician*, 42, 111. <http://www.jstor.org/stable/2684482>
- Ball, W. H., Chaplin, W. J., Schofield, M., et al. 2018, *The Astrophysical Journal Supplement Series*, 239, 34, doi: [10.3847/1538-4365/aedbc](https://doi.org/10.3847/1538-4365/aedbc)
- Balona, L. A. 2012, *MNRAS*, 423, 3420, doi: [10.1111/j.1365-2966.2012.21135.x](https://doi.org/10.1111/j.1365-2966.2012.21135.x)
- . 2021, *Frontiers in Astronomy and Space Sciences*, 8, doi: [10.3389/fspas.2021.580907](https://doi.org/10.3389/fspas.2021.580907)
- Barndorff-Nielsen, O.E. Kendall, W., & van Lieshout, M. 1998, *Stochastic Geometry: Likelihood and computation* (1st ed.) (Routledge), doi: [10.1201/9780203738276](https://doi.org/10.1201/9780203738276)
- Benz, A. O. 2016, *Living Reviews in Solar Physics*, 14, 2, doi: [10.1007/s41116-016-0004-3](https://doi.org/10.1007/s41116-016-0004-3)
- Benz, A. O., & Güdel, M. 2010, *Annual Review of Astronomy and Astrophysics*, 48, 241, doi: [10.1146/annurev-astro-082708-101757](https://doi.org/10.1146/annurev-astro-082708-101757)
- Benz, A. O., & Krucker, S. 2002, *ApJ*, 568, 413, doi: [10.1086/338807](https://doi.org/10.1086/338807)
- Berghmans, D., Clette, F., & Moses, D. 1998, *A&A*, 336, 1039. <https://ui.adsabs.harvard.edu/abs/1998A&A...336.1039B>

- Berry, S., Giraldo, N. A., Green, B. F., et al. 2021, *Science*, 372, eaba2609, doi: [10.1126/science.aba2609](https://doi.org/10.1126/science.aba2609)
- Biskamp, D. 1993, *Nonlinear Magnetohydrodynamics*, Cambridge Monographs on Plasma Physics (Cambridge University Press), doi: [10.1017/CBO9780511599965](https://doi.org/10.1017/CBO9780511599965)
- Blackwell, R. 2006, *Behind the scenes at Galileo's trial : including the first English translation of Melchior Inchofer's Tractatus syllepticus* (Notre Dame, Indiana: University of Notre Dame Press)
- Boerner, P., Edwards, C., Lemen, J., et al. 2012, *Solar Physics*, 275, 41, doi: [10.1007/s11207-011-9804-8](https://doi.org/10.1007/s11207-011-9804-8)
- Boyat, A. K., & Joshi, B. K. 2015, CoRR, abs/1505.03489. <https://arxiv.org/abs/1505.03489>
- Bradshaw, S. J., Klimchuk, J. A., & Reep, J. W. 2012, *ApJ*, 758, 53, doi: [10.1088/0004-637X/758/1/53](https://doi.org/10.1088/0004-637X/758/1/53)
- Brasseur, C. E., Osten, R. A., & Fleming, S. W. 2019, *ApJ*, 883, 88, doi: [10.3847/1538-4357/ab3df8](https://doi.org/10.3847/1538-4357/ab3df8)
- Brewis, I., & McLaughlin, J. A. 2019, arXiv e-prints, arXiv:1902.01233. <https://arxiv.org/abs/1902.01233>
- Brillouin, L. 1959, *Information and Control*, 2, 45, doi: [https://doi.org/10.1016/S0019-9958\(59\)90074-9](https://doi.org/10.1016/S0019-9958(59)90074-9)
- Brookes, B. C., & Dick, W. F. L. 1969, *Introduction to Statistical Method* (Heinemann Educational Books Ltd.)
- Browning, M. K. 2008, *ApJ*, 676, 1262, doi: [10.1086/527432](https://doi.org/10.1086/527432)
- Buitrago-Casas, J. C., Christe, S., Glesener, L., et al. 2020, *Journal of Instrumentation*, 15, P11032, doi: [10.1088/1748-0221/15/11/P11032](https://doi.org/10.1088/1748-0221/15/11/P11032)
- Butler, C. J., Rodono, M., Foing, B. H., & Haisch, B. M. 1986, *Nature*, 321, 679, doi: [10.1038/321679a0](https://doi.org/10.1038/321679a0)
- Byrne, H. J., Bermudez, V. M., Wang, Z., et al. 2013, *ISRN Spectroscopy*, 2013, 230858, doi: [10.1155/2013/230858](https://doi.org/10.1155/2013/230858)
- Canny, J. 1986, *IEEE Transactions on Pattern Analysis and Machine Intelligence*, PAMI-8, 679, doi: [10.1109/TPAMI.1986.4767851](https://doi.org/10.1109/TPAMI.1986.4767851)
- Cardelli, J. A., Clayton, G. C., & Mathis, J. S. 1989, *ApJ*, 345, 245, doi: [10.1086/167900](https://doi.org/10.1086/167900)
- Cargill, P. J., Warren, H. P., & Bradshaw, S. J. 2015, *Philosophical transactions. Series A, Mathematical, physical, and engineering sciences*, 373, 20140260, doi: [10.1098/rsta.2014.0260](https://doi.org/10.1098/rsta.2014.0260)
- Carrington, R. C. 1859, *MNRAS*, 20, 13, doi: [10.1093/mnras/20.1.13](https://doi.org/10.1093/mnras/20.1.13)

- Chaplin, W. J., Houdek, G., Elsworth, Y., et al. 2009, *ApJ*, 692, 531, doi: [10.1088/0004-637X/692/1/531](https://doi.org/10.1088/0004-637X/692/1/531)
- Chapman, G. H., Thomas, R., Thomas, R., et al. 2015, in 2015 IEEE International Symposium on Defect and Fault Tolerance in VLSI and Nanotechnology Systems (DFTS), 41–46, doi: [10.1109/DFT.2015.7315133](https://doi.org/10.1109/DFT.2015.7315133)
- Cheng, J., Ji, G., Feng, C., & Zheng, H. 2009, in 2009 International Conference on Information Technology and Computer Science, Vol. 2, 73–76, doi: [10.1109/ITCS.2009.153](https://doi.org/10.1109/ITCS.2009.153)
- Christe, S., Hannah, I. G., Krucker, S., McTiernan, J., & Lin, R. P. 2008, *The Astrophysical Journal*, 677, 1385, doi: [10.1086/529011](https://doi.org/10.1086/529011)
- Christensson, M., Hindmarsh, M., & Brandenburg, A. 2001, *PhRvE*, 64, 056405, doi: [10.1103/PhysRevE.64.056405](https://doi.org/10.1103/PhysRevE.64.056405)
- Chudasama, D., Patel, T., Joshi, S., & Prajapati, G. I. 2015, *International Journal of Computer Applications*, 117, 16, doi: [10.5120/20654-3197](https://doi.org/10.5120/20654-3197)
- CIA. 2008, CIA World Factbook, Central Intelligence Agency. <https://web.archive.org/web/20120128032332/https://www.cia.gov/library/publications/the-world-factbook/rankorder/2042rank.html>
- . 2015, CIA World Factbook, Central Intelligence Agency. <https://www.cia.gov/the-world-factbook/countries/world/#energy>
- Clerk, A. A., Devoret, M. H., Girvin, S. M., Marquardt, F., & Schoelkopf, R. J. 2010, *Reviews of Modern Physics*, 82, 1155, doi: [10.1103/RevModPhys.82.1155](https://doi.org/10.1103/RevModPhys.82.1155)
- Cliver, E. W., & Dietrich, W. F. 2013, *Journal of Space Weather and Space Climate*, 3, A31, doi: [10.1051/swsc/2013053](https://doi.org/10.1051/swsc/2013053)
- Colak, T., & Qahwaji, R. 2008, *Solar Physics*, 248, 277, doi: [10.1007/s11207-007-9094-3](https://doi.org/10.1007/s11207-007-9094-3)
- Cook, B. A. 2019, arXiv e-prints, arXiv:1903.12180. <https://arxiv.org/abs/1903.12180>
- Cox, V. D. 2012, *Assay Guidance Manual* (Eli Lilly Company and the National Center for Advancing Translational Sciences, Bethesda (MD)). <http://europepmc.org/books/NBK53196>
- Cromey, D. W. 2010, *Science and engineering ethics*, 16, 639, doi: [10.1007/s11948-010-9201-y](https://doi.org/10.1007/s11948-010-9201-y)
- . 2013, *Methods in molecular biology* (Clifton, N.J.), 931, 1—27, doi: [10.1007/978-1-62703-056-4_1](https://doi.org/10.1007/978-1-62703-056-4_1)
- Darwish, I. A. 2006, *International journal of biomedical science : IJBS*, 2, 217. <https://pubmed.ncbi.nlm.nih.gov/23674985>
- Davies, E. 1989, *Pattern Recognition Letters*, 9, 87, doi: [10.1016/0167-8655\(89\)90041-X](https://doi.org/10.1016/0167-8655(89)90041-X)
- Delouille, V., Chainais, P., & Hochedez, J. F. 2008, *SoPh*, 248, 441, doi: [10.1007/s11207-008-9131-x](https://doi.org/10.1007/s11207-008-9131-x)

- Desmars, J., Arlot, S., Arlot, J. E., Lainey, V., & Vienne, A. 2009, *A&A*, 499, 321, doi: [10.1051/0004-6361/200811509](https://doi.org/10.1051/0004-6361/200811509)
- Dhillon, V. S., Marsh, T. R., Stevenson, M. J., et al. 2007, *MNRAS*, 378, 825, doi: [10.1111/j.1365-2966.2007.11881.x](https://doi.org/10.1111/j.1365-2966.2007.11881.x)
- Dhillon, V. S., Marsh, T. R., Bezawada, N., et al. 2016, in *Society of Photo-Optical Instrumentation Engineers (SPIE) Conference Series*, Vol. 9908, Proc. SPIE, 99080Y, doi: [10.1117/12.2229055](https://doi.org/10.1117/12.2229055)
- Di Mauro, M. P. 2016, in *Frontier Research in Astrophysics II (FRAPWS2016)*, 29. <https://arxiv.org/abs/1703.07604>
- Dillon, C. J., Jess, D. B., Mathioudakis, M., et al. 2020, *ApJ*, 904, 109, doi: [10.3847/1538-4357/abbfa8](https://doi.org/10.3847/1538-4357/abbfa8)
- . 2022
- Dumusque, X., Glenday, A., Phillips, D. F., et al. 2015, *ApJL*, 814, L21, doi: [10.1088/2041-8205/814/2/L21](https://doi.org/10.1088/2041-8205/814/2/L21)
- Durney, B. R., De Young, D. S., & Roxburgh, I. W. 1993, *SoPh*, 145, 207, doi: [10.1007/BF00690652](https://doi.org/10.1007/BF00690652)
- Edlén, B. 1941, *Arkiv för Matematik, Astronomi och Fysik*, 28B
- . 1943, *ZA*, 22, 30. <https://ui.adsabs.harvard.edu/abs/1943ZA.....22...30E>
- Efron, B., et al. 1979, *Annals of Statistics*, 7, 1. <https://www.jstor.org/stable/2958830>
- Einstein, A. 1905, *Annalen der Physik*, 322, 132, doi: <https://doi.org/10.1002/andp.19053220607>
- Eugene, S. 1935, *Journal of Educational Psychology*, 2, 154, doi: [10.1037/h0056326](https://doi.org/10.1037/h0056326)
- Falla, D. F., & Potter, A. G. 1999, *MNRAS*, 310, 784, doi: [10.1046/j.1365-8711.1999.02979.x](https://doi.org/10.1046/j.1365-8711.1999.02979.x)
- Finsterle, W., Montillet, J. P., Schmutz, W., et al. 2021, *Scientific Reports*, 11, 7835, doi: [10.1038/s41598-021-87108-y](https://doi.org/10.1038/s41598-021-87108-y)
- Fisher, R. A. 1930, *Proceedings of the Royal Society of London. Series A, Containing Papers of a Mathematical and Physical Character*, 130, 16. <http://www.jstor.org/stable/95586>
- FitzGerald, S. P., Lamont, J. V., McConnell, R. I., & Benchikh, E. O. 2005, *Clinical Chemistry*, 51, 1165, doi: [10.1373/clinchem.2005.049429](https://doi.org/10.1373/clinchem.2005.049429)
- Föhring, D., Wilson, R. W., Osborn, J., & Dhillon, V. S. 2019, *MNRAS*, 489, 5098, doi: [10.1093/mnras/stz2444](https://doi.org/10.1093/mnras/stz2444)
- Fossati, L., Koskinen, T., Lothringer, J. D., et al. 2018, *ApJL*, 868, L30, doi: [10.3847/2041-8213/aaf0a5](https://doi.org/10.3847/2041-8213/aaf0a5)

- Frank, S. A. 2009, *Journal of Evolutionary Biology*, 22, 1563, doi: [10.1111/j.1420-9101.2009.01775.x](https://doi.org/10.1111/j.1420-9101.2009.01775.x)
- Gary, D. E., Chen, B., Dennis, B. R., et al. 2018, *ApJ*, 863, 83, doi: [10.3847/1538-4357/aad0ef](https://doi.org/10.3847/1538-4357/aad0ef)
- Gehrels, N. 1986, *ApJ*, 303, 336, doi: [10.1086/164079](https://doi.org/10.1086/164079)
- Gershberg, R. E. 1975, *Symposium - International Astronomical Union*, 67, 47–64, doi: [10.1017/S0074180900010032](https://doi.org/10.1017/S0074180900010032)
- Gilliland, R. L. 1992, in *Astronomical Society of the Pacific Conference Series*, Vol. 23, *Astronomical CCD Observing and Reduction Techniques*, ed. S. B. Howell, 68. <https://ui.adsabs.harvard.edu/abs/1992ASPC...23...68G>
- Gold, T. 1965, in *IAU Symp (North-Holland Pub. Co.)*, 390
- Gosling, J. T. 1993, *J. Geophys. Res.*, 98, 18937, doi: [10.1029/93JA01896](https://doi.org/10.1029/93JA01896)
- Gough, D. 2007, *An introduction to the solar tachocline*, ed. D. W. Hughes, R. Rosner, & N. O. Weiss (Cambridge University Press), 3–30, doi: [10.1017/CBO9780511536243.002](https://doi.org/10.1017/CBO9780511536243.002)
- Green, B., Berry, S., Giraldo, N., et al. 2021, in *Where the Earth meets the Sky*, 12, doi: [10.5281/zenodo.5031887](https://doi.org/10.5281/zenodo.5031887)
- Grotian, W. 1939, *Naturwissenschaften*, 27, 214, doi: [10.1007/BF01488890](https://doi.org/10.1007/BF01488890)
- Güdel, M. 2004, *A&A Rv*, 12, 71, doi: [10.1007/s00159-004-0023-2](https://doi.org/10.1007/s00159-004-0023-2)
- Güdel, M., Audard, M., Kashyap, V., Drake, J. J., & Guinan, E. F. 2002, in *Astronomical Society of the Pacific Conference Series*, Vol. 277, *Stellar Coronae in the Chandra and XMM-NEWTON Era*, ed. F. Favata & J. J. Drake, 491. <https://ui.adsabs.harvard.edu/abs/2002ASPC..277..491G>
- Güdel, M., Audard, M., Kashyap, V. L., Drake, J. J., & Guinan, E. F. 2003, *The Astrophysical Journal*, 582, 423, doi: [10.1086/344614](https://doi.org/10.1086/344614)
- Güdel, M., Benz, A. O., Schmitt, J. H. M. M., & Skinner, S. L. 1996, *ApJ*, 471, 1002, doi: [10.1086/178027](https://doi.org/10.1086/178027)
- Guenther, D. B., Kallinger, T., Gruberbauer, M., et al. 2008, *ApJ*, 687, 1448, doi: [10.1086/592060](https://doi.org/10.1086/592060)
- Gundersen, G. 2020. <https://gregorygundersen.com/blog/2020/04/11/moments/>
- Gunn, J. E., Siegmund, W. A., Mannery, E. J., et al. 2006, *The Astronomical Journal*, 131, 2332, doi: [10.1086/500975](https://doi.org/10.1086/500975)
- Günther, M. N., Zhan, Z., Seager, S., et al. 2020, *The Astronomical Journal*, 159, 60, doi: [10.3847/1538-3881/ab5d3a](https://doi.org/10.3847/1538-3881/ab5d3a)
- Handler, G. 2013, *Asteroseismology*, ed. T. D. Oswalt & M. A. Barstow, Vol. 4, 207, doi: [10.1007/978-94-007-5615-1_4](https://doi.org/10.1007/978-94-007-5615-1_4)

- Hewish, A. 1965, *Science Progress* (1933-), 53, 355. <http://www.jstor.org/stable/43419370>
- Heyvaerts, J., & Priest, E. R. 1983, *A&A*, 117, 220. <https://ui.adsabs.harvard.edu/abs/1983A&A...117..220H>
- Hicks, C., Kalatsky, M., Metzler, R. A., & Goushcha, A. O. 2003, *Appl. Opt.*, 42, 4415, doi: [10.1364/AO.42.004415](https://doi.org/10.1364/AO.42.004415)
- Hodgson, R. 1859, *MNRAS*, 20, 15, doi: [10.1093/mnras/20.1.15](https://doi.org/10.1093/mnras/20.1.15)
- Howell, S. B., Ellis, R., Huchra, J., et al. 2006, *Handbook of CCD Astronomy*; 2nd ed. (Cambridge: Cambridge Univ. Press). <https://cds.cern.ch/record/991614>
- Huang, S. Y., Hadid, L. Z., Sahraoui, F., Yuan, Z. G., & Deng, X. H. 2017, *The Astrophysical Journal*, 836, L10, doi: [10.3847/2041-8213/836/1/L10](https://doi.org/10.3847/2041-8213/836/1/L10)
- Hudson, H. S. 1991, *SoPh*, 133, 357, doi: [10.1007/BF00149894](https://doi.org/10.1007/BF00149894)
- Hudson, H. S., Acton, L. W., Hirayama, T., & Uchida, Y. 1992, *PASJ*, 44, L77. <https://ui.adsabs.harvard.edu/abs/1992PASJ...44L..77H>
- Isobe, H., Kubo, M., Minoshima, T., et al. 2007, *PASJ*, 59, S807, doi: [10.1093/pasj/59.sp3.S807](https://doi.org/10.1093/pasj/59.sp3.S807)
- Jackman, J. A. G., Wheatley, P. J., Pugh, C. E., et al. 2018, *MNRAS*, 477, 4655, doi: [10.1093/mnras/sty897](https://doi.org/10.1093/mnras/sty897)
- . 2019a, *MNRAS*, 482, 5553, doi: [10.1093/mnras/sty3036](https://doi.org/10.1093/mnras/sty3036)
- Jackman, J. A. G., Wheatley, P. J., Bayliss, D., et al. 2019b, *MNRAS*, 485, L136, doi: [10.1093/mnras/slz039](https://doi.org/10.1093/mnras/slz039)
- . 2019c, *MNRAS*, 489, 5146, doi: [10.1093/mnras/stz2496](https://doi.org/10.1093/mnras/stz2496)
- Jackman, J. A. G., Wheatley, P. J., Acton, J. S., et al. 2020, *MNRAS*, 497, 809, doi: [10.1093/mnras/staa1971](https://doi.org/10.1093/mnras/staa1971)
- . 2021, *MNRAS*, 504, 3246, doi: [10.1093/mnras/stab979](https://doi.org/10.1093/mnras/stab979)
- Jess, D. B., Mathioudakis, M., Crockett, P. J., & Keenan, F. P. 2008, *ApJL*, 688, L119, doi: [10.1086/595588](https://doi.org/10.1086/595588)
- Jess, D. B., Mathioudakis, M., & Keys, P. H. 2014, *ApJ*, 795, 172, doi: [10.1088/0004-637X/795/2/172](https://doi.org/10.1088/0004-637X/795/2/172)
- Jess, D. B., Dillon, C. J., Kirk, M. S., et al. 2019, *ApJ*, 871, 133, doi: [10.3847/1538-4357/aaf8ae](https://doi.org/10.3847/1538-4357/aaf8ae)
- Jess, D. B., Snow, B., Houston, S. J., et al. 2020, *Nature Astronomy*, 4, 220, doi: [10.1038/s41550-019-0945-2](https://doi.org/10.1038/s41550-019-0945-2)
- Johnstone, C. P., Bartel, M., & Güdel, M. 2021, *A&A*, 649, A96, doi: [10.1051/0004-6361/202038407](https://doi.org/10.1051/0004-6361/202038407)

- Johnstone, C. P., & Güdel, M. 2015, *A&A*, 578, A129, doi: [10.1051/0004-6361/201425283](https://doi.org/10.1051/0004-6361/201425283)
- Kashyap, V. L., Drake, J. J., Güdel, M., & Audard, M. 2002, *ApJ*, 580, 1118, doi: [10.1086/343869](https://doi.org/10.1086/343869)
- Kastner, J. H., Crigger, L., Rich, M., & Weintraub, D. A. 2003, *The Astrophysical Journal*, 585, 878, doi: [10.1086/346182](https://doi.org/10.1086/346182)
- Kawate, T., Ishii, T. T., Nakatani, Y., et al. 2016, *ApJ*, 833, 50, doi: [10.3847/1538-4357/833/1/50](https://doi.org/10.3847/1538-4357/833/1/50)
- Khan, F. A. 2020, *Physics Education*, 56, 013002, doi: [10.1088/1361-6552/abbcbc](https://doi.org/10.1088/1361-6552/abbcbc)
- King, H. C. 1956, *History of the Telescope*. https://books.google.co.uk/books/about/The_History_of_the_Telescope.html?id=PvQfAQAAIAAJ&redir_esc=y
- Kjeldsen, H., Bedding, T. R., Viskum, M., & Frandsen, S. 1995, *AJ*, 109, 1313, doi: [10.1086/117363](https://doi.org/10.1086/117363)
- Klimchuk, J. A. 2006, *Solar Physics*, 234, 41, doi: [10.1007/s11207-006-0055-z](https://doi.org/10.1007/s11207-006-0055-z)
- Klimchuk, J. A. 2015, *Philosophical Transactions of the Royal Society of London Series A*, 373, 20140256, doi: [10.1098/rsta.2014.0256](https://doi.org/10.1098/rsta.2014.0256)
- Klimchuk, J. A., & Cargill, P. J. 2001, *ApJ*, 553, 440, doi: [10.1086/320666](https://doi.org/10.1086/320666)
- Kretzschmar, M. 2011, *A&A*, 530, A84, doi: [10.1051/0004-6361/201015930](https://doi.org/10.1051/0004-6361/201015930)
- Krucker, S., & Benz, A. O. 1998, *ApJL*, 501, L213, doi: [10.1086/311474](https://doi.org/10.1086/311474)
- Lacy, C. H., Moffett, T. J., & Evans, D. S. 1976, *ApJS*, 30, 85, doi: [10.1086/190358](https://doi.org/10.1086/190358)
- Leavers, V. F. 1992, *Shape Detection in Computer Vision Using the Hough Transform* (Berlin, Heidelberg: Springer-Verlag), doi: [10.1007/978-1-4471-1940-1](https://doi.org/10.1007/978-1-4471-1940-1)
- Leighton, R. B. 1964, *ApJ*, 140, 1547, doi: [10.1086/148058](https://doi.org/10.1086/148058)
- Lemen, J. R., Title, A. M., Akin, D. J., et al. 2012, *SoPh*, 275, 17, doi: [10.1007/s11207-011-9776-8](https://doi.org/10.1007/s11207-011-9776-8)
- López-Santiago, J., Crespo-Chacón, I., Micela, G., & Reale, F. 2010, *ApJ*, 712, 78, doi: [10.1088/0004-637X/712/1/78](https://doi.org/10.1088/0004-637X/712/1/78)
- Loureiro, N. F., & Uzdensky, D. A. 2016, *Plasma Physics and Controlled Fusion*, 58, 014021, doi: [10.1088/0741-3335/58/1/014021](https://doi.org/10.1088/0741-3335/58/1/014021)
- Lu, E. T., & Hamilton, R. J. 1991, *ApJL*, 380, L89, doi: [10.1086/186180](https://doi.org/10.1086/186180)
- Lupton, R. 1993, *Statistics in Theory and Practice* (Princeton University Press). <https://books.google.co.uk/books?id=d6O2d7dLJEoC>
- Lustig, M., Donoho, D. L., Santos, J. M., & Pauly, J. M. 2008, *IEEE Signal Processing Magazine*, 25, 72, doi: [10.1109/MSP.2007.914728](https://doi.org/10.1109/MSP.2007.914728)

- Machado, M. E., Emslie, A. G., & Avrett, E. H. 1989, *SoPh*, 124, 303, doi: [10.1007/BF00156272](https://doi.org/10.1007/BF00156272)
- Maehara, H., Shibayama, T., Notsu, Y., et al. 2015, *Earth, Planets and Space*, 67, 59, doi: [10.1186/s40623-015-0217-z](https://doi.org/10.1186/s40623-015-0217-z)
- Maehara, H., Shibayama, T., Notsu, S., et al. 2012, *Nature*, 485, 478, doi: [10.1038/nature11063](https://doi.org/10.1038/nature11063)
- Marcelot, O., Goiffon, V., Raine, M., et al. 2015, *IEEE Transactions on Electron Devices*, 62, 2965, doi: [10.1109/TNS.2015.2497405](https://doi.org/10.1109/TNS.2015.2497405)
- McLaughlin, J. A., Nakariakov, V. M., Dominique, M., Jelínek, P., & Takasao, S. 2018, *SSRv*, 214, 45, doi: [10.1007/s11214-018-0478-5](https://doi.org/10.1007/s11214-018-0478-5)
- Minoshima, T., Yokoyama, T., & Mitani, N. 2008, *ApJ*, 673, 598, doi: [10.1086/523884](https://doi.org/10.1086/523884)
- Mitra, J., Chandra, A., & Halder, T. 2013, *Electronic Letters on Computer Vision and Image Analysis*, 12, 57, doi: [10.5565/rev/elcvia.529](https://doi.org/10.5565/rev/elcvia.529)
- Mohanty, S., Basri, G., Shu, F., Allard, F., & Chabrier, G. 2002, *ApJ*, 571, 469, doi: [10.1086/339911](https://doi.org/10.1086/339911)
- Mullan, D. J., & Houdebine, E. R. 2020, *ApJ*, 891, 128, doi: [10.3847/1538-4357/ab6ffa](https://doi.org/10.3847/1538-4357/ab6ffa)
- Muller, C. 2014, *Origins of life and evolution of the biosphere : the journal of the International Society for the Study of the Origin of Life*, 44, 185, doi: [10.1007/s11084-014-9368-3](https://doi.org/10.1007/s11084-014-9368-3)
- Muthukrishnan, R., & Radha, M. 2011, *International Journal of Computer Science & Information Technology*, 3, 259, doi: [10.5121/ijcsit.2011.3620](https://doi.org/10.5121/ijcsit.2011.3620)
- Nakariakov, V. M., Inglis, A. R., Zimovets, I. V., et al. 2010, *Plasma Physics and Controlled Fusion*, 52, 124009, doi: [10.1088/0741-3335/52/12/124009](https://doi.org/10.1088/0741-3335/52/12/124009)
- Nakariakov, V. M., & Verwichte, E. 2005, *Living Reviews in Solar Physics*, 2, 3, doi: [10.12942/lrsp-2005-3](https://doi.org/10.12942/lrsp-2005-3)
- Narain, U., & Pandey, K. 2006, *Journal of Astrophysics and Astronomy*, 27, 93, doi: [10.1007/BF02702511](https://doi.org/10.1007/BF02702511)
- NASA. 2012, SDO Loop Structures. <https://sdo.gsfc.nasa.gov/gallery/main/item/125>
- Nasyrova, M., & Vítek, S. 2017, *Contributions of the Astronomical Observatory Skalnaté Pleso*, 47, 208. <https://ui.adsabs.harvard.edu/abs/2017CoSka..47..208N>
- Neidig, D. F. 1989, *SoPh*, 121, 261, doi: [10.1007/BF00161699](https://doi.org/10.1007/BF00161699)
- Neidig, D. F., & Kane, S. R. 1993, *SoPh*, 143, 201, doi: [10.1007/BF00619106](https://doi.org/10.1007/BF00619106)
- Neupert, W. M. 1968, *ApJL*, 153, L59, doi: [10.1086/180220](https://doi.org/10.1086/180220)
- Nevalainen, J., Markevitch, M., & Lumb, D. 2005, *ApJ*, 629, 172, doi: [10.1086/431198](https://doi.org/10.1086/431198)

- Newton, E. R., Mondrik, N., Irwin, J., Winters, J. G., & Charbonneau, D. 2018, *The Astronomical Journal*, 156, 217, doi: [10.3847/1538-3881/aad73b](https://doi.org/10.3847/1538-3881/aad73b)
- Ng, C. S., Lin, L., & Bhattacharjee, A. 2012, *The Astrophysical Journal*, 747, 109, doi: [10.1088/0004-637x/747/2/109](https://doi.org/10.1088/0004-637x/747/2/109)
- Oelkers, R. J., Rodriguez, J. E., Stassun, K. G., et al. 2017, *The Astronomical Journal*, 155, 39, doi: [10.3847/1538-3881/aa9bf4](https://doi.org/10.3847/1538-3881/aa9bf4)
- Osborn, J., Föhring, D., Dhillon, V. S., & Wilson, R. W. 2015, *MNRAS*, 452, 1707, doi: [10.1093/mnras/stv1400](https://doi.org/10.1093/mnras/stv1400)
- O'Brien, S. M., Bayliss, D., Osborn, J., et al. 2021, *Monthly Notices of the Royal Astronomical Society*, 509, 6111, doi: [10.1093/mnras/stab3399](https://doi.org/10.1093/mnras/stab3399)
- Papini, E., Landi, S., & Del Zanna, L. 2019, *ApJ*, 885, 56, doi: [10.3847/1538-4357/ab4352](https://doi.org/10.3847/1538-4357/ab4352)
- Parfrey, K. P., & Menou, K. 2007, *ApJL*, 667, L207, doi: [10.1086/522426](https://doi.org/10.1086/522426)
- Parker, E. N. 1955, *ApJ*, 122, 293, doi: [10.1086/146087](https://doi.org/10.1086/146087)
- Parker, E. N. 1957, *Journal of Geophysical Research (1896-1977)*, 62, 509, doi: <https://doi.org/10.1029/JZ062i004p00509>
- Parker, E. N. 1963, *ApJS*, 8, 177, doi: [10.1086/190087](https://doi.org/10.1086/190087)
- . 1965, *SSRv*, 4, 666, doi: [10.1007/BF00216273](https://doi.org/10.1007/BF00216273)
- . 1988, *ApJ*, 330, 474, doi: [10.1086/166485](https://doi.org/10.1086/166485)
- Parnell, C. E., & Jupp, P. E. 2000, *ApJ*, 529, 554, doi: [10.1086/308271](https://doi.org/10.1086/308271)
- Pedersen, M. G., Antoci, V., Korhonen, H., et al. 2017, *MNRAS*, 466, 3060, doi: [10.1093/mnras/stw3226](https://doi.org/10.1093/mnras/stw3226)
- Petitpas, G. R. 2019, *Dumb Or Overly Forced Astronomical Acronyms Site (or DOOFAAS)*. <https://lweb.cfa.harvard.edu/~gpetitpas/Links/Astroacro.html>
- Petschek, H. E. 1964, *Magnetic Field Annihilation*, Vol. 50, 425. <https://ui.adsabs.harvard.edu/abs/1964NASSP..50..425P>
- Philip, K., Dove, E., McPherson, D., et al. 1994, *IEEE Transactions on Medical Imaging*, 13, 235, doi: [10.1109/42.293916](https://doi.org/10.1109/42.293916)
- Pipin, V. V., & Seehafer, N. 2009, *A&A*, 493, 819, doi: [10.1051/0004-6361:200810766](https://doi.org/10.1051/0004-6361:200810766)
- Podesta, J. J. 2011, *Journal of Geophysical Research (Space Physics)*, 116, A05101, doi: [10.1029/2010JA016306](https://doi.org/10.1029/2010JA016306)
- Port, S. 1994, *Theoretical Probability for Applications*, *Wiley Series in Probability and Statistics (Wiley)*. <https://books.google.co.uk/books?id=MqEZAQAIAAJ>
- Prasad, S. K., Jess, D. B., Van Doorselaere, T., et al. 2017, *ApJ*, 847, 5, doi: [10.3847/1538-4357/aa86b5](https://doi.org/10.3847/1538-4357/aa86b5)

- Priest, E. R., Phillips, K. J. H., & Haines, M. G. 1991, *Philosophical Transactions: Physical Sciences and Engineering*, 336, 363. <http://www.jstor.org/stable/53823>
- Procházka, O., Reid, A., Milligan, R. O., et al. 2018, *ApJ*, 862, 76, doi: [10.3847/1538-4357/aaca37](https://doi.org/10.3847/1538-4357/aaca37)
- Radox. 2013, Radox Technology: HaBio: Queen's University Belfast. <https://www.qub.ac.uk/sites/habio/HaBioStudy/RadoxLaboratories/RadoxTechnology/>
- Reale, F. 2014, *Living Reviews in Solar Physics*, 11, 4, doi: [10.12942/lrsp-2014-4](https://doi.org/10.12942/lrsp-2014-4)
- Reale, F. 2016, *ApJL*, 826, L20, doi: [10.3847/2041-8205/826/2/L20](https://doi.org/10.3847/2041-8205/826/2/L20)
- Reid, I. N., & Hawley, S. L. 2005, *New light on dark stars : red dwarfs, low-mass stars, brown dwarfs* (Springer-Verlag Berlin Heidelberg), doi: [10.1007/3-540-27610-6](https://doi.org/10.1007/3-540-27610-6)
- Ricker, G. R., Winn, J. N., Vanderspek, R., et al. 2014, in *Society of Photo-Optical Instrumentation Engineers (SPIE) Conference Series*, Vol. 9143, *Proc. SPIE*, 914320, doi: [10.1117/12.2063489](https://doi.org/10.1117/12.2063489)
- Robinson, R. D., Carpenter, K. G., & Percival, J. W. 1999, *ApJ*, 516, 916, doi: [10.1086/307133](https://doi.org/10.1086/307133)
- Robinson, R. D., Carpenter, K. G., Percival, J. W., & Bookbinder, J. A. 1995, *ApJ*, 451, 795, doi: [10.1086/176266](https://doi.org/10.1086/176266)
- Rodríguez, E., Rodríguez-López, C., López-González, M. J., et al. 2016, *MNRAS*, 457, 1851, doi: [10.1093/mnras/stw033](https://doi.org/10.1093/mnras/stw033)
- Rodríguez-López, C., MacDonald, J., Amado, P. J., Moya, A., & Mullan, D. 2014, *MNRAS*, 438, 2371, doi: [10.1093/mnras/stt2352](https://doi.org/10.1093/mnras/stt2352)
- Ryle, M., & Vonberg, D. D. 1946, *Nature*, 158, 339, doi: [10.1038/158339b0](https://doi.org/10.1038/158339b0)
- Saad Saoud, T., Moindjie, S., Munteanu, D., & Autran, J. 2016, *Microelectronics Reliability*, 64, 68, doi: <https://doi.org/10.1016/j.microrel.2016.07.138>
- Sakamoto, Y., Tsuneta, S., & Vekstein, G. 2008, *The Astrophysical Journal*, 689, 1421, doi: [10.1086/592488](https://doi.org/10.1086/592488)
- Sarkar, A., & Walsh, R. W. 2008, *The Astrophysical Journal*, 683, 516, doi: [10.1086/589552](https://doi.org/10.1086/589552)
- Sarkar, A., & Walsh, R. W. 2009, *ApJ*, 699, 1480, doi: [10.1088/0004-637X/699/2/1480](https://doi.org/10.1088/0004-637X/699/2/1480)
- Schad, T. 2017, *Solar Physics*, 292, 132, doi: [10.1007/s11207-017-1153-9](https://doi.org/10.1007/s11207-017-1153-9)
- Schmitt, J. H. M. M., Kanbach, G., Rau, A., & Steinle, H. 2016, *A&A*, 589, A48, doi: [10.1051/0004-6361/201628199](https://doi.org/10.1051/0004-6361/201628199)
- Shapiro, L., & Stockman, G. 2001, *Computer Vision* (Prentice Hall). <https://books.google.co.uk/books?id=FftDAQAIAAJ>
- Shi, C., Velli, M., & Tenerani, A. 2018, *ApJ*, 859, 83, doi: [10.3847/1538-4357/aabd83](https://doi.org/10.3847/1538-4357/aabd83)

- Shibata, K., & Magara, T. 2011, *Living Reviews in Solar Physics*, 8, 6, doi: [10.12942/lrsp-2011-6](https://doi.org/10.12942/lrsp-2011-6)
- Shibayama, T., Maehara, H., Notsu, S., et al. 2013, *The Astrophysical Journal Supplement Series*, 209, 5, doi: [10.1088/0067-0049/209/1/5](https://doi.org/10.1088/0067-0049/209/1/5)
- Simpson, G., & Mayer-Hasselwander, H. 1986, *A&A*, 162, 340. <https://ui.adsabs.harvard.edu/abs/1986A&A...162..340S>
- Sirianni, M., Jee, M. J., Benítez, N., et al. 2005, *PASP*, 117, 1049, doi: [10.1086/444553](https://doi.org/10.1086/444553)
- Song, Y., Tian, H., Zhu, X., et al. 2020, *ApJL*, 893, L13, doi: [10.3847/2041-8213/ab83fa](https://doi.org/10.3847/2041-8213/ab83fa)
- Spanos, A. 1999, *Probability Theory and Statistical Inference: Econometric Modeling with Observational Data* (Cambridge University Press), doi: [10.1017/CBO9780511754081](https://doi.org/10.1017/CBO9780511754081)
- Spiegel, E. A., & Zahn, J. P. 1992, *A&A*, 265, 106. <https://ui.adsabs.harvard.edu/abs/1992A&A...265..106S>
- Sprinthall, R. 2012, *Basic Statistical Analysis* (Boston, MA : Allyn and Bacon)
- Stassun, K. G., Oelkers, R. J., Pepper, J., et al. 2018, *AJ*, 156, 102, doi: [10.3847/1538-3881/aad050](https://doi.org/10.3847/1538-3881/aad050)
- Suvarna, S. K., & Ansary, M. A. 2001, *Histopathology*, 39, 441, doi: <https://doi.org/10.1046/j.1365-2559.2001.01312.x>
- Sweatman, M. B., & Coombs, A. 2018, *Decoding European Palaeolithic art: Extremely ancient knowledge of precession of the equinoxes*. <https://arxiv.org/abs/1806.00046>
- Tabachnick, B. G., & Fidell, L. S. 2006, *Using Multivariate Statistics* (5th Edition) (USA: Allyn & Bacon, Inc.)
- Takahashi, H. R., Kudoh, T., Masada, Y., & Matsumoto, J. 2011, *ApJL*, 739, L53, doi: [10.1088/2041-8205/739/2/L53](https://doi.org/10.1088/2041-8205/739/2/L53)
- Tavabi, E. 2012, *Journal of Modern Physics*, 3, 1786, doi: [10.4236/jmp.2012.311223](https://doi.org/10.4236/jmp.2012.311223)
- Tenerani, A., Velli, M., Rappazzo, A. F., & Pucci, F. 2015, *ApJL*, 813, L32, doi: [10.1088/2041-8205/813/2/L32](https://doi.org/10.1088/2041-8205/813/2/L32)
- Terrell, J. 1977, *ApJL*, 213, L93, doi: [10.1086/182417](https://doi.org/10.1086/182417)
- Terzo, S., Reale, F., Miceli, M., et al. 2011, *ApJ*, 736, 111, doi: [10.1088/0004-637X/736/2/111](https://doi.org/10.1088/0004-637X/736/2/111)
- Torode, R. K. E. 1992, *Journal of the British Astronomical Association*, 102, 25. <https://ui.adsabs.harvard.edu/abs/1992JBAA..102...25T>
- Tsuneta, S., & Katsukawa, Y. 2004, *Astronomical Society of the Pacific Conference Series*, Vol. 325, *Coronal Heating with Sweet-Parker Picoflares*, 289. <https://ui.adsabs.harvard.edu/abs/2004ASPC..325..289T>

- Tsurutani, B. T., Gonzalez, W. D., Lakhina, G. S., & Alex, S. 2003, *Journal of Geophysical Research: Space Physics*, 108, doi: [10.1029/2002JA009504](https://doi.org/10.1029/2002JA009504)
- Ulrich, R. K. 1970, *ApJ*, 162, 993, doi: [10.1086/150731](https://doi.org/10.1086/150731)
- VanderPlas, J. T. 2018, *The Astrophysical Journal Supplement Series*, 236, 16, doi: [10.3847/1538-4365/aab766](https://doi.org/10.3847/1538-4365/aab766)
- Vaughan, S. 2012, *Philosophical Transactions of the Royal Society of London Series A*, 371, 20110549, doi: [10.1098/rsta.2011.0549](https://doi.org/10.1098/rsta.2011.0549)
- Vekstein, G. 2009, *A&A*, 499, L5, doi: [10.1051/0004-6361/200911872](https://doi.org/10.1051/0004-6361/200911872)
- Viall, N. M., & Klimchuk, J. A. 2011, *The Astrophysical Journal*, 738, 24, doi: [10.1088/0004-637x/738/1/24](https://doi.org/10.1088/0004-637x/738/1/24)
- . 2012, *The Astrophysical Journal*, 753, 35, doi: [10.1088/0004-637x/753/1/35](https://doi.org/10.1088/0004-637x/753/1/35)
- . 2013, *The Astrophysical Journal*, 771, 115, doi: [10.1088/0004-637x/771/2/115](https://doi.org/10.1088/0004-637x/771/2/115)
- . 2015, *The Astrophysical Journal*, 799, 58, doi: [10.1088/0004-637x/799/1/58](https://doi.org/10.1088/0004-637x/799/1/58)
- . 2016, *The Astrophysical Journal*, 828, 76, doi: [10.3847/0004-637x/828/2/76](https://doi.org/10.3847/0004-637x/828/2/76)
- . 2017, *The Astrophysical Journal*, 842, 108, doi: [10.3847/1538-4357/aa7137](https://doi.org/10.3847/1538-4357/aa7137)
- Vlahos, L., Georgoulis, M., Kluiving, R., & Paschos, P. 1995, *A&A*, 299, 897. <https://ui.adsabs.harvard.edu/abs/1995A&A...299..897V>
- Vršnak, B., Sudar, D., & Ruždjak, D. 2005, *A&A*, 435, 1149, doi: [10.1051/0004-6361:20042166](https://doi.org/10.1051/0004-6361:20042166)
- Walker, C., Hall, J., Allen, L., et al. 2020, in *Bulletin of the American Astronomical Society*, Vol. 52, 0206, doi: [10.3847/25c2cfcb.346793b8](https://doi.org/10.3847/25c2cfcb.346793b8)
- Walker, C. Rosa, R. R. C. J. E. R. 2012, *Journal of Computational Interdisciplinary Sciences*, 3, doi: [10.6062/jcis.2012.03.03.0059](https://doi.org/10.6062/jcis.2012.03.03.0059)
- Walkowicz, L. M., Basri, G., Batalha, N., et al. 2011, *AJ*, 141, 50, doi: [10.1088/0004-6256/141/2/50](https://doi.org/10.1088/0004-6256/141/2/50)
- Webb, N. A., Coriat, M., Traulsen, I., et al. 2020, *A&A*, 641, A136, doi: [10.1051/0004-6361/201937353](https://doi.org/10.1051/0004-6361/201937353)
- Weber, E. J., & Davis, Leverett, J. 1967, *ApJ*, 148, 217, doi: [10.1086/149138](https://doi.org/10.1086/149138)
- Welch, P. D. 1961, *IBM Journal of Research and Development*, 5, 141, doi: [10.1147/rd.52.0141](https://doi.org/10.1147/rd.52.0141)
- Welsh, B. Y., Wheatley, J., Browne, S. E., et al. 2006, *A&A*, 458, 921, doi: [10.1051/0004-6361:20065304](https://doi.org/10.1051/0004-6361:20065304)
- Westfall, R. S. 1980, *Isis*, 71, 109. <http://www.jstor.org/stable/230315>

- Wheatley, P. J., West, R. G., Goad, M. R., et al. 2018, MNRAS, 475, 4476, doi: [10.1093/mnras/stx2836](https://doi.org/10.1093/mnras/stx2836)
- Winebarger, A. R., Emslie, A. G., Mariska, J. T., & Warren, H. P. 2002, ApJ, 565, 1298, doi: [10.1086/324714](https://doi.org/10.1086/324714)
- Withbroe, G. L. 1988, ApJ, 325, 442, doi: [10.1086/166015](https://doi.org/10.1086/166015)
- Woods, T. N., Kopp, G., & Chamberlin, P. C. 2006, Journal of Geophysical Research (Space Physics), 111, A10S14, doi: [10.1029/2005JA011507](https://doi.org/10.1029/2005JA011507)
- Wright, N. J., & Drake, J. J. 2016, Nature, 535, 526, doi: [10.1038/nature18638](https://doi.org/10.1038/nature18638)
- Wright, N. J., Newton, E. R., Williams, P. K. G., Drake, J. J., & Yadav, R. K. 2018, MNRAS, 479, 2351, doi: [10.1093/mnras/sty1670](https://doi.org/10.1093/mnras/sty1670)
- Yang, H., Liu, J., Gao, Q., et al. 2017, The Astrophysical Journal, 849, 36, doi: [10.3847/1538-4357/aa8ea2](https://doi.org/10.3847/1538-4357/aa8ea2)
- Yao, J. M., Manchester, R. N., & Wang, N. 2017, MNRAS, 468, 3289, doi: [10.1093/mnras/stx729](https://doi.org/10.1093/mnras/stx729)
- Zharkova, V., IPSON, S., BENKHALIL, A., & ZHARKOV, S. 2005, Artificial Intelligence Review, 23, 209, doi: [10.1007/s10462-004-4104-4](https://doi.org/10.1007/s10462-004-4104-4)
- Zmuidzinas, J. 2015, ApJ, 813, 17, doi: [10.1088/0004-637X/813/1/17](https://doi.org/10.1088/0004-637X/813/1/17)

ACKNOWLEDGEMENTS

It's been a funny four years. Even in normal circumstances, a PhD is considered a pretty stressful time. A large portion of my PhD took place in the midst of a global pandemic. Generally speaking, living through a major historical event is not conducive to doing your best work. Thankfully, I was surrounded by brilliant people who made the whole process a lot easier. I regret that I lack the words to adequately express my gratitude, but I shall try my best.

Thanks to Dave for all of his advice, encouragement, and excellent supervision. You were a fantastic supervisor, and I'm very grateful for everything you've taught me. Thanks as well to Michail Mathioudakis for his advice throughout my PhD, and for suggesting I investigate a nanoflare link to periodic brightenings. Thanks to Chris Watson, for his help in facilitating a collaboration with the NGTS, and for his patience while explaining the basic principles of observing (at a point where I should probably have already understood them). Thanks to all the administrative staff in the Physics department, who keep the department running and helped me numerous times throughout my PhD. Special thanks to Emma Finnegan, for all her hard work which made the submission process a breeze. Thanks to the NGTS consortium, for their input to my published work, and access to their data products. Thanks to Radox and Invest NI for their funding and support. Thanks to the QUB PGR awards team for a 3 month stipend extension to mitigate delays induced by the pandemic. Thanks to NASA for the use of their SDO image of the sun. I'm very grateful to everyone who turned up to the daily coffee calls during the Covid lockdown. Those daily video calls were a great lifeline during an isolated period. Special thanks to Meg Schwamb for organising those calls, and generally working to keep the department cohesive and in touch even before the onset of a global pandemic.

I'd also like to thank my dear friends/desk-wine enthusiasts Shannon and Steph. From the heady pre-pandemic days of (greatly) extended coffee breaks and daily Tesco meal deals, to the lockdown-induced move to a group chat, you made the PhD a lot more fun and were always there for reassurance that I was in fact a real scientist. An additional thanks to Steph, for their excellent proofreading skills on the first draft of this work. This helped me to reign in my errant use of commas, Capital letters, and so on without which, this, Thesis would have, probably, looked, like , this.

Thanks to everyone at Pfizer, and all the volunteers and staff involved in the Covid vaccination program. Turns out it's a lot easier to focus on work when your underlying sense of dread is returned to its normal mildly crippling level.

Saving the most important people for the end, I'd like to thank my family. Thanks Mum and Dad. You encouraged me my entire life to work hard, and always supported my curiosity. All of my achievements are thanks to you. Thanks Kathryn for all of your encouragement. You're the best sister I could ever ask for. Finally, thanks to my fiancée Amber for her constant support and unwavering belief in me. I love you utterly!